Experimental and numerical investigation of air blast mitigation of single and multi-scale structures

Omar Ghareeb M Alshammari

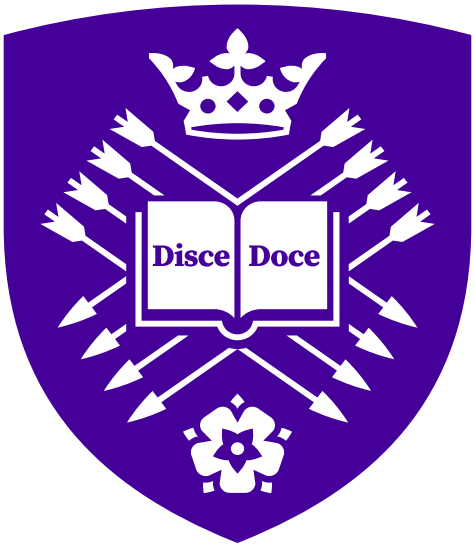

A thesis is submitted towards the fulfilment requirements for the degree of

Doctor of Philosophy in

The Department of Civil and Structural Engineering

At The University of Sheffield

October 2023

Declaration

I, Omar Ghareeb M Alshammari, declare that all the material included in this thesis is my own work, except where it is clearly referenced to others.

October 23, 2023

Abstract

In order to protect civilians and infrastructure against the damaging effects of explosions, understanding blast wave interactions with structures in complex environments is fundamental for effective blast mitigation development. Obstructing the direct propagation of blast waves towards targets using a small, porous structure formed as an array/matrix of smaller structural elements is usually a preferred protective strategy in urban environments due to issues related to sustainability including material use and public perceptions of hazard.

The blast wave mitigation induced by interaction with obstacles in downstream region is primarily dominated by configuration- shapes and lengths of individual elements- of the obstacle itself. Whilst the blast wave mitigation behaviour of obstacles arranged as an array/matrix comprising single-length scale and regular shape is well known, the mitigation behaviour of obstacles arranged as fractals involving multi-scale length and self-similarity features is not clear yet.

The primary aim of this thesis was to extensively understand the blast mitigation behaviour of fractal obstacles of increasing complexity for developing protection strategies and predictive methods. To achieve this, an experiment on blast wave interaction with fractal obstacles was conducted to measure the blast attenuation and observe the mitigation behaviour. CFD numerical models simulating air blast loading in free-field and complex interaction scenarios were validated against experimental data. Utilising the validated numerical models, the mitigation behaviour of blast loading through blast-obstacle

interactions process was studied for single obstacle case, and fractal obstacles with increasing complexity scenarios.

The experimental findings exhibited that obstacles with shapes closely resembling true fractals can induce local significant blast attenuation up to 26% in pressure and 16% in peak specific impulse attributed to a mechanism known as trapping. This indicated that the mechanism of blast mitigation of fractal obstacles of increasing complexity is fundamentally different from singular or arrays of regular obstacles. Furthermore, blast wave parameters behind different arrangements of fractal obstacles were found to be inherently determinable.

The numerical simulations revealed that the development of a complex flow-field downstream is comprised of two zones: wave shadowing and wave interference in which mitigation patterns, specifically behind the single obstacle, can be predictable despite the complex interactions. It was also shown that increasing the fractal obstacles complexity can produce a better impedance and substantially alter the direction of the incident wave. This has demonstrated that the effectiveness of obstructing a blast wave, measured in terms of blast intensity mitigation, is classified according to the fractal complexity configuration from the lowest level to the highest level. The peak reduction in pressure and specific impulse in the downstream region of fractal obstacle with highest level of complexity was numerically found to be 60% and 40% respectively. Therefore, the finding of this can be utilised in structural design and optimization of protective structures with improved blast mitigation.

Acknowledgement

Firstly, I would like to express my gratitude to my supervisors, Dr Samuel Rigby and Prof. Samuel Clarke, for their intellectual assistance on all of my academic and career levels. You have brilliantly supported me during all stages of my PhD, during which I have gained significant knowledge and developed excellent skills. I will be eternally thankful to you, and I hope we can continue to learn from and work together in the future.
Sam Rigby, your brilliant demonstration of the Blast course in 2018 inspired me to pursue my PhD in blast protection engineering and since ever I have been aspiring to be Dr and blast protection engineer which now it is becoming true by completing this thesis. Who can imagine that little chats during break time in a class could lead to a project ending with a scientific thesis? I learnt from you so much in many ways. You have been so generous, friendly, and tolerant. You are a great role model in academia. Sam Clarke, your insightful look into my work is your brilliant fingerprint which had a magnificent effect on my success. I appreciate every single technical consultation you have provided for me. You have been so supportive and friendly to me.

Furthermore, I would like to show gratitude to Dr Obed Samuelraj Isaac, a postdoctoral researcher who joined the Blast group for 18 months. Throughout that time, you acted like a third supervisor by directing me toward success. You made great efforts running the experimental program with its details and also you helped to improve my academic and professional skills. I will hold memories of work trips to Blastech laboratory at Buxton and the nice moments we spent together in Sheffield. Thank you so much for everything.

I would like to thank the University of Hail in Saudi Arabia represented by the Royal Embassy of Saudi Arabia Cultural Bureau in London and the UK Engineering and Physical Sciences Research Council for the huge financial support of this project. Without their support, this thesis was not possible.

Also, special thanks to the Blastech team: Roy, Andrew, Jack, Ash, Richard, Tommy, Dain and Scott for running and helping with the experimental programme. Also, thanks to every member of the Blast and Impact Dynamics team, especially my colleagues in room D105. I furtherly express my thanks to my close friends in Sheffield, Dr Ismail Abuzayed, Dr Alzamzami, Dr (to be). Ibrahim Abuzayed, Dr Nasser Alanzai, Mr Abdulaziz Ayad Alharbi, and all others in the Civil and Structural Engineering department, for many hours of conversations and the fantastic times we spent together.
I would like to thank my parents, Ghareeb and Mutaah, you have always encouraged me to learn and complete my studies since childhood. I will not fulfil your rights no matter what I do. You are the heaven of this life. Also, thanks to my sisters and brothers for every little help. Many thanks to my cousins, Yousef Saud Alshammari with his brother Marrik Saud, Mutaz Eid, and Abduallah Awad Shatty for their moral support during my all studies stages.

Lastly, I wish to thank my lovely wife, Hala, the great mother of my future child, who has stayed beside me through all my travails, my absences, my fits of pique and impatience. You gave extreme support and help. You made the PhD life in Sheffield easy and pleasant. You have cared for me and arranged unforgettable holiday trips during my tough time to relieve my stress. We will not forget the memorable trips of the stunning views at Bamford Edge and Mam Tor in the peak district. I dedicate this thesis to you.

Contents

List of Figures

List of Tables

Nomenclature

A, TA	-	target area,
a_0	-	sound speed
A_{Obs}	-	frontal area of pre-fractal obstacle
α	-	angle of incident
α_k	-	learning rate of ANN model
β	-	sloping rear face angle
C_1, C_2, R_1, R_2	-	constants for JWL model
${C_D}^2$	-	drag coefficient
C_r	-	reflection coefficient
c_v	-	specific heat constant
D	-	cylinder diameter ,
		square obstacle width of pFI-1
R, SoD	-	stand-off distance from explosive center
d_o	-	distance from explosive center to obstacle face
d_t	-	distance between obstacle and target
E	-	total energy
e	-	specific internal energy
EEI	-	energy equivalent impulse
f	-	raise of structure

g_k	-	gradient of ANN learning
γ	-	specific heat ratio
H	-	height of structure
h	-	mesh resolution in CFD domain
I_{equiv}	-	equivalent peak impulse on cylindrical surface
I_f	-	factored peak impulse
I_{free}	-	peak specific impulse measured in free-field
$I_{max,obstructed}$	-	peak specific impulse measured behind obstacle
I_{ratio}	-	peak specific impulse ratio
I_s, I_{so}	-	incident specific impulse
I_s^-	-	negative phase impulse
I_s^+	-	positive phase impulse
L	-	Span or length,
		zone length in CFD domain
L_{eff}	-	effective length
m_n	-	predicted equivalent energy impulse ratio
M_s	-	incident Mach number
MSE	-	mean square error
N	-	resolution level in CFD domain
o_n	-	target equivalent energy impulse ratio
OR	-	obstruction ratio
P_0	-	stagnation pressure
P_o	-	ambient pressure
P_{equvi}	-	equivalent peak pressure on cylindrical surface
P_f	-	factored peak pressure
P_{free}	-	peak overpressure measured in free-field
P_{ideal}	-	undisturbed reflected pressure
$P_{max,obstructed}$	-	Peak pressure measured behind obstacle

P_r	-	reflected overpressure
P_{ratio}	-	peak overpressure ratio
p_s	-	static blast load
P_s, P_{so}	-	incident overpressure
P_τ	-	transmitted reflected pressure
q_s	-	dynamic pressure
R	-	specific gas constant
R^2	-	coefficients of determination
R_{Obs}	-	radius of the blast wave
${R_t}^2$	-	Young's correlation coefficient
ρ	-	density
ρ_0	-	initial density
S	-	dimensions of an object
t	-	time
T	-	Temperature
t_a	-	arrival time
t_c	-	clearing time
t_d	-	decay time
T_n	-	natural frequency time of a structural system
θ	-	inclination angle of barrier
TL	-	target length
U	-	shock velocity
v	-	vector velocity
W	-	explosive mass
x_k	-	vector of weights and biases in ANN
Z, Z_R, Z_{do}	-	scaled distance $((R \text{ or } d_o)/W^{1/3})$

Chapter 1

Introduction

1.1 Background and Motivation

In the mid-20th century, engineers tasked with designing structures for resilience against blast effects were accustomed to evaluating situations of relative simplicity, viz., large-scale (e.g. nuclear) blasts detonated at large distances from the target structure. For such scenarios, simple formulations, available in textbooks and design codes, were sufficient to specify the loading that the structure would be subjected to. But ever since, with a marked increase in both terrorist activity and urbanisation, the challenge has shifted to smaller, targeted explosions in crowded urban environments. Such malicious attacks using high explosives would have a devastating impact on human life and infrastructure as seen in the detonation of 2200 kg of explosives in front of Alfred P. Murrah federal building in Oklahoma City, Oklahoma, USA (Irving 1995) which left 168 casualties and damaged 324 surrounding buildings, and also the bombing of Norwegian government buildings in Oslo (950 kg of ANFO), on 22nd July 2011, which killed 8 people and left 209 injured.

Person-borne explosives, such as those at Istanbul Airport (June 2016, 45 fatalities), Manchester Arena (May 2017, 22 fatalities), and the failed bombing of the London Underground (September 2017), have brought attention to the increasing tendency of terrorist

organisations to target - and consequently the increasing demand to protect - transport hubs and crowded public places.

Yet, the challenge of blast protection engineering is not restricted to malevolent attacks. There have been a number of severe accidental explosions on a big scale, including those in Hemel Hempstead, United Kingdom (2005), Tianjin, China (2015), Beirut, Lebanon - approximately, 2750 tones of Ammonium Nitrate - (2020), and the present conflict in Ukraine, which have resulted in substantial losses of life and high expenses for damaged property and businesses highlighting the need to better understand explosions in complex urban scenarios situations.

With the aim of protecting buildings and their occupants that may be exposed to an explosion, various forms of protective structures are often erected around target buildings to provide perimeter protection as a form of passive mitigation. Blast wave mitigation occurs as a combination of blast wave reflection by the front face of the protective barrier, blast energy absorption due to the deformation of the (flexible) barrier, diffraction around edges, and transmission through a permeable surface or through the openings in the protective structure. In addition to this, the interference between the transmitted and diffracted waves in certain regions behind the protective structure can enhance the level of mitigation. This describes a typical blast wave interaction with a barrier.

Now, solid walls have been considered a common type of protective structure over the last few decades. However, the interaction of a blast wave with a solid wall of finite width leads to a strong reflection and diffraction around the free edges, allowing the wave to propagate further behind the wall, resulting in complex wave patterns (such as the formation of a Mach stem which can result in load amplification (Beyer 1986)). In addition, solid walls do not simply fit into an urban landscape because of the additional risk of fragmentation on catastrophic failure (Zong et al. 2017). Clearly, these massive, robust structures pay little consideration to sustainability aspects (including material use and perception of risk/danger amongst the general public). As a result, researchers have

begun to investigate the idea of employing small obstacles and posts, such as bollards and trees, which frequently appear in urban streetscapes, to mitigate blast waves.

Alternately, blast mitigation can also be achieved through blast-obstacle interaction when a standalone obstacle or an array of semi-infinite, nominally rigid obstacles such as a fence wall/matrix of solid obstacles (hereafter referred as multiple obstacles) are placed around or ahead of a target structure to reflect/deflect the impinging blast, thereby allowing it to propagate through openings and around the barrier's edges (Chaudhuri et al. 2013, Hao et al. 2017, Hahn et al. 2021). Here, the properties of a blast wave can be substantially reduced due to the dual aspects of diversion of the wavefront away from its primary path, and diffraction around the obstacle edge(s), inducing vortices and further diverting momentum. This reduction relies on several factors including the cross-section and shape of an obstacle (Gebbeken & Döge 2010), the blockage ratio (Skews et al. 1998, Shin & Whittaker 2019), and the location of the obstruction in blast wave path (Christiansen & Bogosian 2012).

While these factors have been found to be effective in altering the blast wave properties, it should be noted that they were characterised for single length-scale scenarios, where the relevant major dimensions of an obstacle were similar. However, mitigation from blast wave interaction with obstacles having multiple length scales and self-similarity - which can augment the ability to break down the blast wave - has not yet been investigated. Multi-scale obstacles are a cluster of individual, self-similar objects of different dimensions, each of which is a larger or smaller version of a primary shape (the original obstacle.)

The mathematical construct of a fractal has the distinct form required of multi-scale features for such an obstacle. By definition, a fractal is a mathematical concept of an object that has a self-repeating pattern embedded within itself, i.e., it is multi-scale and self-similar by definition. It is in other words, a method to generate an obstacle of increasing complexity as illustrated in Figure 1.1 – from a single obstacle in Figure 1.1a to highly complex obstacles in Figure 1.1d. Research in such blast wave interaction with multi-

scale and self-similar obstacles is still limited and in its infancy. However, recent studies into mitigation of blast due to interaction with plants and hedges - naturally occurring fractal-like structures- (Gebbeken et al. 2017, Warnstedt & Gebbeken 2020, Nguyen-Van et al. 2021, Tomasz et al. 2022) indicate that the concept of self-similarity and multi-scale features, inherent in fractal shapes, holds promise. Hence, it is imperative to study the interaction of blast waves with fractals with the main goal of better understanding these novel, sustainable, nature-inspired blast protection techniques.

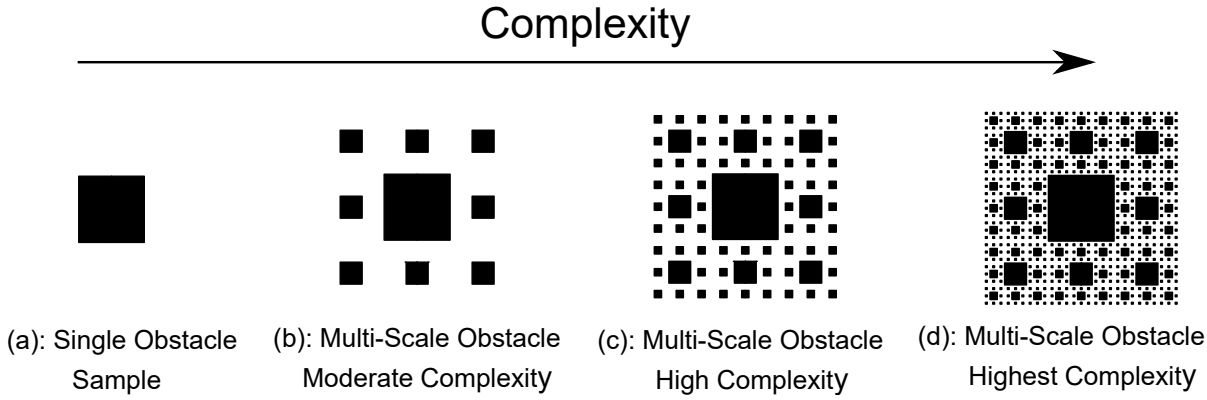

Figure 1.1: Formation of obstacles with increasing complexity from **(a)** to **(d)**

Fractals have been used for several engineering applications such as for transmission antennae, industrial mixing, and for efficient heat exchanger design. In fluid flow applications, fractal obstacles with increasing complexity were seen to increase downstream turbulence and vorticity in flow problems (Higham & Vaidheeswaran 2022). This leads to the main scientific question of this thesis: *Can fractal obstacles of increasing complexity increase the propensity for a blast wave to divert energy away from its original path, thereby mitigating the blast load downstream of the obstacle?* If so, *what then are the characteristics of the blast mitigation behaviour of fractal obstacles?*

To date, there has been no research into the effect of obstacles with fractal patterns of increasing complexity on the propagation of blast waves, nor have there been any attempts to quantify attenuation and characterise the mitigation behaviour for protection purposes. Thus, the content of the thesis focuses on experimentally and numerically investigating

the blast mitigation behaviour resulting from the interaction of blast waves with fractal obstacles with increasing complexity.

1.2 Aim and objectives

This thesis aims to develop a comprehensive understanding of the blast mitigation behaviour of fractal obstacles of increasing complexity. This will be achieved through a combined experimental and numerical study in order to provide new insights into protection strategies and predictive techniques.

This thesis, therefore, has the following main objectives

1. To review current literature on blast mitigation arising from interaction with obstacles where the behaviour and prediction of mitigation are discussed, together with the key mechanisms and factors governing the attenuation.

2. To experimentally quantify the blast wave attenuation after interaction with a functional arrangement of different fractal obstacles of increasing complexity and understand the performance of each obstacle, and develop relations for blast loading mitigation behind fractals.

3. To implement a high-fidelity CFD numerical model that can accurately simulate the propagation of blast waves both in free-field and complex- domains involving interaction with fractal obstacles having various levels of complexity, with a view to accurately predicting the blast loading behind them.

4. To perform a parametric numerical study of the interaction of blast waves of different strengths with a single obstacle to understand and characterise the altered flow field in its downstream region due to wave interference with a view to developing a fast-running tool to predict blast mitigation behind the obstacle.

5. To perform numerical analysis of blast wave interaction with fractal obstacles of

increasing complexity to explain the precise mechanisms governing blast mitigation, and to study the role of increasing complexity on attenuation patterns, and to characterise the spatial bounds of mitigation due to fractals in the downstream.

1.3 Thesis outline

The remainder of the thesis is organised into the following chapters:

Chapter 2 – Literature review

This chapter provides a theoretical consideration of blast loading generation and the aspects of blast loading mitigation acting on targets. Blast loading reduction due to direct interaction of blast wave with structural target itself, and the indirect interaction of obstructing techniques of blast wave propagation are discussed. Key mechanisms governing blast loading mitigation are identified for highlighting the role blast wave-obstacle interaction plays in protecting targets.

Chapter 3 – Experimental investigation of blast mitigation of pre-fractal obstacles

This chapter describes experiments conducted to obtain the attenuation of blast waves after interacting with fractal obstacles of increasing complexity. It further explores the mechanics of blast-obstacle interaction with complex obstacles to better understand blast mitigation behaviour as an aid to developing a fast prediction tool for quick design calculations, and to also effectively evaluate the role of increasing fractal complexity on blast attenuation.

Chapter 4 – Air blast modelling in Apollo blastsimulator

This chapter is concerned with modelling explosives using a computational fluid dynamic (CFD) solver. The sensitivity of pre-processing techniques such as computational mesh refinement, on the propagation of blast waves in free-field and in the presence of obstacles is studied. Changes to the blast loading parameters such

as overpressure and specific impulse due to the presence of the obstacles are then validated against experimental data of Chapter 3.

Chapter 5 – Numerical analysis of blast mitigation of single obstacle

This chapter provides an insightful understanding of the blast loading mitigation behaviour brought about by a single obstacle using the previously established computational model. A parametric study was undertaken to explore the influence of key factors, using the experimental results from Chapter 3 as a guideline. This was then used to develop a predictive approach of blast mitigation in the downstream region of such an obstacle using an artificial neural network (ANN).

Chapter 6 – Numerical analysis of blast mitigation of multi-obstacles

This chapter provides a complementary explanation of the promising findings of Chapter 3 by numerically investigating the blast wave interaction with fractal obstacles of increasing complexity. The mechanisms governing the blast attenuation were demonstrated, and the role of increasing fractal shape complexity in enhancing the mitigation is then described. Finally, the relationship between spatial bounds of mitigation at downstream and fractal complexity is characterised, to serve as an aid for blast safety design.

Chapter 7 – Summary and Conclusion

This chapter summarises the present work and provides recommendations for future research

1.4 Published work

The work provided in this thesis has been published in peer-reviewed academic journals and is listed below:

- Alshammari OG, Isaac OS, Clarke SD and Rigby SE (2022), 'Mitigation of blast loading through blast–obstacle interaction', *International Journal of Protective Structures*: 20414196221115869.

- Isaac OS, Alshammari OG, Pickering EG, Clarke SD and Rigby SE (2022), 'Blast wave interaction with structures–An overview', *International Journal of Protective Structures*: 20414196221118595.

- Isaac, O.S., Alshammari, O.G., Clarke, S.D. and Rigby, S.E. (2022), 'Experimental investigation of blast mitigation of pre-fractal obstacles', *International Journal of Protective Structures*: p.20414196221144066.

- Alshammari OG, Isaac OS, Clarke SD and Rigby SE (2023),'Numerical modelling of blast mitigation of pre-fractal obstacles', *Submitted for publication in International Journal of Protective Structures*

Chapter 2

Literature review

2.1 Introduction

This chapter provides a comprehensive overview of recent literature on blast mitigation due to interaction with structures. The main focus of this chapter is to provide a brief theoretical considerations of blast loading which explains the formulation of blast wave. Then, the aspects of blast mitigation behaviours caused by two different types of interactions with structures involving loading mitigation and predictive tools are provided. This chapter indicates the importance of blast-obstacle interaction approach in reducing the blast loading and revels the necessity for better understanding and developing new approach for protective structure design.The primary content of this chapter was derived from the published paper titled: ***Blast wave interaction with structures–An overview***, as elucidated in Chapter 1 (refer to section 1.4).

2.2 Theoretical consideration of blast loading

As the shock front advances from the source, the explosion energy is rapidly distributed over an increasingly larger volume, leading to a reduction in the peak overpressure p_s and

the impulse of the blast wave I_s.The blast wave duration increases with distance, however, the impulse of the blast wave, which is the temporal integral of pressure with respect to time, also reduces as the reduction in pressure with distance is much more substantial than the increase in duration. An illustration demonstrating such a decay of pressure values along a radial line from the centre of the explosion, at different time instances, may be seen in Fig. 2.1a. At each point in the affected region, following the initial pressure jump, the blast pressure exponentially decays and undershoots below the ambient values, and then recovers comparatively slowly. This demarcates the positive and negative phases of the blast wave as depicted in Fig. 2.1b. It is worth noting that the 'shock wave' refers to the infinitesimal region across which the pressure increases instantaneously, whereas the 'blast wave' is the entire region over which the blast wind acts (Fig. 2.1b).

On interacting with a rigid surface, the shock pressure enhances owing to the drop in the kinetic energy of the air molecules. This enhancement, called reflected overpressure p_r, depends on the compliance of the surface, and the incident angle α at which the shock wave impinges the surface. It is also influenced by the value of the incident pressure itself as shock wave reflection, unlike acoustic wave reflection, is a highly non-linear process. It should be noted that as the scaled stand-off distance increases, it tends to be an acoustic interaction. These reflected pressure values may be obtained (Kinney 1985) in terms of the reflection coefficient, C_r, as shown in Fig. 2.2c. It is to be noted that the use of the term overpressure is preferred in blast literature as the pressure difference from the ambient level is what causes damage to structures (Needham 2010). For the sake of convenience, in this thesis, 'overpressure' has been used only where the meaning is not clear.

Types of Loading: The major contribution to the total blast load on a building arises from the front face (Glasstone & Dolan 1977, Gauch et al. 2019), and so this review focuses mostly on frontal loads. On the front face of a structure being impacted by a blast wave, the pressure instantly rises to the said reflected value p_r, and then begins to decay at a

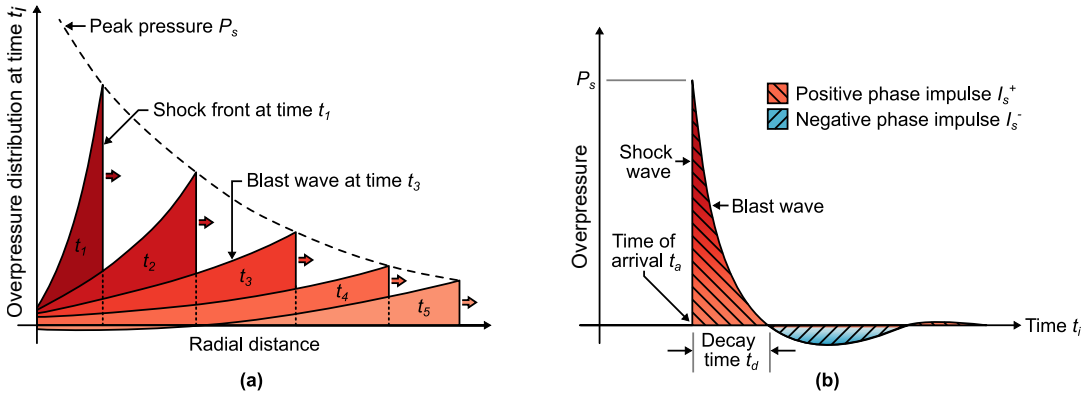

Figure 2.1: A graphical representation of the overpressure evolution resulting from a blast wave shown **(a)** spatially at a given time t_i and **(b)** temporally at a fixed point.

rate that initially depends on the intensity of the blast itself, and also on the shape and size of the structure. The wave then progressively loads the side walls and subsequently the rear portion of the structure, eventually engulfing the entire unit. This entire process is referred to as diffraction loading (Norris et al. 1959). After the passage of the shock wave, (the momentum of) the blast wind loads the structure, and the stagnation pressure (p_0, see Fig. 2.3), which is the sum of the static blast load p_s and the drag coefficient C_D[1] multiplied by the dynamic pressure q_s, causes drag loading on the structure. The negative phase of the blast wind then exerts a load on the structure in the opposite direction of the initial blast load.

While diffraction loading is relevant for short duration blast waves, drag loading, on the other hand, is the dominant contributor to the total load for longer duration blasts commonly encountered in atomic and nuclear explosions. The negative phase load, although typically much lower, can still influence structural response. It can be highly relevant for flexible structures (Rigby et al. 2017b) based on relative values of the decay time of the blast load and the response time of the structure. Nevertheless, to keep things simple, the contribution of the negative phase to the total load has been excluded from the scope

[1]Usually ignored, as C_D is taken to be 1 for the front face.

of this review.

2.3 Blast wave interaction with structures

2.3.1 Overview

The loads on a structure as a result of a high explosive detonation, can be due to (i) the impact of the shock wave and the drag force from the blast wave, (ii) the impact of the flying debris set in motion by the wind behind the shock wave (Gebbeken et al. 2017), and/or (iii) due to the ground shock (Barakat & Hetherington 1999, Beshara 1994*b*). This section presents a comprehensive overview of recent literature on the first aspect, restricting this to address aspects pertaining to (air) pressure loading on a structure.

Early research on blast loading studies predominantly report the use of high explosives in the range of kt or Mt TNT equivalent to replicate the effects of a nuclear explosion (Beshara 1994*a*). Therefore, blast effects were typically measured at stand-off distances that were hundreds of metres away (Biggs 1964, Norris et al. 1959). This would allow for sufficient time for the spherical shock front to transition into a planar wave relative to the size of the domestic homes, nuclear shelters, etc. that were usually tested (illustrated at time t_4 in Fig. 2.2a.) Under such conditions, relatively simple semi-empirical methods found in blast textbooks (Kinney 1985, Kingery & Bulmash 1984, Hyde 1991) could be made use of to obtain the total loading on the structures. Further details on such formulations may be found in the review by Beshara (1994*a*,*b*).

Over the last few decades, however, an increase in terrorist activity has led to blast loading and blast resilient design becoming an increasing aspect of modern structural engineering. This was not only for high risk buildings (FEMA 2007, Remennikov 2003), but also for 'soft' civilian infrastructure. In a congested urban environment, where the explosives are more likely than not to be set-off on a street, or in a parking lot, the shock wave radii on impact would be comparable to the dimensions of the structure itself. For such conditions,

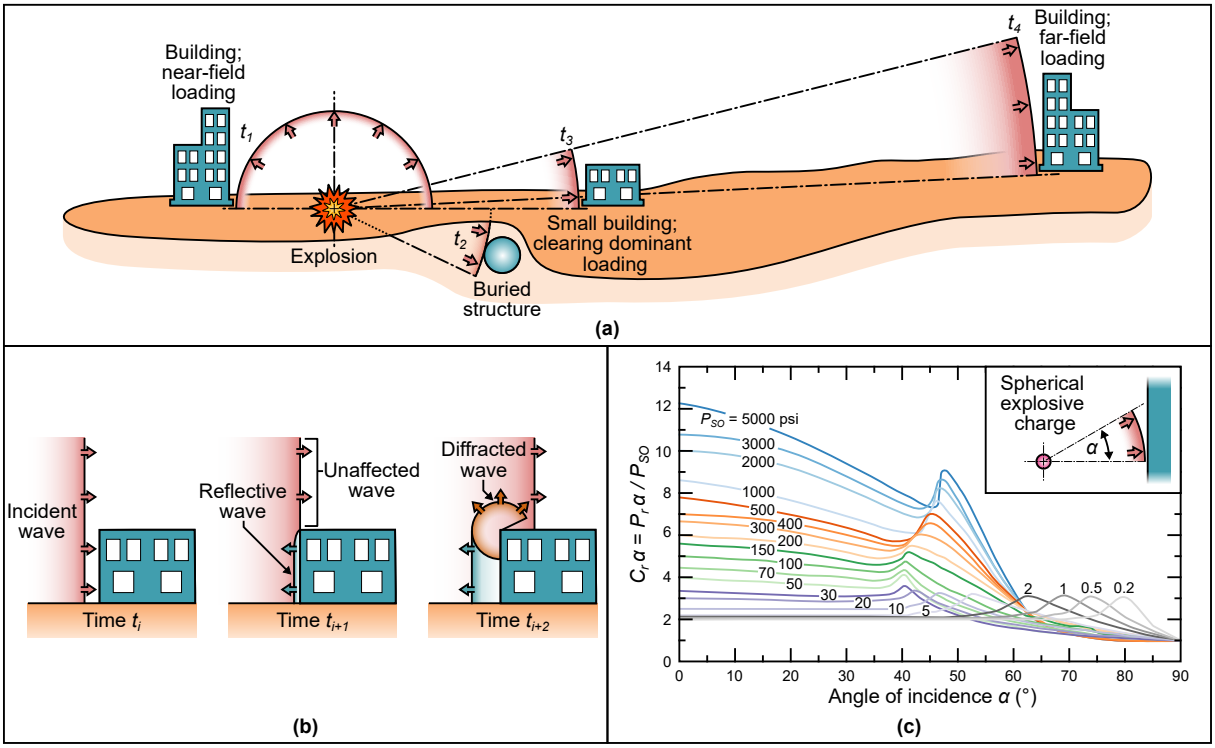

Figure 2.2: 1. (a) An illustration demonstrating the different loading types resulting from a single explosion as a function of their stand-off distance and building size. (b) A schematic representation of the development of the clearing effect on a small building. (c) Graph illustrating the effect of the angle of incidence(α) of the blast on the reflection coefficient C_r of a building structure (Kinney 1985).

the use of simplifying assumptions for estimating the load over the entire building would no longer be possible. Instead, a spatially varying, time-dependent pressure value would have to be evaluated at each point on the structure (e.g., at time t_1 in Fig. 2.2a.) This level of detail is necessary to arrive at a more effective and efficient design for such non-planar loads. It is therefore clear that depending on the stand-off distance and the relative size of the building, we can have different scenarios for the evaluation of blast loads, ranging from very simple cases to complex ones. It is also common in blast resilient design to incorporate passive techniques to ameliorate the blast load on a structure by modifying the blast wave itself and/or the nature of its interaction with a structure.

This section presents an overview of research on characterizing the blast overpressure load given the size and shape of a structure and its distance from the site of the explosion; and the mitigation of this pressure load using passive techniques that depend on the shape/ex-

ternal profile of the structure. The following sub-sections have hence been organized as below:

- First, aspects pertaining to direct blast loading on structures of various shapes are addressed.
- The next three sub-sections cover the (indirect) loading of a planar surface after the incident blast wave has interacted with one of these:
  (i) *Quasi-2D wall-like structures/barriers*; where the length of the barrier (running perpendicular to the direction of the blast wave) exceeds the height. The length and height surpass the depth of the structure.
  (ii) *Quasi-1D pole-like structures/obstacles*; where one dimension of the structure (typically the height) exceeds the other two dimensions.
  (iii) Combinations of type *(i)* and *(ii)*, which we term here as *hybrids*.
- Finally, a sub-section containing a brief description of the methods and tools that are available to estimate the loads on a structure following a direct or indirect blast event has been included for completeness.

2.3.2 Direct Loading on Structures

2.3.2.1 Clearing Mechanism

As mentioned previously, the front face of a structure loaded by a blast wave experiences a reduction in the magnitude of pressure due to the shape of the structure. This phenomenon, which is in addition to the free-field blast pressure decay, is termed as 'clearing' (Fig. 2.2b.) and this occurs due to the presence of the free edges in a finite-sized structure. The peak reflected overpressure p_r of the blast load, however[2], does not change as

[2]Except under a narrow set of conditions (Monti 1970)

the reflection of an incident blast wave is effectively instantaneous and is unaffected by clearing (Mulligan 2018).

Now, consider a finite-sized structure such as a cuboid being impacted by a blast (Fig. 2.2b). As soon as the shock front impacts a point (or region[3]) on the front face of the cuboid, it reflects, leading to a sudden increase in pressure at that point (or region). On reflection, the direction of travel of this disturbed portion of the wave reverses, whereas in the surroundings of the cuboid the undisturbed blast front continues to travel ahead, unimpeded. There is thus a pressure discontinuity that propagates inwards from the edges of the cuboid, leading to the formation of an expansion wave to counteract the pressure gradient. Unlike the discontinuous and sudden nature of the shock wave, the expansion wave is a continuous, acoustic wave (Liepmann & Roshko 2013). Therefore, the reflected pressure is lowered progressively over the front face of the cuboid, starting from the edges and then to the center. Relative to the air velocity behind the reflected wave, the expansion (clearing) wave travels at the local sound speed. The air velocity in the reflected region being usually negligible, especially for cases where the incident and the reflected waves are planar with no other disturbances, the clearing wave can propagate quite quickly. This leads to a substantial reduction in pressure on the face of such finite object (Rigby et al. 2014b, Tyas et al. 2011) during the 'clearing time' t_c as illustrated in Fig. 2.3. At the end of this clearing phase, the pressure is usually taken to follow the stagnation pressure p_0.

2.3.2.1.1 Special Case 1: Infinitesimal and Infinite size structures

A simple scenario presents itself when the frontal portion of the structure itself can be considered small enough, relative to the radius of the wave, to resemble a point. For such a case, the incident free-field values of pressure and impulse (Kinney 1985, Kingery &

[3]depending on the curvature of the incident wave

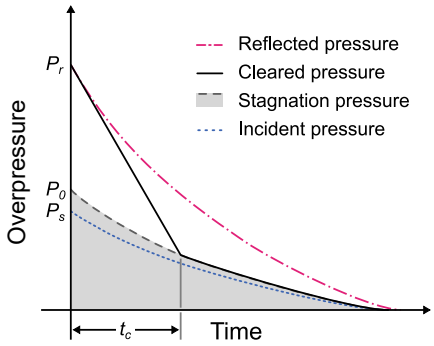

Figure 2.3: A graphical representation of the different transient pressure histories encountered in blast interaction with structures; incident/static pressure P_s, reflected pressure P_r, stagnation pressure P_0 and cleared pressure. The reduction in pressure loading due to clearing in the time period t_c is clearly illustrated.

Bulmash 1984, Hyde 1991) may be readily used to obtain the loading on the structure [4]. This is because the clearing time t_c is effectively *zero* and the cross-section area to resist the flow and attain stagnation pressure p_0 is also minuscule for such structures (cf., Fig. 2.3.)

The other extreme would be a case where the structure is infinitely large, such as the floor/ground being impacted by an air blast, leading to a complete wave reflection off the surface. The loading parameters for such a scenario would then be the ideal peak reflected overpressure and impulse values. These may be determined from standard semi-empirical methodologies (Kinney 1985, Kingery & Bulmash 1984, Hyde 1991), or from the incident pressure charts in conjunction with a ground interaction parameter (Baker 1973) or a reflection coefficient (Fig. 2.2c.)

2.3.2.1.2 Special Case 2: Finite target sizes, longer stand-off distances

For the case illustrated at time t_3 in Fig. 2.2, where the explosion occurs at a large distance from the target structure and the distance from the edges to the center of the target object

[4]Incidentally, this is how the structure for an incident blast pressure sensor is designed (Sachs & Cole 1976).

is small relative to the stand-off distance, clearing is said to occur 'completely'. This is when the clearing wave completes traversing the half-width of the structure much before the completion of the (undisturbed) blast loading phase. Under such circumstances, the clearing wave can therefore counteract and almost completely negate the increase in pressure due to reflection. This can lead to an almost undisturbed state of the blast wave (with 'clearing time' $t_c \sim 0$, see Fig. 2.3) for such structures.

This is a reasonable expectation for structures subjected to a large scale explosion, where the blast duration is quite long (thousands of milliseconds), and the clearing wave can quickly traverse the face of the structure (a few milliseconds.) For larger structures, however, assuming that an undisturbed state exists throughout the face of the structure is not valid. Nonetheless, for such cases, one may expect the clearing to begin simultaneously at all points on the face of the target. It is then sufficient to obtain a single characteristic 'clearing time' t_c for the entire structure. Over this time t_c, the overpressure may be taken to drop linearly from the peak reflected pressure p_r to the stagnation pressure p_0 as shown in Fig. 2.3. In other words, for this special case, even if the values cannot be read off directly from a chart, a single pressure trace may be easily constructed to estimate the load over the entire front face of the structure. To estimate the clearing time, several formulae, which are essentially variations of Eq. 2.1 are available, as proposed by Kinney (1985), and UFC 3-340-02 (US Department of Defence 2008).

$$t_c = \frac{\text{Representative Clearing Dimension}}{\text{Representative Velocity}} \tag{2.1}$$

This methodology has been numerically validated (Rigby et al. 2014b) for cases where the representative dimensions of the object, S, are much lower than the scaled stand-off distance[5], i.e., $S << Z$. For relatively small buildings with $S/Z << 1$, as mentioned

[5] $S < Z/250$

earlier, the clearing time is often negligible compared to the blast duration, and the loading essentially follows the incident pressure curve if the drag load is negligible. Thus, when the loading of the structure is in the impulsive regime, the *incident* impulse data would suffice to predict the response of these structures. The use of SDOF methods (Biggs 1964, US Department of Defence 2008) can then offer a means to quickly and reliably design simple structures for direct loading scenarios (Rigby et al. 2013). However, it is not always straightforward to obtain the loading curve for other complex scenarios.

2.3.2.1.3 Finite target sizes, comparable stand-off distances

Due to an increase in terrorist activity in the last few decades, the research focus has shifted from blast load estimates on isolated small shelters to that on modern buildings in an urban setting. Here, the scaled sizes of the target structures such as buildings, shopping malls, stadia would be comparable to the scaled distance from the explosive. This is because in urban terrorism, the use of explosives ranging from 5 to 1000 kg, at stand-off distances of just a few meters is commonplace. For these conditions, one can no longer assume clearing effects to equalize quickly relative to the duration of the blast wave. For example, Rose et al. (2006) numerically demonstrated that clearing waves are initiated from different free edges at different times when an explosion occurs at an oblique angle to a tall building, which will render the simple relations incorrect. And so each point on the face of the target will have a unique pressure trace, thereby rendering the previous methods unsuitable as they would be highly conservative (Rigby et al. 2013). While clearing always implies a reduction in the blast wave pressure, Rigby et al. (2012, 2014a), used an SDOF model to demonstrate that clearing can produce a counter-intuitively higher displacement for certain t_d/T_n ratios. Thus, to obtain the final response of the structure whose dynamic aspects cannot be neglected, a holistic view needs to be adopted towards understanding the clearing response. However, estimating the response of the structure is beyond the scope of this thesis.

The following sub-subsections report studies on clearing loads on objects of different

shapes under the following headings:

- Obstacles with straight faces,
- Obstacles with curved faces.

Obstacles with straight surfaces:

Several researchers have studied the role of clearing over the last few decades, primarily to understand the limitations of the extant simplified models that were previously described. New models were then proposed, which are mostly valid only for a planar wave impacting a structure. Essentially, the proposed methods attempt to approximate the start time of clearing at each point, and then the deviation from the non-cleared (reflected) pressure is predicted in terms of a relief function (Rigby et al. 2013), or Hudson parameter (Rigby et al. 2014b, Tyas et al. 2011), or a Friedlander profile (Qasrawi & Heffernan 2016). This concept of tracking the deviation from the reflected pressure is a noticeable shift from the earlier methods, where reliance on stagnation pressure as the baseline value was paramount.

Rickman & Murrell (2006) explored the validity of the simple clearing formulas (Eqn. 2.1) for a box-shaped structure whose dimensions were comparable to the stand-off distance. Experiments were conducted using C4 explosive on two structures having dimensions of $0.33 \times 0.33 \times 0.46$ m and $0.572 \times 0.572 \times 0.737$ m. A 92 g TNT equivalent charge was used at $0.323 < Z < 9.11$ m/kg$^{1/3}$ and $0.54 < Z < 5.35$ m/kg$^{1/3}$ for the smaller and the larger structure, respectively. They reported clearing pressures on the face of the structure (for Z > 1.8 m/kg$^{1/3}$) that were far lower than the stagnation pressures, which was contrary to the conventional thinking of that day. They concurred that this may be due to the disturbance introduced in the flow field by the structure. To account for this experimental finding into a model for the clearing pressure, the authors then proposed a relief function, defined as the difference between the actual pressure on the face of a structure and the

un-cleared (ConWep[6]) reflected pressure value. Now, to use the relief function, the time instant from which the pressure starts deviating from the ConWep value is required. For this, they proposed the use of an empirical formula for the velocity of the clearing wave from which the clearing initiation time may be obtained. The empirical relief function was then successfully validated for stand-off distances ranging from 0.82 m to 5.5 m for a 92 g TNT equivalent charge.

Tyas et al. (2011) show how clearing reduces the average impulse over a finite sized target when the stand-off distances are increased (Z = 6–14.9 m/kg$^{1/3}$). They then proposed a method to calculate the load on a finite sized object, similar to the methodology adopted by Rickman & Murrell (2006). Essentially, this method was based on the work of Hudson (1955) that had largely been overlooked. Hudson's method was used to account for waves arriving at a given point from each edge, which were then combined using simple linear superposition. Excellent agreement with experimental data was found as shown in Fig. 2.4. The authors suggest that the overestimated pressure drop seen in the latter stages could be the result of the simplifying assumptions that were used, viz., Hudson's method to calculate speed, and the use of linear superposition. Overall, the prediction of the clearing was seen to improve with increasing stand-off distance as the wave tended towards becoming a weak, planar shock. This modified Hudson's approach was later validated using large-scale test data as well (Rigby et al. 2017a). Here again, it is worth noticing in Fig. 2.4 that the pressure, on completion of clearing, does not follow the stagnation pressure as had been originally postulated.

Subsequent to the experimental validation by Tyas et al. (2011), Rigby et al. (2014b) presented a refined version of the Hudson (1955) clearing theory. They showed for conditions typical of far-field (Z = 8 m/kg$^{1/3}$) i.e. a weak, planar shock, that diffraction waves do

[6]an empirical blast model used to calculate blast wave parameters based on Kingery and Bulmash equations (Hyde 1991)

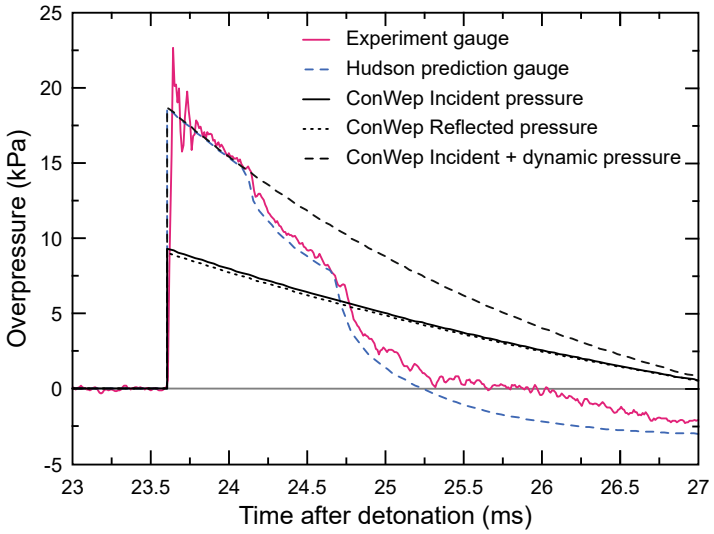

Figure 2.4: A plot showing the results of the method proposed by Tyas et al. (2011) to obtain cleared pressure, compared against experimental data and simplified ConWep based approximations.

not repeatedly travel along the face of the obstacle until equilibrium is achieved. Instead, the clearing wave traverses the face of the target just once. Then, subject to favourable conditions, it reflects off the ground (or another shock from the opposite edge), and transverses along the face once again and finally escapes into the surrounding volume. They also reviewed different methods of estimating clearing against a validated LS-Dyna model for objects of different heights, S, ranging from $Z/256$ to $Z/32$. The Hudson method was found to be excellent at predicting the loading on the front face of a finite sized cuboid. Incidentally, they also show that a commonly used simple prediction model based on Eq. 2.1 (described in detail later, see Eq.2.6) is valid for building sizes that are much smaller than the scaled distance ($S << Z$). This shows that the simple model is valid for predominately drag-type loading, whereas the Hudson model works for both diffraction and drag-type loading at these ranges of pressures. Having observed increasing over-expansion of the pressure i.e., cleared overpressure dropping below the stagnation pressure for larger structures, the authors report that the extent of over-expansion of the air could be connected to the size of the structure itself.

Since the aforementioned models are valid for only far-field Z values (Rigby et al. 2014b,

Tyas et al. 2011), an improved scheme that could also account for stronger shocks ($1 < Z < 5$ m/kg$^{1/3}$) was proposed by Qasrawi & Heffernan (2016). Simulations were carried out to study the clearing on the circular, flat face of a cylinder of radius 500 mm, at three stand-off distances (D=10, 25, 50 m). For each stand-off distance, three different scaled-distances (Z=1, 2.5, 5 m/kg$^{1/3}$) were used, each of which were chosen to ensure planarity of the wave impacting the front face. They found the speed of the clearing wave to be a constant value close to the local speed of sound for each scaled distance. They then developed and validated an empirical Friedlander-type wave profile to estimate the effect of clearing at each point on the front face of a finite cuboidal target (Fig. 2.5). The authors attribute the slight discrepancy in the plots to the fact that the clearing waves are different for a cylindrical (for which the model was developed) and a cuboidal obstacle (against which it was tested). Unlike the earlier studies, here they found that on completion of clearing, the pressure followed the stagnation pressure values for all but few cases – D = 10 m, Z = 2.5 and 5 m/kg$^{1/3}$ and D = 25 m, Z= 5 m/kg$^{1/3}$. All these cases have scaled radius of the cylinder lower than $Z/20$. It thus appears that the threshold of validity of the simple UFC models for the closer stand-off distance scenario is different from the $Z/256$ for the far-field (Rigby et al. 2014b). Combining this with the observation by Rigby et al. (2014b) regarding the over-expansion of the flow, it seems that the disturbance introduced by an object in a high-speed flow (small values of Z) is much lesser than that introduced by a similar sized object in a lower speed flow (bigger values of Z). This has potential ramifications on the sizing of structures for blast mitigation in the downstream (wake) region, depending on the scaled stand-off distance Z.

Recently, a comprehensive semi-analytical method to obtain the total force on a 2D object by using overpressure histories on the front and rear face of the object was proposed by Gauch et al. (2019). This method was primarily intended for deflagration loading and for low intensity blast loading. So the blast parameters that were considered range from an incident overpressure of 1 bar & 10 ms decay time to 3 bar & 1 ms decay time for a box height of 346 mm and ambient conditions of 1 bar, 15°C. The method has been

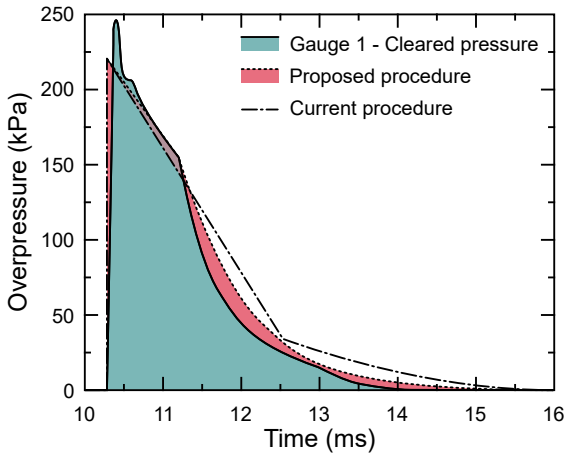

Figure 2.5: The procedure proposed by Qasrawi & Heffernan (2016) to model the clearing effect for a *cylindrical model* validated against numerical data (gauge 1) for a *cuboidal obstacle*. The pressure curve from a simple clearing model (standard text book procedure) has been included for reference. Figure reworked from Qasrawi & Heffernan (2016).

numerically validated and several inferences on the rise time of the total force on the front face, the rear face, and the relative contribution of different physical phenomenon to the total force term have been made available.

For scenarios where the loading is not at *zero* angle of incidence, an empirical formula in terms of the angle of incidence and the energy of the explosion were provided to estimate the pressure load on a 3D box structure by Trélat et al. (2007). This was based on experiments using an explosive gaseous charge and a parallelepiped structure of dimensions $0.14 \times 0.18 \times 0.4$ m ($W \times H \times D$). The TNT equivalent masses ranged from 0.159–2.023 g at stand–off distances of 0.1 m to 0.2 m. The box was positioned at 5 different angles (0, 30, 45, 60 & 90°) with respect to the charge. Here, the first and last case involved the box being positioned perpendicular to the small face and the large face respectively. It is worth reiterating that all the aforementioned predictive models assume an impingement of a planar wave and usually correspond to the far-field, where clearing plays a prominent role.

For the near-field ($0.2 < Z < 3$ m/kg$^{1/3}$), Shin & Whittaker (2019) present a comparison of a validated AUTODYN simulation against the simple clearing formulae and demon-

strate their inaccuracy in the near-field. In addition to that, using plots of the particle velocity along the front face of the object (Fig. 2.6), they suggest that clearing cannot occur in the near-field as the expansion wave is prevented from travelling inwards. This is due to the particle speeds being higher than the local sound speed. They also go on to show that predicting clearing for these conditions is made difficult by the variability of the particle speed along the face of the object. This is more so when the wave is not planar. As an aside, one may note that the speeds are more or less constant for $Z > 1$ m/kg$^{1/3}$ as reported by Qasrawi & Heffernan (2016). For non-planar, close range blast loads, they therefore suggest the use of CFD tools to estimate clearing loads.

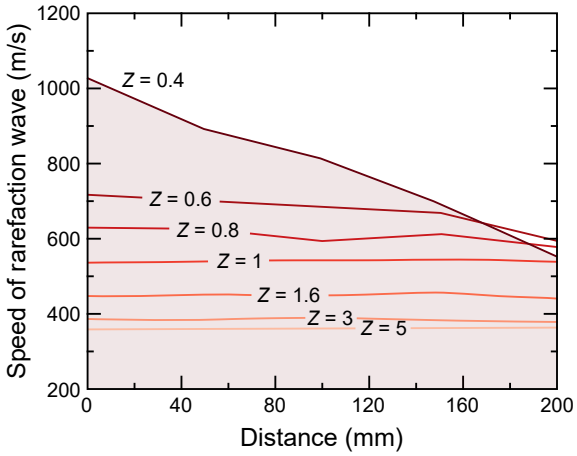

Figure 2.6: A plot showing the variation of rarefaction (clearing) wave speed for different scaled blast values (Z) along the face of a target as a function of the distance from the centre of the target (Shin & Whittaker 2019).

Obstacles with curved surfaces:

For obstacles with curved surfaces, one major difference is that the clearing load is further reduced because of the relieving effect provided by the three-dimensional nature of the surface. For simple loading cases, viz., far-field of large ($>$ 0.1 MT of TNT) explosions, for a spherical dome and for structures with simple curved surfaces, load estimation formulae are available in text books (Biggs 1964, Norris et al. 1959, Glasstone & Dolan 1977). These predictions are not applicable for smaller charges, and recently Qi et al. (2020) quantified the inaccuracy in using existing conventional models (e.g. UFC 3-340-02) to

obtain overpressures on a hemispherical dome. This formula uses scaled distance and inclination angle at a location on the dome as inputs. Discrepancies of up to -150% for overpressure, and up to -90% for impulse was reported, as clearing plays an important role in this reduction (Qi et al. 2020). Thus, load estimation on curved surfaces for such blast parameters has been an ongoing area of research in the last few years.

Due to a lack of experimental data for curved faces of structural columns, Shi et al. (2007) report numerical studies on columns loaded by blast waves at scaled distances ranging from $Z = 0.5$ to 10 m/kg$^{1/3}$. For rectangular columns, they found that the peak overpressure and impulse at a point on the front face of the column were not affected by the depth of the column. But then, the reduction was inversely proportional to the width of the column, until an asymptotic limit was reached at 1.6 m. For a circular column, a similar limit was reached at 3 m diameter. For the pressure evolution on the rear face, the width of the column had a stronger effect than the depth. The reflection off the rectangular column was stronger, whereas the diffracted wave was stronger on the rear face of the circular column. They also report an anomalous increase in reflected impulse at 1/3$^{\text{rd}}$ the height of the column for $Z < 1$ m/kg$^{1/3}$ which they attribute to a combination of shock reflection off the ground and deflection of the column, both of which increase the positive pulse duration. Empirical predictions for the overpressure and impulse on the front and rear faces along the column height were made in terms of the respective values at the base of the column, which were again obtained empirically.

Since depth does not appear to play an important role, this work can be compared with the work of Ballantyne et al. (2010) who studied the role of clearing in reducing the impulse on the flange face of commonly used structural W-sections (wide-flange sections, also called H-sections.) Parametric numerical studies were carried out for values of Z between 2 and 10 m/kg$^{1/3}$ and they report that the impulse reduction due to clearing tends to be essentially constant for these flange sections. The constant value was found to be 50% of the reflected impulse on an infinite surface. The authors then derived an

empirical formula to estimate the impulse for Z = 1–10 m/kg$^{1/3}$. These results are for the impulse values on the front face alone.

Glasstone & Dolan (1977) provide relations for estimating the area-averaged overpressure history on the front, sides, and rear face of a cylinder for the case of planar loading and $Z > 3$. After this, in the last decade, several numerical and experimental works were carried out to improve on these highly conservative estimates.

Qasrawi et al. (2015) used numerical simulations to study the development of pressure on a circular section. The cylinder radii ranged from 0.1 m to 1.0 m, the stand-off distance was 2 m, and the scaled distances were from Z = 0.8 m/kg$^{1/3}$ to 2.4 m/kg$^{1/3}$. The variation around the cylinder was found to be well represented by a sinusoidal function, and they then derived the following expressions for predicting overpressure (Eqn. 2.2) and impulse (Eqn. 2.3) acting on the circular column.

$$P_{equiv} = \frac{2}{3\pi}[2P_r + P_{so}] \tag{2.2}$$

$$I_{equiv} = \frac{2}{3\pi}[2I_r + I_{so}] \tag{2.3}$$

For columns of large radii, they recommend the use of incident blast parameters (P_{so} & I_{so}) at the side of the cylinder, as the cylinder radius can add to the stand-off distance from the charge and lead to incorrect results. These formulas are an improved, yet conservative estimate that may be used for preliminary design calculations for circular columns.

While Qasrawi et al. (2015) had neglected the overpressure on the rear surface of the cylinder as they were interested in providing a conservative estimate, Mulligan (2018) provides some empirical relations for the front and rear face of a circular cylinder for similar scaled ranges, based on small-scale experiments. C4 charges ranging from 0.09 kg to 0.272 kg, placed at a stand-off distance of 1.32 m from a 167 mm diameter cylinder,

were used in these experiments (the reflected overpressures were in the range of 3–9.5 bar.) The empirical relations were provided as a function of the azimuth angle, giving improved prediction values over that given previously by Glasstone & Dolan (1977). Beyond the 90° azimuth, they found that turbulence and surface roughness on the cylinder play an important role in the overpressure evolution over the cylinder.

Experiments have also been reported on a hemi-cylindrical obstacle to simulate conditions over a transport cask/industrial facility (Trélat et al. 2020). To do so, the obstacle was positioned so that the 0.4 m diameter hemi-cylinder's axis that was 1.6 m long was perpendicular to the direction of propagation of the blast wave. For these experiments, a 50 g equivalent TNT charge was used at three different stand-off distances – 0.4, 0.6, 1.6 m. The pressure enhancement measured along the front face of the cylinder could be predicted quite successfully by TM5-1300 (US Army Corps of Engineers 1990) using the reflection model for a plane target. However, the drop in pressure in the expansion region of the cylinder could not be predicted as this includes complex diffraction effects. And so, an empirical model (called *Model S*) was proposed for predicting the overpressure values in the expansion region with the help of a modified coordinate system. This model was then successfully validated against a factor two scaled-up experiment.

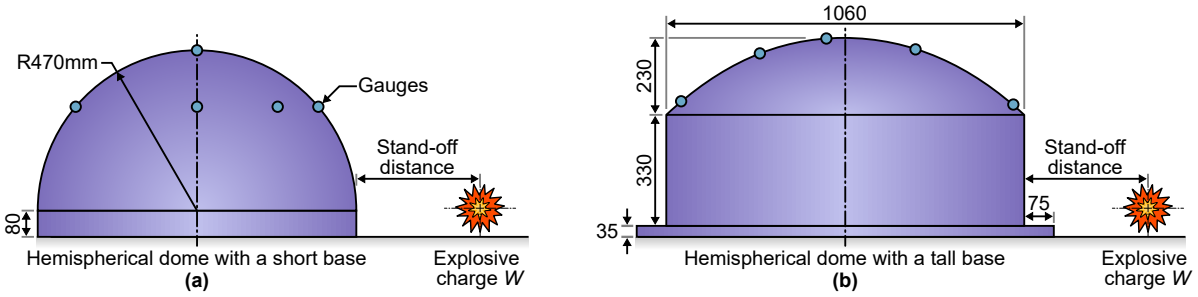

Figure 2.7: A schematic drawing of the hemispherical dome setups used by (a) Zhi et al. (2019) and (b) Qi et al. (2020) to investigate the variation in pressure development on a curved surface.

The overpressure evolution on a perfectly hemispherical dome having a rise to span ratio, $f/L = 0.5$ (Fig. 2.7a) was experimentally studied for $Z = 1.7$–3.4 m/kg$^{1/3}$ (see Table 2.1) by Zhi et al. (2019). The authors performed numerical simulations for a wide range of

Table 2.1: Summary of literature on predicting blast loading on objects with curved surfaces

Structure Shape	Representative Scale	TNT Eq. Weight (or Incident Pressure)	Stand-off Distance (or decay time)	Loading Estimates
Circular & Square Column (Shi et al. 2007)	Φ 500 - Φ 3000 mm	$1 - 8000$ kg	10 m	Empirical
Cylinder & Flat Plate (Mulligan 2018)	Φ 168 mm	$0.09 - 0.27$kg	1.32 m	Empirical
Hemicylinder (Trélat et al. 2020)	Φ 400 mm $\times$ 3.2 m	0.05 kg	0.4-1.6 m	Empirical
-do-	Φ 800 mm $\times$ 3.2 m	0.4 kg	3.2 m	-do-
Hemisphere (Zhi et al. 2019)	Φ 940 mm (f/L=0.5)	$0.055 - 0.4$ kg	1, 2 m	Pseudo-analytical Formula
Hemisphere (Qi et al. 2020)	Φ 940 mm (f/L=0.5)	$0.055 - 0.4$ kg	1, 2 m	Pseudo-analytical Formula
-do-	Φ 1060 mm (f/L=0.217)	$0.055 - 0.4$ kg	1, 2 m	Pseudo-analytical Formula

parameters and developed empirical formulae for blast parameters such as the reflected pressure, impulse, and decay time. This was for points over the surface of the hemisphere as a function of the span of the hemisphere and the scaled distance from the charge. In an interesting finding, pressure values at points on the hemisphere along a direction perpendicular to the blast wave and away from the centre line were found to be the same. This was named by authors as *parallel effect*.

Extending these tests further, Qi et al. (2020) carried out experiments for this and another hemispherical dome having a rise to span ratio, f/L, of 0.22 (Fig. 2.7b) with a taller cylindrical base. This was done for Z ranging from 1.2 to 3.7 m/kg$^{1/3}$ to study the effect of the height of the supporting base and the new rise to span ratio. Using a numerical parametric study, and they identified the following dimensionless variables – scaled span $L/W^{1/3}$, distance-span ratio R/L, rise-span ratio f/L and height-span ratio H/L as important parameters in the loading process. Then, empirical formulas to predict the blast load on the structure were obtained and were validated fairly successfully.

2.3.2.2 Buildings in Urban Scenarios: Simulations and Experiments

To study the overpressure load on actual building shapes, there is a relative dearth of data in the literature apart from the simple structures described thus far. As load relieving aspects of curved surfaces were recognized early by Barakat & Hetherington (1998), shapes that an architect may use to minimize the loading on a building were explored and identified. On the whole, structures with curved surfaces were found to have a reduced magnitude of the imparted blast load as the reflected waves can then be directed away

from the structure. Provisions for such a design were incorporated in the design of a new building (US General Services Administration 2004) to replace the damaged Alfred P. Murrah building and similar examples of such buildings may be found in the FEMA (2007) design manual. Convex building façade shapes are usually preferred for blast resilient design with a view to avoid wave reflection hot-spots (US Army Corps of Engineers 1990). To illustrate, a building designed as shown in Fig. 2.8a is to be avoided whereas the design ought to be as recommended in Fig. 2.8b. But then Gebbeken & Döge (2010), using CFD simulations, show how an intelligently designed non-convex shape (Fig. 2.8c) can also lead to a reduction in blast pressure loading on the building structure.

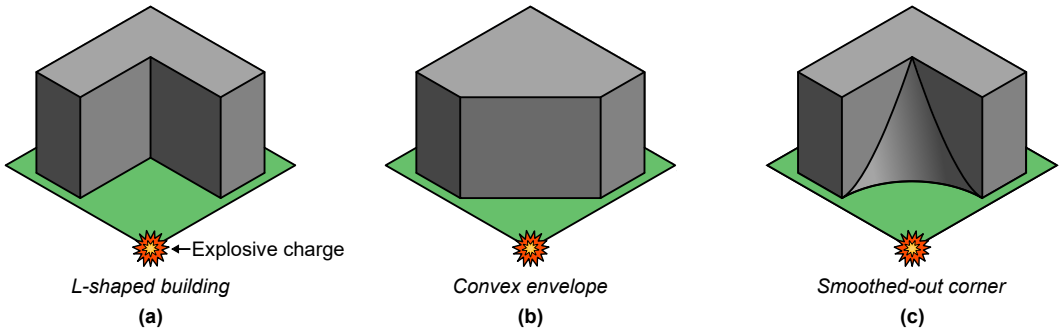

Figure 2.8: Schematic drawings of the three building shapes numerically investigated by Gebbeken & Döge (2010) comprising (a-b) two common shapes and (c) a non-convex design which reduced the blast loading.

To understand the effect of building design parameters such as the overhang of the roof of a gable roof building, Xiao et al. (2021) report experiments for two different loading scenarios, one on the eave side and the other on the gable side, as shown in Fig. 2.9. An LS-Dyna numerical model was initially validated against 4 experiments at different scaled distances; some facing the gable side, and some facing the eave side of the building. Following this, a numerical parametric study on the building design parameters was carried out. They found that an overhang in the roof led to an increase in the pressure and impulse on the (side) wall. The overpressure was found to increase with increasing roof overhang and roof slope. On the other hand, the impulse increased with roof overhang, but remained unaffected by a change in the slope of the roof.

The role played by the landscape ahead of a building in modifying the blast load even before it impacts a building was numerically investigated by Barakat & Hetherington (1999). They show how careful planning of landscaping in the regions surrounding the building, illustrated in Fig. 2.10, can help reduce the blast intensity. Pits, trenches, and humps are another elegant method to reduce the load in the framework of architectural design. The TNT charge mass that was used for these simulations was not mentioned, but the study aimed at evaluating vehicle bomb threats ($25 - 230$ kg TNT) at distances ranging from $20 - 50$ m. Reductions of up to 35% on impulse, and up to 40% on pressure, were shown to be possible by employing such techniques (Barakat & Hetherington 1999).

While all these are studies on different aspects of blast loading on a stand-alone building, the design loads will be different for buildings in an urban, congested environment. Additional factors which can modify the evolution of pressure loading such as the width of the street, building height, the type of façade, and the presence of openings in the building envelope ought to be taken into consideration. Recent large-scale blast events such as the 2020 Port of Beirut explosion (Rigby et al. 2020) have highlighted the need

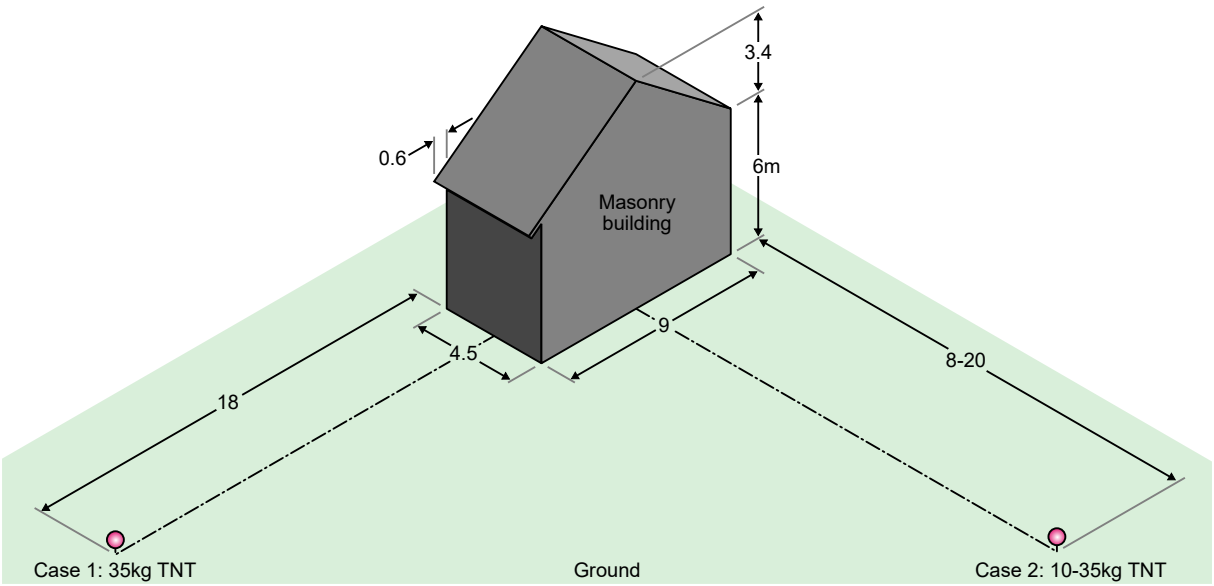

Figure 2.9: A schematic representation of the two test cases investigated by Xiao et al. (2021) to experimentally determine the pressure evolution on a gable roof building subjected to different explosive loadings.

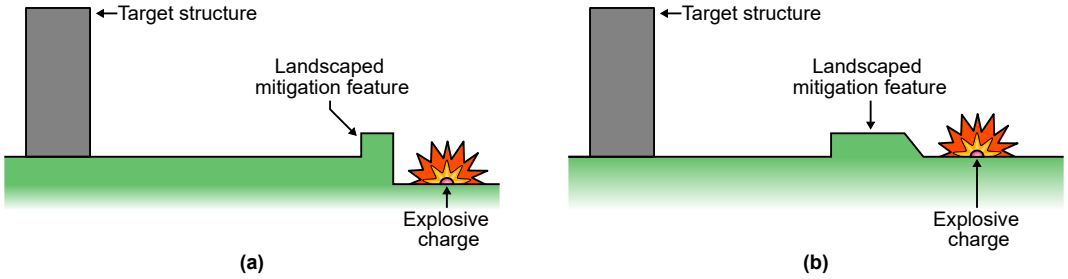

Figure 2.10: A representation of landscaping techniques that may be used to improve blast mitigation (Barakat & Hetherington 1999)

to consider the complexities of cityscapes and their influence on blast loading in urban environments. The following paragraphs describe aspects of cityscapes that have been probed by researchers over the last few decades.

Smith & Rose (2006) experimentally measured the pressures along different street configurations: straight, cul-de-sac, 2, 3, & 4 street intersections. The cul-de-sac was found to have the maximal pressure amplification amongst the various combinations that were tested. They also found that for each configuration, the volume available for the blast wave to expand may be used as a metric to evaluate the attenuation characteristics. Another interesting finding was that the pressure amplification down a street lined by buildings was found to depend on the height of the buildings and the street width, viz., wider streets and shorter buildings would minimize amplification. For these purposes, a scaled street width of 4.8 m/kg$^{1/3}$ and scaled building height of 3.2 m/kg$^{1/3}$ were experimentally found to be as good as infinite extents for minimizing and maximizing the blast amplifications respectively. It was also observed that the distance of the charge from the junction influences the extent to which the blast diffracts, and enters the other streets leading off the junction. The larger the distance of the charge from the junction, the greater the degree of diffraction that occurs at the junction, as opposed to the reflection and transmission down the street in which the charge is located.

Fouchier et al. (2017) report a 1:200 scale table-top experiment to carry out an in-depth study on the effect of street junctions and channelling in an urban environment. The

conclusions from this study are broadly similar to those reported earlier by Smith & Rose (2006) – that overpressure enhances downstream of a narrow street as the incident wave coalesces with that from reflection off the walls of the street. They explored the effect of an 136 mg TNT equivalent explosion using an RP80 detonator on a building configuration shown in Fig. 2.11. Paradoxically, channelling (confinement) was shown to have a beneficial effect here as the pressure and impulse values recorded amidst the buildings were similar to the free-field scenario. This could be because the buildings were not tall enough to be considered as confined (i.e., scaled building height $\not> 3.2\ \mathrm{m/kg^{1/3}}$.) At the exit point of this building complex (shown in Fig. 2.11), the pressure was reduced by up to 80%. The authors further noted based on their experiments that straight streets were deemed to be the more destructive street configuration, whereas a four way intersection was found to be the least destructive.

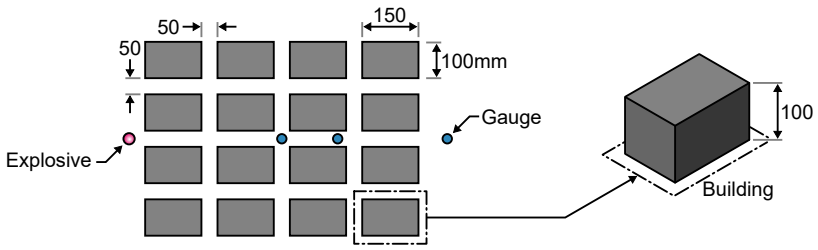

Figure 2.11: A schematic of the test setup used by Fouchier et al. (2017) to investigate the effect of blast wave channelling between densely spaced buildings.

Conditions typical of streets in European cities ($6 - 20$ m wide, and 20 m tall buildings), and explosions ranging from 100 to $10,000$ kg to include truck bombs were considered by Codina et al. (2013). Two different scenarios of an explosion were simulated, one initiated at the centre and the other one off-center, so as to recreate an explosion initiated on the pavement at 2.2 m distance from the building. They report that channelling (confinement, leading to coalescence of waves) is a serious effect as increases in overpressure of up to 8 times were observed. Expanding on the previously reported research, they provide a broader reason for the pressure amplification in confined spaces based on their identification of four zones – Unconfined Area, the Regular Reflection Area, the Mach Reflection Area and the Confined Area (Fig. 2.12a). But unlike the overpressure, for impulse, the

increase is attributed to the confinement itself and not due to the interaction amongst the multiple waves. The confined area occurs at 1.65×width, irrespective of the TNT charge mass, suggesting that a street wider than 30 m ($1.4 - 6.5$ m/kg$^{1/3}$) will lead to an absence of confinement. This is quite different from the 4.8 m/kg$^{1/3}$ value that was proposed earlier (Smith & Rose 2006) and the reasons for this discrepancy are not fully clear. A similar identification of zones was also undertaken for the case of an asymmetric explosion (Fig. 2.12b). While the classification of zones was unchanged, their locations were slightly different.

Research on the role of frangible façades on buildings along a street revealed two contrasting aspects (Smith et al. 2003). Frangible façades can minimize the pressure amplification down the street. But then, the amplified overpressures inside the building would be high enough to cause harm to the occupants of the building. So they recommend the use of façades robust enough to withstand an explosion in the mid- to far-field, but not near-field. Parenthetically, mention is made of some studies where the role of an opening on a structure may be taken to simulate a broken window. The effect of such 'pre-formed openings' on the failure mode are available for a metal wall (Aune et al. 2017) and a concrete wall (Mays et al. 1999).

With regard to a cluster of buildings, it was consistently observed that the interaction of a blast with the first row of buildings was the dominant factor in defining the extent of shielding offered to the subsequent rows of buildings. The effects of channelling and attenuation that may be produced by buildings in a residential layout were explored for a 1:34 scale representation of two storey 'semi-detached' buildings (Smith et al. 2004). A scaled down 25 g TNT equivalent charge was placed within a residential zone, each having different areal ratios, defined as the ratio of the footprint of the building area to the total area available. Air3D simulations were then validated against this data and then used for subsequent analyses. An average reduction in loading of only 10% was observed for areal ratios ranging from 17.9% to 28.6%. The final loading, as the authors

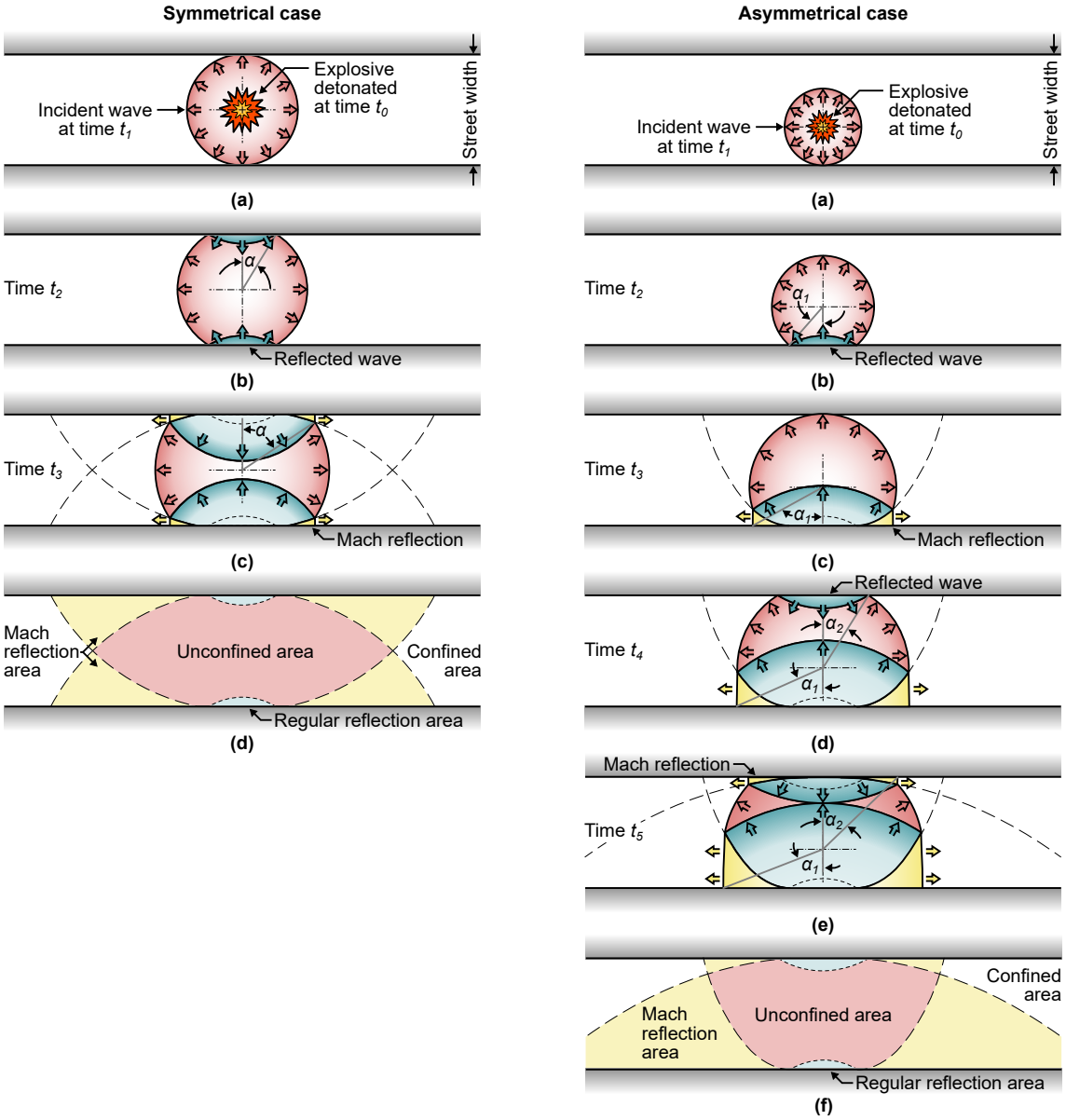

Figure 2.12: A schematic representation of the propagation of waves resulting from an explosive detonated at time t_0 in a street layout for (left) a symmetrically located charge and (right) an asymmetrical one. (Codina et al. 2013)

report, is a complex combination that depends on both the channelling and the shielding effect produced by neighbouring buildings. The more congested buildings (higher areal ratio) had a lower reduction in pressure, suggesting that channelling is more dominant than shielding. They suggest that complete numerical simulations for each scenario are required to understand the loading evolution in such conditions. In a related but different set of simulations on buildings, Remennikov & Rose (2005), show how a building in the

shadow region of another shorter building can be shielded and thus experience reduced loads. The asymptotic limits on the street width that were mentioned earlier (Smith & Rose 2006) were also validated in this work.

To evaluate the overpressure loads arising on a building due to an explosion in the street, an engineering method (von Rosen et al. 2004) to superpose the loads is available. This was adapted by Johansson et al. (2007) for buildings at an intersection (Fig. 2.13a) using a combination of incident pressure values and diffraction coefficients. The resultant plots were compared with AUTODYN data that had been validated against a $1/5^{\text{th}}$ scale experiment. Fairly good correspondence (given the minimal computational effort) was obtained, as shown in Fig. 2.13b. This validation was for the overpressure range of $50 - 100$ kPa.

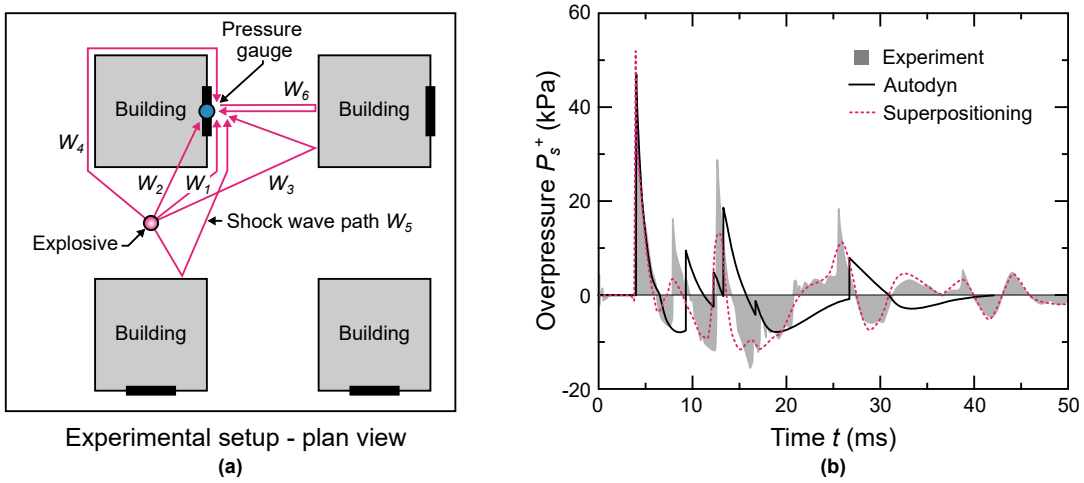

Figure 2.13: (a) A schematic plan view of the test setup used by Johansson et al. (2007). The experimental results are shown in (b) alongside the response numerically predicted by Autodyn and the estimation based on the superpositioning method (von Rosen et al. 2004).

2.3.2.3 General Outlook on Direct Loading

The role of clearing in reducing the overpressure on objects with straight faces was explored and several empirical approaches to estimating the loading on W-sections, cuboids, flat face of a cylinder, and parallelepipeds were presented. The addition of curvature to finite-sized objects causes a further reduction in pressures due to the relieving effect introduced by the (concave) curvatures. Empirical models are available for a full cylinder,

curved face of a hemi-cylinder, and hemispherical structures with a cylindrical neck. While these are applicable to individual buildings, for structures in an urban setting, the effect of street width and height of buildings in confining a street explosion have been documented using experiments at different scaling ratios, with 1:200 and 1:10 scale experiments, all reaching similar findings. The role of different junctions – straight, cul-de-sac, 2, 3, & 4 street intersections – in modifying the intensity of an explosion have also been studied, although the length down the street for which a blast wave may be considered to have weakened considerably has not been clearly documented yet.

Having presented aspects of direct blast wave loading on target structures of various shapes, we next move on to indirect loading cases, where the properties of the blast wave are modified by another structure *before* it impacts the structure of interest. In other words, here we consider the evolution of a blast wave *downstream* of an obstacle on, rather than on itself.

2.3.3 Indirect Loading on Structures

2.3.3.1 Barriers

2.3.3.1.1 Introduction

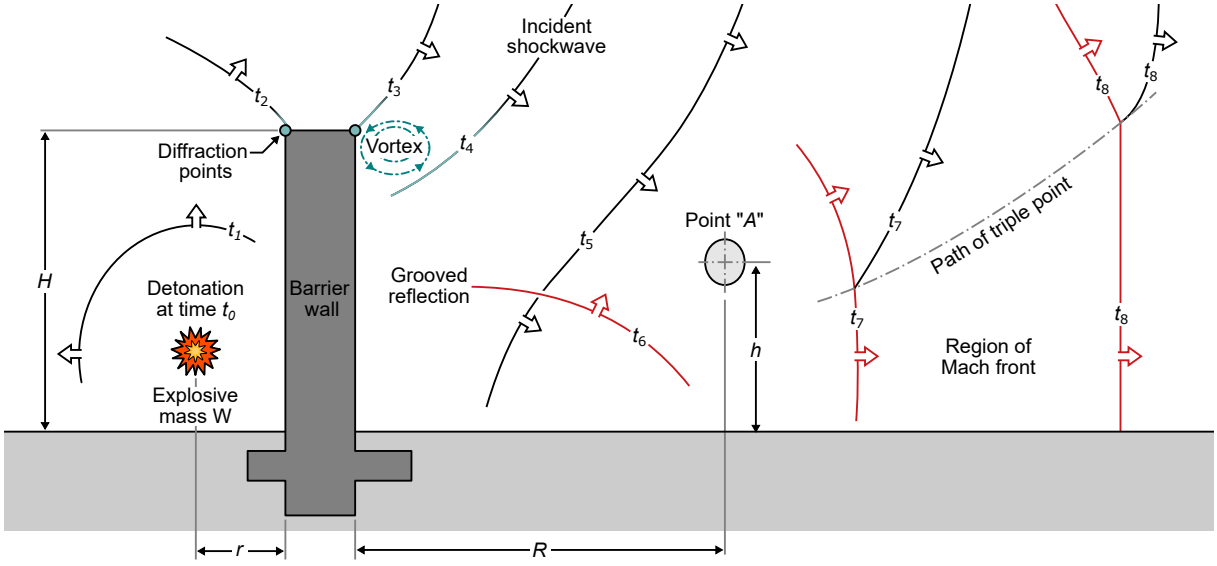

Figure 2.14: A schematic illustrating the complex shock wave development arising from an explosive detonated at time t_0 that interacts with a barrier wall. Figure adapted from Beyer (Beyer 1986).

A barrier is defined here as a wide blockade in the path of the blast wave that results in a strong reflection wave (Fig. 2.14) directing energy away from the protected structure. Further, due to the presence of a barrier, a diffracted wave arises from each free edge of the barrier, and these diffracted waves further weaken the transmitted wave. In this context, research on the effect of the height of the barrier, the distance behind the barrier where shielding occurs, and the role of a canopy placed over this edge have been undertaken (Beyer 1986, Xiao et al. 2019). The thickness of the wall (Sha et al. 2014), referring to the breadth in Fig. 2.15; the detrimental effect of increasing height of burst (HoB) (Chapman et al. 1995*b*); the inclination of the face of the barriers (Sugiyama et al. 2015); the structural integrity of the wall (Rose et al. 1998); and even a not so obvious aspect such as the roughness of the barrier (Hajek et al. 2016), all play a role in weakening the wave transmitted beyond the barrier. Moreover, if the length of the barrier is short,

waves diffracted from either end propagate towards the centre line of the shadow region of the barrier and can cause pressure amplification under certain conditions. The extent to which these parameters affect the strength of the transmitted wave has been an ongoing topic of research (Beyer 1986, Chapman et al. 1995*b*, Rose et al. 1995, 1997) and a brief summary of these aspects is provided in this section.

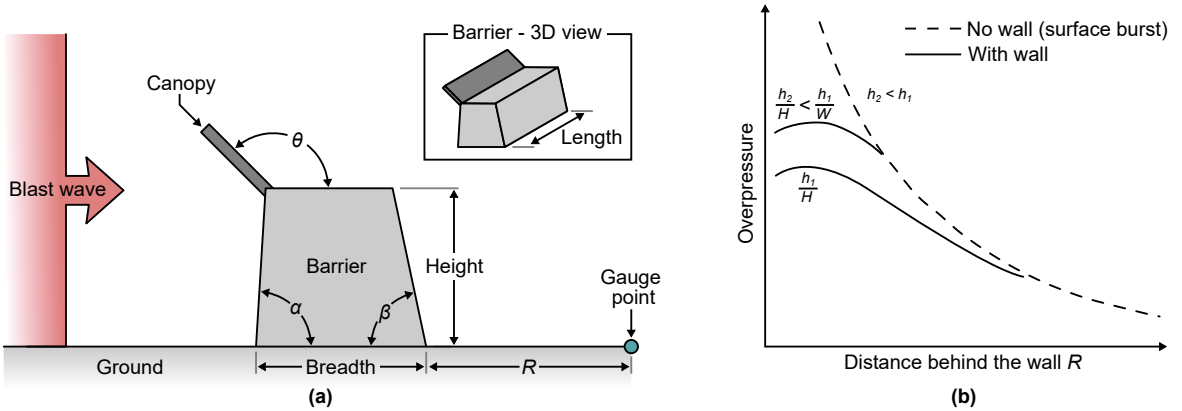

Figure 2.15: (a) A schematic diagram detailing the barrier nomenclature used in this paper. (b) A graph illustrating the peak pressure distribution as a function of distance behind a barrier wall contrasted with a no wall (surface burst) case (Beyer 1986).

Clearly, the protection offered by a barrier depends on the dimensions, especially, the height of the barrier. To this end, Beyer (1986) conducted 1:6 scale experiments using different masses of C4 placed near an armour steel wall, with Z_{TNT} ranging from $0.18 - 0.44$ m/kg$^{1/3}$. The charge was centrally located at a height of 0.3 m above the ground and 0.3 m in front of the barrier. The authors reported attenuated pressure values behind the barrier, in the form of tables and charts, along a line drawn from the charge and:

- perpendicular to the wall ($1H$–$8H$) and
- at 45° to the barrier ($2H$–$8H$), and
- at points at a height H directly above the previous locations ($2H$ for the last one in the array).

The extent of attenuation reduced with increasing distance away from the barrier, as shown in a typical pressure plot in Fig. 2.15b, but for most tests reported, this protected

region extended all the way up to $8H$ behind the barrier.

Covering a broader region behind the wall, a similar set of experiments ($Z_{TNT} = 0.17$ m/kg$^{1/3}$) were reported by Rose et al. (1995). This was for a 1:10 scale experiment using 75 g TNT equivalent mass at a distance of 0.138 m from the wall and 0.109 m above ground. The wall was a steel structure 0.35 m tall (H), 2.1 m long. Pressure measurements up to a height of $3H$ and until a length of $6H$ were carried out behind the barrier, on a plane perpendicular to the barrier and the ground, passing through the mid-point of the barrier. Except for a small region above and behind the wall where the effects of the reflected wave persisted, substantial pressure and (slightly lower) impulse attenuation were observed at all measurement locations. Broadening the scope of the experimental campaign to include scales ranging from 1:8 to 1:14, pressure and impulse charts behind barriers of different scaled heights were later reported in Rose et al. (1997). The combined dataset behind the barrier from both studies covered a wide range of scaled distances from $0.5 - 4$ m/kg$^{1/3}$ and from $0 - 2$ m/kg$^{1/3}$ above the ground. The scaled heights of the wall ranged from $0.5 - 1.0$ m/kg$^{1/3}$.

Chapman et al. (1995*b*) performed experiments at 1:10 scale, with $Z_{B,TNT}$ = 0.38–3.5 m/kg$^{1/3}$ to the wall. They used a barrier that was H_B = 300 mm tall, with TNT charge masses ranging from 40 g to 80 g, placed at HoBs from 0.05 to 0.3 m. Pressure was measured at different heights (H_T=0.5H–2H) along the centreline of a target structure placed at a distance (d_T=0.15–0.6 m) behind the barrier. An empirical relationship was also developed to obtain the pressure and impulse values on the wall (cf., sub-section on *Indirect Loading*).

In the aforementioned studies, the depth of the walls were small enough for their thickness to *not* influence the properties of the blast wave. Zhou & Hao (2008) numerically studied an infinitely long blast wall of 250 mm thickness (as varying thickness from 150–300 mm showed insignificant difference in loading), varying the mass of explosive from 10–10,000 kg of TNT. The height of the barrier was varied from 1–4 m, the height of the building varied

from 3–40 m, the distance from charge to building varied from 5–50 m (barrier location was set between 0.2–0.8 of this value, i.e., 1–40 m), and the HoB was fixed at 0 m. Based on these results, empirical formulae were developed for prediction of peak pressure, peak impulse, arrival time, and decay time, on a building behind the barrier. It was noted that there exists a location along the height of the building where maximum reduction in pressure and impulse may be observed. This was then correlated to the input conditions. Using these findings, a linear piece-wise function was developed for predicting the variation of pressure over the face of the building.

2.3.3.1.2 The Role of Barrier Dimensions

Payne et al. (2016) carried out a parametric study using CFD to determine regions in the wake of a cuboid shaped obstacle ($3.50 \times 3.95 \times 3.00$ m) where the overpressure and impulse values were *unaffected* by the presence of the obstacle, i.e. where incident blast conditions were restored. It was found that the pressure field behind the obstacle is reduced only in the near-field, with the mid and far-field largely unaffected. Conversely, impulse values were significantly reduced even until the mid-field, while also increasing slightly in certain regions due to complex wave interactions, and eventually returning to incident conditions in the far-field. The authors provided a table showing distances beyond which free-field incident impulses recover. The converse of this finding being that within this region, some attenuation is generally observed, which is the focus of this article. As a rule-of-thumb, the shadow region behind the target was seen to extend to a maximum of 60° from the rear corner. The TNT charge mass was fixed at 100 kg and the stand-off distances were varied from 15–50 m in steps of 5 m.

A parametric study to understand the role played by each dimension of a barrier was reported by Miura et al. (2013) for a TNT equivalent explosive mass of 3400 kg. Numerical simulations were carried out for blast propagation over a structure that may be considered to be a barrier with finite dimensions. Its dimensions were varied with the intention of studying the potential mitigation effects of dikes that surround energetic material storage

sites. For the narrowest length that was simulated (1.17 m/kg$^{1/3}$, from the range of 1.17–7.71 m/kg$^{1/3}$), overpressures on the ground were found to be higher downstream of the wall, although all the other simulated lengths resulted in a pressure reduction in the downstream. This was attributed to the interaction of the diffracted wave from the edges of the barrier, with the wave reflecting off the ground surface behind the barrier. For long enough lengths, the differences were negligible, and so 2D axisymmetric simulations were subsequently used for a parametric study of the dimensions. This was because the 2D simulations gave similar pressure histories as the 3D simulations but at a significantly lower computational cost. The investigated parameters were: scaled heights of barrier: 0.13–0.8 m/kg$^{1/3}$, scaled distance to front face of barrier: 2–4.3 m/kg$^{1/3}$, and scaled width of barrier: 0.067–1.064 m/kg$^{1/3}$.) The height of the dike was identified as the most significant parameter in influencing attenuation, but since constructing a tall barrier is not always practical, the effect of stand-off to the dike and the dike width were also explored. The most significant attenuation was obtained for the maximum dike height and minimum scaled distance, as the diffraction angle of the wave at the dike edges would then be the highest. For the cases where the dike was far from the blast source, unlike the other stand-off scenarios, the breadth played a minimal role. This was thus approximately simulated by using an infinitely thick barrier (or a back-step), and a correlation for the maximum pressure behind the dike and an empirical "effective thickness" of dike was provided.

A preliminary numerical and experimental study, using 0.5 g of PETN (stand-off distance of 40 mm) explored the role of two small dikes (Sugiyama et al. 2015). The first: a flat faced obstacle, with a flat top, and a sloping rear face ($\beta < 90°$), and the second: an inclined front face ($\alpha < 90°$), a flat top, and a sloping rear face ($\beta < 90°$). While the effects of the dike on the flow-field were found to be non-existent in the far-field, in the near-field, the obstacle with the flat face performed marginally better. Intensification of the blast wave in the intermediate downstream regions was reported, and this was attributed to complex wave interactions.

Numerical simulation of a shock tube were carried out to study the effect of barrier geometry on an incident shock wave by Sha et al. (2014) using an incident shock overpressure of 300 kPa. Not including structural strength considerations, the breadth of a barrier element was found to amplify the interaction between the reflected wave and the incident wave. So the breadth ought to be as narrow as possible to achieve the best attenuation. Adding a positive slope ($\alpha > 90°$) on the windward side gave an improved attenuation (Fig. 2.16). Incidentally, as described later, Berger et al. (2015) in a slightly different context, have experimentally validated this concept. On the other hand, the effect of the slope on the rear face was found to be comparatively small. Zhou & Hao (2008) had also reported an insensitivity to barrier thickness, this may also be due to the insignificant values of scaled thickness of the barrier. But for blast pressure downstream and not far off from a dikes (Miura et al. 2013), the width was shown to modify the pressure values. This could perhaps be attributed to the use of a planar wave in the work of Sha et al., where the incidence angle between the shock and the barrier is always the same, unlike in the work of Miura et al. (2013), where the blast wave was curved and not planar.

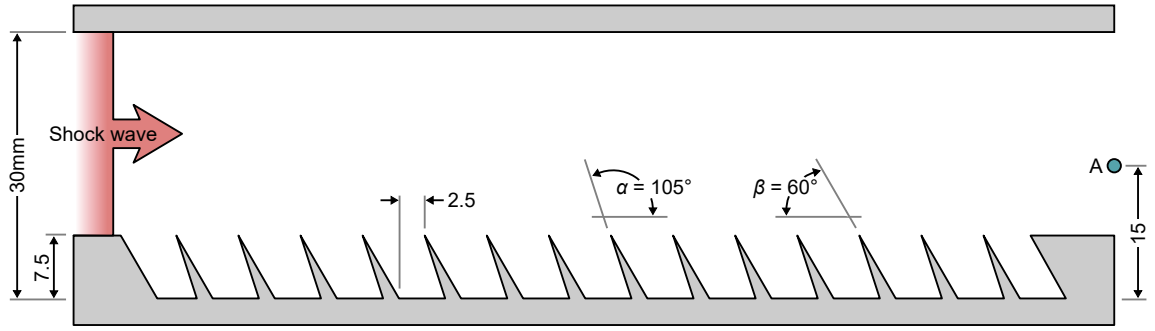

Figure 2.16: The shape of an optimized barrier for maximal attenuation downstream (at location **A**) reported by Sha et al. (Sha et al. 2014) using 2D numerical simulations.

2.3.3.1.3 The Role of a Canopy

The role of a metal canopy (Fig. 2.15) was first explored by Beyer (1986), and the details of the experiment may be found in the previous subsection and also in Table 2.2. Three canopies (1st: 21 kg/m^2, 3 m long, 0.3 m wide; 2nd: 40 kg/m^2, 3 m long, 0.3 m wide; and 3rd: 40 kg/m^2, 3 m long, 0.45 m wide) were tested. In general, they were all found to

provide improved mitigation than the reference (no canopy) case. Between the canopies, no clear trend could be determined, but the lighter one performed slightly better in terms of impulse, and the heavier one performed better in terms of overpressure.

Recently, Xiao et al. (2019) extended this work to understand the role of the canopy angle. Experiments were carried out using a 3.9 kg PETN charge, placed at the centre of a 10 m diameter circle (on plan), 0.4 m above ground level. Three types of gabion walls were placed equidistantly along the perimeter of the circle (Z_{TNT} = 2.92 m/kg$^{1/3}$); one was fitted with a forward inclined metal canopy, one with a rear inclined canopy, and one was left without a canopy. The barriers measured $2.0 \times 1.0 \times 2.0$ m, and the canopies were 0.75 m long, with inclination angles (θ, Fig. 2.15) of 135° and 45° respectively. Reflected pressure measurements were made at distances of 10 m from the charge, and 5 m from each gabion wall barrier. Since the breadth of each gabion was not sufficient to prevent the sideward ingress of the diffracted blast wave, a series of numerical simulations (initially validated against these experiments), were then used to compute the flow evolution for an infinite-breadth wall to avoid this sideward ingress. The results showed that the addition of canopies improved the blast attenuation performance and the forward inclined (θ =135°) canopy gave the best attenuation. The optimal values for the inclination of the canopy were in a narrow band around θ =115°. As described earlier, using a shock tube, Sha et al. (2014) had also reported that a forward inclined obstacle[7] produced improved attenuation. Contrary to this finding, Hajek et al. (2016) report that the overpressure values behind a barrier are almost insensitive to the forward facing angles of canopies, possibly due to the charge (0.5 kg) being detonated closer to the barrier (0.75 to 5 m, Z_{TNT} = 0.9–6.3 m/kg$^{1/3}$.) This, it may be noted, adds credence to the earlier comment on the (non)-planarity of the wave altering the physics of the interaction.

[7]although these obstacles (Fig. 2.16) can be taken to be the front face of the barrier, the results should be equally valid for a canopy as well

2.3.3.1.4 Additional Barrier Parameters

Experiments on frangible walls were reported by Rose et al. (1998) using 75 g of TNT equivalent charge placed close to the barrier; conditions similar to their earlier work (Rose et al. 1995). In this work, 'walls' of water, sand, and ice were shown to perform better than a steel wall, both in terms of overpressure and impulse attenuation. Experiments using walls of other materials, such as geotextiles and plastics, were also undertaken. All materials, including material such as thin balsa wood (< 2 mm) and even polythene sheet (< 1 mm) gave a reduction in overpressure (but not impulse) as compared to a no wall case. They concluded that so long as a wall stays in place to cause the wave to diffract around it, either by means of its inertial mass or due to the shape of a resistant structure, the system can mitigate a blast wave.

While frangible walls can cause harm to people in the surroundings due to fragmentation, the use of water filled 'walls' can avoid such a scenario. This shows how barriers can mitigate a blast wave by reflection, diffraction or even absorption of energy (Xiao et al. 2019). A summary of these and related work in the recent period, and details on the construction of barriers may be found in the review by Smith (2010). The effect of contact charges, which are used to pulverise the barriers, was studied by Coughlin et al. (2010). Such studies involve considering energy absorption by the material of the barrier, which is beyond the scope of this review. Additional details on such research may be found in the work of Zong et al. (2017).

The role of roughness on the face of a barrier has also been shown to introduce disruption to the flow and attenuate blast pressures (Hajek et al. 2016). Pyramid shaped corrugations made of concrete and acoustic foam panels were attached to the face of a concrete barrier and attenuations were found to increase behind the barrier for $Z \sim 1.5$–10 m/kg$^{1/3}$. Incidentally, the acoustic foam material performed better than the bare concrete elements for reasons that were not immediately clear, but it proves the hypothesis that roughness plays a role in reducing the attenuation. Such an attenuation was also reported by Makki

(2017) for shock loading experiments on rough metal plates using a shock tube. A zigzag shape (plan view) of a sand wall (Rose et al. 1998) was also shown to result in an improved performance (measured at $Z = 3.5$–4.2 m/kg$^{1/3}$). All these suggest that roughness on the surface of barriers can indeed enhance attenuation.

To understand the effect of stacking several barriers, Benselama et al. (2010) experimentally studied blast propagation over a series of three barriers. Barriers of dimensions $8.5 \times 0.6 \times 0.6$ m, spaced 1.2 m apart (in the direction of blast propagation) were used in this experiment. A 416 g TNT equivalent mass was detonated at a distance of 1.7 m from the first barrier and they found that blast pressure attenuation is effective only beyond the second barrier. They also reported that height-to-spacing-between-barriers ratio played a more important role than the breadth-to-spacing-between-barriers ratio.

While the use of barriers is more common outdoors, Santos et al. (2018) discuss the role of a 'meandering wall' placed ahead of an access control zone inside a building. This could be helpful, in spaces such as in a hotel lobby, to mitigate the effect of an explosion from a luggage bomb. They report a reduction in peak overpressure and impulse values in the protected region, based on a numerical experiment conducted using 25 kg TNT at a distance of 3–5 m from the rigid wall. This shows the potential use of having barriers even inside buildings under special conditions.

2.3.3.1.5 General Outlook on Barriers

A reduction in overpressure values was found for distances of up to 8 times the height of a blast wall. Experiments on frangible walls showed attenuated pressure values downstream.

Table 2.2: Summary of literature on barriers and blast wave interaction

Barrier Type	Representative Scale	TNT Eq. Weight (or Incident Pressure)	Stand-off Distance (or decay time)	Loading Estimates
Metal wall with canopy,	0.68×8.6 m, canopy 0.3,0.45 m	0.5, 4, 7.6 kg	0.3	Tabulation (Beyer 1986)
Metal wall	0.35×2.1 m	0.075 kg PE4	0.138	Tabulation (Rose et al. 1995)
Metal wall	0.35×2.1 m	0.075 kg PE4	0.138	Extension (Rose et al. 1997) of (Rose et al. 1995)
Metal wall	0.3×2.1 m	$0.04 - 0.08$ kg TNT	$0.15 - 1.2\ m$	Empirical Formula (Chapman et al. 1995*b*)
Wall	L:Infinite, B:300 mm, H:$1 - 4$ m	$10 - 10000$ kg TNT	$1 - 40$ m	Empirical Formula (Zhou & Hao 2008)
Finite Barrier	$3.50 \times 3.95m \times 3.00$ m	100 kg	$15 - 50$ m	Tabulation (Payne et al. 2016)
Frangible walls	0.3×1.5 m (approx.)	75 g ($eq.\ TNT$)	138 mm	Plots (Rose et al. 1998)
Finite Barrier (Dike)	B:$1.95 - 12$ m, H: $1 - 15.96$ m	3400 kg ($eq.\ TNT$)	$30 - 64.5$ m	Empirical Formula (Miura et al. 2013)

This suggests that the strength of the wall is not the primary contributor to attenuation but instead, it is shock diffraction that plays a dominant role. While it is intuitive to understand the prominent role played by the height of the barrier, the importance of having a long wall to avoid hotspots of overpressure behind the wall, and the relatively low importance of thickness of the barrier to enhance attenuation have been key findings of research on this topic. Empirical formulae to obtain the pressure on a plane target wall behind a barrier are available for a wide range of parameters. A forward inclined canopy, and a rough surface for the barrier, were both found to enhance attenuation. It is worth noting at this point that the role of target clearing has not explicitly been considered thus far in any of these studies, as the focus was on explosions located relatively close to the barrier.

In an urban environment, blast protective structures (e.g. blast walls and other obstacles) should be unobtrusive, and ideally, blend in with the surroundings. A number of suggestions have been provided in FEMA (2007) guidelines. While the research on barriers and canopies has shown an appreciable increase in protection in the immediate shadow region, the use of these barriers in a cityscape may not be appropriate as they give the unwanted appearance of a garrison. The additional risk of fragmentation is also an important consideration, and so barriers do not easily go with an urban landscape (Zong et al. 2017).

Researchers thus began exploring the possibility of using small barriers and posts, such as bollards, which are part of any urban streetscape, to mitigate a blast wave. Can smaller obstacles and a transition from an absorption-type to a deflection-type blast attenuation technique still return similar levels of protection? This forms the topic of the next subsection, namely, the use of obstacles, rather than barriers, to achieve mitigation.

2.3.3.2 Obstacles

The interaction of a blast wave with a structure is characterized by several complex flow features, such as reflection, diffraction, vortices, and the various interactions within these features. Bazhenova et al. (1984) describe how the study of shock wave motion over simple objects – e.g., a case of reflection off a concave corner or a diffraction off a convex corner along the direction of propagation of a shock wave – can be used to understand flow patterns over more complex structures. In the following sub-subsections, we first address relevant research on simple obstacles and then progress on to groups of obstacles.

2.3.3.2.1 Single Obstacle

Typically, previous studies on obstacles involved a flat-top pressure profile – generated by a shock tube – than the decaying pressure profile that is characteristic of blast waves. Since these loads have a steady pressure for at least a few milliseconds after the instantaneous shock pressure jump, the decay time of these waves is not clearly defined. Thus, most descriptions of the strength of the wave are in terms of the Mach number. Typically, they are in the range of 1.2–1.8, whose scaled stand-off distances would then be between 2 and 3.5 $m/kg^{1/3}$ for a surface blast.

Analytical predictions for the shape of the diffracted wave were given by Whitham (1957). To validate this method, high Mach number ($M_s = 3$) shock tube experiments on the flow involving steady, strong shocks over cones, a cylinder, and a sphere were carried out (Bryson & Gross 1961). It was then shown how the flow field may be reconstructed for a particular obstacle shape using numerical integration of the appropriate flow equations or by using the method of characteristics. Interestingly, the authors found that the diffraction pattern was independent of the Reynolds number, and it is suggested that this is likely to also be true for blast waves since they are both impulsive flows.

The role of a circular pole ($\sim$ 64 mm diameter) in disturbing the flow field was studied using CFD (Christiansen & Bogosian 2012). For a single pole placed between the target

and explosive, overpressure and impulse reduction were achieved on the target for stand-off distances between 0.52–0.72 m/kg$^{1/3}$. Using three poles (one $\sim$ 64 mm and two $\sim$ 50 mm diameter) in a triangular arrangement, with the bigger pole facing the explosion and the smaller ones behind it, the reduction in overpressure and impulse was enhanced twofold. Dey et al. (2020) used ANSYS Fluent to study the pressure field around generic obstacles: sphere; cone; and cylinder, all having equal frontal dimension and overall length. They found that the strongest initial wave reflection was seen for the cylinder, followed by the sphere and then the cone. The re-attachment of the shock behind each of these objects was found to be the quickest for the sphere, then the cylinder and finally the cone.

Hahn et al. (2021) performed CFD simulations in order to study the pressure and impulse field that evolved on a façade behind a cylinder at high Mach numbers, which corresponds to scaled distances of $Z \sim 0.4$–1.5 m/kg$^{1/3}$. The authors noted the presence of a pressure increase behind the column, even up to a distance of $12D$, excluding a very narrow region of $0.5D$ behind the pole, where the values were 15%–20% lower than the corresponding free-field value. A subsequent increase in impulse, to almost double the incident value, was observed behind the column, occupying a narrow band extending approximately 45° behind the pole. The high pressure immediately behind the pole arises because the pressure wave wraps around the circular cross-section of the column and re-forms, leading to multiple reflections. For a specific case ($Z \sim 0.6$ m/kg$^{1/3}$, $D = 0.3$ m), where a façade was located 1 m behind the cylinder, a 14% increase in pressure was observed. The column height effects were not considered, as analyses were performed in 2D.

2.3.3.2.2 Multiple Obstacles: state-of-the-art

Dosanjh (1956) studied the transmission of a shock wave through a wire grid, and showed that the flow is influenced by the choked area of the grid. This is because area reduction, as expected, inhibits the flow. This finding has since been confirmed repeatedly by several researchers, all of whom showed that the area ratio controls the flow downstream of an array of obstacles (Monti 1970, Honghui & Yamamura 2004, Epstein & Kudryavtsev 2012).

Honghui & Yamamura (2004) studied the passage of a shock wave (M_s = 1.4–1.9) through spheres and cylinders arranged as rows of ball and stick (3 & 4 mm diameter) models. They observed a direct correspondence between the attenuation and the blockage introduced by each model. Increasing the spacing between rows beyond 15 mm did not influence attenuation in the case of smaller spheres (10 mm) diameter, but for the larger spheres (20 mm diameter), it proved beneficial. It is to be noted that for the larger sphere experiments, the maximum spacing inspected was up to 30 mm. The authors also reported increased attenuation with more rows, and also with stronger shocks (higher Mach number).

Britan et al. (2006) investigated shock transmission through porous barriers (porosity: 0.15–0.7) of different geometries for M_s ranging from 1.35–1.7. They concluded that the porosity and not geometric factors (including shape, thickness, hydraulic diameter of the opening) determined the level of attenuation. Increasing the distance between the end wall and the barrier caused a linear reduction in overpressure and for distances beyond 50 hydraulic diameters, viscosity began to play a role.

Sasoh et al. (1998) investigated the effects of pseudo-perforated walls on very weak shock waves (M_s = 1.02–1.12) travelling in ducts, building on previous work and showed that, unlike weak shocks, it takes relatively shorter lengths to attenuate a Mach 1.5 shock wave (Craig 1977). They found that the length of the pseudo-perforated wall section is an essential parameter and should be increased to achieve better attenuation. This concept has implications on the roughness of elements implemented for blast attenuation studies, and is also well corroborated by earlier work on roughness of a barrier surface.

A flap valve is a dynamic barrier whose orientation depends on the shock strength (Fig. 2.17). Investigating the potential benefits of a flap valve for Mach numbers 1.2 and 1.4, Berger et al. (2015) report that for the same porosity ratio, a barrier inclined at α=135° (upstream) to the flow showed 15% higher attenuation than the one at 45° (downstream). As an aside, the overpressure data for these angles are similar to the

findings of Xiao et al. (2019) for a canopy on a barrier wall.

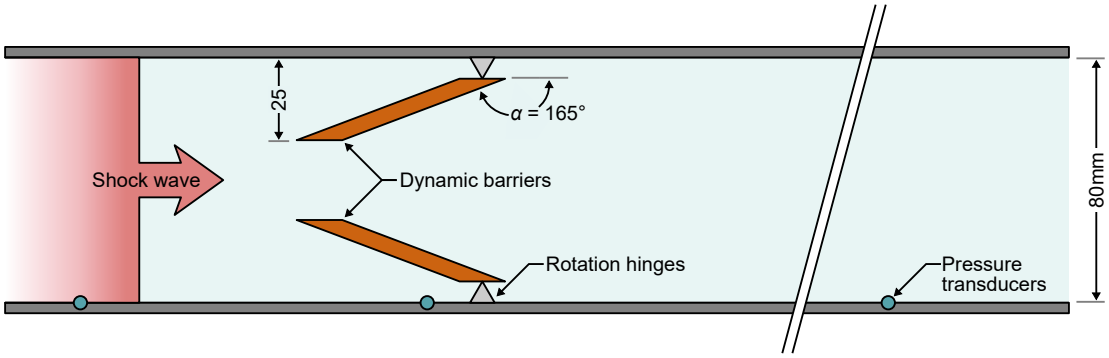

Figure 2.17: A schematic representation of the dynamic barrier concept as reported by Berger et al. (2015), comprising of a pair of hinged barriers inclined towards the incident shock wave.

Chaudhuri et al. (2013) studied the transmission of shock wave ($M_s = 1.4$) through 4 rows of obstacles with the following shapes:

- triangle (vertex pointing upstream),
- triangle (vertex pointing downstream),
- square,
- and circle.

2D numerical simulations showed that the backward facing triangle (a divergent opening) was the most effective in attenuating a shock wave. This was also confirmed by Prasanna Kumar et al. (2018) for a higher incident Mach number of around 2.7. This finding shows that at low porosities ($\sim$ 0.25), the geometry of the obstacle also plays a role in the attenuation. However, for the upstream side of the obstacle, i.e., the reflected shock wave, they observed that the wave is attenuated when the obstacles have a converging shape (upstream facing triangle). In what is essentially a combination of these two concepts, Skews et al. (1998) reported the concept of shock trapping to enhance the mitigation of a shock wave. This concept was further validated in the work by Seeraj & Skews (2009).

A logarithmic spiral is a well known arrangement used to focus shock waves. Instead of placing obstacles along straight rows perpendicular to the flow direction, Wan & Eliasson (2015) extended these M_s=1.4 simulations further to study the effect of placing them along a (longer) logarithmic spiral. This contrivance has a lower porosity value and could thereby improve the attenuation performance. While it provided good attenuation at the spiral's design Mach number, an enhanced attenuation performance was observed for a stronger than design incident shock ($M_s = 1.5$.) However, the logarithmic spiral generally under-performed for lower Mach numbers. Surprisingly, the pressure upstream of these obstacles did not increase in a manner commensurate with the higher blockage ratio that should have led to a stronger reflection. This implies that the use of a logarithmic spiral can be explored for situations where protection is desired along both sides of the barrier.

Niollet et al. (2015) used 20–70 g PE4 in a blast tube to study the mitigating effect of an arrangement of cylindrical poles ahead of a target structure (a metal plate). They found that the target experiences either amplification or amelioration of the blast load, depending on the arrangement of the bars. A staggered arrangement of the cylinders was shown to be more beneficial towards amelioration. They also noted that placing the bars too close to the test plate would cause more damage as the reflected wave gets trapped, leading to an increased loading duration. The impulse of these tests ranged from approximately 40–100 N.s over an exposed area of 200 × 200 mm.

The role of surface roughness was experimentally and numerically explored by Ivanov et al. (2019) for $M_s = 1.2$ by using obstacles (10 × 10 mm) with and without small undulations (dimples of $R = 0.58$ mm) on its surface. Despite observing additional vorticity in the downstream of the flow due to these serrations, they did not detect any significant difference in the attenuation values. This was attributed to the small sizes used for the simulations, whose disturbances were perhaps not sufficient to give rise to a marked improvement in attenuation. This should be contrasted against the results reported in the previous section, where the surface roughness played a significant role in

attenuation.

For further reports on studies over obstacles, one may refer to the detailed review by Igra et al. (2013) and a summary of the literature in Wan & Eliasson (2015).

2.3.3.2.3 Multiple Obstacles: Rigid Porous Media

A very special case of the multiple obstacle scenario is the interaction of a shock wave with porous media. The resultant transmitted pressure is (usually) not instantaneous, providing additional time for the structure to be loaded fully, which can result in the target structure experiencing a less severe, non-impulsive load. Ram & Sadot (2013) describe an elegant semi-analytical method to estimate such overpressure loads on the end wall of a shock tube, located at a distance L from the rear face of a slab of porous media. Due to the presence of voids in the porous barrier, the effective (open) length from the rear face of the porous barrier would now be longer; L_{eff}. This zone may be considered to be a confined zone filled with ambient air having specific heat ratio, γ. As the blast wave travels across the barrier and transmits to the other side, it may be taken to be the equivalent of pressurizing this confined zone from the upstream side of the porous barrier following an isentropic process. From this, a simple equation (Eqn. 2.4) for the evolution of pressure was then proposed and experimentally validated using a shock tube.

$$\frac{P(\tau)}{P_{ideal}} = 1 - e^{-\alpha\tau}, \quad \texttt{where} : \tau = \frac{t}{(L + L_{eff})^{\gamma}}, \tag{2.4}$$

Here the parameter α represents a characteristic value for the porous media, and it depends on aspects specific to the internal structure of the media such as the porosity, the tortuosity, frictional coefficient, etc. This value may be determined from a single characterization experiment to generate the shock transmission pressure trace behind the porous barrier. From Eq. 2.4, we may note that the transmitted reflected pressure value, P(τ), given enough time will eventually reach the undisturbed reflected pressure value (P_{ideal}), which implies a complete pressure recovery. In the context of a Friedlander blast

wave, where unlike a shock wave, the pressure decays immediately upon arrival of the wave front, the pressure value $P_{max}(\tau)$ is expected to be lower than P_{ideal}, resulting in an attenuation in terms of the peak pressure as well.

2.3.3.2.4 Multiple Obstacles: Flow Path

A review of both experimental and numerical studies of shock waves (M_s = 1.4–1.9) entering a region of sudden area change was provided by Abate & Shyy (2002). This work showed that the basic flow structures in the early times are very similar, regardless of whether the shock expands along one, two or three dimensions. This is expected to hold even for blast wave propagation. They also show that very little dissipation occurs within the flow structures, apart from the region near the expansion corner and the shock wave itself. High-strain rate regions due to vorticity that develops at later times, and dilation due to shock waves, were identified as the major causes for the dissipation.

Shock attenuation (M_s = 1.45) was studied through various configurations of double bend ducts with differing internal roughness (Igra. et al. 2001). It was found that a bend of length L that was *four times* the shock propagation channel width (H) was the optimal value to maximize shock attenuation and minimize volume increase (or the occupied space). Roughness was also found to enhance attenuation. It was also shown that viscosity plays a role only in the later times and that an inviscid simulation is sufficient for the early times.

Instead of the 'attenuation by blockage' concept that was addressed thus far, a convoluted "zigzag" path for the shock wave was numerically evaluated (Kumar R & Pathak 2020), with a view to developing a lightweight protective structure. The effective open passage for the flow, different from the projected open space, remains the same despite the convoluted path, giving a blockage ratio of *zero*. For purposes of comparison, staggered cylinders with a blockage ratio of 0.6 and a zigzag path with cylindrical obstacles resulting in a blockage ratio of 0.4 were used. The idea was to weaken the shock wave by repeated interactions

with the convoluted wall, instead of a single reflection occurring off an obstacle block. For the first case, it was found that alternate reflection and diffraction occurring in the zigzag path contributed significantly to attenuation. In the second case, reflection off the cylindrical obstacle was the contributing factor, in addition to some attenuation arising from reflection, and diffraction off the cylinders in the downstream rows. In the last case, the presence of cylindrical obstacles added to the attenuation produced in the first case by means of the extra reflections off the cylinders. The attenuation measured in terms of incident and reflected pressure reductions was found to be increasing in this order (34%, 36%, 64% respectively) showing that weight reduction may be achieved without compromising on the attenuation performance.

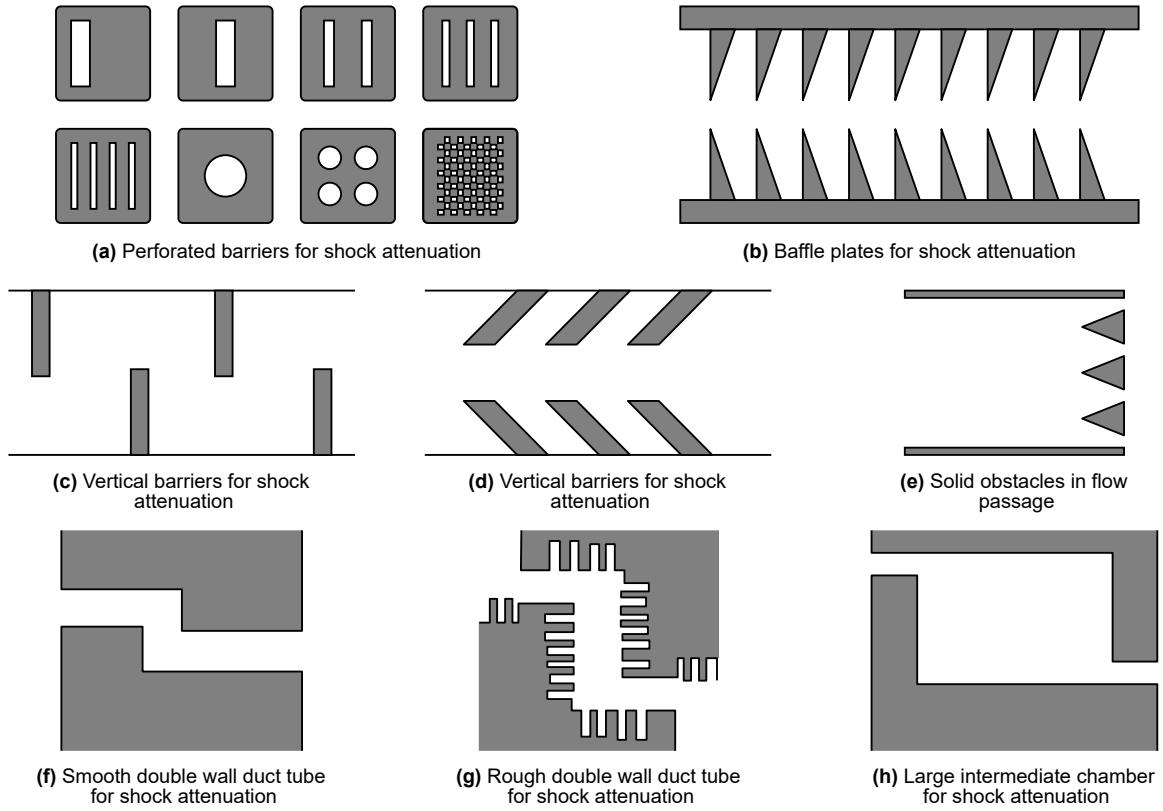

Figure 2.18: A selection of obstacles (a-h) that have been investigated as forms of shock attenuation as reported by Kumar R & Pathak (2020).

Fig. 2.18 shows the test objects on which shock propagation studies have been carried out. It is to be noted that most or all of these studies were for shock waves. To understand the difference between the response to a blast wave and a shock wave, a few studies are

available in the open literature and are briefly summarized in the next sub-subsection.

2.3.3.2.5 Multiple Obstacles: Contrasting Shock Wave and Blast Wave Interactions

Ritzel et al. (2018), as part of their studies on the drag loading of a free sphere, suggest that if shock wave loading were considered to be an unsteady flow problem, then blast wave loading ought to be considered a doubly unsteady flow problem. It is not always clear as to how shock tube-based experiments would correspond to a field explosion, as the duration and decay of the pulse are quite different. Ofengeim & Drikakis (1997) report numerical studies on wave propagation behind infinitely tall cylinders for three types of waves having the same peak pressure value corresponding to $M_s = 1.7$:

- a shock wave (t_d=∞, for mathematical consistency),
- a long duration blast wave ($t_d = 15$ ms), and
- a short duration blast wave ($t_d = 3.2$ ms).

The authors show that for the shorter duration blast waves the viscous-inviscid interactions are weaker, the shock front interactions are different at later times, and the vortices do not move downstream. With regard to the peak initial pressure, the behaviour is expected to be similar, as Epstein & Kudryavtsev (2012) showed using CFD, but the applicability of shock tube experiments for impulse loading is still not clear. For instance, the contrasting results on the role of structural thickness in the attenuation brought about by a barrier – for a blast wave by Miura et al. (2013); and for a shock wave by Sha et al. (2014) – may be attributed to the non-consideration of curvature of the blast wave in the shock tube based work of Sha et al. (2014). Nonetheless, it appears that shock wave based data are an excellent way to understand how the instantaneous pressure rise, which is also associated with a blast wave, may be mitigated.

2.3.3.2.6 Multiple Obstacles: Modelling Realistic Scenarios

A simple model of a railway station was studied by Hajek & Foglar (2015) with a view to understanding the role of obstacles in mitigating the pressures (Fig. 2.19). However, no reduction in overpressure due to the barriers was observed both experimentally and numerically. The authors suggested that barriers are effective in reducing pressure only in a localized region in its vicinity and not in the far-field.

Gan et al. (2022) studied the influence of randomly-placed obstacles on the development of pressure and impulse within an internal environment. They found that channelling is highly localised and results in increased loading near the explosive, the effect of which increases with obstacle density. Shielding was shown to be a cumulative effect which increases with distance from the explosive, and with increasing obstacle density.

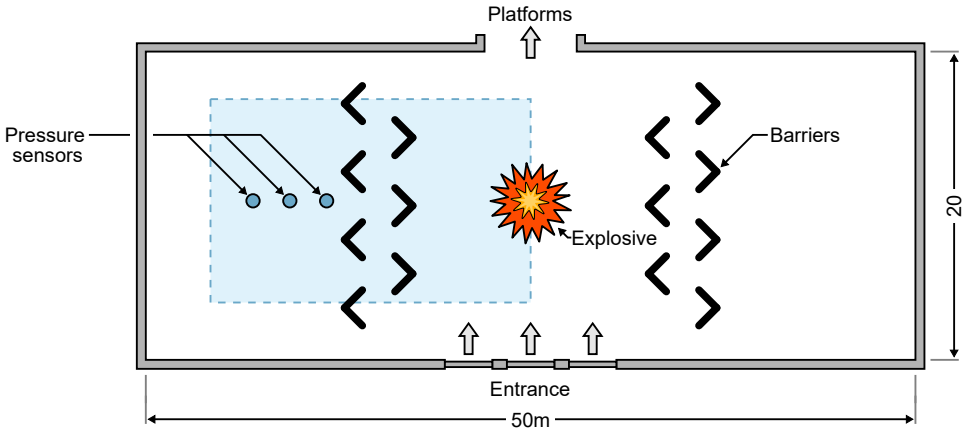

Figure 2.19: A schematic diagram of the layout used to simulate the effectiveness of barriers for attenuating the blast loading from an explosive detonated in a railway station building (Hajek & Foglar 2015). The experimentally tested area is shaded blue.

2.3.3.2.7 General Outlook on Obstacles

Shock tubes have been primarily employed to study the evolution of loading on different shapes of obstacles – individually, and as groups – as it is a convenient means to generate an instantaneous rising pressure load that is characteristic of any blast loading. For the loading of multiple obstacles, an important finding has been that the shape of the obstacle is of secondary importance. The dominant characteristic has been identified as

the blockage ratio of the obstacles, i.e. some measure of the restricted volume that the shock/blast has to propagate through. Additional concepts which may be incorporated in designing novel blast protection obstacles include a sudden volume expansion, a change of direction of the wave (zigzag path), and the use of perforations or rough-walls. The relevance of shock tube-based research for blast wave studies was also highlighted.

From the few studies modelling realistic scenarios, it appears that the shock attenuation observed at small scales do not fully translate to a full-field scenario. This is because the height of the obstacles, which were modelled as 2D in shock tubes, cannot be scaled up to infinity in the real world. Researchers therefore have begun to adapt to account for the inability to have tall (infinite) obstacles, by proposing a new combination of structures, termed here as hybrids, which form the topic of discussion for the next sub-subsection.

2.3.3.3 Hybrid Types

2.3.3.3.1 Fence Wall

The mechanism by which a barrier attenuates a blast wave is primarily due to diffraction, or the shadowing effect. For multiple obstacles having low porosity, it is a combination of the blockage induced by the obstacles, and the dissipation brought about by travelling through such constricted openings. Combining these two mechanisms, and arranging multiple obstacle like a barrier, one can have a realistic structure that can help mitigate an explosion in urban scenarios. This gave rise to the concept of what is now referred to as a 'fence wall' (Fig. 2.20).

Gencel et al. (2015) studied the effectiveness of a 2 m long barrier comprising a series of 13 GFRP poles, each 2.5 m tall and having an outer diameter of 85 mm, as shown schematically in Fig. 2.20. The aim of this study was to evaluate the effectiveness of protecting airport terminals using barriers whilst maintaining radio transparency. Experiments conducted using a 4 kg TNT equivalent explosive placed at a height of 1.5 m above the ground (to avoid reflections) showed promising results in terms of blast attenuation

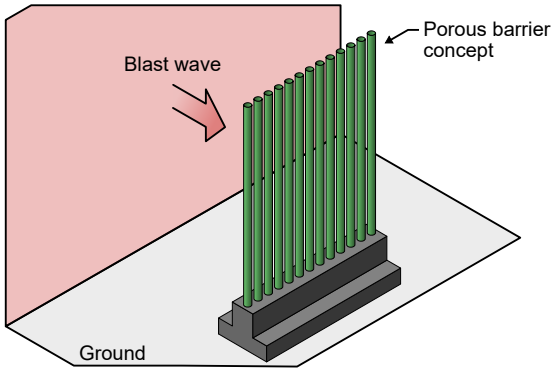

Figure 2.20: An illustration of the fence wall concept comprising obstacles (poles) spaced apart to create a hybrid (blast wall) which is a novel concept in passive blast wave mitigation.

at stand-off distances ranging from 0.5–3.0 m.

Similarly, Zong et al. (2017) proposed the use of a fence wall concept using poles having various cross-sections for blast mitigation in a cityscape. Preliminary studies considered the shape of the obstacle, the spacing between obstacles, the effect of scaling up the dimensions, the obstacle layers, and separation between the layers. Experimental validation of these numerical findings were then reported in a follow-up study (Hao et al. 2017). The authors suggest that although a square section generally performed better due to the stronger reflection that it generates, a circular section is to be preferred for reasons of better structural strength to weight ratio (Jin et al. 2019).

Xiao et al. (2018, 2020*b*) conducted experiments to study the role of increasing the number of square poles on the attenuation performance of a fence wall system. The aim was to understand the role of the relative opening fraction – similar to the concept of porosity – on blast mitigation. These experiments were used to validate a numerical model, which was then used to carry out subsequent optimization studies. It was found that a square shaped obstacle outperformed the other equivalent sized shapes (forward facing triangle, rear facing triangle, circle) that were considered. This mitigation, however, should be considered in conjunction with the fact that the loading on the barrier was also increased, as previously noted by Zong et al. (2017). Xiao et al. (2018, 2020*b*) also observed an

increasing mitigation as the number of poles were increased. Interestingly, multiple rows of poles were not shown to increase attenuation in their study. It is well known that spacing between poles in the first row is the controlling factor for downstream attenuation (Dosanjh 1956). Since this was the same for both scenarios, it could perhaps explain why an enhanced attenuation was not observed.

2.3.3.3.2 Non-Conventional Techniques

Barriers such as bollards, benches, landscaping, plants, etc. are considerably less imposing than hardened structures such as blast walls. Accordingly, Gebbeken & Döge (2010) proposed the use of plants as barriers for attenuating a free-field blast wave. In a preliminary study carried out on different species of plants (Gebbeken et al. 2017), pressure reductions of up to 60% were shown to be possible, with most of the biomass remaining intact despite repeated impacts. Interestingly, the authors observed that the pressure profile changed from a typical Friedlander exponential decay to a shock wave-like flat-topped pressure profile. Criterion for the choice of plants, such as the use of narrow leaves (coniferous ones), and having a large biomass to account for inertial resistance, were formulated as part of this study. These experiments were conducted using 5 kg of TNT at approximately 5 m stand-off distance.

In subsequent experiments with a similar charge and sensor positioning but slightly different dimensions of the plants, a reduction of up to 45% in overpressure values were reported (Warnstedt & Gebbeken 2020). Again, the authors did not observe a reduction in biomass (Yew and Thuja trees) after being impacted repeatedly by blast waves, although tilting was observed[8]. Bamboo and barberry exhibited a reduction of 30% in overpressure values behind the plants, but with significant reduction in biomass, thus rendering them less effective should there arise repeated explosion loads. The authors

[8]The plants were not grown in the soil but were transplanted to the test site, back-filled with sandy soil which was then watered and compacted to minimize tilting

report, however, that this reduction in pressure is valid only up to a limited distance as the unimpeded blast wave travels over the plants and meets with the transmitted wave beyond a certain distance, leading to an almost complete recovery in pressures. Again, 5 kg TNT was used in these experiments, at a stand-off distance of 4 m. The sensors were placed approximately 1 m behind the plants and the overpressure reduction had almost halved at sensor locations that were just 0.5 m beyond. For example, for the Bamboo, it dropped from 28.8% to 9.9%; for the Yew, from 43.4% to 26%; and for the Thuja, from 42.8% to 35.4% – an anomaly which could possibly be linked to the shock wave type profile behind these coniferous trees (Gebbeken et al. 2017), which do not decay as rapidly as the Friedlander-type waves. These plants were all approximately 2 m tall.

The role of trees in mitigating a blast wave were further explored recently by Gan et al. (2021) using a large shock tube blast wave simulator. Two Juniperus Spartan trees, 1.6 m high, were subjected to varying blast loads (25–50 kPa, $\sim$ 15 ms) and overpressure and impulse reductions of up to 20% were measured on a target wall behind the trees. Enclosing the trees in a wrap to make them less porous enhanced the attenuation performance, as the overall blockage ratio would go up. These trees were found to be resilient, and the trunk and most leaves were intact after 9 tests. The ability of the tree to continue to grow after exposure could not be tested as the trees were uprooted and embedded in concrete to perform the blast tests. For a similar range of explosive mass (5 kg) and stand-off distance (5 m), a steel mesh made up of rings of different sizes (with the potential to trap flying debris) was shown to help mitigate a blast wave (Gebbeken et al. 2018), and the inclusion of a water curtain indicated that further appreciable attenuation may be attained.

Using a similar test arrangement, another method was reported by Xiao et al. (2020*a*) using a wire mesh instead of an obstacle-based fence wall system. Although the reported attenuation of pressure (up to 31%) was a little lower than what was measured for the barriers (Xiao et al. 2020*b*), it was found to render similar performance for a much lighter

'barrier' mass. Recently, a small scale experiment using an explosive-driven shock tube was used to study the wave attenuation characteristics across a 'wire mesh' made of expanded metal (Schunck & Eckenfels 2021). The reference reflected pressure was around 20 bar, and the impulse was 3.2 bar-ms. The open area of each mesh was 24%, which gave rise to reduction of up to 75% (pressure) and up to 90% (impulse) when two layers of this perforated plate were used. Similar results were also reported at lower pressures (3 bar) for a free-field experiment, suggesting that this is a potential technique that could be used in a cityscape. Using two layers or even a single layer with water film over it helped increase the amount of wave reflection and this, according to the authors, helped improved the mitigation.

2.3.3.3.3 General Outlook on Hybrid Types

With a view to overcoming the limitations imposed by the other attenuation techniques, hybrid methods, which are a combination of barriers and obstacles, were briefly reviewed. Several successful hybrid methods are now available, viz., optimized fence walls, wire meshes/ring fences, and even plants, all of which have been verified using field experiments and shown to provide mitigation of at least 20%, albeit for a limited region behind the obstacle. These methods have attempted to incorporate aspects of protective design which can fit into a cityscape without appearing to be disruptive or imposing, yet provide protection to the structures they aim to protect. The next sub-section reviews methods that are available to quantify the evolution of pressure loads due to a blast wave, for both direct and indirect loading scenarios.

2.3.4 Prediction Tools

The determination of the blast load and structural response are carried out using either first-principles methods like CFD, which solve the equations of motion according to the laws of physics. For certain simple scenarios, (semi-) empirical methods, derived either in-part or entirely using experimental data are relevant. Additionally, machine learning

methods are increasingly being used in engineering applications, including blast load and response prediction.

2.3.4.1 Direct Loading

For direct loading on structures, simple techniques may suffice for geometrically idealized settings. The more sophisticated approaches are only necessary for situations where the blast wave has been impeded by other obstacles or a barrier. As outlined in the section on direct loading, for certain scenarios, the free-field blast parameters may be directly used to estimate the load for certain structure and stand-off distance combinations. For such special cases, such as on isolated buildings at great distances from an explosion, the surface burst and/or air blast parameters may be calculated using a variety of semi-empirical techniques (Kinney 1985, Kingery & Bulmash 1984, Hyde 1991). For a review of simplified techniques to predict blast loads, the reviewer is directed to Remennikov (2003)

For scenarios where a single value of clearing can be applied to the entire face, a simple correction was first proposed by Bleakney using shock-tube experiments at Princeton in 1952. Additional details of this experiment may be found in Shin & Whittaker (2019). The correction is available in terms of the clearing time t_c (Norris et al. 1959), defined as the duration required for the reflected pressure to decay to the stagnation pressure (Fig. 2.3). This is estimated using the distance to an edge on the obstacle S, and the shock velocity U as given in Eq. 2.5.

$$t_c = \frac{3S}{U} \tag{2.5}$$

A slightly improved variant of this formula was then included in the UFC 3-340-02 (US Department of Defence 2008), with the clearing distance S taken to be $min(h, W/2)$, as illustrated in Fig. 2.21. The improved formula is given in Eq. 2.6.

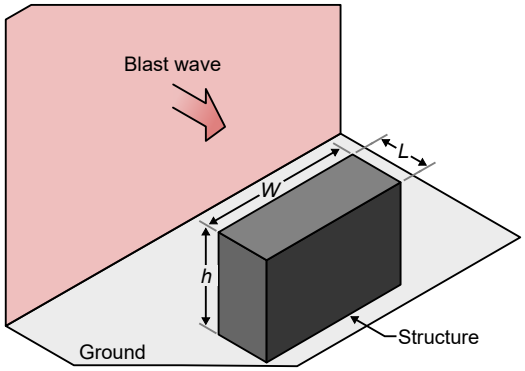

Figure 2.21: An illustration showing a blast wave impacting a finite sized structure, for which the clearing distance is given by $S = min(h, W/2)$.

$$t_c = \frac{4S}{(1+R)C_r} \tag{2.6}$$

To obtain the structural response, SDOF-based techniques as recommended in TM5-1300 (US Army Corps of Engineers 1990) can provide a good first estimate, and they can be readily adapted to implement cleared pressure values using the formulae in Eqns. 2.5 & 2.6 and several similar ones as described in other detailed reviews on the topic (Bhatti et al. 2017, Ullah et al. 2017).

2.3.4.2 Indirect Loading

The case of indirect loading is more complicated as it involves aspects such as shock reflection, diffraction, vorticity etc., rather than the simple case of clearing. Accordingly, this often requires the use of a full CFD simulation. Nevertheless, given a porosity value for an obstacle configuration, some simple analysis carried out using 1D modelling can give insights into the final attenuation values.

2.3.4.2.1 Quasi-1D Gas Dynamics Code For Porous Structures

Britan et al. (2006) report the use of a quasi-1D nozzle model to simulate the blockage introduced by a porous obstacle to the blast transmission. This involves numerically solving the relevant conservation equations for an unsteady inviscid flow in a quasi-1D

geometry to obtain the pressure downstream of the nozzle. This value may then be correlated to the pressure behind a porous barrier. Good correspondence between the experimental data and the numerical results was observed, suggesting that this can be a quick method to accurately estimate average pressure history over a region.

Instead of the geometric area reduction that was simulated by Britan et al. (2006) for a blast wave travelling through a channel with packed cylinders, Suzuki et al. (2000) suggested the use of a drag force term in the 1D Euler equations. The drag force in the source term may be obtained either from an experiment, or using other empirical methods. This model was also found to perform well against experimental data.

As described earlier, Ram & Sadot (2013) proposed the use of a simple formula to obtain the pressure evolution over a wall placed at some distance from a rigid porous barrier impacted by a shock wave. A single shock loading experiment using a block of porous material would suffice to obtain the value of a bulk parameter (α) that encapsulates the porosity, tortuosity, friction loss etc. through the material. Inserting this value into Eq. 2.4 would then provide the pressure history on a wall beyond the porous barrier.

Since blast waves are usually a non-linear phenomena, the advantage of these quasi-1D methods is that the actual conditions – shock speeds and overpressure values – are used, which will result in reproducing the flow conditions faithfully. It should be noted, however, that these are essentially single point data models, and so they cannot describe the spatial variation over the target. However, they can still provide reliable estimates of the pressure that a target surface would experience.

2.3.4.2.2 Empirical Methods For Barriers

As described earlier, the empirical formula for predicting the overpressure and impulse on a building face behind a barrier wall of a given height was first given by Chapman et al. (1995*b*) in terms of a modified scaled distance. The authors developed an empirical relationship between a modified form of reflected pressure (termed 'factored peak pres-

sure', P_f) and a combined distance parameter that accounts for the total distance from charge to the target, the HoB, the wall height, and the target height (termed 'protection factor', F_p.) A similar relationship for 'factored peak impulse' was also used to arrive at a correlation for impulse, and all these are given in Eqn. 2.7.

$$
\begin{aligned}
F_p &= (Z_{B,TNT} + Z_{T,TNT})\frac{H_B}{HoB \times \ H_t} \\
P_f &= P_r \frac{HoB + H_T}{(d_B + d_T) \times \ H_B} \\
i_f &= i_r \frac{(HoB + H_T)}{(d_B + d_T) \times \ H_B \times \ W^{1/3}} \\
&where, \\
P_f &= 10^{2.881} {F_p}^{-2.363} \\
i_f &= 10^{2.155} {F_p}^{-2.399}
\end{aligned}
\tag{2.7}
$$

Zhou & Hao (2008) then generated a more comprehensive numerical simulation dataset that was used to derive an empirical formula for pressure, impulse, arrival time and decay time of the pressure load at each point on the wall. This methodology was then adapted for a fence wall barrier by Gencel et al. (2015). The work of Zhou & Hao (2008) was extended by Steven & Khaled (2017) for frangible walls, by using a correction factor based on the effectiveness (in alleviating pressure and impulse) of 12 materials that were available in literature. This method was then compared with the VAPO software, and the results were found to be on the conservative side. The advantage, however, is in the extremely short time taken to arrive at the results, which will be useful to make a decision for or against a given concept in the preliminary stages of design. Other prediction methods for barriers, may be found in the review by Bhatti et al. (2017).

Heuristic/statistical – Prediction on the Ground:

Éveillard et al. (2013) presented a fast-running method for obtaining pressures on the ground behind a barrier having an inclined rear face, based on data from TM5-1300 (US

Army Corps of Engineers 1990). Estimates were made for the reflected shock pressures at points on the ground, based on the incident Mach number and the angle of incidence. For diffraction around the barrier edges, sample simulations were run to obtain attenuation coefficients based on deflection angle and incident Mach number. This was an improvement over the work of Miller (2004), who had used a single diffraction factor (0.35) for all cases. A simplified version of the LAMB model (Needham 2010) was then used to combine the pressure contributions from multiple rays running from a source located on the ground and the symmetry plane of the barrier to obtain the pressure evolution at each point behind the barrier. The overpressure values predicted by the fast running method were in the range of -30% to $+100\%$ of the numerical computation values, which was deemed reasonable for proof-of-concept studies.

Heuristic/statistical – Prediction on a Target Wall:

A fast-running method also involving segregating the loading regions by using certain critical points (Zhou & Hao 2008) along the height of the target wall was proposed by Sung & Chong (2020). Three points were identified along the height of the wall (Fig. 2.22) to delineate the loading regions:

1. direct incident wave loading region;
2. incident wave and a single diffraction wave loading region; and
3. at the lower portion of the target wall, where a reflected ground shock wave and both diffracted waves from two edges on the top of the barrier interact.

FEM simulations were used to optimally locate these points, and approximate calculations based off the KB relations were proposed. The reflected pressure predictions were found to be reliable unlike the impulse values, which they attributed to the inherent errors in the KB impulse predictions. The authors recommend the use of this technique for first estimates in designing a structure, but suggest the use of advanced CFD software for a finer analysis.

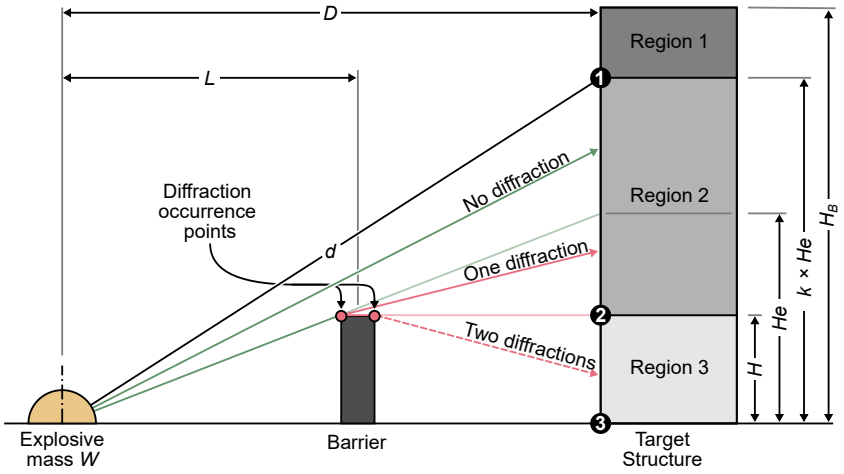

Figure 2.22: A schematic detailing the critical points (1-3) on a target structure loaded by an explosive charge detonated behind a barrier wall. Figure taken from Sung & Chong (2020).

2.3.4.3 Engineering Models

The assessment of blast effects for buildings would require complex calculations involving high-level FEA or CFD, which are computationally very expensive and require expert users. However, there are certain engineering tools that are quick and are available for estimating the blast loading even for certain complex scenarios:

BlastX (Robert et al. 2001) and SHOCK (Wager 2005) are extended semi-empirical engineering codes which can provide blast loading estimates for either external or internal scenarios such as the calculation of explosion parameters inside a chamber bound by 1 to 4 reflecting surfaces.

The Vulnerability Assessment and Protection Option (VAPO) program as an integrated environment can provide a rapid characterization, analysis and vulnerability assessment for complex urban environments such as landscape sites, buildings, and vehicles while using semi-empirical formulas to generate the blast loading (Nichols & Doyle 2014).

Another program which utilises the curve fits data extracted from TM5-1300 (US Army Corps of Engineers 1990) is called VecTor-Blast (Miller 2004). It can produce the blast loading parameters such as pressure, impulse and Mach number acting on cuboid structure

using ray path method considering reflection, diffraction, and Mach phenomenon.

2.3.4.4 Deep Learning Methods

Remennikov & Rose (2007) used experimental data and an artificial neural network (ANN) to predict the pressure and impulse contours in the region behind a barrier where protection is intended. The input parameters were the scaled value of stand-off distance, charge elevation, distance behind the wall, height of the barrier and height of the point of interest. Having trained a model and validated it, they also showcase how such a contour plot may be used by the designer to adjust the location and height of the barrier to enhance protection at the intended location. An ANN (using a radial Gaussian architecture with an incremental learning paradigm) was trained using an extended dataset, generated using DYSMAS software, to predict roof loads on a simple building (Bewick et al. 2011). The pressure and arrival time were predicted quite well, but the non-linearity in the impulse and decay time values made it more challenging. Nevertheless, the ANN was shown to be able to predict the roof loads on the building within a fraction of a second, making it a promising technique for future fast-running codes. Recently, the use of ANNs for confined loading (Dennis et al. 2020) and for near-field loading (Pannell et al. 2021, 2022a,b) were also successfully demonstrated.

In order to obtain the post-explosion blast environment in an urban space, one can perhaps consider dividing the physical space into a digital space, where a binary system may be used to specify the presence or absence of a building/structure as part of the input conditions. This is similar to what was proposed in Zhang et al. (2021) for a different problem. It is to be noted that these fast-running methods and deep learning based techniques are for blast evolution behind a barrier. Such techniques are still not available for the more complex case of flow around an obstacle, as the 3D effect would then start dominating.

2.3.4.5 Computational Fluid Dynamics (CFD)

Smith & Rose (2006) suggested that well-resolved, three-dimensional CFD analyses of blast wave propagation in complex urban environments will be commonplace among the structural engineering community 'within a few years'. Since then, several CFD solvers have been developed, each with their specific strengths and limitations. A non-exhaustive list may be found in Table 2.3.

Table 2.3: A list of common software in use for blast interaction studies

Computer code	Developer
ABAQUS	ABAQUS Inc. (Mougeotte et al. 2010)
APOLLO blastsimulator	Fraunhofer, EMI (Fraunhofer EMI 2018)
AUTODYN	Century Dynamics, ANSYS (Fairlie 1998)
blastFoam	Synthetik Applied Technologies (Heylmun et al. 2019)
CTH	Sandia National Laboratories (McGlaun et al. 1990)
LS-Dyna	Livermore SoftwareTechnology, ANSYS (Hallquist 2006)
ProSAir	Cranfield University (Cra 2009)
SHAMRC	Applied Research Associates, Inc. (Crepeau et al. 2001)

Each of these is characterized by various methods of solving the governing equations (conservation equations and equations of state) of fluid flow for a given set of initial and boundary conditions. They may differ in terms of the methodology of solving the temporal equations, which can use either an explicit or an implicit type solver; the solution may be computed either on a structured grid or on an unstructured one; the frame of reference for the motion could be one of Lagrangian (Lag), Eulerian (Eul), or an Arbitrary Lagrangian Eulerian (ALE). Additionally, the method of initializing the blast load; the scope of including after-burn models (Af-B); the ability to map the solution from an initial mesh to a different one (Remap); the provision of automatic mesh refinement (AMR) which can reduce the computational time; and fluid-structure interaction capabilities (FSI) which can couple the structural and fluid dynamic solvers, can also differ. A summary of capabilities of these solvers may be found in Table 2.4.

Table 2.4: A compilation of capabilities of common CFD software

Software	Solver Type		Discretisation			Remapping	AMR	FSI	Af-B
	Implicit	Explicit	Lag	Eul	ALE				
Abaqus/CEL		✓	✓	✓	✓		✓	✓	
Apollo blastsimulator		✓		✓		1D :3D	✓	✓	✓
AutoDyn		✓	✓	✓	✓	1D : 2D :3D		✓	✓
blastFoam		✓	✓	✓		1D : 2D : 3D	✓	✓	✓
CTH		✓	✓	✓		1D :2D :3D	✓	✓	
LS-Dyna	✓	✓	✓	✓	✓	1D: 2D :3D	✓	✓	
ProSAir		✓		✓		1D : 2D : 3D			
SHAMRC		✓		✓		2D: 3D	✓		✓

Initialization :In any CFD simulation, the procedure to initiate the solution is an important aspect of the process and may be done by one of the following methods: using the mass of the explosive and modelling the detonation process in the solid explosive; using a compressed balloon of (hot) gas to initiate the solution; remapping data from a previous numerical solution; using ConWep data or other semi-empirical models; and using a pre-defined pressure time curve. The interested reader may refer to the review of Larcher & Casadei (2010).

Material Models : The equation of state (EOS) (Éveillard et al. 2013) and material model (Langlet et al. 2015) should be carefully chosen to simulate the explosive and the surrounding medium, especially in the events consisting of a large explosive mass and for cases where near-field detonation is the focus (Hao et al. 2016). The explosive charge shape, orientation, and detonation initiation point should be taken into account, especially when modeling near-field detonation as charge shape can affect the overpressure distributions.

Boundary Conditions : Careful attention should also be paid to the choice of boundary conditions. For example, to recreate a symmetric planar experiment involving an explosion, a semi-infinite barrier, and the target wall (Chapman et al. 1995*b*), numerical validation using AUTODYN (Chapman et al. 1995*a*) was successfully carried out using an axi-symmetric model. This, according to the authors, is a better technique when

compared to using a planar symmetry for the numerical model as it avoids overestimation. Symmetry planes may also be exploited in order to perform experimental studies in reduced dimensions, e.g. quarter-symmetry (Anthistle et al. 2016).

Numerical Methodology : The choice between Eulerian or Lagrangian, and coupled or uncoupled approaches is critical in cases where the structure can deform and offer resistance when internal pressure rises suddenly (Børvik et al. 2009).The model can be explicitly or implicitly solved in time, depending on the type of the software. For more details on the solution process and the advantages and disadvantages of each type, the reader is referred to the review paper by Hao et al. (2016). Although CFD computes the solution from first principles, an experimental validation is always necessary as the solution process includes detonation and turbulence models that are not always from first principles. The size of the mesh (Remennikov & Rose 2005, Benselama et al. 2010) and the number of mesh elements per physical object (Remennikov & Rose 2007), all contribute to the validity and fidelity of a solution. Therefore, carrying out a mesh sensitivity analysis and validating numerical results against experiments is an essential aspect of any simulation.

2.4 Summary and Conclusion

This chapter has focused on reviewing the current knowledge of blast-structures interactions as direct interaction highlighting the blast loading amelioration due to clearing phenomena, indirect interaction in the presence of the wall barrier, single obstacle, multi-obstacles, and hybrid obstacle with particular focus on blast mitigation due to the the evolution of blast wave at downstream, and the determination of the blast loading acting on structural target among a various predictive tools.

Solid barriers have been studied, and some correlations to assist the designer are available in various forms. The role of a canopy over the barrier has also been investigated and found to be effective in mitigating blast pressure. Shock tubes have been used to study effectively infinite length obstacles, and some concepts for pressure mitigation may be incorporated into the design of (high explosive) blast protection strategies in the urban environment. Although the overpressure is almost always lowered in the wake of a rigid blast wall-type obstacle, increases in impulse have been observed in certain regions, attributed to diffracted wave interaction and coalescence. Thus, a holistic approach should be taken when considering the role of protective barriers and obstacles. Furthermore, the risk of fragmentation of frangible barriers cannot be neglected as well as the non-aesthetic view in urban environment which all potentially eliminate the utilisation of solid wall as preferable choice in blast protection.

Wave disruption by using intermediate-scale obstacles to reduce the loading on target is another possible attenuation technique for urban scenarios. Strategies such as poles, wire meshes, plants, and water jets have been implemented in past studies, and it is generally found that these strategies are highly effective at mitigating near-field blast loading (higher Mach numbers). A significant finding in these studies is that the blockage ratio is the single most important factor in dictating the level of mitigation, while other factors such as shape, number of obstacles and rows, and arrangement, play a secondary

role. Key mechanisms governing blast attenuation were identified as diffraction, reflection (diverting away from the target structure), expansion/volume increase, vortex creation/-growth, porosity, and surface roughness. A number of quick-running engineering tools were reviewed. These enable the designer to rapidly analyse a comprehensive parameter space with little computational expense. The accuracy of such methods vary, however their suitability for scoping and probabilistic studies is clear. Sophisticated machine learning methods, trained using datasets from comprehensive physics-based modelling studies and/or experimental work, provide an interesting outlook for the development of predictive approaches in this area, since they potentially balance the accuracy of FEM/CFD with the low computational expense of quick running engineering tools.

Excellent blast mitigation behaviour was seen when the blast wave interacted with multi-scale and self-similar structures like hedges and plants leaving the need of developing such nature-inspired blast protection systems such as fractals obstacles.

To this date, the characterisations of blast wave mitigation behaviour of fractal obstacles have not been well demonstrated. Therefore, there is a need for assessing the performance of fractal obstacles with increasing complexity from single element to multi-scale components in mitigating blast wave with particular focus on mechanisms that enable the approaching toward prediction tools.

Chapter 3

Experimental investigation of blast mitigation of pre-fractal obstacles

3.1 Introduction

As previously mentioned in Chapter 2, there is a clear and pressing need to protect civilians and infrastructure against the damaging effects of explosions, either intentional (e.g. terrorist attacks) or accidental (e.g. the 2020 Port of Beirut explosion Rigby et al. (2020)). One such measure is through the use of engineered protective structures. Typically these are formed of hardened, monolithic barriers (Smith 2010), however recently a new type of blast wall has been proposed (Gencel et al. 2015), termed a 'fence-type' blast wall. Fence-type blast walls are formed using an *array* of smaller obstacles and aim to match the mitigation properties of a monolithic blast wall with substantially reduced structural weight and enhanced portability (Hao et al. 2017). The unimposing aesthetics of such a 'wall', the aforementioned reduced structural material, and potential portability/temporary nature, make them appealing choices for 'softer' blast mitigation strategies in urban environments.

Gebbeken et al. (2017) and Warnstedt & Gebbeken (2020) extended this concept by proposing the use of plants and hedges to construct a natural fence-type blast wall. This concept was further studied by Gajewski et al. (2022).In the immediate shadow region of the plants ($0.5H$, where H is obstacle height), attenuation in the order of 40% was reported. It is particularly noteworthy that coniferous (thuja) plants resulted in a reduced magnitude and flat-topped pressure profile, whereas cherry laurel hedges exhibited a more typical exponential decay behind the plants. It is clear therefore that not only does the *presence* of an obstacle result in downstream mitigation, but the *type* of obstacle has significant influence also. Specifically, the enhanced mitigation of the coniferous plants is hypothesised to be due to their multi-scale nature (i.e. the presence of many smaller scale substructures within the obstacle, compared to the cherry laurel leaves which are all of similar size).

Multi-scale, self-similar structures are prominent in nature – trees, ferns, clouds, coastlines, shells. As mentioned previously, self-similarity is hypothesised to have contributed to the observed blast mitigation behaviour of plants and hedges. This Chapter aims at studying this further by experimentally investigating the blast mitigation behaviour of self-similar structures. Whilst the findings are aimed at better understanding the performance of natural fence-type blast barriers, the true influence of self-similarity must first be studied in isolation.

Fractals are mathematically self-similar structures, and are formed as an infinitely-repeating pattern of a given starting shape (see Fig. 3.1), hence the term self-similarity. It should be stated that that fractals are not simply a pure mathematical concept; they have been successfully implemented in various engineering fields such as antennae, industrial mixing, and heat exchangers. Fractals exhibit many favourable characteristics for these applications, such as (i) their scale similarity (Sreenivasan 1991, Turcotte 1988), (ii) the presence of multiple length scales (Higham & Brevis 2018, Higham et al. 2021, Higham & Vaidheeswaran 2022), and (iii) their higher surface area per unit volume (Werner & Ganguly

2003). All these characteristics make fractals potentially suitable candidates for efficient blast mitigation in the urban environment.

Since a fractal is a pattern that repeats *infinitely*, it is not possible to achieve a *true* fractal in real life, and only a finite number of iterations of self-similarity can be practically achieved. Such intermediate shapes are called 'pre-fractals'. Therefore, this study is aimed at investigating the interaction of blast waves with pre-fractal obstacles.

In this Chapter, the choice of a fractal achieving increasing complexity condition is explained in accordance to some key mechanisms concluded in Chapter 2. Next, experimental work and experimental results are presented in detail, typically with reference to baseline free-field data at select sensor locations. Following this, the performance pre-fractals of increasing complexity is presented with an engineering model to predict pressures in the vicinity of the obstacle, using an equivalent blockage factor. The primary content of this chapter was derived from the published paper titled: ***Experimental investigation of blast mitigation of pre-fractal obstacles***, as elucidated in Chapter 1 (refer to section 1.4).

3.2 Methodology

3.2.1 Fractal design requirements

For conventional geometric shapes, a straight line equally partitioned into two units, an area (square) split into two equal parts along each dimension, or a volume (cube) divided into two equal portions along each dimension would lead to 2^1, 2^2, and 2^3 identical units each, with the exponents here referring to the 'dimensions' of the original object. However, for a 2D fractal, this dimension is usually more than two, and for a 3D fractal, it is more than three, as fractal shapes have an effectively infinite surface area in a finite volume. This relationship between surface area and volume is a key fractal characteristic which, it is posited, will lead to enhanced blast mitigation.

To help identify the most appropriate self-repeating shape, the following observations were made based on reviewing the relevant literature in Chapter 2:

- Lower porosity or a high blockage factor is the key contributor to blast mitigation (Dosanjh 1956, Monti 1970, Epstein & Kudryavtsev 2012, Chaudhuri et al. 2013, Xiao et al. 2017).
- A flat frontal area of an obstacle is more effective (at mitigating loading) than a curved or pointed obstacle shape (Chaudhuri et al. 2013)
- Within the obstacle, a volume decrease followed by an increase along the blast wave transmission path enhances attenuation (Zong et al. 2017).
- As the phenomenon of diffraction helps weaken the incident blast wave, the presence of edges is possibly useful. This can also increase the possibility of vortex formation which has a potential for further attenuation (Prasanna Kumar et al. 2018, Suzuki et al. 2000).
- Increasing the number of rows can enhance attenuation but this has not yet been fully clarified in the literature (Jin et al. 2019).

The Sierpinski carpet, such as the first three iterations of which are shown on plan in Fig. 3.1 with colours being used to represent each pre-fractal shape, and the markers under each shape to represent data pertaining to these obstacles in all results figures reported in this Chapter unless where specifically noted, was chosen to configure obstacles of increasing complexity in this thesis since it satisfies the above criteria. Namely: the blockage factors vary for each iteration; the obstacles are flat-fronted and formed into rows; diffraction waves can arise due to the presence of multiple corners, and; voids between the obstacles may be considered as converging-diverging volumes. Furthermore, the pre-fractal is simple to fabricate since it is a vertical extrusion of this 2D pattern (i.e. shown on plan in Fig. 3.1), and therefore it can be made from standard square sections. The dimensions of the pre-fractal shapes used in this work may be found in Table 3.1.

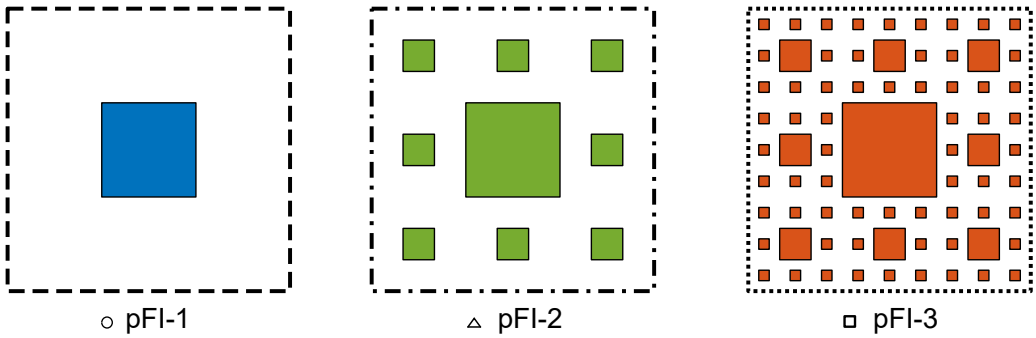

Figure 3.1: An illustration showing the first three iterations of the Sierpinski carpet.

3.2.2 Overview of Experimental Work

250 g PE4[1] was used as the explosive for all the tests. The pre-fractal obstacles were fixed onto a concrete ground slab and placed in front of a nominally rigid blockwork wall whose dimensions extend sufficiently in the horizontal and vertical directions such that clearing from its edges can be neglected (Rigby et al. 2014b). This blockwork wall may be taken to represent the structure being protected by the obstacle. The experiments were carried out on three iterations of a Sierpinski carpet-based fractal: pFI-1, pFI-2, pFI-3 (see Fig. 3.1). A case without any obstacle (pFI-0) was also tested to obtain the reference free-field parameters.

For each iteration, experiments were conducted with the explosives placed at three different stand-off distances, 1.25 m, 1.5 m, and 2 m, measured from the front face of the central obstacle. To reduce the likelihood of the fireball impinging on the pre-fractal obstacles whilst still aiming to maximise the strength of the incident shock, the closest stand-off distance (SoD) was set at 1.25 m giving a Hopkinson-Cranz scaled distance of 1.87 m/kg$^{1/3}$, assuming a TNT equivalence of PE4 of 1.20 after Rigby & Sielicki (2014). This distance was seen sufficient to prevent the formation of fireball around obstacle when observing through high speed video camera. The other two distances were selected to ap-

[1]Actually 12 % Plasticizer/Taggant, and 88% RDX

proximately represent mid-field and far-field scenarios (Hopkinson-Cranz scaled distances of 2.24 and 2.99 m/kg$^{1/3}$ respectively).

In this work, for ease of reference, these stand-off distances have been termed as SoD125, SoD150, and SoD200. Triplicates were performed for each experimental condition (4 obstacle iterations including iteration zero, 3 SoDs each, plus two additional repeats to account for data drop-out), therefore 38 experiments were conducted in total.

3.2.3 Experimental Set-up

3.2.3.1 Obstacle Design

Using a 180 mm square hollow section as the central obstacle for the first fractal iteration (pFI-1) in the Sierspinki carpet, the second iteration (pFI-2) incorporated eight 60 mm square pipes around the 180 mm square section. The third iteration (pFI-3) had eight 20 mm square rods surrounding each 60 mm square pipe from the previous iteration. This corresponds to a *fractal dimension*, $D = \log(N)/\log(S) = 1.89$, where N is the number of copies of the original on each iteration ($N = 8$), and S is the scale factor between an original and its copy ($S = 3$). There was a 60 mm air gap between the 180 mm and 60 mm obstacles, and a 20 mm air gap between the 60 mm and 20 mm obstacles, maintaining self-similarity. All obstacles were 1 m high.

Preliminary numerical analyses were performed using ABAQUS/Explicit. Each section was subjected to the full ConWep (Hyde 1991) reflected pressure, which is highly conservative given the small projected area of each obstacle. For the 1.25 m SoD case, wall thicknesses of 12.5 mm for the 180 mm pipe and 5 mm for the 60 mm pipes resulted in deformations <1 mm and were specified for fabrication. Peak stresses were <220 MPa throughout, therefore yield strengths were specified as 355 MPa for the 180 mm section[2],

[2]A higher strength was specified for the central obstacle since it was used for all 27 tests with obstacles present

Table 3.1: A summary of obstacle types employed in this study and their geometric properties.

Iteration	Obstacle dimensions (mm)	Mass (kg)	Surface area (cm^2)	Enclosed volume (cm^3)	Area:volume
pFI-1	□180	65.7	7200	32400	0.222
pFI-2	□180, 8×□60	134.8	26400	61200	0.431
pFI-3	□180, 8×□60, 64×□20	335.8	77600	86800	0.894

235 MPa for the 60 mm hollow sections, and 275 MPa for the 20 mm sections, which were formed of solid rods. Properties of each iteration are provided in Table 3.1.

The obstacles were rigidly bolted onto tapped holes on a thick metal baseplate (650×650×25 mm). This baseplate was in turn held against the concrete pad using threaded rods that were chemically anchored to the ground. Prior to this, the concrete pad was cut out and filled up with screed to ensure that the baseplate would be flush with the rest of the pad once in situ. Three (thin) square alignment plates with appropriately sized cut-outs were positioned at approximately (i) 330 mm and (ii) 670 mm above the floor, and (iii) at the top of the obstacle assembly. Each plate was then tack welded to the square pipes at certain spots to maintain the alignment of each configuration with respect to the central obstacle. These tack welded plates also served to add to the stiffness of the overall structure and restrict deformation. All the square pipes had cover plates rigidly fixed on the top to prevent ingress of the blast wave.

The 180 mm square section had two cut-outs on the rear face – one at mid-height, and one near the bottom – for access to the central sensor mounting pad on the front face, and to fasten the mounting bolts, respectively. The cut-outs were then closed with flush mounted cover plates. The 60 mm pipes also had a cut out at the bottom, on the rear face, to access the fastening nuts that were used to hold them down against the heavy baseplate. These cut-outs were also flush closed with suitable cover plates. The 20 mm square rods were fully welded as a set of eight on a small baseplate and these sets were fastened onto the heavy baseplate using bolts on the periphery of each small baseplate. These bolt heads, however, could not be installed fully flush and they had to be left protruding out. The

head being only 10 mm thick, the protrusion is negligible in comparison to the overall size of the obstacles. The alignment plates, used for pFI-2 and pFI-3 are also comparatively thin (5 mm and 3 mm) and parallel to the direction of blast wave travel, so they cannot introduce any strong flow structures that can drastically alter the flow physics of these short duration events.

For practicality and ease of transitioning from one obstacle type to the other, the tests were carried out in reverse order; starting from pFI-3, then pFI-2, and then pFI-1. The obstacles were installed at the site and were left mostly undisturbed until the end of the experiment campaign. The sensors however, were uninstalled at the end of each day and reinstalled, so as to protect them from accumulation of overnight moisture. A photograph of the installed obstacles is shown in Fig. 3.2. A high speed camera was also used to visualize the shock evolution against a zebraboard and a smaller board with a dot pattern. A few circular markers were placed on the side face of the obstacles to track the motion of the pipes during the experiment. This was done to confirm the absence of noticeable obstacle deformation during the loading process.

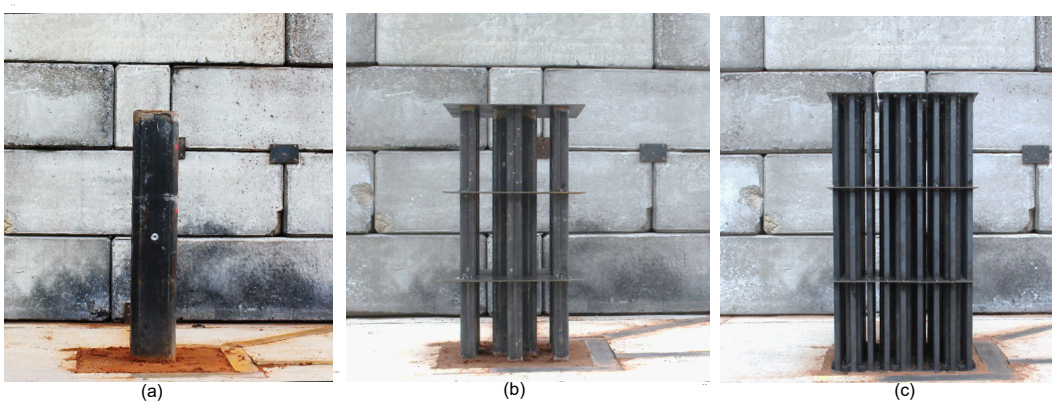

Figure 3.2: A photograph of the pre-fractal shapes **(a)** pFI-1, **(b)** pFI-2, and **(c)** pFI-3 as installed at site. In **(a)**, the sensor mounted on the center of the 180 mm pole is clearly visible. The mounting plate for a sensor on the wall is also seen, while for the other two (top right and bottom left of the 180 mm section) it is partly visible. The metal channels on the ground where the other sensors were mounted may be seen as well.

3.2.3.2 Pressure Gauge Locations

Piezo-resistive Kulite dynamic pressure sensors were used to measure the overpressure at locations carefully selected to capture different aspects of the physics of the blast interaction. A custom made signal conditioner unit was used and a TiePie oscilloscope was used to record the data at 312.5 kHz. Four sensors were employed to measure reflected pressure, of which three sensors (S_1, S_2, and S_3) were fastened onto a 100×100×10 mm square plate (on the wall in Fig. 3.2) and positioned at chosen locations on the block work wall behind the obstacle. Another sensor was secured in a short metal bush that was then mounted flush on the front face of the 180 mm section (S_{12}, cf. Fig. 3.2a) to measure the clearing pressure. The rest were incident pressure gauges, mounted onto steel U-channels that were placed into cut-outs on the concrete pad. The space inside the U-channel was filled with sand and then levelled off to ensure that the metal surface was flush with the ground surface (Fig. 3.2). The following are the locations of the incident sensors:

- S_4, S_5: These sensors were located behind the obstacle and along the 90° ray. They were placed at approximately $2D$ and $4D$ from the rear face of the central obstacle (where D refers to the depth of the main obstacle, i.e. 180 mm).

- S_6, S_7: These were placed along a 45° ray behind the obstacle. They were placed at approximately $3D$ and $6D$ from the rear corner of the central obstacle.

- S_8, S_9: These were along the line passing through the front edge of the 180 mm section and parallel to the 0° ray line. They have been placed at approximately $3D$ and $6D$ from the side face of the central obstacle.

- S_{10}, S_{11}: These were placed ahead of the obstacle and along the -90° ray. They were spaced ∼75 mm apart, primarily to measure incoming shock speed.

The co-ordinates of each of these measuring stations have been provided in Table 3.2, along with the stand-off distance to each pressure gauge from the explosive.

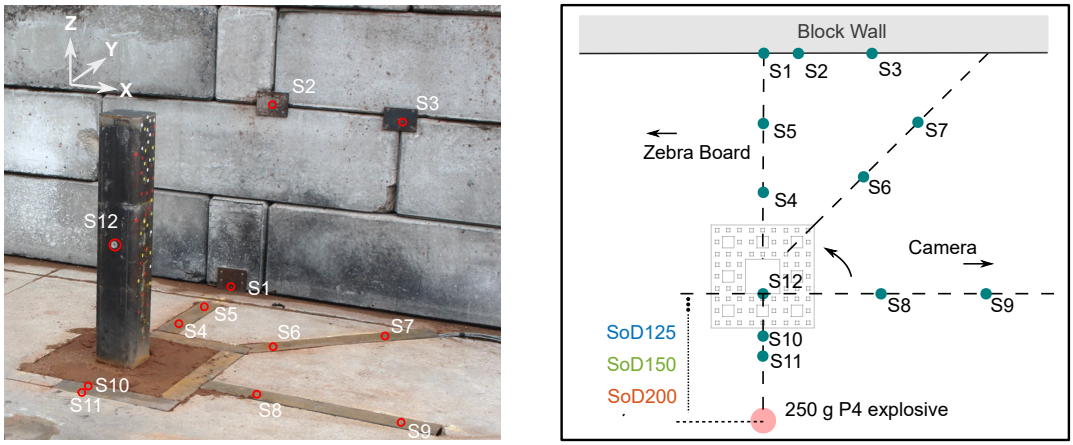

Figure 3.3: A photograph of the sensor arrangement at site (L) and a schematic diagram (R) of the arrangement. The incident shock pressure sensors are placed along rays that are at 0°, 45°, 90°, and -90° from the center of the 180 mm obstacle. The sensor distances may be found in Table. 3.2. NB.: S_8 and S_9 are located slightly off the 0° ray, on a line passing through the front edge of the 180 mm obstacle.

Position	**Co-ordinates**			**Stand-off distance**		
Sensor/ charge	Y L (m)	X B (m)	Z H (m)	$SoD125$ (m)	$SoD150$ (m)	$SoD200$ (m)
W_{SoD125}	-1.25	0	0	0	-	-
W_{SoD150}	-1.50	0	0	-	0	-
W_{SoD200}	-2.00	0	0	-	-	0
S_1	1.25	0	0.02	**2.50**	**2.75**	**3.25**
S_2	1.25	0.16	0.92	**2.66**	**2.90**	**3.37**
S_3	1.25	0.76	0.89	**2.75**	**2.98**	**3.45**
S_4	0.55	0	0	**1.80**	**2.05**	**2.55**
S_5	0.91	0	0	**2.16**	**2.41**	**2.91**
S_6	0.54	0.39	0	**1.84**	**2.09**	**2.58**
S_7	0.93	0.77	0	**2.32**	**2.56**	**3.04**
S_8	0	0.55	0	**1.40**	**1.63**	**2.09**
S_9	0	1.10	0	**1.72**	**1.90**	**2.32**
S_{10}	-0.23	0	0	**1.02**	**1.27**	**1.77**
S_{11}	-0.30	0	0	**0.95**	**1.20**	**1.70**
S_{12}	0	0	0.51	**1.35**	**1.59**	**2.06**

Table 3.2: The co-ordinates (as installed) of each pressure sensing station for the three stand-off distances. The origin is at the front, centre, and base of the 180 mm obstacle. The uncertainty in these measurements is ±5 mm.

3.2.4 Data Analysis

All 445 pressure sensor traces (3 SODs $\times$ 4 iterations $\times$ 12^3 sensors $\times$ 3 repetitions, and two additional repeats) had to be pre-processed before they could be automatically extracted using MatLab. For most runs, the data from the sensors were acquired and saved faithfully. However, for a few cases where the recording had spurious data due to mechanism issues in the Kulite sensor type , it had to be manually identified and excluded from further analysis.

To retain as much as possible the essential nature and frequency content of the signals, a wavelet filter was used to clean the pressure traces instead of a low pass filter. The de-noising of the signal was done using MatLab's 5^{th} order `mlptdenoise` as it can accommodate non-uniformly sampled signals (i.e. those traces which had content manually removed). Certain spurious spikes introduced in the resulting de-noised signal were then removed using a 5-point median filter. Subsequently, to clean the pre-shock portion of the signal, instead of using a single value to arrive at the reference level of the signal, an average value of 100 points ahead of the first pressure jump was used. This value was then subtracted from the original signal.

Now since the pattern of arrival of the reflected wave at each measuring station varies, the signals had to be processed differently depending on where they were located. For pressure traces in this work, the reflected waves can arrive from either the wall, or the obstacle, often before the end of the positive phase. To decide if such reflections needed to be included within the impulse calculation, a custom script was written in MatLab to automatically process the signals. Typically, conventional methods involve the use of concepts such as first maximum in the cumulative impulse (Farrimond et al. 2022), or the use of a curve-fit to determine impulse (Rigby et al. 2014c). Due to the diverse

[3] 11 for pFI-0

nature of reflection patterns at each sensor location, the cumulative impulse signal can be influenced by these reflections. While some sensors under certain conditions may not have these reflections, to maintain consistency, decay time was not estimated using the conventional methods that are established in literature for the blast wave analysis. The methodology that has instead been adapted to obtain these values has been briefly described in Table 3.3, with parameters from an example trace shown illustratively in Fig. 3.4.

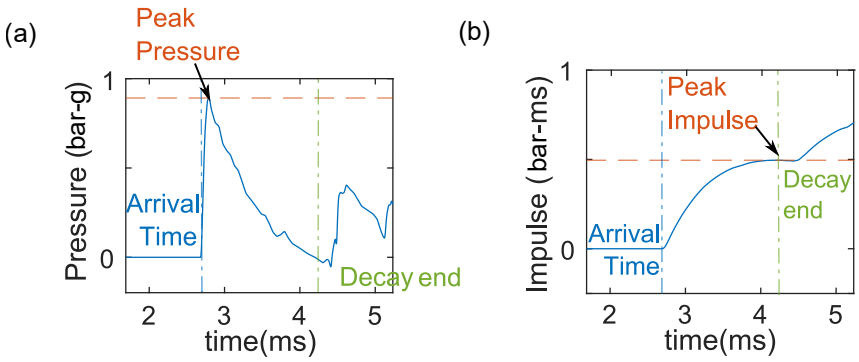

Figure 3.4: An illustration showing how the peak overpressure, impulse value and decay time were obtained in this study.

Using these methods, the peak pressure, impulse and arrival time were extracted at each station for each experiment.

3.3 Experimental Results

3.3.1 Comparison of pFI-0 against ConWep

Before evaluating the performance of each obstacle, a data validation exercise was first undertaken to compare the present experimental data for the no obstacle case (pFI-0) against ConWep (Hyde 1991) semi-empirical predictions. A TNT equivalence of 1.20 was assumed for PE4, after Rigby & Sielicki (2014). Ratios of measured (average of the three repeat tests) to predicted data are plotted in Fig. 3.5a, b, & c as heatmaps for arrival time, peak overpressure, and peak specific impulse. Here, data from each particular sensor

Table 3.3: Methods for extracting blast parameters from experimental pressure signals

Parameter	Method
Peak overpressure	Taken as the maximum overpressure value of the filtered signal
Arrival time	*if a single peak exists:* taken to be the first instance of time at which the signal reaches 5% of the peak overpressure value defined as above. *else:* limit this search to the time ahead of the first peak
Decay end	*if no secondary reflections present:* Taken as the global minima of the absolute filtered overpressure signal, evaluated using the `islocalmin` function in MatLab *else:* The signal was truncated immediately prior to arrival of secondary reflections and this was defined as decay end
Impulse	Determined through numerical (trapezoidal) integration of the pressure signal between the limits of arrival time and decay end

location occupies a given row, with the reflected gauges (S_1–S_3) and then incident gauges sorted in decreasing distance from the explosive (i.e. S_7 is furthest from the charge, S_{11} is closest).

As a guide to the reader, in all the heatmaps presented in this Chapter, the location of a given sensor has been provided against each row using a simplified marker along the left-hand side of the heatmap. The approximate location of the sensor with reference to the obstacle, and the type of the pressure being reported – incident (grey) or reflected (dark) – have been indicated in those markers.

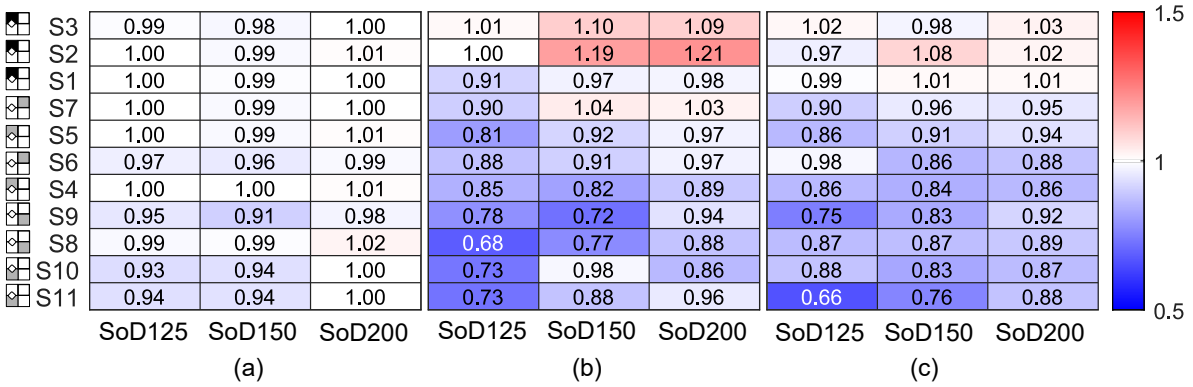

Figure 3.5: Comparison of pFI-0 data against ConWep for (a) time of arrival, (b) peak overpressure, and (c) peak specific impulse. Gauges grouped by reflected (S_1–S_3) and incident conditions, and sorted in order of decreasing stand-off distance

Generally, the arrival time data is in excellent agreement with ConWep, with a maximum deviation of 9%. The agreement is particularly good for the furthest gauges (S_4 and further for the SoD125, and SoD150 tests, and all gauges for the SoD200 tests), where the deviation does not exceed 6% and is typically within 2%. Consistency of time-of-arrival measurements is discussed in detail in Rigby (2021).

Normally reflected pressure and specific impulse (S_1) is also in good agreement with ConWep (9% deviation in peak pressure, 1% deviation in peak specific impulse), however the oblique gauges (S_2 and S_3) differ from ConWep somewhat, likely due to angle of incidence/Mach stem effects (Rigby et al. 2015) which have not been accounted for in the ConWep predictions.

At all incident gauges, the deviation of the measured peak pressure values from ConWep is inversely proportional to the stand-off distance to each gauge, ranging from 3% deviation at the furthest distance (S_7 for the SoD200 tests; 3.04 m, $Z = 4.54$ m/kg$^{1/3}$) to a maximum of 32% for S_8 in the SoD125 tests (1.40 m, $Z = 2.09$ m/kg$^{1/3}$). This trend is also borne out in the specific impulse data, with a clearer trend of ConWep underpredictions as SoD decreases, up to a maximum of 34%. This is in general agreement with the observations of Bogosian et al. (2002) and believed to be a limitation of ConWep incident predictions. Therefore, in this Chapter, results from pFI-0 are used as more reliable

free-field benchmark data.

3.3.2 Pressure and Impulse Behind the Obstacle

In the following sections, example pressure and specific impulse histories are presented at S_1, S_4, S_7, S_{12}, and S_{10} for each test series (stand-off and iteration number). These are used to make comments on the properties of the attenuated blast wave in various regions surrounding the obstacle, namely: on the target wall; directly behind the obstacle; behind the obstacle on a 45° ray; on the obstacle, and; in front of the obstacle. In the following plots, the inset provides a diagrammatic representation of the gauge location (for further detail refer to Figure 3.3).

Following this, blast parameters (peak pressure, peak specific impulse, and arrival time) are compiled and compared against the free-field (pFI-0) results in order to make general observations.

3.3.2.1 On the Target Wall

Figures 3.6 and 3.7 show, respectively, pressure and specific impulse histories at S_1 for the 1.25 m, 1.50 m and 2.00 m tests. This is indicative of the loading imparted to a structure which the pre-fractal obstacle aims to protect. The target wall is located 1.25 m behind the front face of the central obstacle.

Peak reflected pressures exhibit a noticeable attenuation, which generally increases with iteration number and is relatively consistent with SoD. The maximum peak reflected pressure attenuation is approximately 20% relative to the pFI-0 case, i.e. full reflected pressure with no prior blast–obstacle interaction (refer to row 3 of Figure 3.5). The pressure histories become noticeably more complex with increasing iteration number; the pFI-0 traces resemble the well known 'Friedlander' exponential decay, whereas the pFI-3 traces exhibit multiple smaller peaks and inflection points, indicative of a more complex regime of blast–obstacle interaction, as expected.

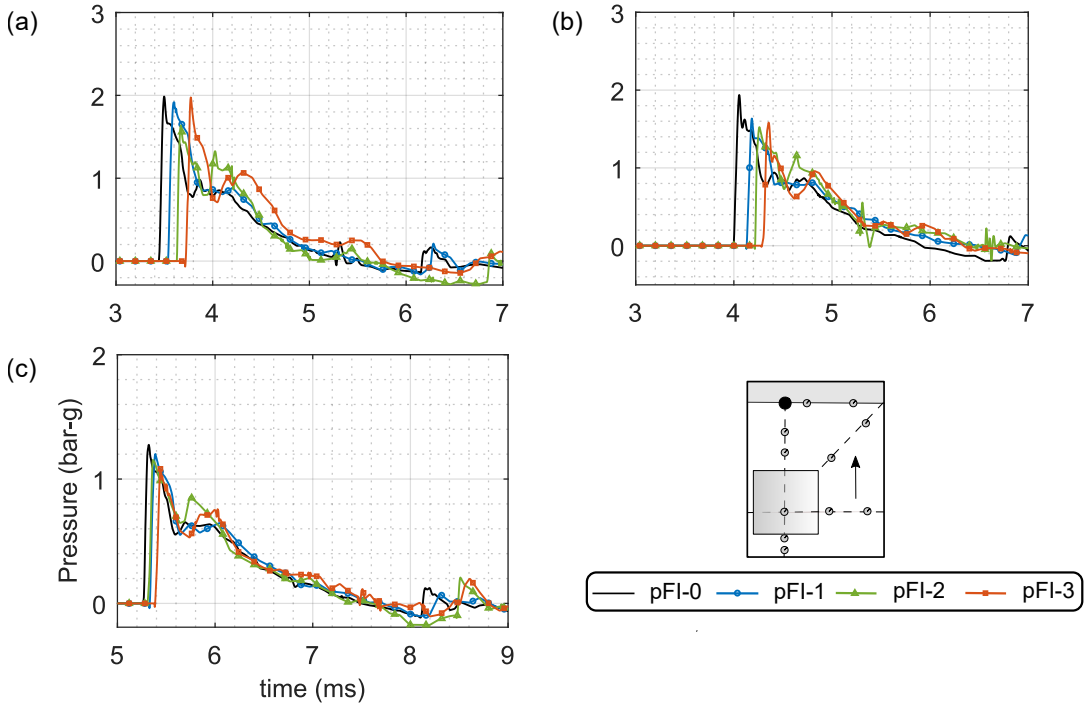

Figure 3.6: Pressure histories at S_1 for: (a) SoD125; (b) SoD150; (c) SoD200.

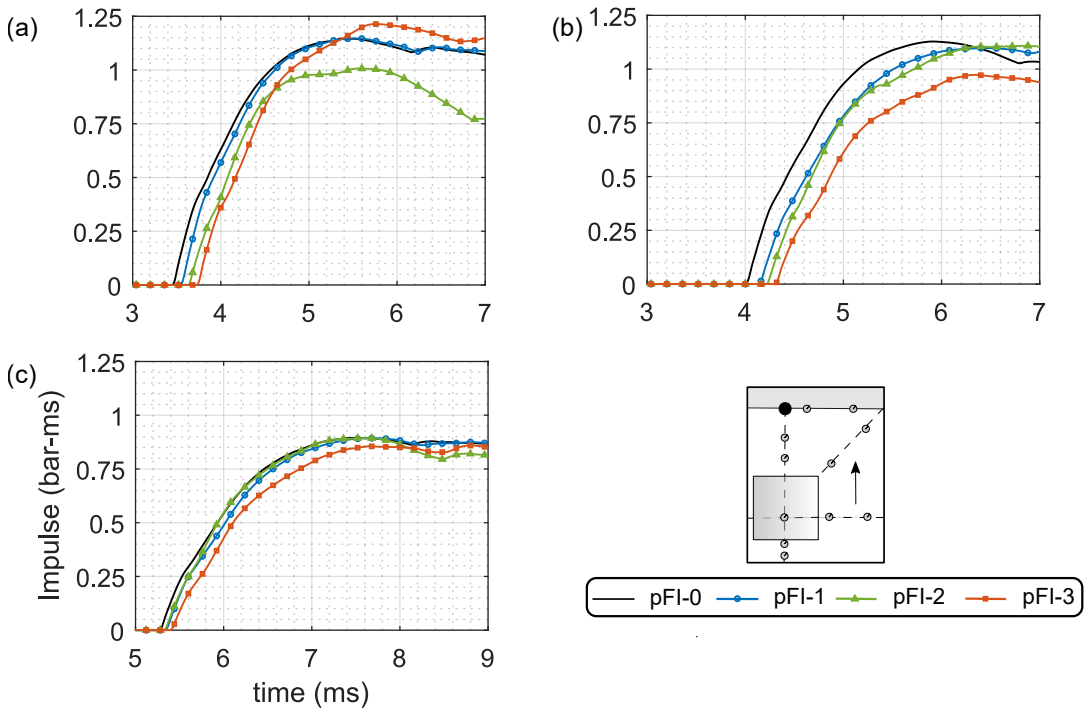

Figure 3.7: Specific impulse histories at S_1 for: (a) SoD125; (b) SoD150; (c) SoD200.

There is a marked delay in time of arrival as a function of iteration number, which again is evidence of a more complex attenuation mechanism as the obstacle becomes more fractal-like. This behaviour is largely borne out in the specific impulse histories also, albeit less clearly; the pFI-3 specific impulse is smallest for the SoD150 test but, surprisingly, largest for the SoD125 test. It is clear that the loading on the target wall is made significantly more complex with the introduction of increasingly complex obstacles in the path of the blast wave.

3.3.2.2 Directly Behind the Obstacle

Figures 3.8 and 3.9 show, respectively, pressure and specific impulse histories at S_4 for the 1.25 m, 1.50 m and 2.00 m tests. This is in the immediate shadow region of the obstacles.

Given the pressure and specific impulse histories on the target wall (S_1), a similar level of attenuation was expected immediately behind the obstacle. This is clearly not the case, as an amplification in peak pressure is seen for pFI-1 and pFI-2, for all SoDs, with pFI-3 demonstrating a significant decrease in peak pressure; a reduction of approximately 25% relative to the pFI-0 case. Although the frontal dimensions of pFI-2 and pFI-3 are similar (420 mm and 500 mm respectively), pFI-3 clearly has a very different attenuation mechanism in the immediate surroundings. There is also a noticeable rounding of the shock front for the pFI-3 cases.

It is likely that the enhancement seen in the pFI-1 and pFI-2 cases is due to the blast wave coalescing and reforming after having been temporarily separated by the obstacle. Despite this localised increase in pressure, the fact that a pressure reduction is observed at the target wall for pFI-1 and pFI-2 (see S_1 results above) suggests that this behaviour does not persist. Conversely, pFI-3 causes much more substantial breakup of the blast wavefront (hence the delayed arrival times at both S_1 and S_4), which therefore takes longer to reform and produces a more pronounced attenuation immediately behind the obstacle.

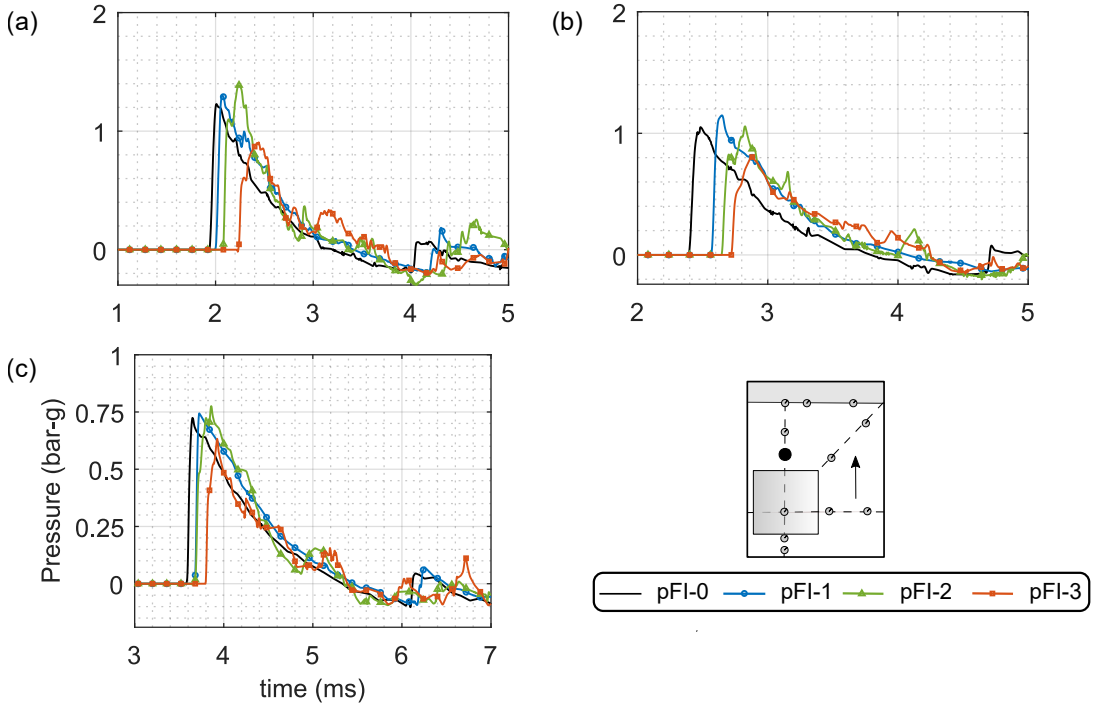

Figure 3.8: Pressure histories at S_4 for: (a) SoD125; (b) SoD150; (c) SoD200.

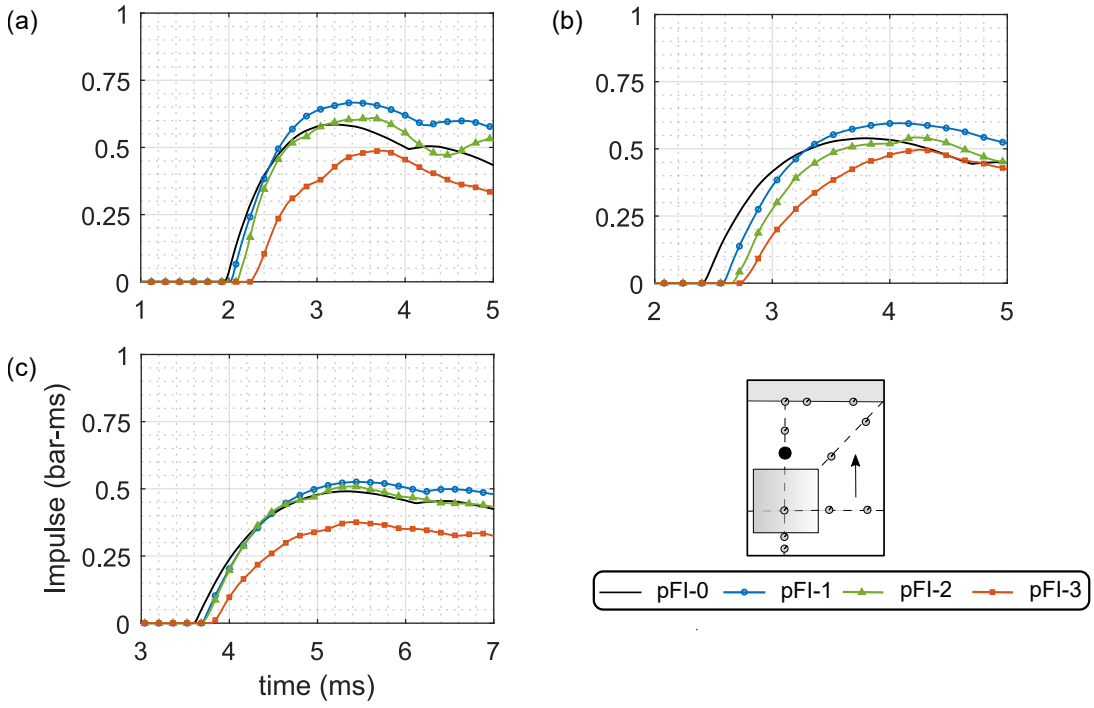

Figure 3.9: Specific impulse histories at S_4 for: (a) SoD125; (b) SoD150; (c) SoD200.

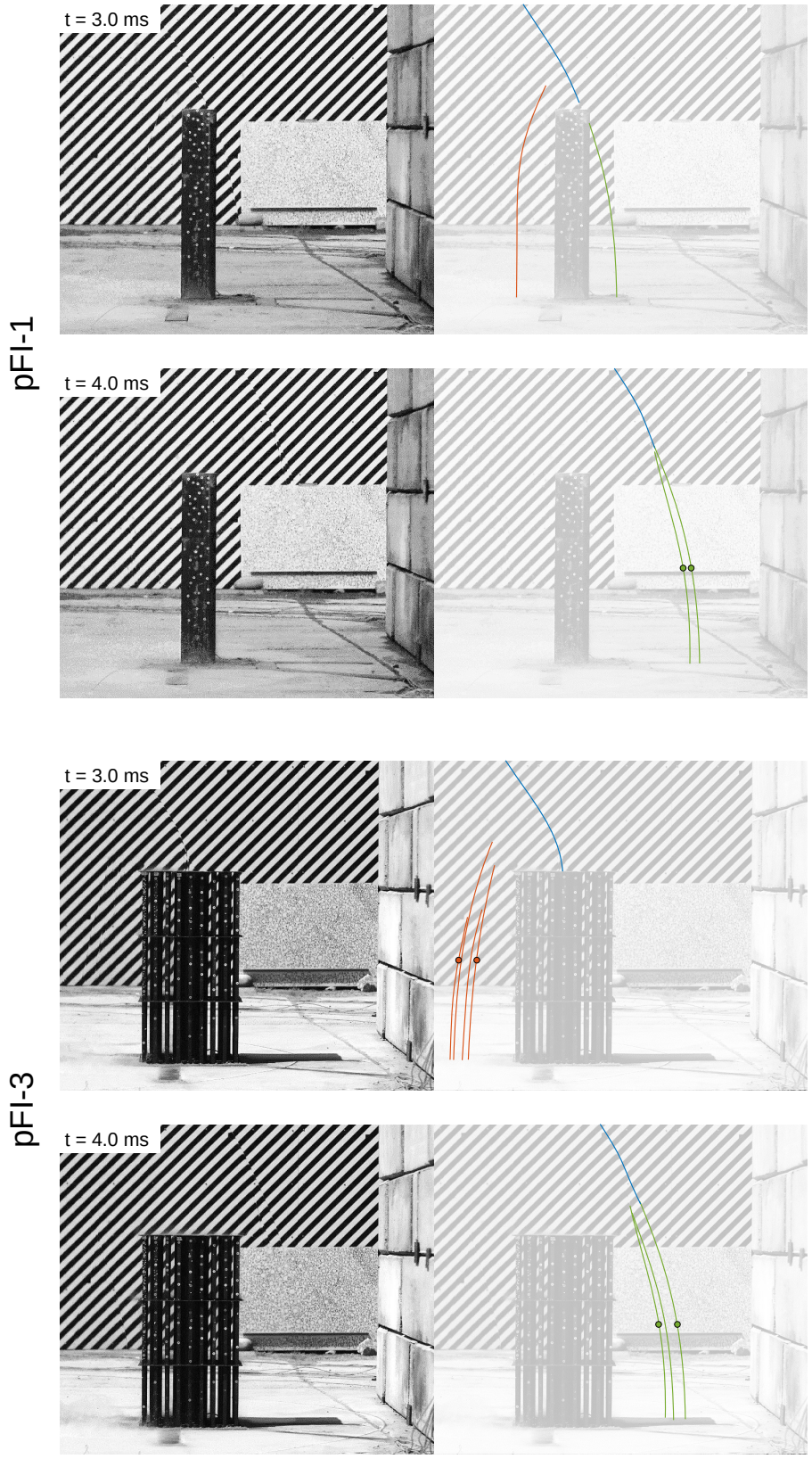

Figure 3.10: Approximate shock front locations determined from high speed video stills for pFI-1 and pFI-3. SoD200 tests at 3 ms and 4 ms after detonation: incident (blue); reflected (red) and; transmitted (green)

This is qualitatively supported with evidence from high speed video, as in Figure 3.10. Here, the incident shock front (above the obstacle), and the components of the shock front that are both reflected by, and transmitted through, the obstacle are visible as disturbances on the zebraboard in the background. For ease of interpretation, approximate shock front locations have been traced and colour-coded in the accompanying images. Note that brightness and contrast values have been slightly increased for presentational purposes. Finally, small markers have been used in the traced plots to mark the foremost and hindmost reflected and transmitted shock fronts at mid-height of the obstacle. A larger number of reflected and transmitted shock fronts are visible for the pFI-3 case relative to the pFI-1 case, which therefore supports the arguments outlined above.

Referring back to Figures 3.8 and 3.9, there is a marked delay in time of arrival with increasing iteration number. Peak specific impulses for pFI-0–2 are generally similar, with pFI-3 exhibiting a consistently lower specific impulse.

3.3.3 Behind the Obstacle on a 45° Ray

Figures 3.11 and 3.12 show, respectively, pressure and specific impulse histories at S_7 for the 1.25 m, 1.50 m and 2.00 m tests. This gauge is located along a 45° ray from the obstacle and can be used to make comments on the extent of the disturbed pressure regions.

There appear to be no clear differences in the magnitude and form of loading as iteration number increases. These gauges can be said to be positioned outside of the zone of influence (Christiansen & Bogosian 2012) of the pre-fractal obstacle (0.77 m laterally and 0.93 m behind the front-centre of the 180 mm obstacle, see Table 3.2) since they do not differ substantially from the free-field loading. A large additional shock can be seen to arrive at the end of the positive phase, which is the reflection of the primary wave off the target wall. For the purpose of compiling and comparing blast parameters later, peak specific impulse values have been taken immediately prior to arrival of this reflected wave.

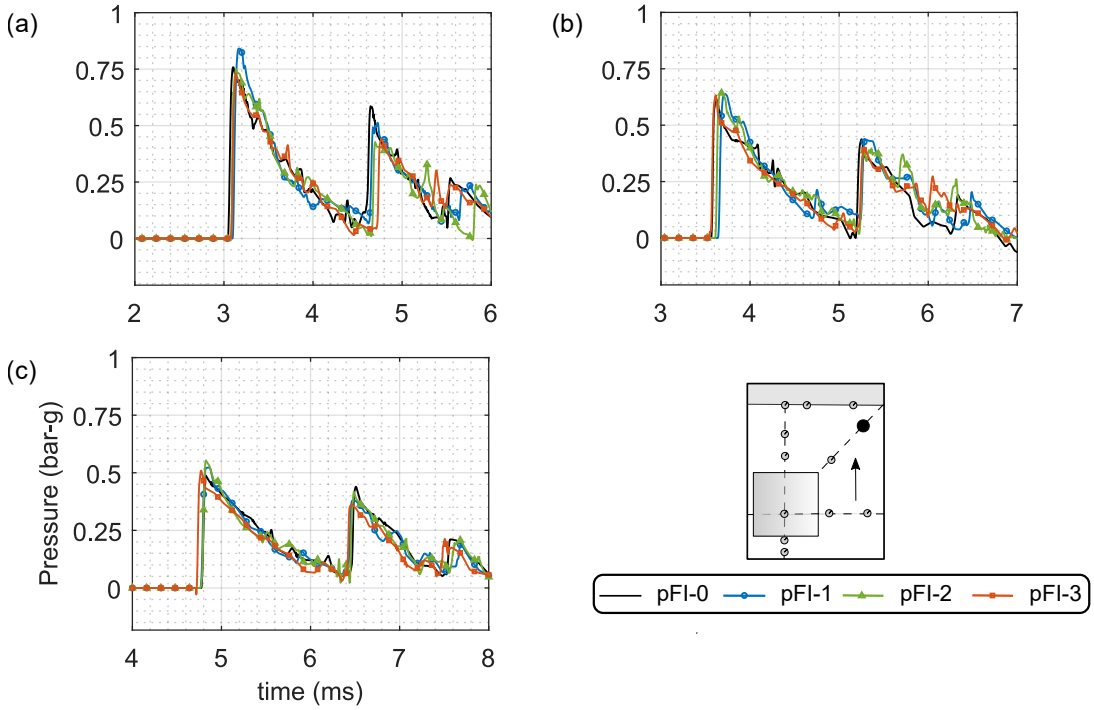

Figure 3.11: Pressure histories at S_7 for: (a) SoD125; (b) SoD150; (c) SoD200.

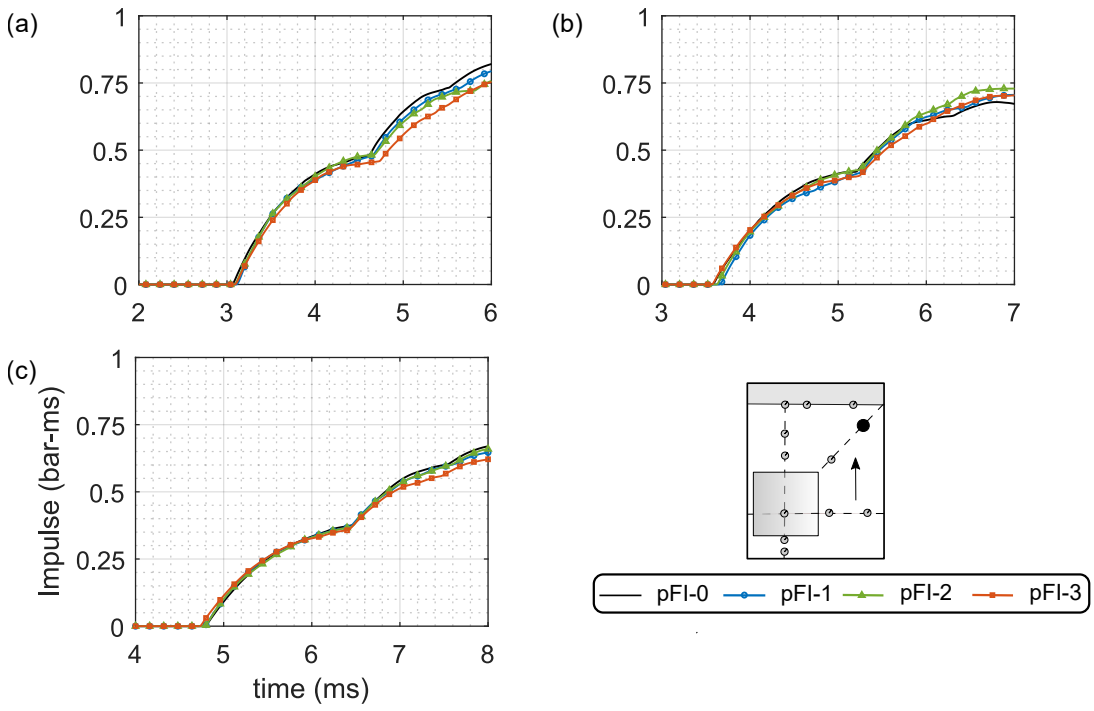

Figure 3.12: Specific impulse histories at S_7: (a) SoD125; (b) SoD150; (c) SoD200.

3.3.4 On the Central Obstacle

Figures 3.13 and 3.14 show, respectively, pressure and specific impulse histories at S_{12} for the 1.25 m, 1.50 m and 2.00 m tests. This is the pressure measured at the centre of the front face of the 180 mm obstacle and therefore there is no free-field equivalent available.

The pFI-2 peak pressure appears slightly lower than in the pFI-1 case, likely due to the small amount of shielding offered by the central 60 mm pole which is located directly in front of the pressure gauge. Whilst there is some later-time deviation between these two signals (with the pFI-2 trace generally increasing above the pFI-1 trace approximately mid-way through the positive phase), the decay times and peak specific impulses are comparable, and there are no noticeable differences in this behaviour with changing SoD.

Conversely, the pFI-3 traces are considerably different, exhibiting a much larger peak pressure and more complex loading history comprising multiple peaks and a substantially greater peak specific impulse. Noticeably, the peak pressure is increased above the pFI-2 value, despite the direct shielding of an additional two 20 mm obstacles. This suggests that a 'trapping' mechanism[4] initiates on the third iteration of the pre-fractal, due to the greatly enhanced area:volume ratio and substantially greater number of reflecting surfaces, and is dominant over the shielding effect. It is hypothesised that this trapping mechanism is what ultimately results in attenuation downstream of the obstacle: momentum of the pressure wave in the forward direction is reduced as the shock front is forced to take an elongated path through the obstacle, with a greater proportion of the shock front being redirected perpendicularly or towards the source of the explosion itself.

Peak values of overpressure and peak specific impulse at S_{12} are compared against ConWep fully reflected values in Fig. 3.15. Peak reflected pressures at pFI-1 are consistently 40–

[4]Previously only observed in confined, shock-tube experiments, e.g. Niollet et al. (2015) and Skews et al. (1998)

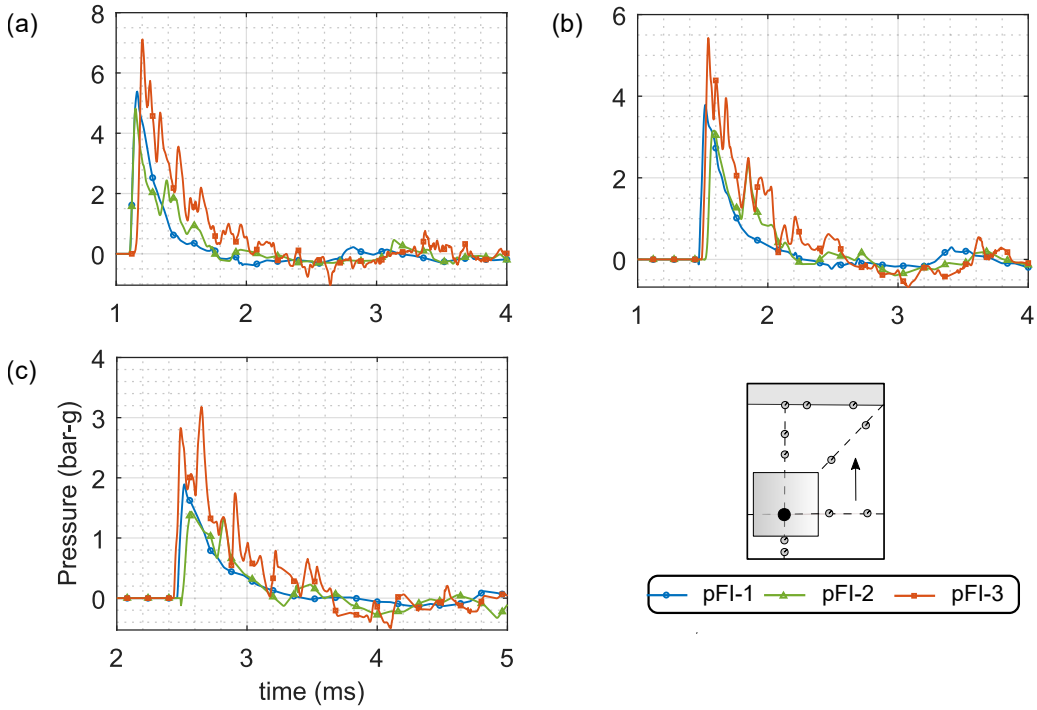

Figure 3.13: Pressure histories at S_{12}: (a) SoD125; (b) SoD150; (c) SoD200.

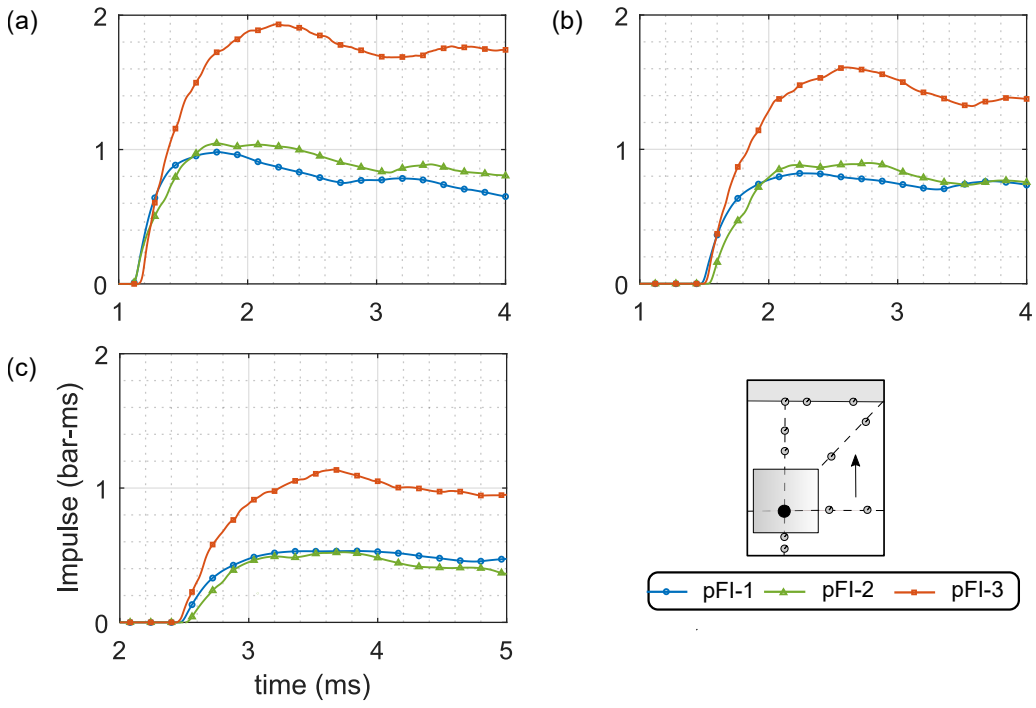

Figure 3.14: Specific impulse histories at S_{12}: (a) SoD125; (b) SoD150; (c) SoD200.

50% lower than ConWep. This suggests that by the time the blast wave reaches mid-height of the 180 mm wide central obstacle, clearing has acted such that the full reflected pressure no longer develops on the loaded surface (Rose et al. 2004). Clearing can also be seen to significantly reduce the pFI-1 peak specific impulse values, to around 40% of the ConWep fully reflected values. This is in agreement with the observations of Ballantyne et al. (2010).

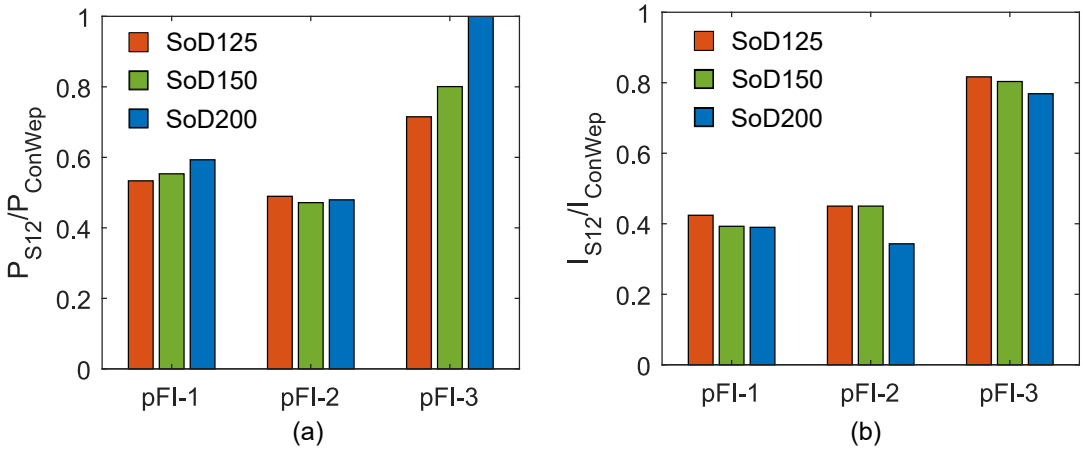

Figure 3.15: Ratios of experimental pressure and impulse values at S_{12} compared against ConWep fully reflected values.

3.3.5 In Front of the Obstacle

Figures 3.16 and 3.17 show, respectively, pressure and specific impulse histories at S_{10} for the 1.25 m, 1.50 m and 2.00 m tests. This is the pressure measured at ground level directly in front of the central obstacle(s); 0.23 m in front of the 180 mm section, 0.11 m in front of the 60 mm pole, and 0.07 m in front of the 20 mm rod for iterations 1–3 respectively.

The pFI-1 results are highly similar to the free-field values up until arrival of the reflected wave from the central 180 mm obstacle. This occurs at approximately 1.5 ms, 1.9 ms, and 3.0 ms after detonation for the SoD125, SoD150, and SoD200 tests respectively. Likewise, the pFI-2 results are similar to the free-field values until the arrival of a reflected wave from

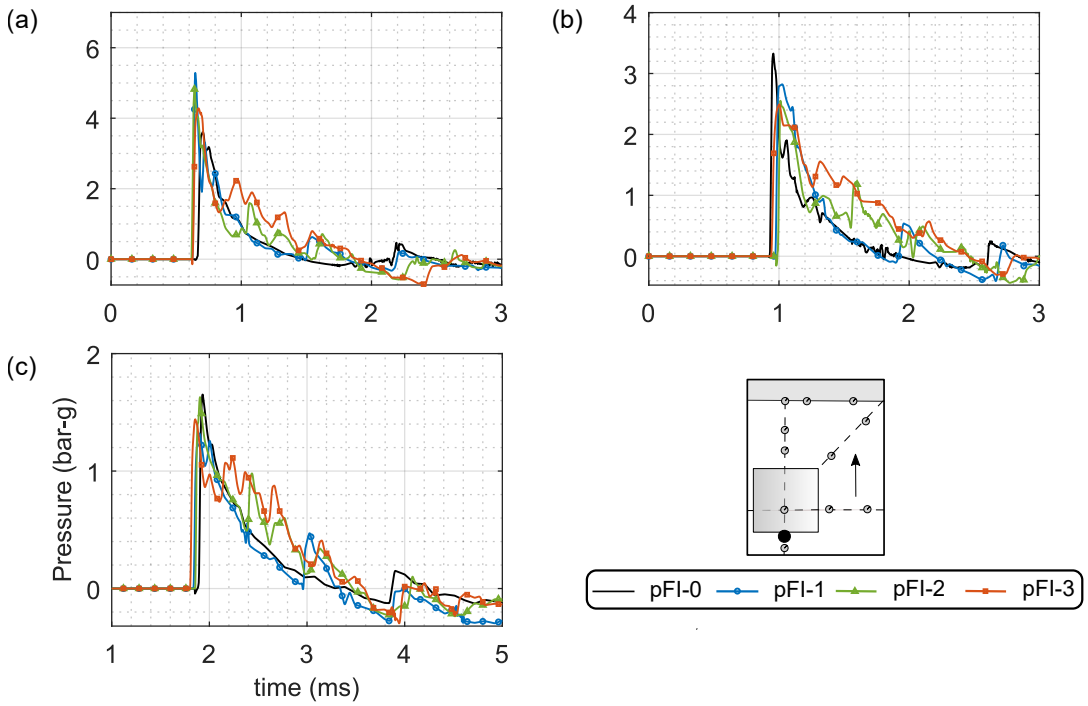

Figure 3.16: Pressure histories at S_{10}: (a) SoD125; (b) SoD150; (c) SoD200.

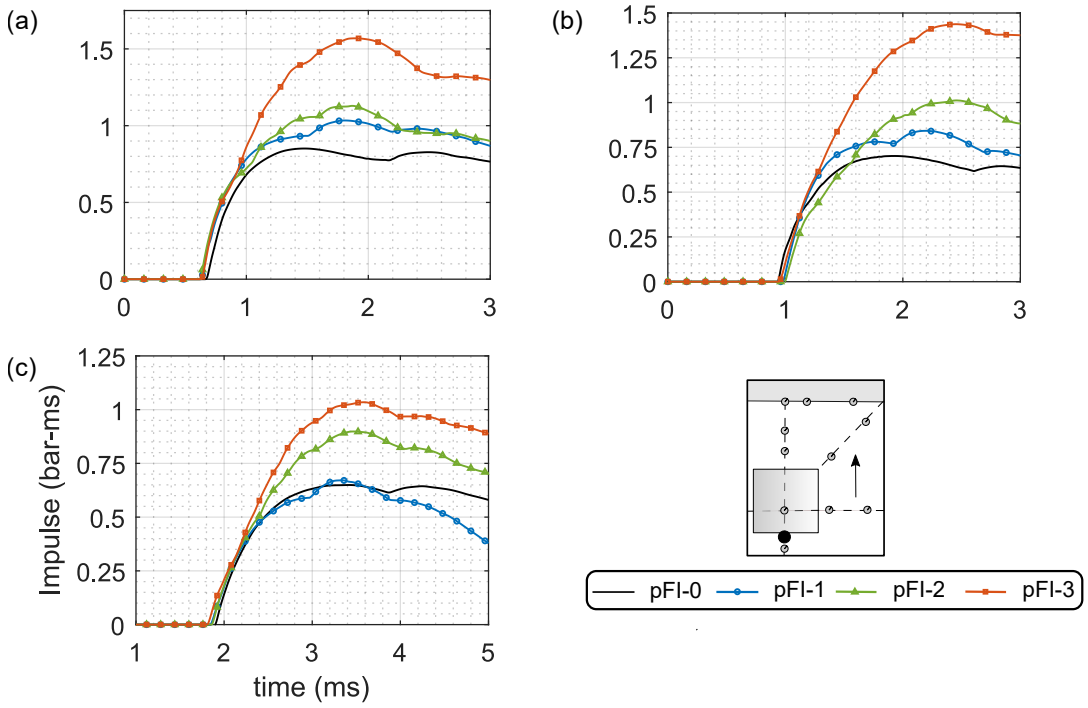

Figure 3.17: Specific impulse histories at S_{10}: (a) SoD125; (b) SoD150; (c) SoD200.

the 60 mm obstacle, at approximately 1.0 ms, 1.5 ms, and 2.4 ms. This is comparatively smaller in magnitude and less well-defined than for the pFI-1 cases due to the much smaller frontal area of the 60 mm obstacle. There is a noticeable rise in pressure in each of the traces due to reflection off the 180 mm obstacles, albeit slightly delayed relative to pFI-1, indicating a slightly elongated travel path or a reduced wave speed. These rises are also observable in the specific impulse histories.

For the pFI-3 cases, the reflected waves are not distinguishable on an individual basis. Instead, they appear to have the combined effect of increasing the pressure value above the free-field case, which persists for the entire positive phase duration. Referring back to Figure 3.10, this is due to the complex nature of the reflected wave, which does not form a single, coherent wavefront as in the pFI-1 case. Peak specific impulse values increase with increasing iteration number.

The results suggest that the iteration 3 pre-fractal behaves more like a collective obstruction, and supports the stipulation previously that a new type of behaviour is observed as the obstacle becomes more fractal-like.

3.4 Discussion

3.4.1 Compiled Results

Arrival time, peak pressure, and peak specific impulse have been compiled at each gauge location, for each pre-fractal iteration and stand off distance. The mean values from each triplicate series tests are presented in Figure 3.18 for arrival time and Figure 3.19 for peak pressure and peak specific impulse. Here, results are presented as a percentage increase above the pFI-0 (free-field) values, with the exception of the S_{12} results which are compared against the pFI-1 values due to there being no free-field equivalent. Using Welch's t-test, the statistically insignificant (at 80% confidence) differences have been masked out with zeroes. Here the gauges have been simply listed in numerical order.

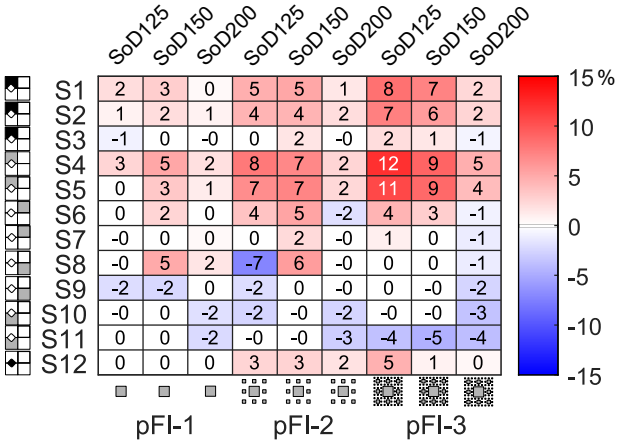

Figure 3.18: Percentage change in arrival time at each sensor location, compared against pFI-0 case (for S_{12}, the comparison is against pFI-1.) Only statistically significant values are reported.

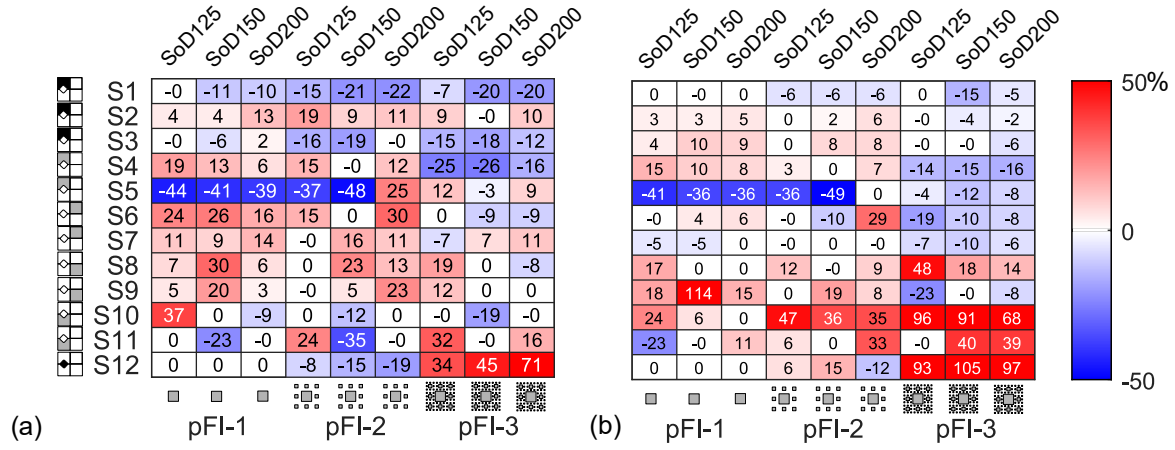

Figure 3.19: Percentage change in (a) pressure and (b) impulse at each sensor location, compared against iteration 0 case (for S_{12}, the comparison is against pFI-1). Only statistically significant values are reported.

A number of general observations can be drawn:

- There is a clear trend of increasing arrival time behind the obstacle (S_1–S_5) with increasing iteration number. This effect is seen to decrease as the vertical/lateral distance along the target wall increases (S_3 arrival times most closely resemble those from pFI-0 throughout).

- Arrival times at S_7 appear unaffected, suggesting the zone of influence does not extend beyond this point on the 45° ray.

- Pressure and specific impulse values do not follow such a simple trend, suggesting that a delayed arrival time is not a direct indicator of a weakened shock wave (Zhou & Hao 2008).

- Generally, peak pressure values can be seen to decrease downstream of the obstacle (S_1–S_5) with 48% maximum reduction at S_5 achieved by pFI-2.

- Whilst pFI-1 exhibits a consistent *increase* in peak specific impulse behind the obstacle (attributed to wave coalescence) such as S_4, pFI-3 exhibits a consistent *decrease* in peak specific impulse behind the obstacle. This suggests that the mitigation properties of the obstacle improve as it approaches a true fractal.

- Mitigation for pFI-1 and pFI-2 is generally restricted to immediately behind the obstacle (S_4), attributed to shadowing. For pFI-3, mitigation is observed over a much greater area, again signifying enhanced mitigation properties as the obstacle becomes more fractal-like.

- Peak pressure and peak specific impulse values are consistently higher at S_{12}, due to the aforementioned 'trapping' mechanism. It is hypothesised that this is what ultimately leads to the observed downstream mitigation.

- Maximum values of attenuation of 26% for peak pressure and 19% for peak specific impulse were observed for pFI-3.

3.4.2 Frequency analysis of the pressure signals

Due to the highly complex pressure and impulse histories at various locations surrounding the obstacle, it is apparent that only considering peak pressure, specific impulse, and time of arrival is not sufficient to fully characterise the obstacle's influence. Therefore, a frequency domain analysis was carried out at select sensor locations, namely S_1, S_4, S_7, and S_{12}, as shown in Figure 3.20. The amplitudes of the frequency spectrum were averaged for the triplicate tests at each SoD, for each pre-fractal arrangement. The following observations can be made:

- There is a small increase in mid-range frequency components (500–700 Hz) at S_1, although this appears to diminish with increasing SoD.
- The spectra at S_1 exhibit a noticeable reduction for pFI-2 and pFI-3 at higher frequencies (>700 Hz). The pre-fractal obstacles can therefore be said to effectively function as low-pass filters.
- Mid to high frequencies (>500 Hz) are generally amplified for pFI-1 and pFI-2 at S_4.
- Lower to mid-range frequencies (300–500 Hz) are reduced for pFI-3 at S_4, particularly at shorter stand-off distances. This may explain the apparent rounding of the shock front seen in the pressure traces.
- There are a number of troughs at specific frequencies at S_4. There is a prominent trough at 1200–1300 Hz which is absent in the pFI-0 case (i.e. that frequency component is *present* in the free-field case), but is particularly significant in the pFI-3 spectra, for all SoDs. This is likely due to the trapping mechanism observed previously.
- There are no noticeable differences in the S_7 spectra, confirming that this gauge lies outside of the zone of influence of the pre-fractal obstacles.

- There are considerable increases in the frequency spectra at S_{12} (on the front face of the central obstacle) when comparing pFI-3 to pFI-1, particularly for frequencies <500 Hz. There are intermittent peaks in the pFI-3 spectra between 600–1100 Hz which are absent in the pFI-1 and pFI-2 spectra. This is best shown in the pFI-3, SoD125 spectra, and is again indicative of the trapping mechanism seen in the pressure and specific impulse histories at this sensor.

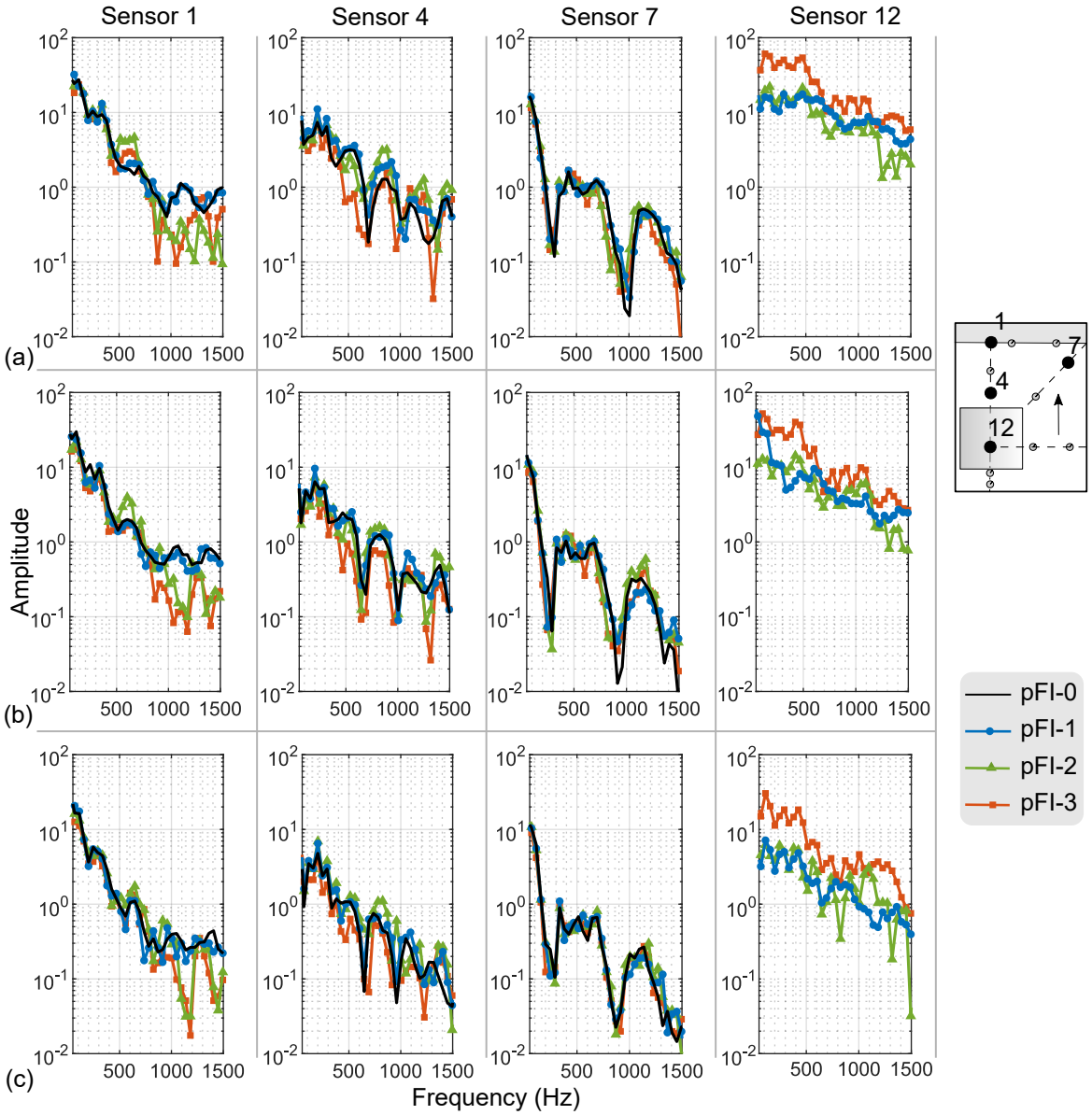

Figure 3.20: Frequency analysis for different stand-off distances (a) 1.25 m, (b) 1.50 mm, (c) 2.00 m

3.4.3 Towards an engineering approach to predict pressures

It is clear from the results discussed previously that the pre-fractal obstacle becomes more effective at attenuating blast pressures as iteration number increases. This is likely due to the provision of a much greater number of reflecting surfaces, which restricts the flow of the blast wave and also gives rise to trapping. In order to better make use of this knowledge, the following sub-section attempts to develop an engineering model to predict this behaviour. Taking inspiration from shock tube studies (Berger et al. 2010, Golovastov et al. 2022, Honghui & Yamamura 2004), a new parameter termed the *obstruction ratio*, OR, is defined, as shown schematically in Figure 3.21.

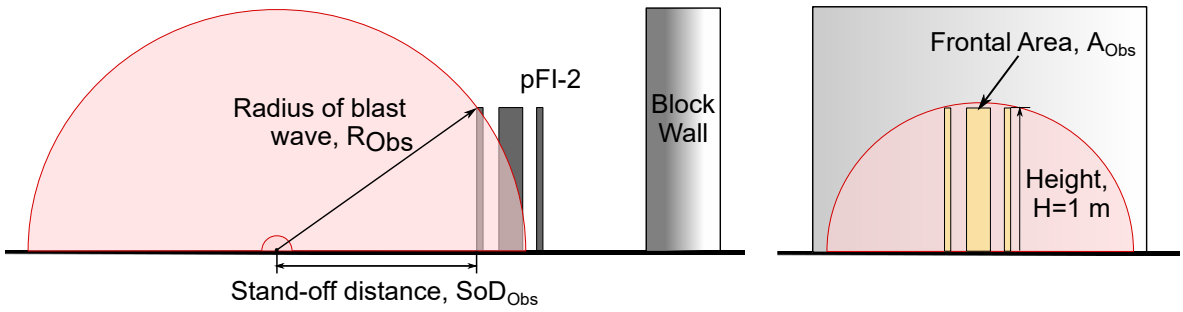

Figure 3.21: An illustration using pFI-2 obstacle to demonstrate the calculation of the obstruction ratio, OR, as defined in Equation 3.1.

Since the purpose of such a parameter is to quantify the obstruction offered by the obstacle to the transmission of the blast wave, the following was reasoned. For an obstacle of a given size, if the explosion were to be closer, the obstruction offered would be greater; and when farther away, it would be lower. This may be quantified by considering the hemispherical surface area of the wave that will be disrupted by the obstacle. An apt measure of the disruption would be the frontal (projected) area of the obstacle A_{Obs} itself. This disruption is seemingly maximal when the blast wave arrives at the top edge of the obstacle (see Figure 3.21). The radius of the blast wave at that instant R_{Obs} can therefore be used to define OR as in Equation 3.1.

$$OR = 1 + \frac{A_{\text{Obs}}}{{R_{\text{Obs}}}^2}$$
$$\text{where, } R_{\text{Obs}} = \sqrt{(\text{SoD}^2 + H^2)} \tag{3.1}$$

Where the height of the obstacles, H, is 1 m. Unity was added to the OR relation to avoid representing the no-obstacle case with a zero (in case, for example, reciprocals are to be taken or if this were to be used as a pre-multiplier).

Arrival time, peak overpressure, and peak specific impulse at S_1, S_4, and S_7 are plotted against OR in Figure 3.22. Also shown are the coefficients of determination, R^2, of a linear relationship fit to the results from each pre-fractal obstacle. There is a clear linear trend in all cases, and with the exception of specific impulse at S_1, the R^2 values range from 0.87 to 1.00. Arrival time, in particular, demonstrates a strong linearity, with R^2 values no lower than 0.96. It is not the intention of this work to derive more sophisticated predictions of blast attenuation, it is necessary only to demonstrate that there is a great degree of *predictability* of blast parameters when compared to the newly-defined obstruction ratio, as this will form the basis of later work on this subject.

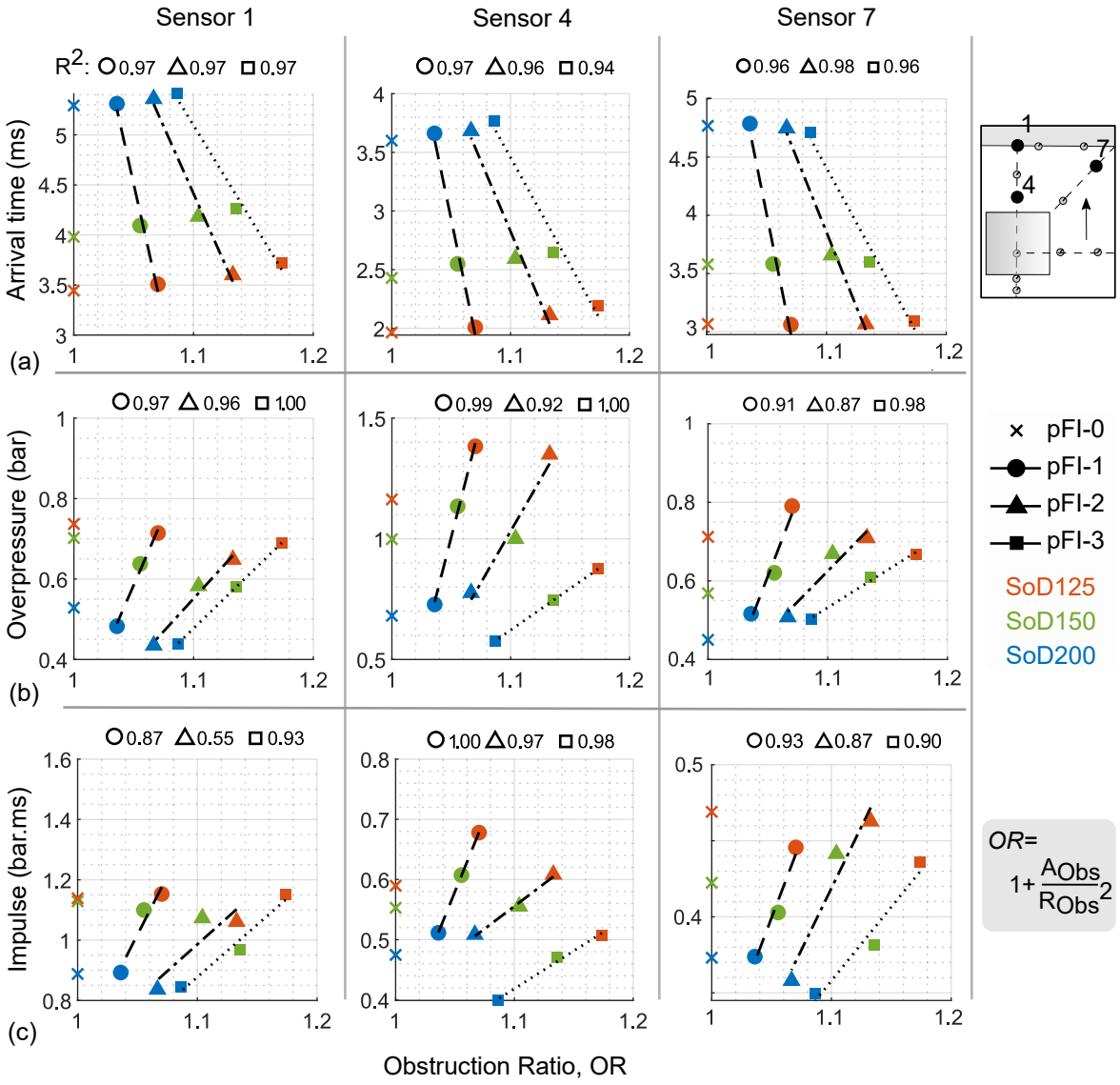

Figure 3.22: Plots of (a) arrival time, (b) overpressure, and (c) impulse for sensors S_1, S_4 and S_8 against the obstacle ratio OR, as defined in Equation 3.1. Unlike previous figures, here the colour represents SoD, and marker shape represents the iteration type

A few comments on the overpressure plots are provided below, but similar conclusions may be drawn when considering the other two parameters.

- The overpressure almost always increases at a slower rate for pFI-3 than the two previous iterations. This slope depends on the location of the sensor and OF.
- It is assumed that this slope is specific to each obstacle configuration. It may then be surmised that an obstacle of pFI-1 type, that has the same width as pFI-3, would result in higher pressures (and thus lower attenuation), in its vicinity.
- This suggests that using an obstacle comprising multiple smaller parts, i.e. a pre-fractal, is more effective than a single, larger obstacle.
- The extent of validity of this linear relationship, however, needs to be investigated further using CFD or additional experiments.

3.4.4 Outlook

The pFI-3 obstacle results in a more significant and uniform disruption of the blast wave, as opposed to previous iterations whose influence is largely restricted to the shadow region immediately behind the obstacle. This disruption is characterised by a reduction in pressure and impulse at the target wall, accompanied by a delayed arrival time and substantial rounding of the shock front (i.e. reduction in mid- and high-range frequency components immediately behind the obstacle and on the target wall respectively). There is also a significant increase in pressure and impulse in the vicinity of the obstacle, with evidence of multiple wave reflections termed 'trapping'. This is only seen for the pFI-3 case, suggesting it is fundamental behaviour observed only as the obstacle becomes more fractal-like.

The pressure reductions on the target wall (S_1) are comparable to reductions seen in similar tests using plants and hedges for blast mitigation (Gebbeken et al. 2017, Warnstedt & Gebbeken 2020)[5]. These similar attenuation properties are particularly noteworthy when considering the following:

- The 20 mm spacing between the obstacles in the current testing is relatively large compared to the spacing between the leaves.
- The obstacles remained elastic throughout the current testing, whereas the plants and hedges could sway and even experience loss of biomass. Although it has been suggested that structural strength of the protective structure is secondary when considering its mitigation properties (Rose et al. 1998), this does provide an additional means for energy dissipation.
- The relatively smooth surface of the square poles compared against the small length

[5]Pressures were measured in the current testing at $1H$ from the obstacle, whereas in the related studies they were measured at $0.75H$ from the obstacle

scales and rough surfaces of the plants, with surface roughness having been identified as a significant parameter (Hajek et al. 2016).

Each of these are believed to have enhanced the mitigation properties of the plants and hedges. Since these are not features of the pre-fractal obstacles tested herein, yet similar levels of mitigation were achieved, the results highlight the good intrinsic mitigation properties of pre-fractals obstacles and make a strong case for the use of pre-fractal obstacles in urban blast protection settings.

Whilst this experiment aimed to evaluate the blast loading mitigation, there are number of key factors affecting the behaviours of blast wave attenuation, some of them were previously identified in Chapter 2, are also seen in the experimental observations and are pointed out for framing the following numerical analyses in Chapters 5 & 6:

- Outer dimensions of the pre-fractals (such as pFI-2 and pFI-3) and individual obstacle size (such as pFI-1) have primary effects on mitigation according to the concept of obstruction ratio as well as
- The relative location of the obstacle to the explosive and the target where the mitigation is quantified has a significant impact on the results.
- The strength of the blast wave as seen for the attenuations of SoD125, SoD150 and SoD200 is another key parameter based on the frequency analysis and also it involves the speed of the wave which is essential for vortex creation.
- The mitigation data for downstream sensors (S1 to S7) reveals that the importance of attenuation spatially depends on the wave's interference type (destructive waves) in which consider the size of the target is a possible factor for calculating such mitigation, and
- Also, the spatial bounds of the mitigation at downstream require further demonstration.

- The mechanism behind the effective mitigation for shapes with fractal-like (such as pFI-3) is also required more clarification.

3.5 Summary and Conclusion

This Chapter aimed to quantify the attenuation of a blast wave after interacting with a pre-fractal obstacle of increasing complexity (i.e. increasing fractal iteration), and, in turn, better understand blast-obstacle interaction with complex obstacles. Experiments were performed using 0.25 kg hemispherical PE4 charges at three different scaled distances, $Z = 1.87$, 2.24, & 2.99 m/kg$^{1/3}$. Three Sierpinski carpet pre-fractal configurations – pFI-1, pFI-2, and pFI-3 – were tested, as well as reference configuration without any obstacle, termed pFI-0, to ascertain equivalent free-field values.

On comparing the performance of the pre-fractal obstacles with the reference case, reductions in peak overpressure up to 26% and peak specific impulse up to 19% were observed. The obstacles were also found to act effectively as low-pass filters, and their disruption of the blast wave was found to be more significant at closer stand-off distances. For the highest iteration number, pFI-3 (i.e. the most fractal-like obstacle), attenuation of the blast wave was spread over a much larger area behind the obstacle, as opposed to being limited to the shadow region immediately behind the obstacle as with previous iterations. This was coupled with a substantial increase in pressure and impulse in the vicinity of the obstacle itself, with a corresponding increase in the frequency spectra, attributed to multiple wave reflections off the smaller obstacles in a process known as 'trapping'.

The results indicate that the mechanism of blast mitigation of pre-fractal obstacles is fundamentally different from singular or arrays of regular obstacles. Blast parameters at any given location were found to be linearly dependent on the newly-defined obstruction factor, OF, suggesting that this behaviour is inherently determinable. This also provides an important metric for the future design of novel pre-fractal protective structures.

Chapter 4

Air blast modelling in Apollo blastsimulator

4.1 Introduction

This Chapter establishes the framework of numerical modelling of simulating the blast wave propagation in free-field and in the presence of obstacles complexity where the blast loading mitigation occurs. The numerical modelling of blast waves within this thesis is implemented using Apollo blastsimulator CFD solver (hereafter abbreviated as Apollo). It first explains the theoretical considerations of Apollo with its numerical solution features. Then, the blast wave propagation in this CFD solver is extensively validated for free-field and obstruction scenarios where the mesh sensitivity analysis with experimental data comparisons are provided. Finally, it concludes the required computational cell element length for a precise prediction of air blast loading after interacting with pre-fractal configurations such as pre-fractal iteration 3 and pre-fractal iteration 1 which will be used for numerical investigations of blast loading mitigation in the following chapters.

4.2 Theoretical considerations

Apollo is a commercial, explicit finite volume CFD software from Fraunhofer EMI (2018) intended for simulating detonations, blast wave propagation, and problems pertaining to gas dynamics. It uses a second-order finite-volume method with explicit time integration to solve the equations of conservation for transient flows of compressible, inviscid, non-heat-transmitting, inactive, or chemically reacting fluid mixtures. In Apollo, the governing equations of the system are inviscid compressible Euler equations – laws of conservation of mass, momentum, and energy – which are time-dependent, non-linear, and hyperbolic in nature where they are presented below in the differential form.

Equation (4.1) below, expresses the differential form of the conservation of mass:

$$\frac{\partial \rho}{\partial t} + \nabla.(\rho v) \tag{4.1}$$

Where ρ is the density treated as scalar quantity and v is velocity vector. Equations (4.2) to (4.4) express the conservation of momentum in three-dimensional terms

$$\frac{\partial \rho u}{\partial t} + \nabla.(\rho u v) + \frac{\partial p}{\partial x} \tag{4.2}$$

$$\frac{\partial \rho v}{\partial t} + \nabla.(\rho v v) + \frac{\partial p}{\partial y} \tag{4.3}$$

$$\frac{\partial \rho w}{\partial t} + \nabla.(\rho w v) + \frac{\partial p}{\partial z} \tag{4.4}$$

Where p is the pressure and u,v and w are the components of the velocity vector. Equation (4.5) expresses the conservation of energy as follows:

$$\frac{\partial E}{\partial t} + \nabla.((E + p)v) = 0 \tag{4.5}$$

Where E is the total energy per unit volume, and e is the specific internal energy; it can

be written as follows:

$$E = \rho(e + \frac{\|v\|^2}{2}) \tag{4.6}$$

Further details about the derivations of these laws of the conservation for a control volume can be found in (Blazek 2015, chap.2)

The fluid system considered for the simulation of detonations of high explosives in Apollo comprises two components: the gaseous detonation products and the surrounding air. Thus, two further equations of state are necessary to be added to the system of equations: the thermal equation of state which expresses pressure as a function of density and temperature, and the caloric equation of state which computes the internal energy as a function of density and temperature. High explosive (HE) modelling in Apollo uses an equation of state data file to deliver the information of both the caloric equation of state and thermal equation of state. The caloric equation of state model for all fluids in Apollo is approximated in the form of a quadratic polynomial function as give:

$$e = e_0 + c_{v1}T + c_{v2}T^2 \tag{4.7}$$

c_{v1} and c_{v2} are specific heat constants which at higher temperatures become temperature dependent. The whole simulations within this thesis contain an explosive reacting in air. The Air modelling is a thermally perfect gas which assumed to be

$$p = \rho RT \tag{4.8}$$

Where R is the specific gas constant under ambient temperature conditions (288 K), and ambient pressure is $p = 101.3$ kPa. The ideal gas caloric equation of state gives the relationship between thermodynamic variable as follows:

$$e = \frac{p}{(\gamma - 1)\rho} \tag{4.9}$$

Where γ is the ratio of specific heat. A linear model is used in Apollo to model the unreacted explosives is

$$p = a_0^2(\rho - \rho_0) + p_0 \tag{4.10}$$

where a_0 is sound speed and p_0 is ambient pressure (101.3 kPa). The detonation products (DP) are modelled in Apollo using Jones Wilkins Lee (JWL) equation of state (Lee et al. 1968)

$$p(\rho, T) = C_1 e^{-R_1\rho_0/\rho} + C_2 e^{-R_2\rho_0/\rho} + \rho RT \tag{4.11}$$

whereρ and ρ_0 are density and initial density, R is gas constant, and T is the absolute temperature. C_1, C_2, R_1, and R_2 are constants for a given fluid. The caloric EOS and thermal EOS parameters for air, TNT and C4 used in Apollo (Fraunhofer EMI 2018) are listed in 4.1

The Chapman-Jouguet theory (CJ) is used to model the reaction process of HE detonation in Apollo. The CJ employs a local initiation condition and a local state-dependent burning velocity which results in the reaction front developing in a physically meaningful way (Fraunhofer EMI 2018).

A finite volume method with explicit time integration is used to solve these equations numerically. The time integration is completed in two steps, the first of which is the Lagrange step (acceleration and deformation of a material volume), and the second of which is the remapping of the updated material volume onto the mesh cells. The pressure and the velocity at cell interfaces are computed using a characteristics-based technique in the Lagrange step, and the donor-cell method is then used to complete the remapping phase. For cells containing gas mixtures, local thermal equilibrium is assumed. All gases in a cell are assumed to have the same temperature, and the pressure in a mixed cell is determined by summing the partial pressures.

Both the Lagrange step and the remap step are computed with interpolated states based on tri-linear reconstructions of the distribution of the conservative variables inside the

Table 4.1: The caloric EOS and thermal EOS parameters for fluids: air, TNT, and C4

Air	Perfect gas model	Caloric EOS
		e_0, c_{v1}, c_{v2}
		2.375×10^5, 723.3, 0.0749
		Thermal EOS
		R
		288
TNT	Linear model	Caloric EOS
		e_0, c_{v1}, c_{v2}
		0, 787.5, 0.2492
		Thermal EOS
		a_0, ρ_0
		6985, 1630
TNT	JWL model	Caloric EOS
		e_0, c_{v1}, c_{v2}
		-4.923×10^6, 787.5, 0.2492
		Thermal EOS
		R, ρ_0, ω, C_1, C_2, R_1, R_2
		315, 1630, 0.29, 527.28×10^9, 6.300×10^9, 4.71, 1.07
C4	Linear model	Caloric EOS
		e_0, c_{v1}, c_{v2}
		0, 669.3, 0.0037
		Thermal EOS
		a_0, ρ_0
		7900, 1660
C4	JWL model	Caloric EOS
		e_0, c_{v1}, c_{v2}
		-5.574×10^6, 669.3, 0.3307
		Thermal EOS
		R, ρ_0, ω, C_1, C_2, R_1, R_2
		365, 1660, 0.33, 734.60×10^9, 8.860×10^9, 4.79, 1.06

grid cells for second order accuracy. One linear reconstruction is regulated for each spatial direction by a slope limiter that resembles the UMIST formulation (Lien & Leschziner 1994) with the coefficients altered to improve accuracy and robustness. To increase the spatial isotropy of the second order scheme, the three originally independent spatial reconstructions were combined into a 3D formulation.

Apollo defines the 3-D domain based on a Cartesian grid which is called a zone grid. Zones divide the domain with a certain discrete limit called zone length, L, that imaginarily extends from $-\infty$ to $+\infty$ (see Fig. 4.1) . Apollo uses multi-block structured grids

which divide the zones into cell elements where its 3-D geometry is hexahedron, but it is finite. Structured grids employ a topology approach to ensure that the cell elements are constructed in an array manner. Therefore, neighbouring cells are implicitly allocated in array indices (i, j, k). This regularity simplifies the execution processes. Although complex geometries can be hardly represented due to this simplicity, this method is suitable for parallelisation and mesh refinement.

The zone length in the domain is considered the coarsest spatial resolution. It is recommended in Apollo to have total number of zones that range from 1 to 100 (Fraunhofer EMI 2018). However, the finest spatial resolution in the domain is determined by the cell element size. It is known thereafter as Resolution, h, which can be calculated with respect to the zone length and selected Resolution levels, N from 0 to 9 according to this relation:

$$h = \frac{L}{2^N} \tag{4.12}$$

Figure 4.1 shows different Resolution levels for a constant zone length. Therefore, it is important to consider both zone length and resolution level in the mesh sensitivity study.

The construction of the computational domain is through assembling the cells and zones which is created by adding or deleting parts specifications. *Block* part is used in this thesis for all simulations to construct a single domain. The boundary conditions (B.C.) for the six-block faces are a combination of *Wall* and *Ambient* which are used for all simulations setups in this thesis. The B.C. *Wall* is a semi-infinite solid surface that enables blast wave reflection whilst the B.C. *Ambient* is an artificial boundary with a weak reflection that permits wave passage with a prescribed state (flow out).

Large, small, and orthogonally objects such as buildings and small poles (obstacles) can be modelled in Apollo with an appropriate assumption of internal and external boundary conditions. This modelling is performed through an embedded objects approach where these objects are solid and impermeable i.e., rigid. The external surface of the object is

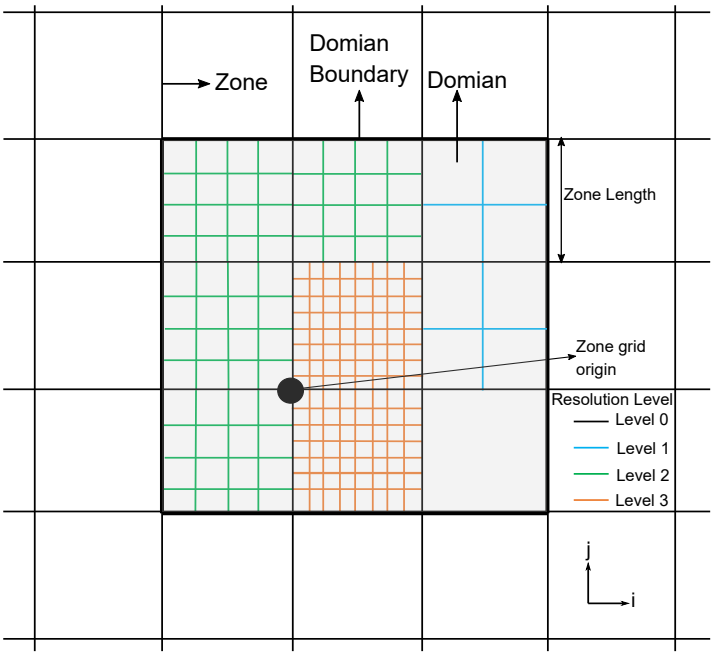

Figure 4.1: A simple 2D face of a block which shapes the computational domain, showing an exemplary non-uniform distribution of mesh resolution levels from 0 to 3 attributed to the zones. Figure adopted from (Fraunhofer EMI 2018)

formed as an ideal wall boundary that prevents friction and heat transfer. The objects are fixed into the computational mesh domain by masking certain individual mesh cells in specific zones and exposing them to the fluid. Objects are represented as voxel approximation models in Apollo. Therefore, it is essential to consider the simplicity of the geometrical shape as the general shape depends on the accuracy. In other words, more complexity in the geometrical style leads to high computational effort due to demanding high resolution.

4.2.1 Apollo features: One-dimensional analysis

One of the significant features of Apollo is the one-dimensional (1D) module. It performs with uniform one-dimensional meshes and allows the intial stage of the simulation to be accomplished in one dimension which exits as a spherically symmetric solution. However, it cannot be utilised for simulating cylinders. Figure 4.2 shows the one-dimensional wave propagation with discrete domains. Whenever a pressure disturbance (such as the shock

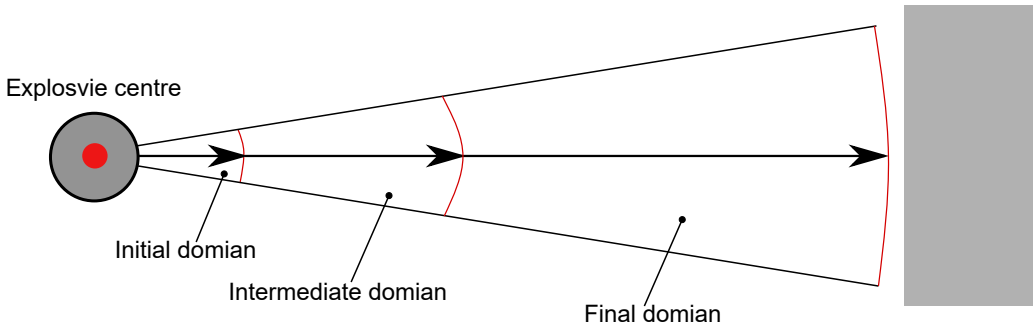

Figure 4.2: Global mesh adaption development in 1D module. Figure taken from (Fraunhofer EMI 2018)

front) reaches the outer limit of the current domain (as in Fig.4.2), it automatically performs mesh resizing. The total number of cells persists approximately constant during the 1D simulation since cell size and domain are increased by each adaptation step. Meshing sensitivity is under user control and relies on the gradients of flow field quantities (with maximum sensitivity meaning that all zones are fixed to the maximum level of resolution). This stage ends when user-inputted termination conditions are met, such as the number of time steps or radial distance.

4.2.2 Apollo features: Dynamic mesh adaption

The dynamic mesh adaptation (DMA) stage runs based on three-dimensional Cartesian meshes which produce various resolutions at the global level. Specific zones of the computational domain (such as those that instantaneously contain the shock front) will need various resolutions as the simulation develops within the time. This can save computational power for the zones that need it by decreasing the computational efforts from zones where it is not required as diagrammatically drawn on the left side of Figure 4.3. The highest mesh resolution is used in this process as directed by the user in the input file.

In the DMA algorithm, it is ensured that the region with the greatest gradient such as pressure is resolved at the highest level, even when there's only one zone left. When

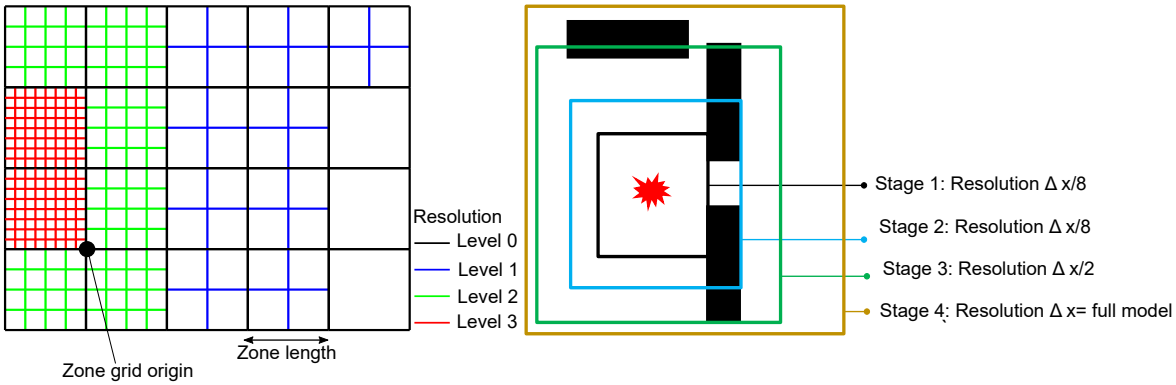

Figure 4.3: The dynamic mesh adaptation technique (left) and the multi-stage approach for global adaptation (right). Figure remade from (Fraunhofer EMI 2018)

there are no objects embedded in the flow field, and it is uniformly at the ambient state, the entire zones will stay at level 0 (Fraunhofer EMI 2018). Like the 1D module, the sensitivity of the DMA technique to the distribution of cell resolution may be stated in simulation. If all of the cells are resolved to the maximum resolution achievable, it would result in a large increase in computational time, and a maximum sensitivity value would be reached.

Another choice in the DMA module is to operate an ALE simulation through a mesh expansion technique. This implies that the mesh can be grew continuously corresponding to a velocity-time equation. When the user selects this option, the computational procedures switches from pure Eulerian (mesh fixed in space) to ALE.

4.2.3 Apollo features: Stages

Stage feature works based on splitting up the entire simulations into muilt-satge simulations for computational efficiency, as seen in Fig.4.3-right.The user may control stage feature in the 3D model by defining the base stage radius, end criteria, and growth rate, or by utilising the built-in "auto-staging" approach. The "auto-staging" approach comprises six stages with scaled end radii of 0.2, 0.5, 0.8, 1.25, 5, and infinite(in $m/kg^{1/3}$). As the simulation progresses, there will be additional resolution levels are implemented for each stage starting with an additional 6 levels. These additional resolution levels are reduced

by 1 when the disturbance attains some termination criteria, and the new domain size will be created according to the defined growth rate. The process remains repeating until the additional levels fall to 0 and the whole CFD domain is involved in the simulation. Consecutive stages are connected by the remapping of the motion area at the completion of the previous stage onto the mesh of the following stage.

Another stage option in Apollo is the ability to perform remapping between 1D and 3D models. In general, it is an execution of 1D model simulation obeying full termination criteria specified by the user and then followed by the 3D model simulation of the entire domain. This step is useful for reducing the computational efforts, especially for blast wave propagation in far-field problems.

4.3 Extensive validation of Apollo blastsimulator

This section demonstrates the ability of Apollo CFD solver in accurately predicting the blast loading parameters specifically overpressure and specific impulse generated in free-field scenario , and pre-fractal scenarios, specifically pFI-3 and pFI-1 setups, by developing mesh convergence analyses. These convergence studies also aid to appropriately model the approximated voxel shapes of the embedded obstacles such as square and circular shapes in order to achieve the correct blast-obstacle interaction process. Therefore, the numerical modelling in this Chapter firstly replicates the geometry of the experimental work in Chapter 3 (see section 3.4), in which 0.25 kg hemispheres of PE4 were detonated on a flat ground surface at different stand-off distances from the central obstacle, to suitably model the square obstacle-interaction process . Then, circular obstacle-interaction process is considered as special case.The Mesh convergence study was carried out in two stages:

Stage 1: An analysis of the effect of the ultimate cell length, $h = L/2^N$ on blast loading parameters with respect to the stand-off distance was carried out for the free-field scenario. This was used to derive the optimal cell length for a variety of blast intensities. Then, it

is compared with free-field experimental data from Chapter 3.

Stage 2: Once the required free-field resolution was determined, further investigations were performed on the sensitivity of the solution to the ratio of the cell length to the smallest length scale of the squared pre-fractal elements for third iteration order. Then, the optimal cell ratio is also compared with experimental records from Chapter 3 for validation purpose. Finally, the accurate cell ratio for modelling cylindrical obstacle as voxel approximation shape in Apollo arranged as first pre-fractal iteration order is determined and compared with data from the literature[1]

4.3.1 Free-Field propagation scenario

4.3.1.1 Mesh sensitivity analysis

A series of numerical simulations using different computational cell sizes was carried out for the free-field case (pFI-0) at the closest SoD (1.25 m) for brevity as seen in Figure 4.4. Explosives were modelled as 0.25 kg C4, which is nominally identical to PE4 (Bogosian et al. 2016). Due to symmetric condition in the numerical domain, the charge was modelled as 0.5 kg sphere in Apollo which was placed at a total stand-off distance of 2.5 m from the rigid wall to match the geometry of the experimental work. The octant domain size was 2.5 x 2.5 x 2.5 m. Rigid boundaries were located along the x=0, y=0, and z=0 planes, with a reflecting wall at y = 2.5m from explosive center. A ground plane was assigned as a reflecting surface and outflow planes were specified for the remaining two sides. Assuming that numerical solution will end before any waves from the artificial rigid wall would arrive the anticipated rigid wall during the propagation of waves in the model and start to impact the sensor readings, the explosion is technically modelled using symmetry planes as if it were located between two walls that were 5 m apart. For each of the domain side lengths, an integer number of zones was defined in each model.

[1]The experimental data in Chapter 3 was based on the square shape of obstacle

Pressure data from the five sensors in the corresponding experimental configuration (pFI-0-SoD125), were used for comparison against CFD data. Of these, four were incident sensors (S_4, S_7, S_8, and S_{10}) and one was a reflective sensor (S_1), resulting in 5 different Hopkinson scaled distances: $Z_{S1} = 3.97$ m/kg$^{1/3}$, $Z_{S4} = 2.86$ m/kg$^{1/3}$, $Z_{S7} = 3.68$ m/kg$^{1/3}$, $Z_{S8} = 2.22$ m/kg$^{1/3}$, and $Z_{S10} = 1.62$ m/kg$^{1/3}$ (see Figure 4.4b).

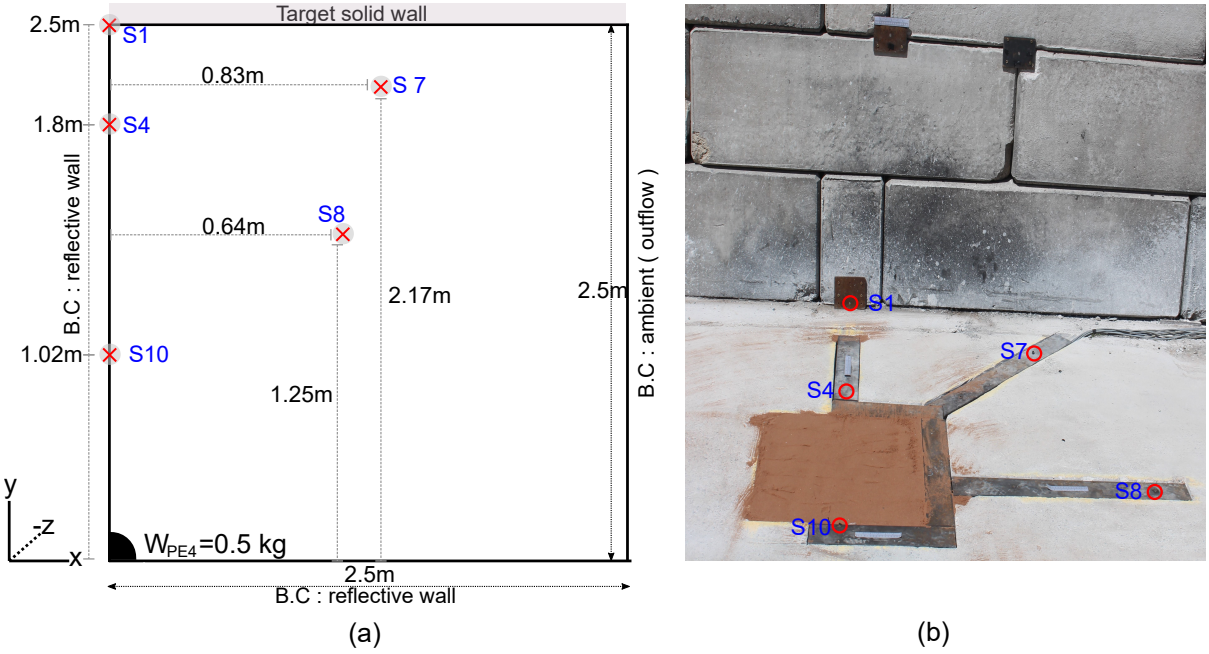

Figure 4.4: **(a)** a plan setup of 3D numerical symmetric domain of pFI-0-SoD125 configuration, and **(b)** photograph of pFI-0 configuration from experiment

As part of a preliminary analysis, 20 sample simulations were run and the results compared against the experimental data from the single numerical sensor (S_1) to iterate towards the optimal cell count to ensure a satisfactory solution. Apollo's 1D module was employed with the restriction set at one zone length from the reflecting sensor, then DMA model was enabled to improve the simulation time. The relevant cell size details including zone length L, resolution level N, and resolution h, for Z_{S1}= 3.97 m/kg$^{1/3}$ have been listed in Table 4.2, and the corresponding cell counts between the charge centre and the sensor S_1 for each of these parameters have been listed in Table 4.3.

The results of these free-field mesh sensitivity analyses in terms of peak overpressure, peak specific impulse; and the computational time (named 'wall time', short for wall-clock

Table 4.2: Ultimate cell length in CFD domain for 20 simulations

Resolution level	**Zone length, L (mm)**				
	1250	500	125	100	20
	Ultimate cell length, h (mm)				
0	1250	500	125	100	20
1	625	250	62.5	50	10
2	312.5	125	31.25	25	
3	156.25	62.5	15.625	12.5	
4	78.125	31.25			

Table 4.3: Number of cells between the charge centre and the sensor S_1 for the simulations in Table 4.2

Resolution level	**Zone length, L (mm)**				
	1250	500	125	100	20
	Number of cell elements				
0	2	5	20	25	125
1	4	10	40	50	250
2	8	20	80	100	500
3	16	40	160	200	
4	32	80			

time), have been plotted in Figure 4.5 against the ultimate cell length (h) normalised against the stand-off distance from S_1. The solid black line represents the average experimental value and the dashed line indicates a 10% deviation from the average experimental value, which has been taken to be an acceptable deviation from the measured value for the purpose of this work.

From these plots, it can be seen that the accuracy of the peak overpressure values depend significantly both on the number of zones and the number of cells between the charge and the target. From these results in Figure 4.5, a mesh having 'number of zones' 20 and a resolution $h < SoD/160$ can be appropriate for the 10% peak pressure convergence, whilst for the specific impulse, since the zone number is less relevant, the mesh resolution can be relaxed to $h < SoD/30$. Based on this, the cell size has been taken to be 15.62 mm ($= SoD/160$) for producing the numerical blast loads of all numerical sensors in Figure 4.4 for free-field case.

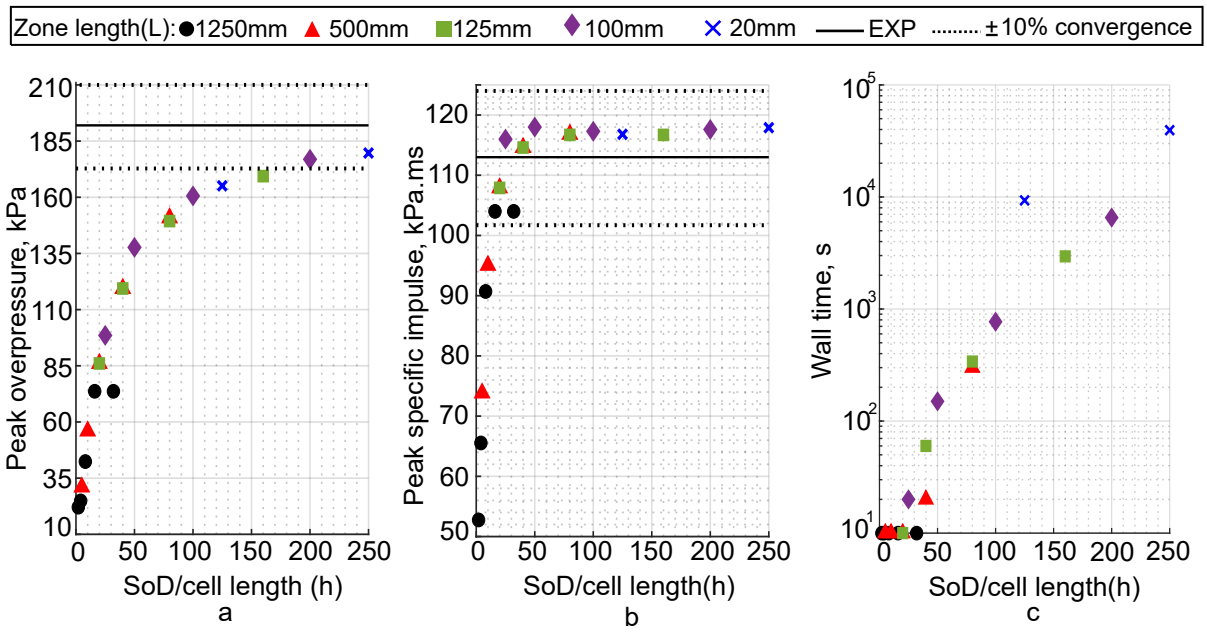

Figure 4.5: Mesh sensitivity analysis based on data from a single sensor (S_1). The results have been grouped in terms of **(a)** peak overpressure values, **(b)** peak specific impulse values, and **(c)** computational time.

4.3.1.2 Experimental validation

The pFI-0-SoD125 numerical model in Figure4.4a was simulated again using the converged mesh size of h = 15.62 mm (satisfying the SoD/160 criterion outlined previously) and compared with free-field experimental data in Chapter 3. Figure 4.6 compares numerical and experimental peak overpressure and specific impulse for simulating the free-field scenario in Figure4.4. As a reminder, S_4, S_7, S_8, and S_{10} are incident gauges and S_1 reflective. Across a variety of scaled distances, the numerically computed peak overpressure and peak specific impulse reliably match the experimental results except S_{10} which came above the average because the stander deviation of experimental pressure values was relatively high (23 kPa). Overall, this shows that the Apollo software can faithfully recreate blast loading for the previously outlined mesh sizes.

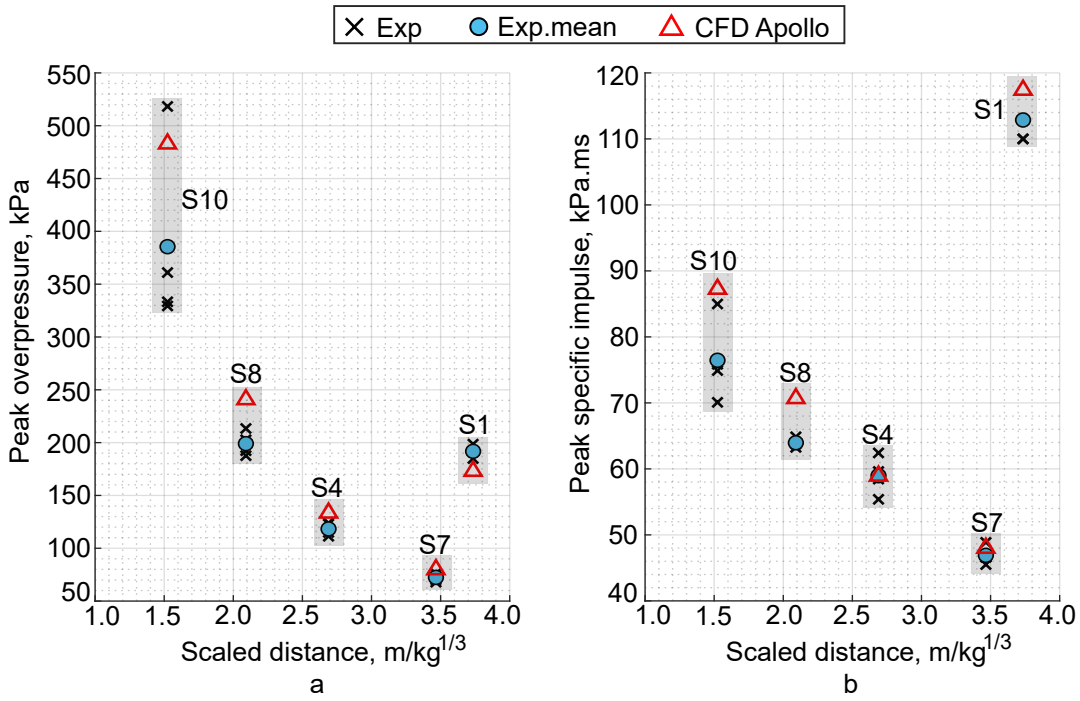

Figure 4.6: The validation of free-field scenario of all sensors in terms of: **(a)** peak overpressure, and **(b)** peak specific impulse

4.3.2 Pre-Fractal interaction scenario

4.3.2.1 Mesh sensitivity analysis: pre-fractal iteration3

While blast loading simulations for a free-field configuration reached convergence with cell element size equal to SoD/160, it is also necessary to refine this value when additional squared obstacle-interactions such as wave diffraction/refraction (see Figure 3.8 in sub-subsection 3.4.2.2), trapping mechanism (see Figure 3.13 in subsection 3.4.4), and downstream wave interference (see Figure 3.10) are expected to occur. To this end, introducing a new factor, called obstacle-cell ratio, can be useful to determine the optimal mesh element size for simulating the flow around each pre-fractal obstacle. Defined as the width of the obstacle over the mesh element size, this ratio physically represents the number of cells used to discretize the smallest geometry in the obstacle. As the element geometry of the structured mesh in Apollo is hexahedron, the formulation of the voxel shape of a square rod in pFI-3 configuration requires only an integer number of cell ratio

to match the exact real obstacle dimensions.

The pFI-3 pre-fractal configuration with an SoD of 1.25 m (SoD125) was chosen to replicate the experimental configuration in Figure 4.7b since this obstacle configuration results in particularly complex shock wave interaction patterns, and so the resulting mesh validation would also be applicable to the other configurations viz., pFI-2 & pFI-1 (see Figure 3.2a& b). The dimensions of the numerical domain was 2.5 x 2.5 x 2.5 m and the explosive size was 0.5 kg C4. The conditions of this model was identical to free-field scenario in the previous subsection.

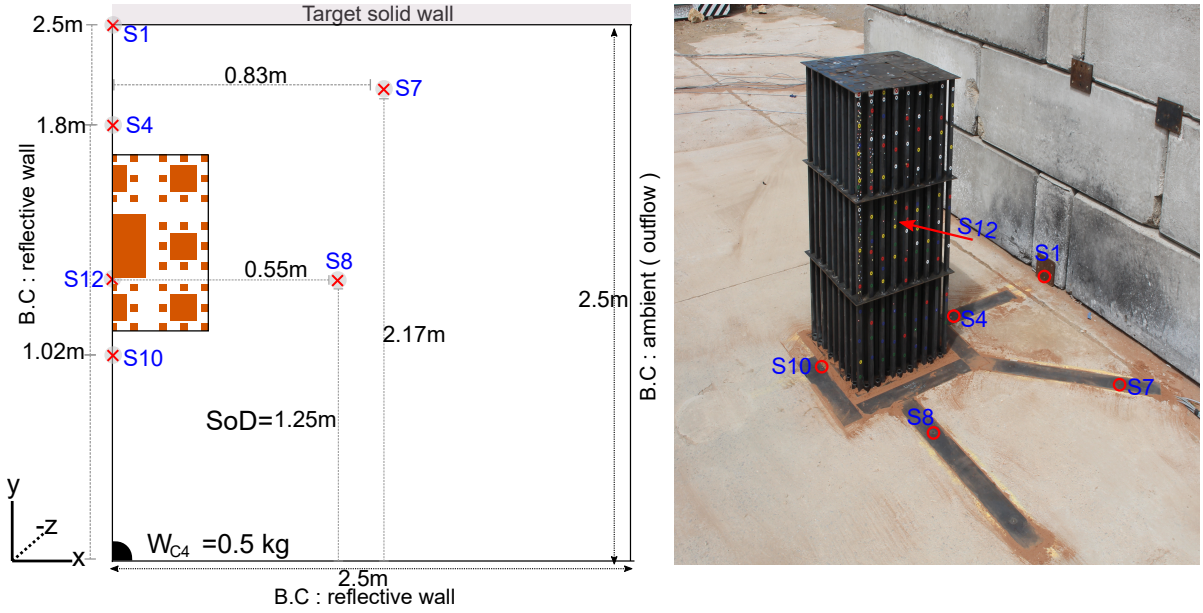

Figure 4.7: **(a)** A plan view of the 3D numerical symmetric domain of pFI-3-SoD125 configuration, and **(b)** photograph of pFI-3 configuration from experiment

For this analysis, instead of using a single sensor, all the 6 sensors in Figure 4.7 have been used in the numerical simulation to clarify the influence of the obstacle-cell ratio significance on different phenomena: sensor 10 for reflection; sensor 12 for the trapping mechanism at the obstacle location; sensor 8 for the blast directionality changes; sensors 4 and 7 for the incident wave interference in the downstream region; sensor 1 for the reflected wave interference. All sensors are palced on the ground expect sensors 1 and 12 which were mounted 0.02 m and 0.51 m respectively above the ground. The computational

Table 4.4: Ultimate cell lengths h for mesh refinement studies of the CFD model in Figure 4.7a. NB.: Smallest obstacle width for the symmetric half of pFI-3 is 10 mm.

Zone length= 160 mm	
Cell element length	**Obstacle-cell ratio**
10 mm	1
5 mm	2
2.5 mm	4

domain parameters have been listed in Table 4.4. Here it should be noted that 10 mm cells have been used as the starting size as that would be the smallest size of the obstacle for a half symmetry model (half the size of the 20 mm square rod in pFI-3), and it has been progressively reduced to 2.5 mm. It is worth noting that refining the mesh will dramatically increase the computational effort; the wall-time for the runs using cell elements of 10mm, 5mm, and 2.5 mm, were 0.5, 7, and 72 hours respectively.

The resulting peak overpressure and peak specific impulse values have been compared against the corresponding mean experimental values in Figure 4.8 as both scatter plots and bar charts. The values at downstream sensors (S_4, S_7, and S_1) closely match with the mean experimental values, with slight differences in overpressure occurring with increasing obstacle-cell ratio. The incident sensor S_8 exhibits a fairly good agreement with experimental overpressure data although it underestimates the specific impulse, perhaps due to the simplifications in the ground-surface explosive modelling incorporated in the CFD model. The peak numerical overpressure values in the upstream sensor S_{10} increase as the obstacle-cell ratio increases, with relative error greater than 10%. This increment is expected here as Apollo has already converged with lower mesh resolution in Fig.4.6a. The numerical specific impulse however, has successfully converged and falls within the limit of the experimental values. Generally, the values in Figure 4.8d indicate the convergence of peak specific impulse values for all the chosen mesh sizes. It is also seen (from Figures 4.8c&d) that the specific impulse converges faster than the overpressure, which agrees well with the previously reported results for Apollo Blastsimulator (Klomfass 2018)

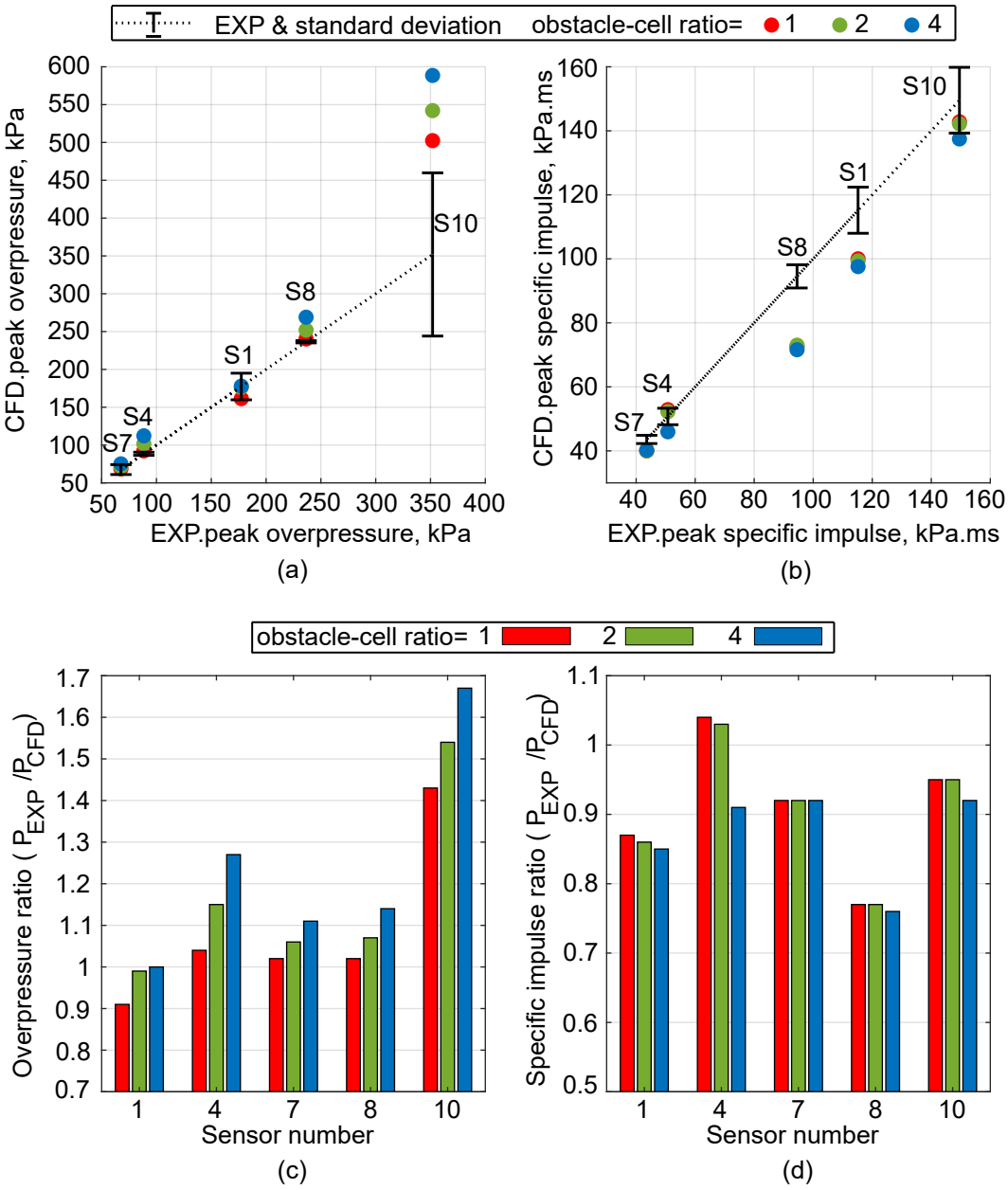

Figure 4.8: The results of mesh convergence study for pFI-3 at SoD of 1250 mm reported at sensor locations S_1, S_4, S_7, S_8, and S_{10}. **(a & b)** is a scatter plot of the numerical and experimental peak overpressure and peak specific impulse values respectively. **(c & d)** is a bar graph of the ratios of peak pressure and peak specific impulse respectively.

Although the influence of obstacle-cell ratio did not play out clearly in Figure 4.8, a closer look at the overpressure histories (Figures 4.9a-c) on the central sensor S_{12}, where the shock trapping occurs, shows the importance of mesh refinement. Obstacle-cell ratios

of 2 and 4 could successfully capture the multiple reflections trapped within the obstacle. The specific impulse histories, though, are not greatly influenced by the changes to the number of cells ahead of the smallest pre-fractal element. It is worth remarking that the increasing pre-fractal complexity such as fourth pre-fractal iteration (pFI-4) will eventually be considered and simulated in the following Chapters, and therefore a larger obstacle-cell ratio may be required to achieve convergence.

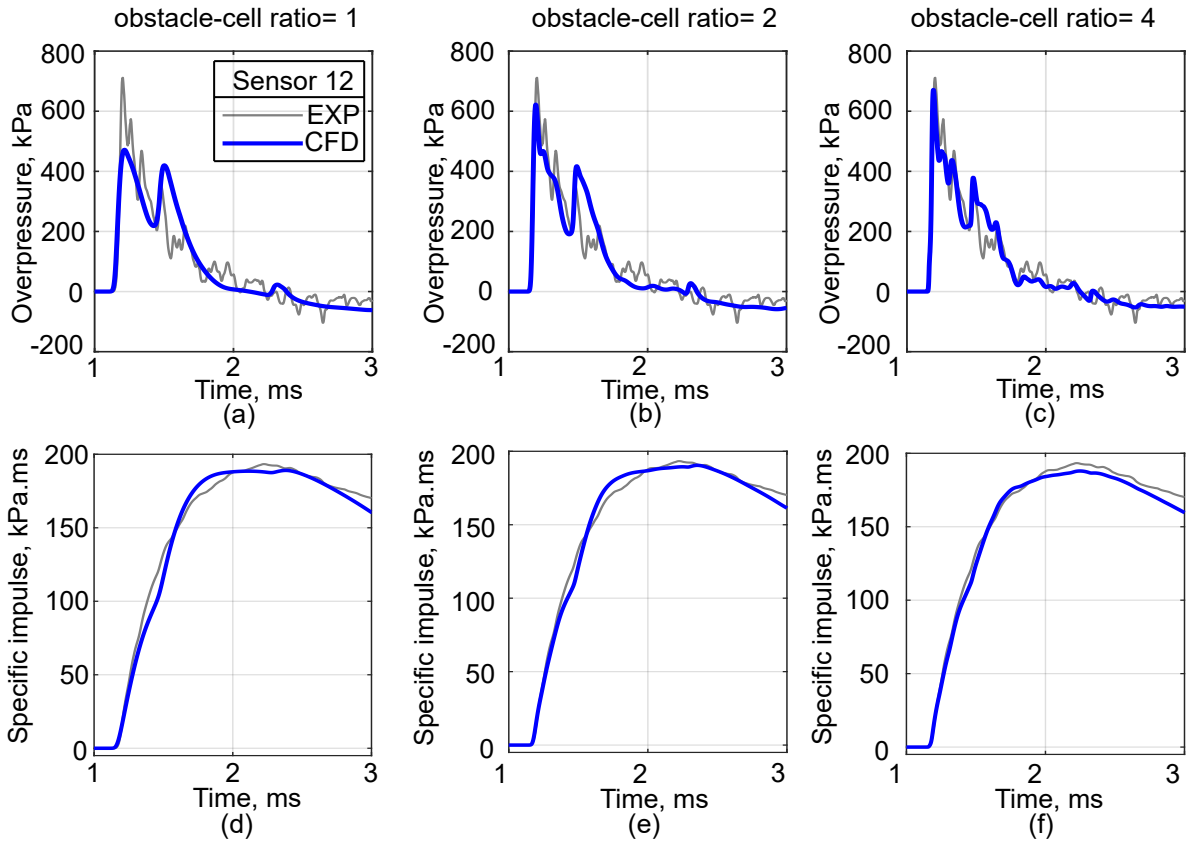

Figure 4.9: The overpressure **(a-c)** and specific impulse histories **(d-f)** at S_{12} for different obstacle-cell ratios.

4.3.2.2 Experimental validation

The validation of blast wave interaction with the iteration 3 pre-fractal obstacle pFI-3 in Apollo CFD solver is presented in this sub-subsection through comparing numerical result including pressure data and visualised numerical solution of shock shape with experimen-

tal data taken from Chapter 3. Here, three octane domains used for the 3D simulations had different dimensions based on the stand-off distance between the explosive and the obstacle, namely 2.5 x 2.5 x 2.5 m , 2.75 x 2.75 x 2.75 m, and 3 x 3 x 3 m for the 1.25 m, 1.50 m and 2.0 m SoDs respectively for pFI-3 configuration. The numerical model conditions for these simulations were similar to Figure 4.7 with using the previously outlined mesh size of 2.5mm, for which the obstacle-cell size ratio was 4.
However, the sensors coordinates in these numerical domains were varied and depended on each SoD. The numerical overpressure and specific impulse histories of the downstream sensors (S_1, S_4), the central pole sensor (S_{12}), and the upstream sensor (S_{10}) have been compared for each SoD. In addition, a qualitative comparison was made between a high speed camera image adopted from experimental data in Figure 3.10 (see Chapter 3) and the numerically generated image of the shock front disturbance. The total run time of these simulations for the SoD125, SoD150 and SoD200 was 217 hours using computational machine with specifications of 128 GB RAM and 16 essential cores.

A time history comparison for numerical and experimental measurements in the downstream region are shown for S_1 and S_4 in Figures 4.10 & 4.11 respectively. Each SoD had its own experimental time history measurements in each sub-figure. The numerical reflective blast loading measurements for S_1 match excellently with experimental patterns for different blast wave intensities. Similarly, the incident pressure and impulse values at S_4 show a fairly good overlap. The increasing mismatch in peak overpressure values with SoD (see Figure 4.11c) could be due to simplifications in the modelling ground-surface explosive interaction in the near-field region.

Figure 4.12 shows an overlay plot of numerical and experimental data for S_{12}, which is mounted centrally on the front face of the 180 mm obstacle in the pFI-3 configuration. These plots are for the overpressure and specific impulse histories at all stand-off distances

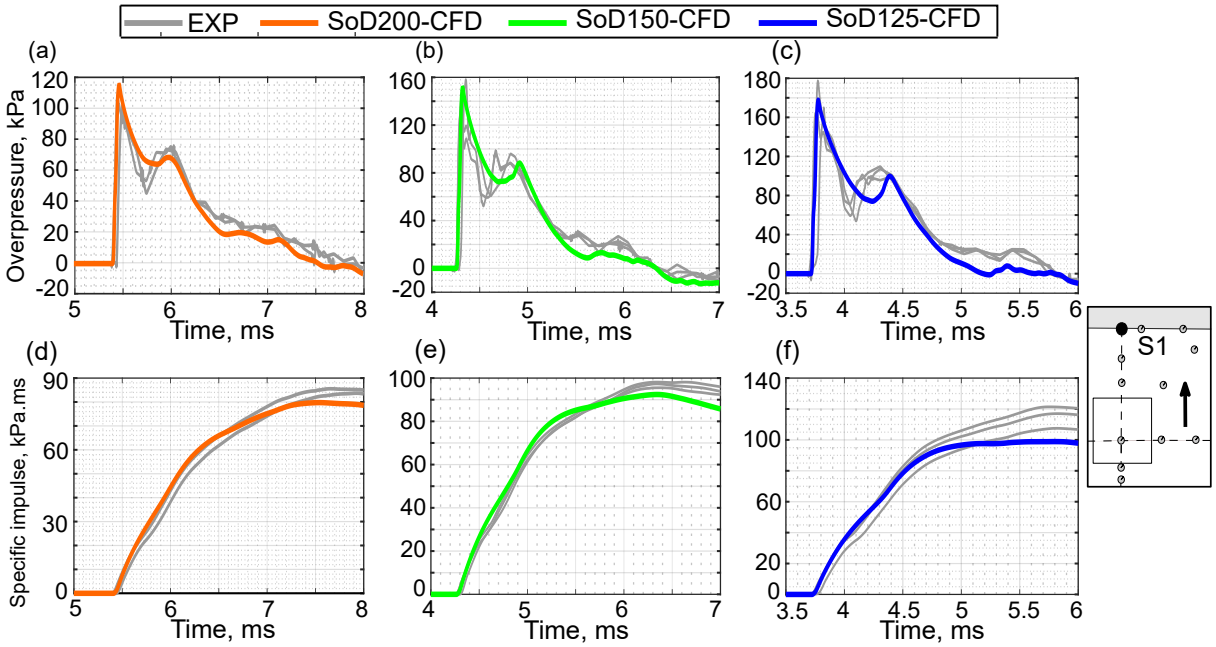

Figure 4.10: The numerical and experimental measurements for pFI-3 compared at S_1. Overpressure histories for **(a to c)** SoD= 2 m, 1.5 m, 1.25 m respectively. Specific impulse histories for **(d to f)** SoD= 2 m, 1.5 m, 1.25 m respectively.

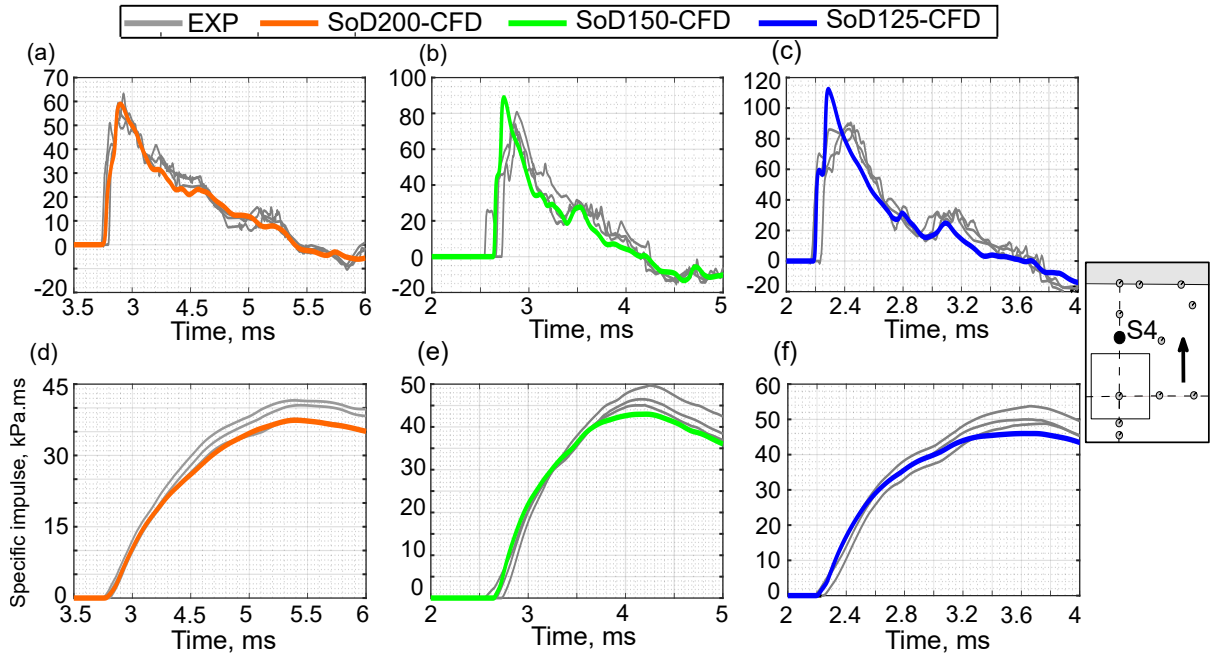

Figure 4.11: The numerical and experimental measurements for pFI-3 compared at S_4. Overpressure histories for **(a to c)** SoD= 2 m, 1.5 m, 1.25 m respectively. Specific impulse histories for **(d to f)** SoD= 2 m, 1.5 m, 1.25 m respectively.

considered in this work, viz., 1.25 m^2, 1.50 m, and 2.00 m. Again, it can be seen that the software has captured the complex overpressure histories with multiple peaks which arise due to wave trapping quite well. The specific impulse history has also been captured well, implying that the use of obstacle/cell ratio of 4 for blast interaction for a potential fourth iteration of similar pre-fractals is quite appropriate.

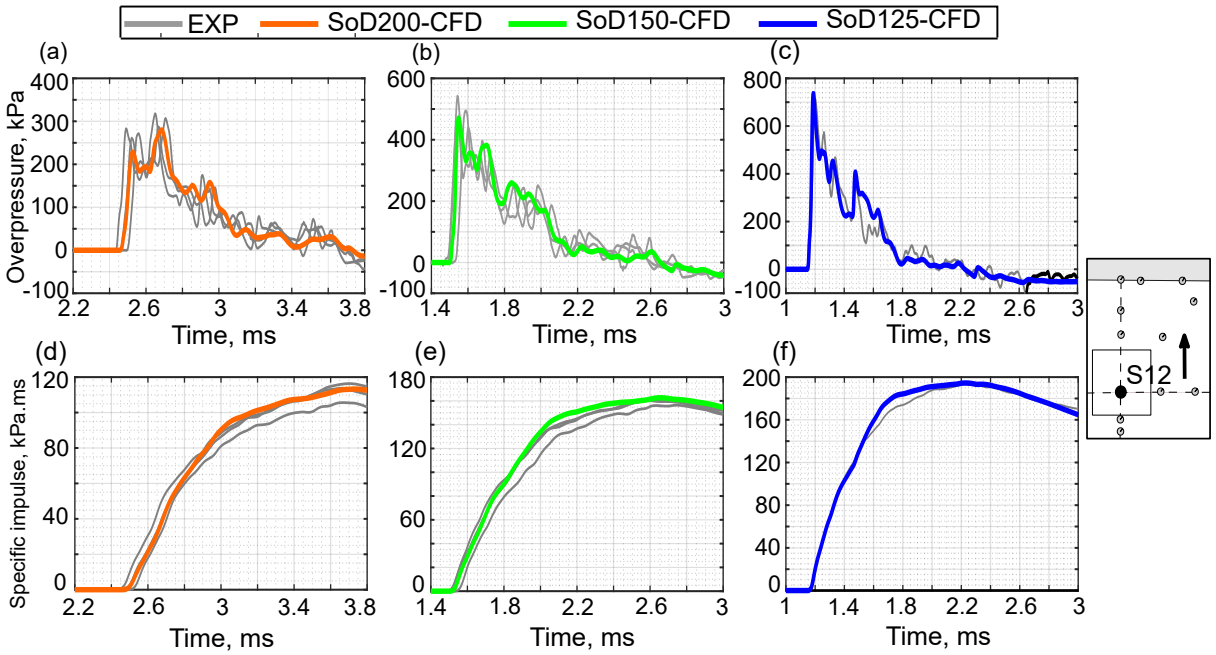

Figure 4.12: The numerical and experimental measurements at S_{12} for pFI-3. The overpressure histories are compared for SoD= **(a)** 2m, **(b)** 1.5m, and **(c)** 1.25 m. The respective specific impulse history comparisons for SoDs = **(d)** 2m, **(e)** 1.5 m, and **(f)** 1.25 m.

Additionally, a sensor in the upstream region (S_{10}) was also chosen to validate the CFD data. The experimental overpressure values for this location (in Figures 4.13a-c) consist of multiple peaks; the first from the incident wave and the remainder from reflections off the obstacle. While the behaviour of the numerical model is excellent in predicting these reflected waves, the peak incident overpressure in Figures 4.13b and 4.13c has been overestimated due to mesh size related constraints as explained earlier (Figure 4.8a). The

[2]The case of pFI-3 with SoD125 in Figure 4.12c is a repeat of Figure 4.9c

important features of the specific impulse history though, have been captured successfully by Apollo (in Figures 4.13d-f), proving its ability to recreate these experiments.

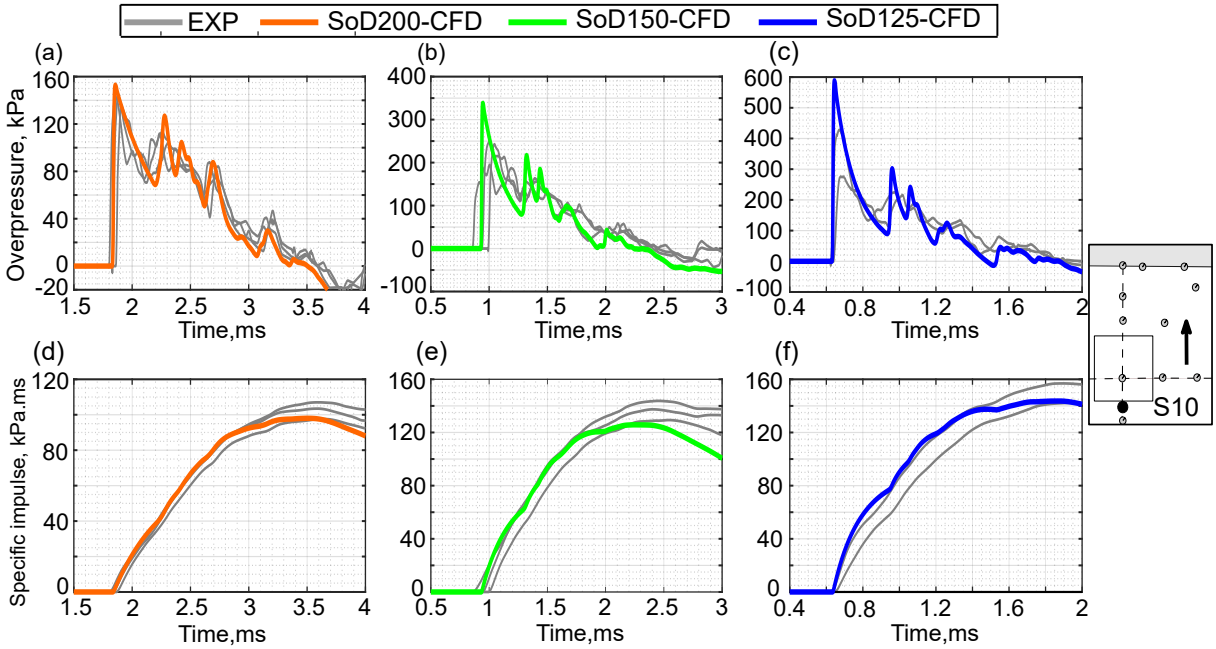

Figure 4.13: The numerical and experimental measurements at S_{10} for pFI-3. The overpressure histories are compared for SoD= **(a-c)** 2 m, 1.5 m, and 1.25 m. The respective specific impulse history comparisons for SoDs=**(d-f)** SoD= 2 m, 1.5 m, and 1.25 m.

Apart from these spatially localised validations, an overall snapshot of the flow field was also used to qualitatively compare against the photographs of the shock wave captured experimentally. In the experimental work, using a high speed camera, distortions while imaging a zebra pattern – due to the presence of a shock wave in its foreground – were captured. Artificial schlieren images were derived from the CFD data (using Paraview) at different time instants as shown in Figure 4.14a-d for the case of pFI-3-SoD200. The comparisons have been made at **(a,b)** 3 ms and **(c,d)** 4 ms after detonation. The incident wave (blue); reflected wave (red) and; transmitted (green) wave in these images are seen to corroborate fairly well. These comparative images show that Apollo has fairly successfully captured the reflections of the incident shock wave at t= 3ms (Figures 4.14a-b), acknowledging the non-exact nature of the overlays of the experimental video stills. Even the transmission of waves through the obstacles (green lines In Figures 4.14c-d) demonstrating the breakup of the shock front that leads to significant mitigation, has

been captured reasonably well. This qualitative agreement is not surprising giving the level of quantitative agreement seen previously.

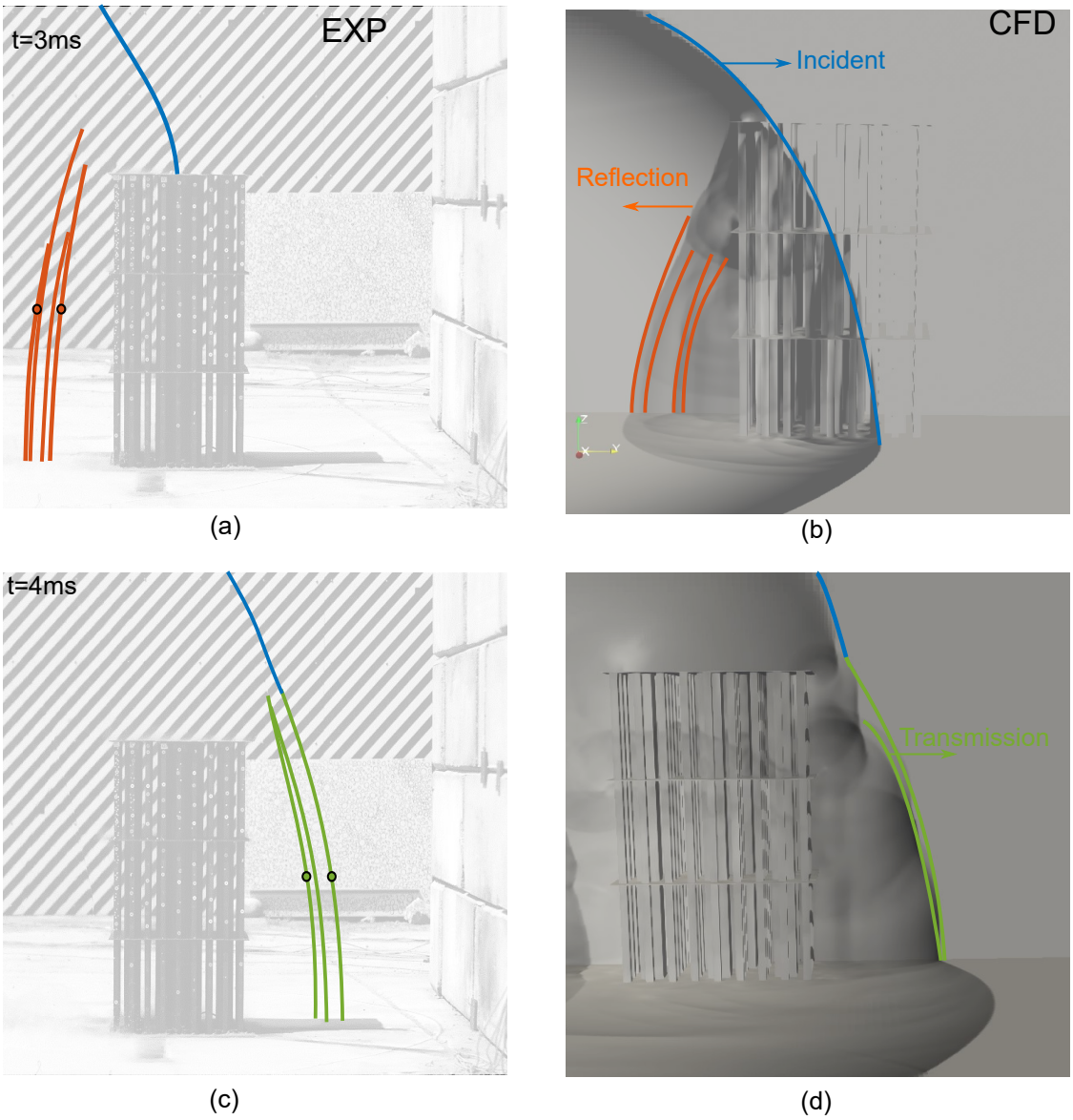

Figure 4.14: Qualitative comparison of shock fronts at two different time instants between experiments **(L)** and numerical data **(R)** for pFI-3-SoD200. Experimental photographs have been adapted from Figure 3.10 in Chapter3.

In the light of these extensive validation runs, it can be stated that Apollo can reliably predict the blast loading for all wave interferences occurring downstream of similar complex obstacles and also less complexity such as pFI-2 and pFI-1, particularly square and rectangular shapes, using obstacle cell ratio ≥ 4.

4.3.2.3 Mesh sensitivity analysis: special case of pre-fractal iteration1

The previous sub-subsections showed that the square shape of a rod in a pre-fractal arrangement requires an obstacle-cell ratio equal to 4 for perfect modelling of diffraction around edges. This would be also applicable for rectangular shapes as well. This sub-subsection adopts a cylindrical rod as a blast wave attenuator (Suzuki et al. 2000, Abe et al. 2001, Gebbeken & Döge 2010) due to its gradual diffraction wave loading and downstream mitigation. Circular cross sections, recommended by Shi et al. (2007), Williams & Williamson (2012), Rajkumar et al. (2020), excel in diffraction over reflection, resulting in a more even load distribution on the obstacle itself which would facilitate the required strength design (Gebbeken & Döge 2010). However, when a cylindrical obstacle is considered in certain pr-fractal arrangements, the voxel shape approximation of this cylinder demands additional computational efforts by decreasing the resolution of the mesh in the domain. This is due to infinite numbers of edges in the circumference of a circle whilst voxel approximation constructs it with finite edges as seen in Figure 4.15b for voxel shapes approximations of cylindrical surfaces with 100 mm radius.

Hence, a mesh convergence study of blast loading influenced by waves interference downstream a cylindrical obstacle in pFI-1 configuration was developed using four numerical simulations. The plan view of the 3D symmetric domain is given in Figure 4.15a for all 4 simulations which all had identical dimensions of 2m x 2m x 2m. Each simulation had a different voxel model of the cylindrical surface as seen in Figure 4.15b according to the specified mesh resolution in Table 4.5. The blast loading was generated using 0.250 kg C4 hemispherical explosive - modelled as 0.5 kg - placed on a ground surface 2 m away from a rigid reflective wall. A cylinder with a 100 mm radius and 2 m height was placed in the middle of the stand-off distance (specifically 1 m away from the explosive) to interact with the blast wave and cause a disturbance with wave interference. Peak overpressure and specific impulse values were given by 41 gauges placed every 2.5 cm along 1 m width on the ground level of the reflective wall to reasonably measure the distributed blast loading

in the shadowing and interference regions.

Table 4.5: Ultimate cell lengths h for mesh refinement study of the CFD models in Figure 4.15

Radius of cylindrical obstacle, R= 100 mm					
Voxel model	Zone length, L mm	Resolution level, N	Resolution, h mm	Obstacle-cell ratio	Simulation time hr
1	80	2	20	5	0.3
2	80	3	10	10	2
3	80	4	5	20	8
4	80	5	2.5	40	50

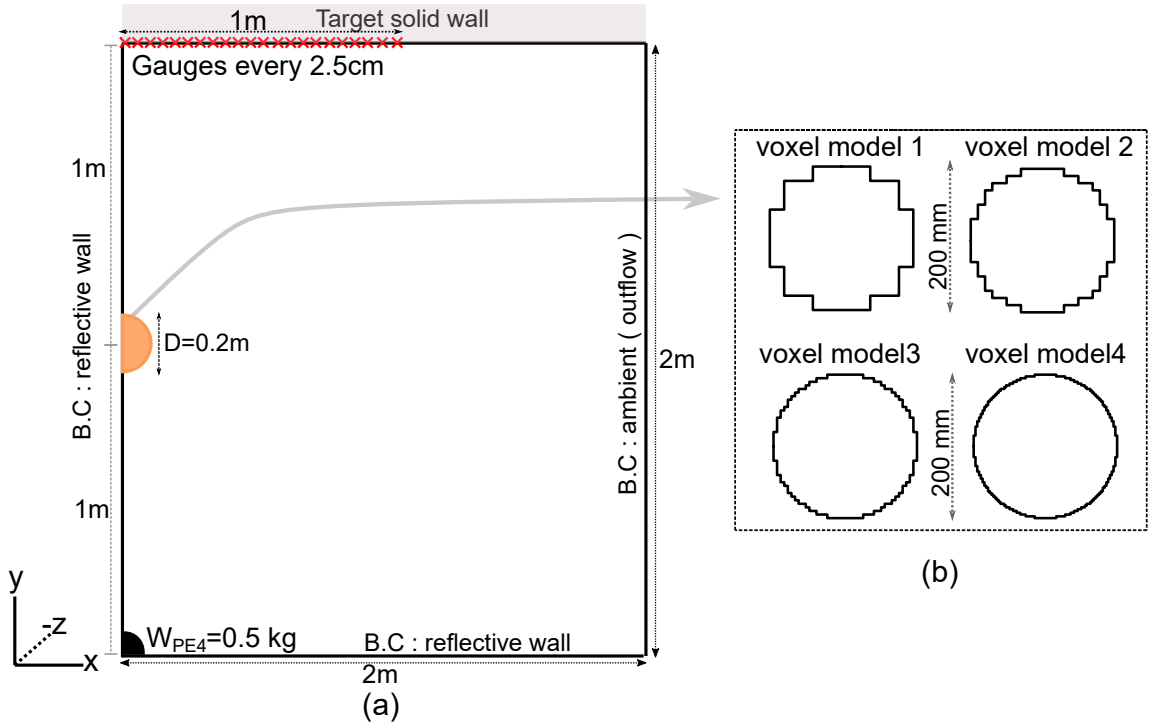

Figure 4.15: **(a)** a plan setup of 3D numerical symmetric domains for simulating four cylinders with 100 mm radius where their voxel shapes approximations in sub-figure **(b)**

The results of distributed peak overpressure and specific impulse values over the 1 m width for all voxel models were produced in Figure 4.16a&b. The percentage relative error of pressure and specific impulse between subsequent numerical models were calculated and plotted with respect to the wall's width in Figure 4.16d&c respectively. Clearly, voxel model 3 has achieved the convergence in peak pressure distribution in Fig. 4.16a although the peak impulse in Fig. 4.16b was not significantly affected by the diffraction process around the finite number of edges in the circular surface. Thus, it can be assumed that the contributions of the finite edges in voxel model 3 would diffract the blast wave and cause

wave interference downstream similar to the contributions of infinite edges in a perfect circular shape.

However, considering the simulation time in Table 4.5, the difference between voxel model 2 and voxel model 3 is four times as much; and as the relative percentage error of pressure between model 3 and model 2 is less than 6.5% in Fig. 4.16c and the relative percentage error of specific impulse is less than 1% in Fig. 4.16d, the obstacle-cell ratio of voxel model 2, which it is 10, is the optimal value for accurately simulating the diffraction of blast wave around the cylindrical section.

4.3.2.4 Experimental validation : special case of pre-fractal iteration1

In the current sub-subsection, a quantitative and qualitative validation of the flow structures is carried out in Apollo solver to prove the suitability of 10 obstacle-cell ratio choice in blast wave diffraction around circular surface problem. Due to the limited data available in literature for pressure distribution over a cylinder exposed to a blast wave, numerical validation is carried out using data from two different sources. First, pressure distribution over a cylinder from the work Yang et al. (1987) has been used. Second, a qualitative comparison was carried out against schlieren images taken from the experimental work of Bryson & Gross (1961).

Yang et al. (1987) numerically solved the shock wave diffraction problem over a 12.5 mm diameter cylinder for an incident Mach number of 2.81 in a 'shock tube' setup. The pressure history at certain angular positions across the circumference, starting from the forward stagnation point (0°) until the rear stagnation point (180°) was reported in increments of 30°. The computed isopycnics of the numerical solution was compared against the experimental schlieren photos of Bryson & Gross (1961). An excellent comparison was obtained, confirming the high fidelity of Yang's model.

For purposes of validation of Apollo in this special case of pre-fractal iteration 1, a larger diameter cylinder of 120 mm was used, as a lower size would mean the use of a highly

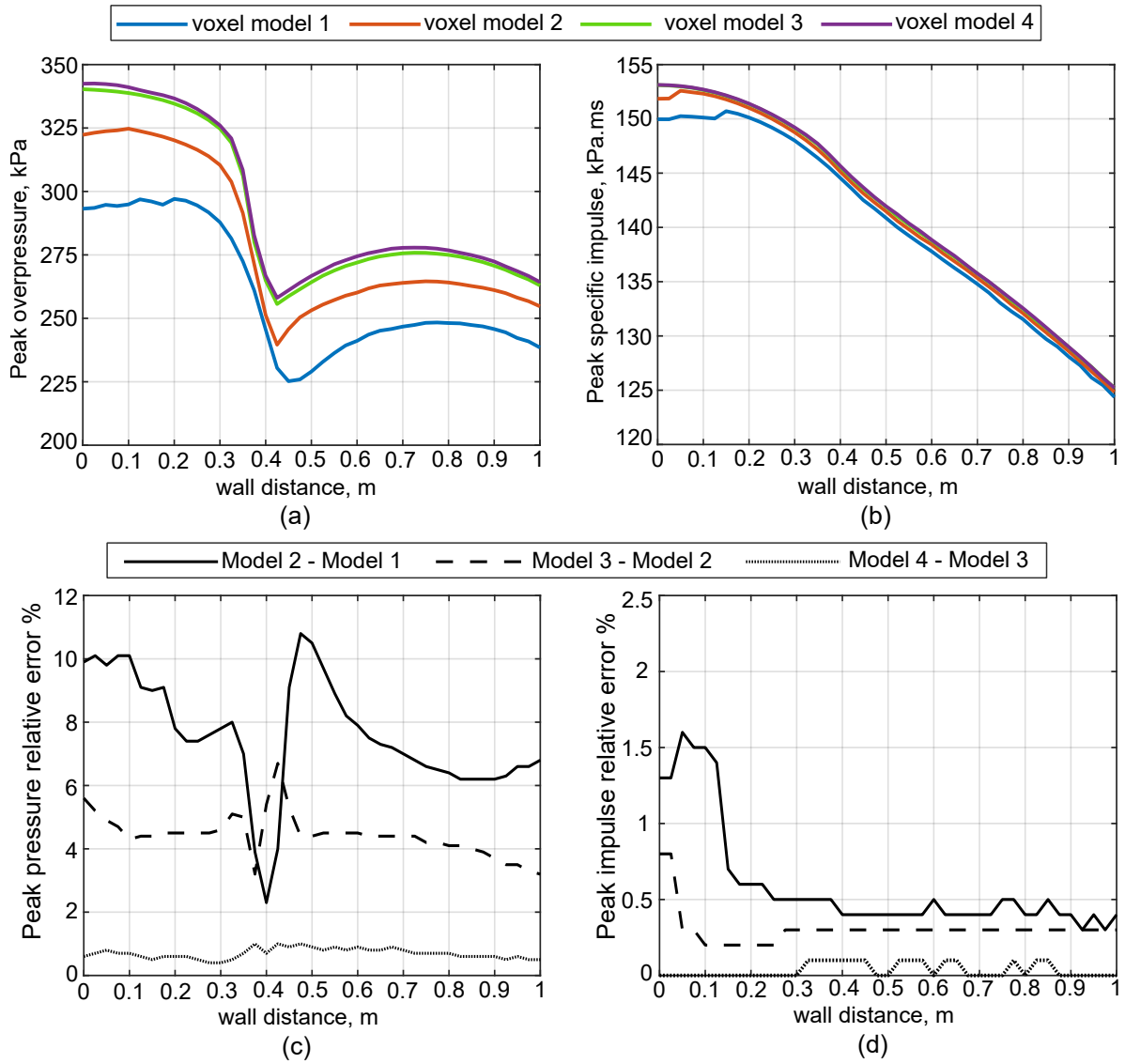

Figure 4.16: **(a)&(b)** are the peak overpressure and specific impulse values distributed over 1m wall-target's width respectively. **(c)&(d)** are relative percentage error between subsequent voxel models of peak overpressure and specifies impulse values respectively

refined mesh which was beyond the capabilities of the available computational hardware. A full 3D model with a semi-infinitely tall cylinder along the positive Z-axis was used to run this simulation over a domain of $2 \times 1.5 \times 2$ m which is schematically drawn in Figure 4.17. A semi-infinite model was simulated to avoid the top diffraction effect to maintain equivalence with Yang's work. The ultimate cell length used for this simulation was 6.25 mm to ensure the cylinder radius is discretized with ∼10 voxel cells. To obtain an inflow Mach number of 2.81, a particle velocity of 710 m/s and static pressure of 910 kPa

were assigned to start the solution process from the quiescent conditions in ambient air (γ_{air}=1.4, p_{amb}=101.325 kPa and T_{amb}=300 K)

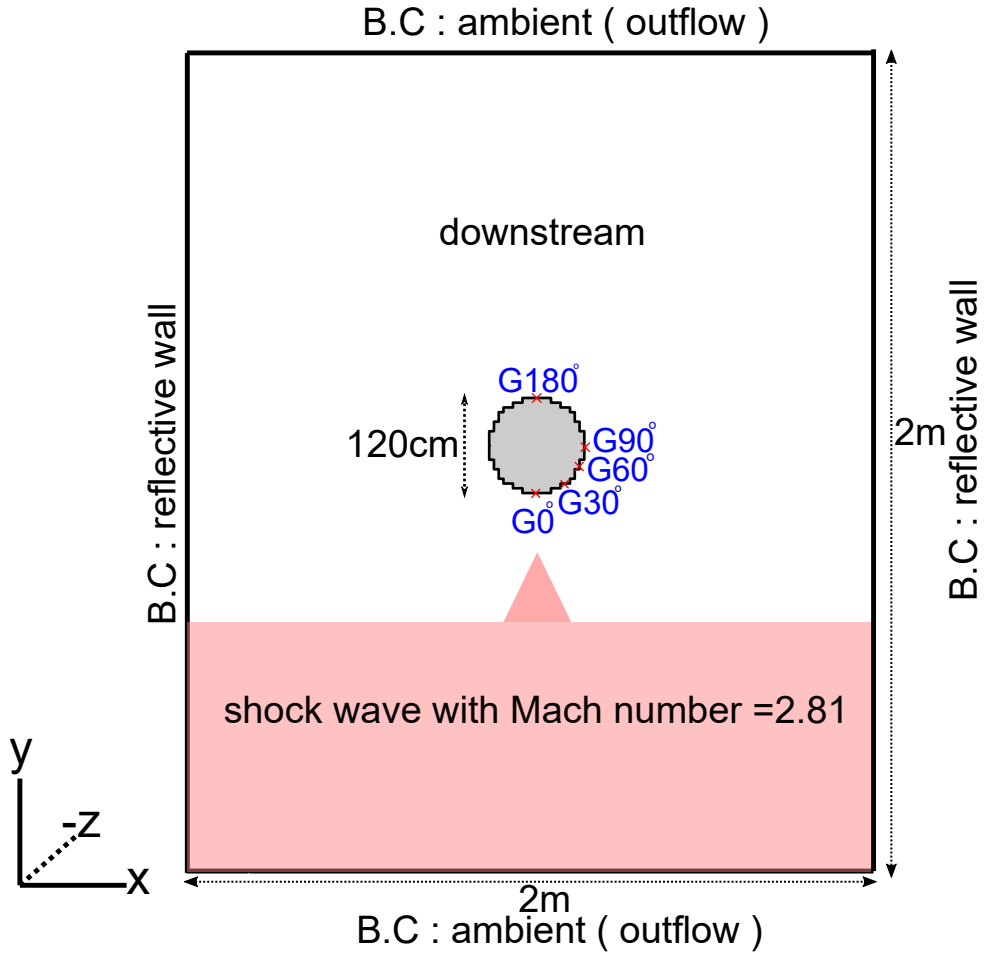

Figure 4.17: a plan of 3D full numerical domain of 2.81 Mach number shock tube simulation

Figure 4.18 shows the comparison of pressure traces at five gauge points, taken from angular positions along the lower half of the cylindrical surface. Although the pressure history at the 180° gauge in Apollo records a lower amplitude, the overall pressure profile closely matches with the numerical results of Yang et al. (1987). The mismatch at the rear stagnation point is quite likely to have risen from the disparity in the size of the cylinders, leading to different separation points along the rear portion of the cylinder.

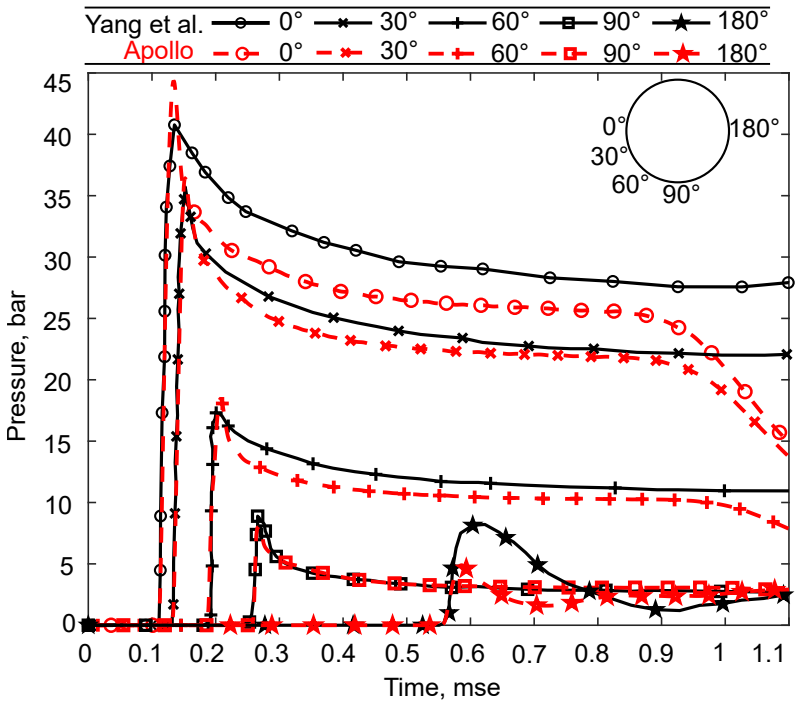

Figure 4.18: Comparison of pressure histories from Apollo CFD and Yang et al. (1987) experiments at 5 angular locations on the cylinder.

The numerical schlieren photos from Apollo were also compared against the experimental schlieren photos of Bryson & Gross (1961) to validate the mechanics of blast wave diffraction around the cylinder. Figure 4.19 shows comparisons for an early t_1 and late time t_2 interaction profile. At time t_1, the transition of regular reflection (RS) into Mach reflection (MS1), and the location of the triple point (TP1) connecting the Mach reflection to the incident shock (IS), have been captured fairly well by Apollo. At time t_2, the subsequent interactions of the Mach wave behind the cylinder involving a second Mach reflection (MS2), a second triple point (TP2), the generation of vortices (V), and the associated complex shock-shock interactions, all have been captured by Apollo in a satisfactory manner.

Overall, the diffraction effects on blast wave interaction with the cylinder have been captured successfully by Apollo software. This demonstrates the ability of the software to simulate wave interactions behind the cylindrical obstacle for ultimate cell sizes at least 10 times smaller than the cylinder radius.

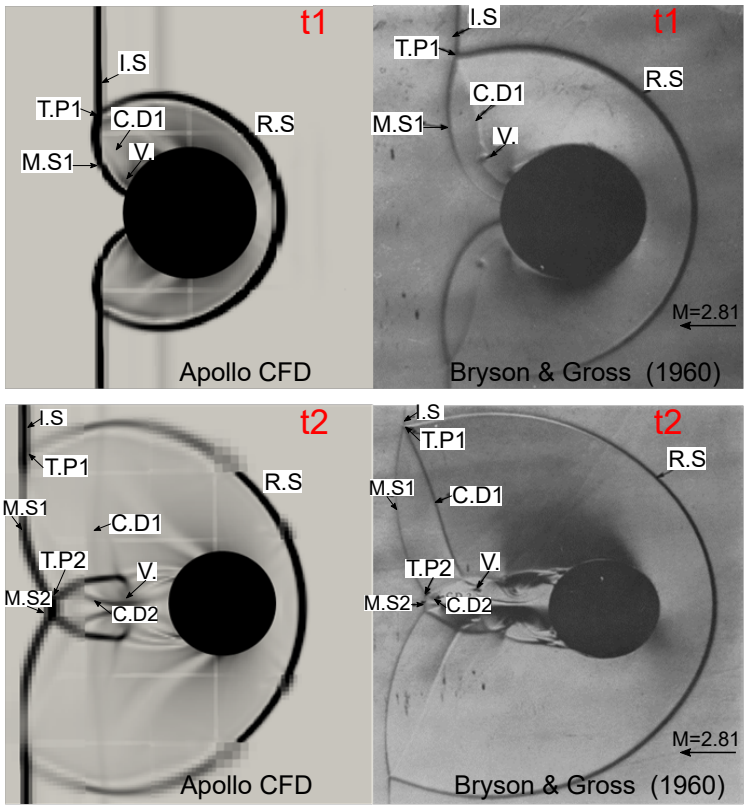

Figure 4.19: Comparison of schlieren snapshots from Apollo CFD and the experimental work of Bryson & Gross (1961) at two time instants. Flow is from right to left. The voxel shape of circular surface for CFD results is replaced with smooth circular surface sketch for better view

4.4 Summary and conclusion

This Chapter focused on describing the framework of CFD numerical modelling of simulating the blast wave propagation in various scenarios using CFD solver named Apollo in which its theoretical background considerations with the additional numerical solution features that improve computational efficiency were firstly mentioned.

The fidelity of Apollo solver in predicting blast loading of free-field scenario and also recreating complex blast wave-obstacle interactions were demonstrated using a detailed, multi-part mesh sensitivity analysis that involved both quantitative and qualitative com-

parisons with pre-fractal experimental data taken from Chapter 3 and special data from the literature.

The validation of blast wave-obstacle interactions included validating blast interaction with square geometry through pressure and specific impulse histories at select locations in the flow domain of pre-fractal iteration 3 arrangement with also qualitative comparison of the numerical shock front with time-resolved flow field images. Also, it included validating blast wave diffraction around voxel shape approximation of cylindrical obstacle in pre-fractal iteration 1 configuration using qualitative comparisons with numerical data from Yang et al. (1987) and experimental schlieren visualisation from Bryson & Gross (1961).

It was found that Apollo can highly capture the waves interference that is resulted from blast wave-obstacle interaction, and therefore be effectively able to predict the consequence blast loading mitigation within 10% error variation. Hence, Apollo CFD solver was chosen to perform the numerical modellings in the next two Chapters.

Chapter 5

Numerical analysis of blast mitigation of single obstacle

5.1 Introduction

As first step towards developing a comprehensive explorations of blast mitigation patterns of pre-fractal obstacles with increasing complexity such as pFI-2 & pFI-3 configurations, this Chapter first focuses on the interaction of blast wave with a single obstacle of pre-fractal iteration 1 and its role in mitigating blast load acting on shadowed structural rigid target. The standalone square rod obstacle, namely pFI-1 configuration, was seen in the pre-fractal experiment in Chapter 3 to produce some level of blast mitigation at downstream region with different blast intensities. However, in this Chapter, the square rod is replaced with cylindrical rod since it is a common, effective blast wave attenuator (Suzuki et al. 2000, Abe et al. 2001, Gebbeken & Döge 2010). This is because the diffraction wave tends to gradually load the rounded profile of a cylinder, and due to the cylinder's mitigation potential in its downstream region. Moreover, a circular cross section was found to have the highest ability to diffract rather than reflect the incoming blast wave (Shi et al. 2007, Williams & Williamson 2012, Rajkumar et al. 2020). This

leads to a more uniform variation of load across the cross-section, leading to a reduced total load on the obstacle itself (Gebbeken & Döge 2010).

This Chapter specifically aims to characterise behaviour and predict the blast loading mitigation occurred behind the cylindrical obstacle (pFI-1 arrangement) for protection purposes. Concerning the effect of the blast wave-obstacle interaction on the downstream flow after a blast wave impacts such an obstacle, it is vital to understand the diffraction/refraction phenomenon around the circular barrier.The phenomenon of diffraction of shock waves over a cylinder was first studied in the 1950s and a general theory of shock wave diffraction over finite objects was established by Whitham (1957, 1959). Subsequent research aimed to study the shock wave diffraction experimentally and analytically over the cylinder (Bryson & Gross 1961, Heilig 1969, Parkinson & Jandali 1970, Ben-Dor & Takayama 1985).

The process of wave diffraction around a circular geometry involves regular and irregular (Mach) reflection waves. Regular reflection starts when the shock wave encounters a stagnation point on the surface whereas a diffraction wave originates from points where the incident shock impinges on a non-normal surface. As the wave travels along the circular surface, the regular reflection configuration persists until the interaction angle of the wave with the surface decreases and reaches a certain limit, leading to a Mach reflection. Such a configuration gives rise to a new composite shock front called a Mach shock, comprising the reflected, Mach, and incident waves intersecting at a point called the triple point (Xiao et al. 2020*b*). As this wave progresses, at some point on the curved surface of the cylinder, the triple point separates and propagates further downstream. By this time, it is worth noting that two regions of flow exist: one processed by the incident wave, and the other processed by the reflected wave. Each region has its own mechanical and thermodynamic properties. A vortex now forms downstream owing to the difference in velocities (slipstream) above and below the locus of the triple point. Furthermore, as the unaffected portion of the incident wave propagates downstream, complex shock-

shock interactions are established because of the collision with the Mach waves at the rear stagnation point just behind the cylinder surface. All of these are responsible for modifying the blast wave in the downstream region.

It needs to be mentioned here that such modifications need not always result in attenuation. There exists the possibility of amplification occurring as well, and this was demonstrated experimentally for a shock wave interacting with cylindrical obstacles by Suzuki et al. (2000) and also by Abe et al. (2001). Moreover, this load amplification was also seen behind the square rod obstacle at the downstream sensors (S_4, S_6, and S_7) in experiment of blast wave interaction with pre-fractals in Chapter 3 (see Figure 3.19a&b). However, this numerical analysis in this Chapter focus only on the blast attenuation, especially in prediction part . To predict such a attenuated load behind a cylindrical obstacle, artificial neural network (ANN) methods can be used since they have successfully demonstrated the ability to estimate complex blast loads in scenarios such as a confined environment (Dennis et al. 2021), near-field blast loading (Pannell et al. 2022a,b, Holgado et al. 2022) and for a target protected by a solid wall (Bewick et al. 2011).

Therefore, a parametric study is required to explore the influences of the following factors on the mitigation behaviour of blast loads which were observed in experimental work in Chapter 3 and pointed out in subsection 3.5.4 :

(i) the size of the obstacle,

(ii) the blast wave intensity,

(iii) the position of the obstruction, and

(iv) the target length/size

As an aside, the findings from this parametric study will also aid in developing a successful ANN prediction approach of blast loading reduction. A primary blast load parameter is specific impulse, i which is quantified in the parametric study. This is because the blast

load duration, especially for near-field explosions, is expected to be considerably shorter than the period of vibration of the structure, which is therefore unlikely to be sensitive to the exact form of the pressure load, only its integral with respect to time, viz. specific impulse. The distribution of impulse across the face of the target is expected to be complex for close-in detonation scenarios. This non-uniformity is addressed by defining an energy-equivalent specific impulse (EEI) which imparts an identical kinetic energy to the object (Rigby et al. 2019) as the distributed load, and was shown to better correlate to structural response than the simple area-integral of specific impulse. Thus, in this Chapter, EEI, as defined in Eq. 5.1, has been utilised as a single-number metric to quantify loading on a given target area (A).

$$EEI = \sqrt{\left(\int_A \frac{(idA)^2}{dA} \right) A} \tag{5.1}$$

The outline of this Chapter, therefore, is as follows: the methodology section first explains in detail the setup of the numerical model using Apollo CFD solver. Then, the results and discussion section illustrates the consequences of shadowing and wave interference on blast loading parameters on the ground and on a target wall downstream of an obstacle. Finally, an ANN is developed to predict blast mitigation behind the cylinder, which is subsequently tested against a number of unseen examples. Finally, the ideas put forward in this work are then summarized and concluded.The primary content of this chapter was derived from the published paper titled: ***Mitigation of blast loading through blast–obstacle interaction***, as elucidated in Chapter 1 (refer to section 1.4).

5.2 Numerical Methodology

5.2.1 CFD data generation

Parameters: Blast wave interaction with a single obstacle depends on the properties of the blast wave and the geometry of the obstacle. However, due to the absence of specific pointers regarding this in the results of the experiment in Chapter 3 and also

in the literature, a global setup has been considered with four input parameters. The parameters are:

1. The mass of the explosive W_{TNT}
2. The scaled distance Z_R=$R/W^{1/3}$ that uses the total stand-off distance of the target R and the explosive of mass W.
3. The cylindrical pole diameter D.
4. The obstacle location ratio, given by d_0/R, where d_0 is the obstacle distance from the explosive.

Table 5.1 displays the input parameters in the numerical domains that were considered, sub-divided into 5 groups, A through E. These combinations have been carefully selected to cover a wide spread of blast wave properties such as overpressure, specific impulse, positive phase duration, and importantly, the shock wave velocity, which has a direct effect on the formation of vortices in the disturbed wake region (Niollet et al. 2015, Ritzel et al. 2018, Hahn et al. 2021). Group E has been included for comparing the effect of each of the cylinder sizes under consideration (in groups A-D) for a given blast wave intensity and obstruction ratio. This was intended to assist the ANN algorithm in learning the effect of each cylinder size on EEI mitigation. While these simulations (106 cases) give the EEI on the reflective wall target downstream of a cylindrical obstacle, the corresponding undisturbed free-field simulations (25 cases) were also performed in order to obtain the EEI mitigation ratio according to the following relation:

$$EEI_{ratio} = \frac{EEI_{pole}}{EEI_{free}} \tag{5.2}$$

To understand the interferences on the target due to the presence of the cylinder, it is also helpful to consider the flow evolution on the ground, in the vicinity of the cylinder. So first, CFD studies focusing on the ground plane downstream of the obstacle were undertaken

Table 5.1: A summary of the input configuration groups that were used for the simulations

Input configuration data					
Group	**A**	**B**	**C**	**D**	**E**
W_{TNT} (kg)	0.2	1	4	12	6
R (m)	4, 2.5, 2, 1.5, 1	6, 5, 3, 2, 1	8, 5, 3.5, 2, 1	7.5, 5, 3, 2, 1	2.7, 3, 3.1, 3.5, 3.9
D (cm)	24	20	16	12	12, 16, 20, 24
d_o/R	0.2, 0.35, 0.50, 0.65, 0.8	0.2, 0.35, 0.50, 0.65, 0.8	0.2, 0.35, 0.50, 0.65, 0.8	0.2, 0.35, 0.50, 0.65, 0.8	0.5

before proceeding to understand the impulse evolution on a target wall downstream.

5.2.1.1 Dataset for studies on the ground behind the obstacle

To study the effect of single obstacle the cylinder on the blast wave propagation downstream, four 3D numerical models were simulated using Apollo. A plan view of such a simulation is shown in Fig. 5.1 and the input variables for the simulations are given in Table 5.2. Cylinders of two diameters (12 cm and 24 cm) that were sufficiently tall in the Z-direction were considered. Each was exposed to a medium intensity (Z_{do}=1.04 m/kg$^{1/3}$, Mach number = 3.5) and a high intensity blast wave (Z_{do}=0.44 m/kg$^{1/3}$, Mach number= 7.3) to clarify the role played by the particle velocity on the development of the wave interference pattern and its consequences on blast loading. The explosive used here is Trinitrotoluene (TNT) and the detonation modelling of a high explosive (HE) is based on the Chapman-Jouget model with Jones-Wilkins-Lee (JWL) model for the products of reaction. As baseline markers, two simulations without obstacles were run to compute the free field peak overpressure and specific impulse values.

The downstream domain (Fig. 5.1) was chosen to be a slightly over 10 pole diameters ($10D$) long as this is the length it takes for the wave interference effects to cease (Christiansen & Bogosian 2012, Hahn et al. 2021). The additional length beyond $10D$ is necessary to prevent spurious reflections from arriving at the gauge location during the positive phase. Mesh elements of size 6.25 mm were used for this simulation which satisfied the requirement of obstacle-cell ratio to be 10 or more for smallest cylinder radius (here is

Table 5.2: A summary of the input conditions for the free-stream simulations in Fig. 5.1

Model	3D domain size	Cylinder size	Explosive size	Obstacle distance	Obstacle scaled distance
	X × Y ×Z (m)	D (cm)	W (kg)	d_0 (m)	Z_{d0} (m/kg$^{1/3}$)
1	3 × 3 × 3	12	1	1	1.04
2	3.5 × 4.5 × 3.5	12	6	1	0.44
3	4 × 5 × 4	24	1	1	1.04
4	4 × 6 × 4	24	6	1	0.44

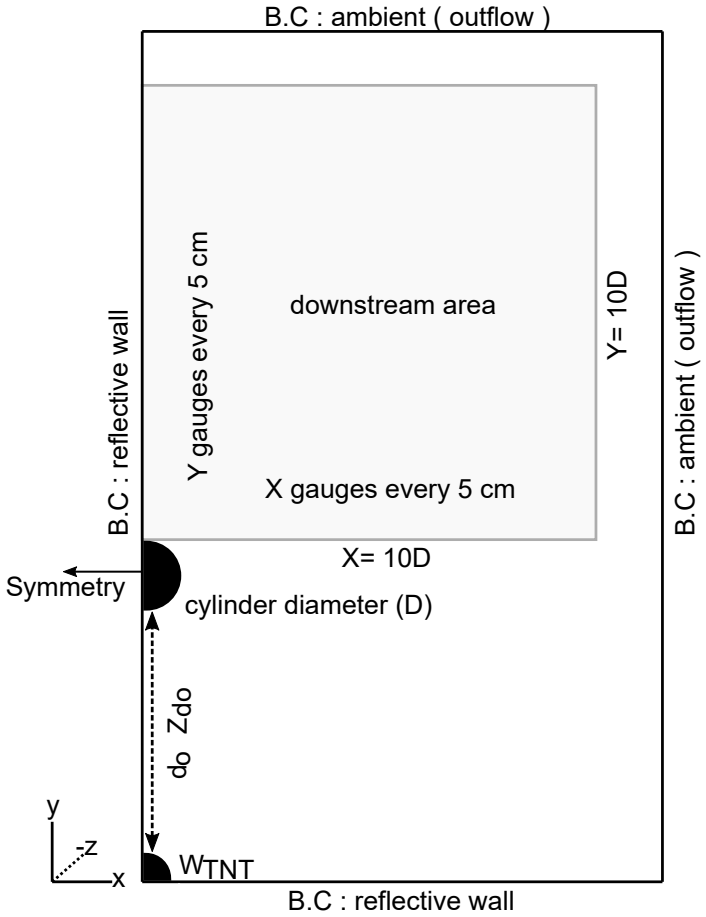

Figure 5.1: A schematic plan view illustrating the setup of 3D symmetric model for a study of the downstream effects of blast interaction with a tall cylindrical pole.

60mm). The stages feature in Apollo was used to enable solution mapping from 1D to 3D to reduce the computational load and CPU time. The 1D stage was terminated at a distance of 0.90 m from the detonation centre, which is just before the impingement of the wave onto the cylindrical surface. Then, the numerical solution was mapped into a 3D model to proceed with the simulation of the diffraction around the cylinder. An array of

gauges was positioned on the ground, spaced 5 cm apart along both X and Y directions. The following ratios were then obtained from the simulations:

$$P_{ratio} = \frac{P_{pole}}{P_{free}} \;\&\; I_{ratio} = \frac{I_{pole}}{I_{free}} \tag{5.3}$$

Here, the subscripts 'pole' and 'free' relate to the obstructed and non-obstructed model results, and P and I refer to pressure and impulse.

5.2.1.2 Dataset for studies on the target plane

For the simulations on the target plan, EEI ratios were to be calculated for the input conditions in Table 5.1. But then, since the location of the obstacle plays an important role in the interaction process, the total stand-off distance R has been split in terms of the distances from the charge to the obstacle d_o, and from the obstacle to the target d_t respectively. To avoid working with two parameters, the obstacle location ratio d_o/R is being used, as it can account for the position of the obstacle in the domain. The blast intensity is captured by the obstacle scaled distance Z_{do} ($d_o/W^{1/3}$). This accounts for different aspects of wave diffraction such as the inclination of the shock-shock path, and also the strength of the vortices and the reflected wave. The target distance d_t is being used as a measure of the reattachment distance of the disrupted waves in the downstream. The EEI is then computed based on reflected specific impulse values acting on the reflective rigid target. This evaluation was carried out over 5 different target lengths, TL, as illustrated in Fig. 5.2. For simplicity, the wall height has been fixed at 1 m since the interest is in understanding the wave disruption along the width and not the height. With the inclusion of these additional parameters, Table 5.1 was slightly emended, and the final input dataset used for the simulations may be found in Table 5.3

Table 5.3: A layout showing the simulation configurations under each group for the simulations of Fig. 5.2.

Group		A	B	C	D	E
Z_{do} (m/kg$^{1/3}$)	max min	5.472 0.342	4.8 0.2	4.03 0.126	2.621 0.087	0.825
d_t (m)	max min	3.2 0.3	4.8 0.35	6.4 0.2	6 0.2	2.4 1.2
TL (m)		1, 0.75, 0.50, 0.25, 0.1	1, 0.75, 0.50, 0.25, 0.1	1, 0.75, 0.50, 0.25, 0.1	1, 0.75, 0.50, 0.25, 0.1	1, 0.75, 0.50, 0.25, 0.1
Sample Counts		24	24	25	25	8
Total		530 data points				

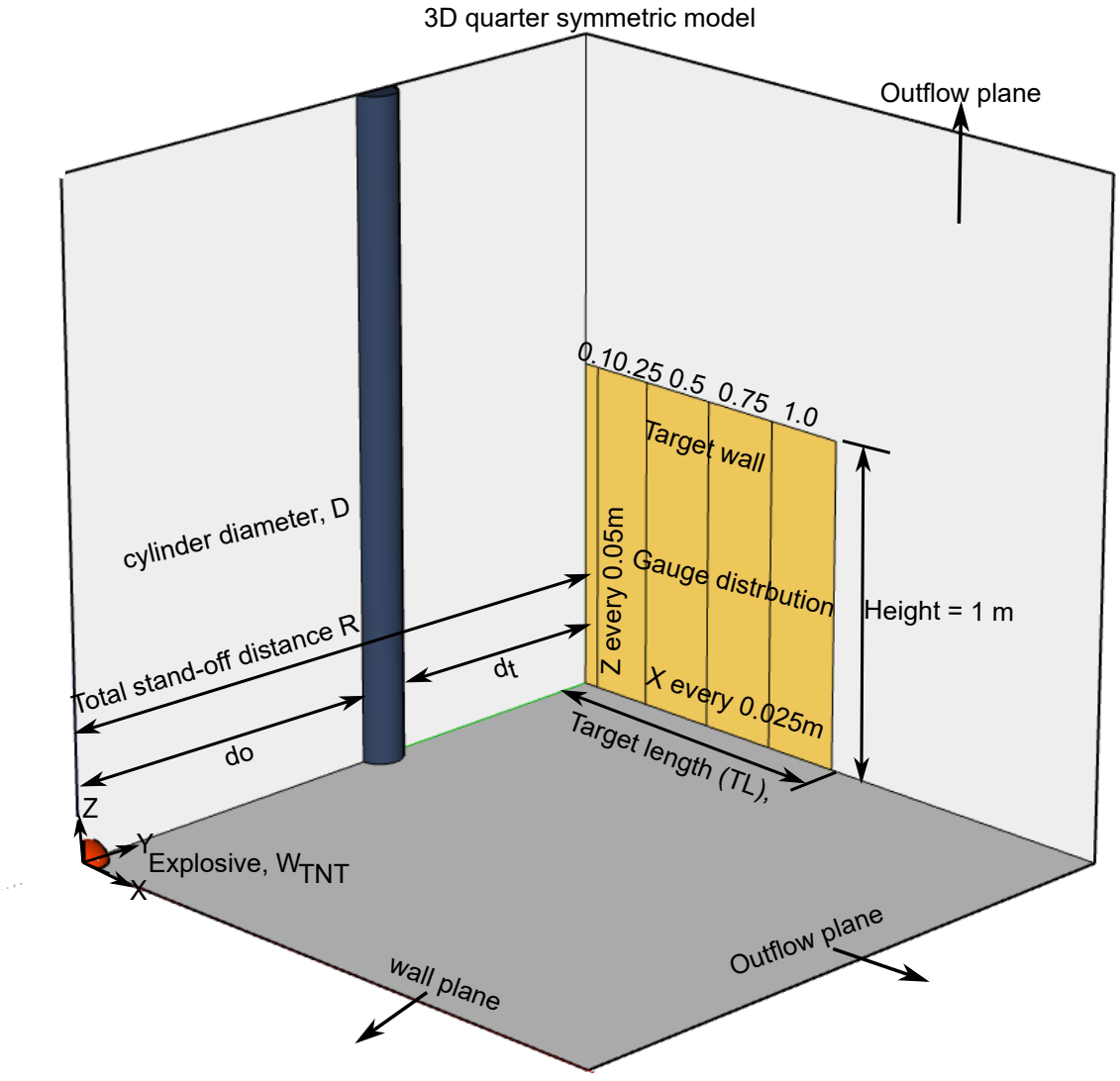

Figure 5.2: A perspective drawing illustrating the 3D CFD domain that was set up to study the role of the indicated parameters on the propagation of an obstructed blast wave

A typical 3D domain for these 106 models (plus 25 free-field models) has been illustrated in Fig. 5.2. The extents of the simulation domain are set up according to the total stand-off distance in each group to prevent artificial reflections from the outflow boundary disturbing the flow evolution inside. The target wall was $R+1$ m tall, and 861 gauges were distributed across the target area TA, as highlighted in Fig. 5.2. The distance between gauges was 25 mm along the X-axis and 50 mm along Z-axis, as this was found to be sufficient to pick up the essence of the variation of the specific impulse on the wall. The cylindrical obstacle was as tall as the domain to eliminate diffraction from the top, and to ensure that the diffraction occurs only along the curved surface of the cylinder. The detonation modelling of TNT explosive in Fig. 5.2 was based on on the Chapman-Jouget model and the products of reaction was based on with Jones-Wilkins-Lee (JWL) model.

The numerical solution was completed in two stages. First, a 1D stage with a fine mesh to ensure proper initiation of detonation and accurate wave tracking until the blast wave approaches the obstacle. This was then remapped to a 3D model. The cell size was 6.25 mm for all datasets which achieved the required obstacle-cell ratio to be more than 10 for smallest cylinder radius (60 mm in Table 5.1).

5.3 Results and Discussion

5.3.1 The influence of wave interference on the ground

In this subsection, a description of the flow on the ground, downstream of the single cylinder is presented. A contour plot of the pressure and impulse ratios (Eqn. 5.3) on the ground, downstream of these cylinders has been shown in Figs. 5.3 & 5.4. The spatial co-ordinates for these plots were normalized using the cylinder diameter.

From Fig. 5.3, one may gather that the evolution of the pressure field depends primarily on blast wave intensity measured in terms of the Hopkinson scaled distance, or the Mach number. It is also influenced by the cylinder size which modifies a given pattern of

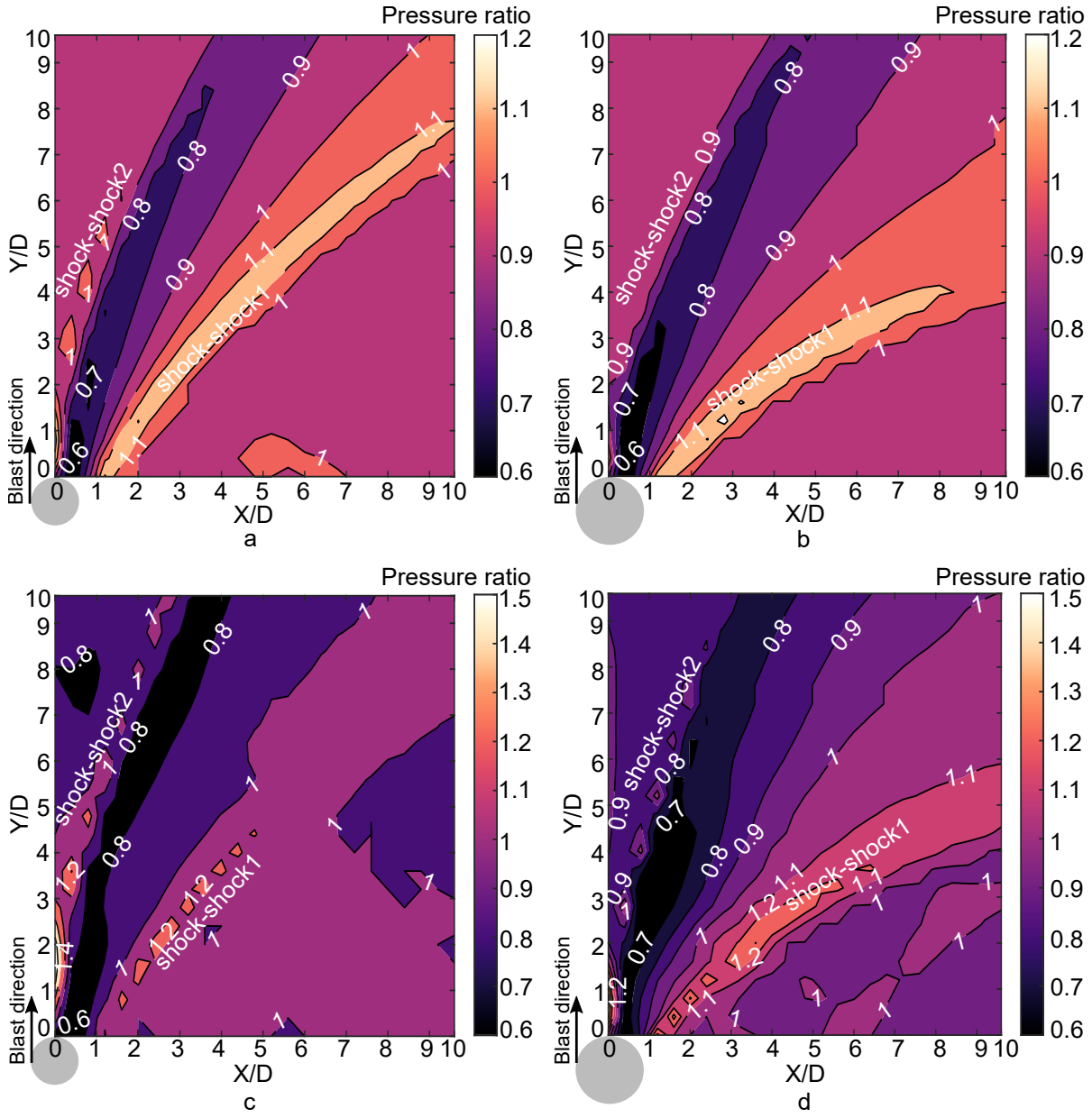

Figure 5.3: A contour plot of the Apollo simulation results showing peak overpressure ratio in the downstream region of a cylindrical obstacle. The origin of the plot is the farthest downstream point on the cylinder. The simulation parameters for these plots were
(a): Z_{do}= 1.04 m/kg$^{1/3}$, M= 3.5, D= 12 cm, (b): Z_{do}= 1.04 m/kg$^{1/3}$, M= 3.5, D= 24 cm,
(c): Z_{do}= 0.44 m/kg$^{1/3}$, M= 7.3, D= 12 cm, (d): Z_{do} = 0.44 m/kg$^{1/3}$, M= 7.3, D= 24 cm.

the diffracted wave. The shock-shock path, also known as the triple point locus that is associated with the pressure rise (Yang et al. 1987, Hahn et al. 2021), is visible here and has been annotated in the figure. As is clear from the figure, this path separates the downstream flow field into distinct zones of amplification and mitigation. Another observation is that the wave interference region extends beyond $10D$, which is consistent with the findings of Hahn et al. (2021).

Intense explosions, characterized by a higher Mach number and a faster shock speed, lead to a more complex wave interaction behind the single cylinder as is evident from the contour plot of the impulse ratios in Fig. 5.4. This serves to improve the mitigation ratio and extend the mitigation region behind the single obstacle, as seen in Figs. 5.4 c–d. This improvement may be attributed to the enhanced vorticity generation at higher particle speeds, resulting in diminishing directional flow velocities. This reduces the kinetic energy, which in turn affects the dynamic pressure, resulting in a pressure amelioration overall. An increase in cylinder size can also extend the wave interference region, resulting in a reduction in specific impulse values over a wider region behind the cylinder.

A plot of the the flow streamlines to help visualize vortices for these configurations has been given in Fig. 5.5. The drastic differences in these flow paths reinforce the view that particle speeds play a significant role in determining the attenuation and the overall wave interaction pattern behind the single obstacle.

5.3.2 The influence of wave interference on a reflective wall target

The interaction of a blast wave with a single obstacle results in altered EEI ratios on the wall. These values are useful to identify the zones of mitigation and amplification, which are influenced by the shadowing and interference patterns of the flow-obstacle interaction. To present the results on the wall, since there were 106 different simulations, a scatter plot involving all the EEI ratios is first presented. The EEI ratios for all pertinent parameters

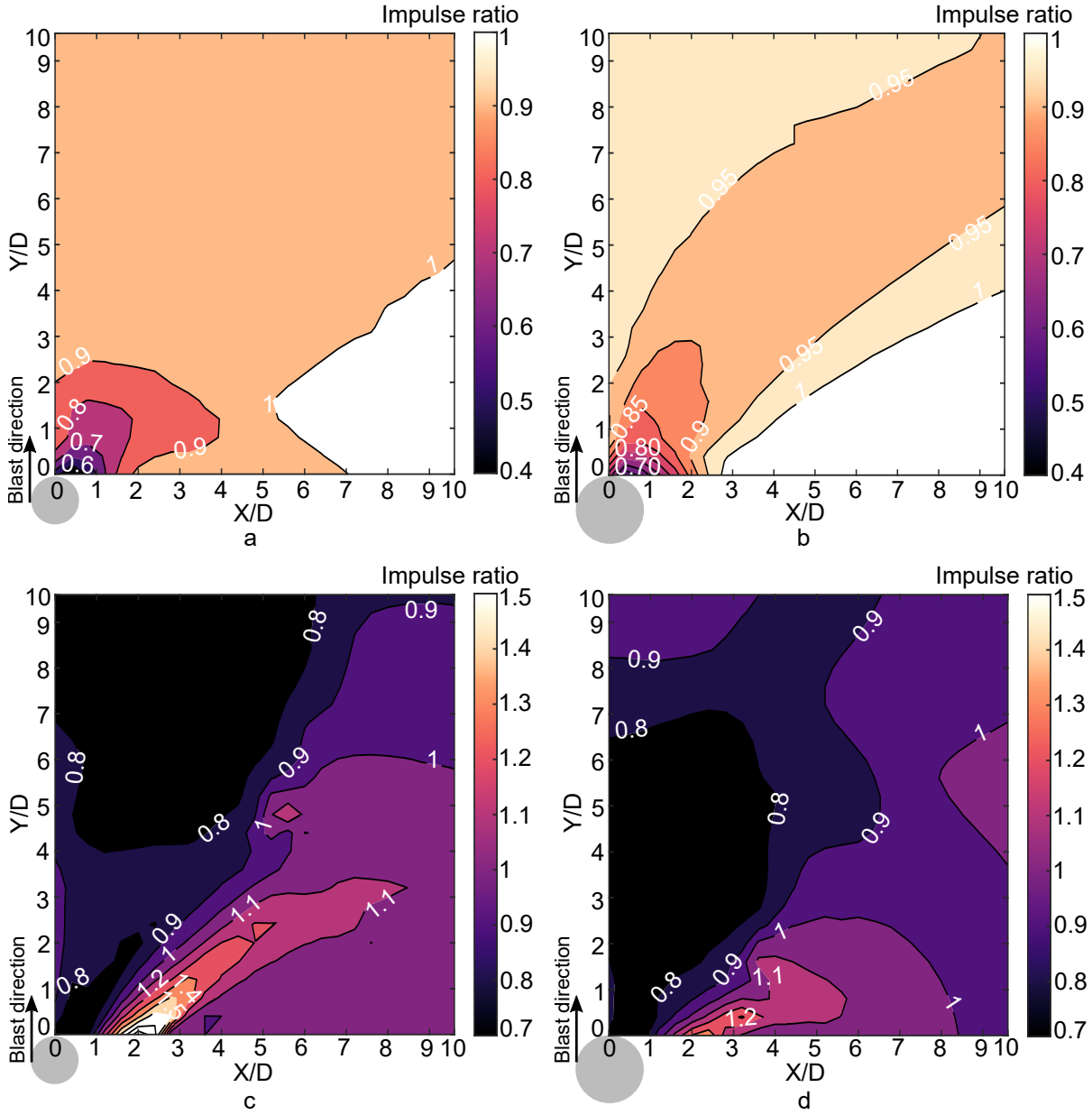

Figure 5.4: A contour plot of the Apollo simulation results showing peak specific impulse ratio in the downstream region of a cylindrical obstacle. The simulation parameters were (a): Z_{do}= 1.04 m/kg$^{1/3}$, M= 3.5, D= 12 cm, (b): Z_{do}= 1.04 m/kg$^{1/3}$, M= 3.5, D= 24 cm, (c): Z_{do}= 0.44 m/kg$^{1/3}$, M= 7.3, D= 12 cm, (d): Z_{do} = 0.44 m/kg$^{1/3}$, M= 7.3, D= 24 cm.

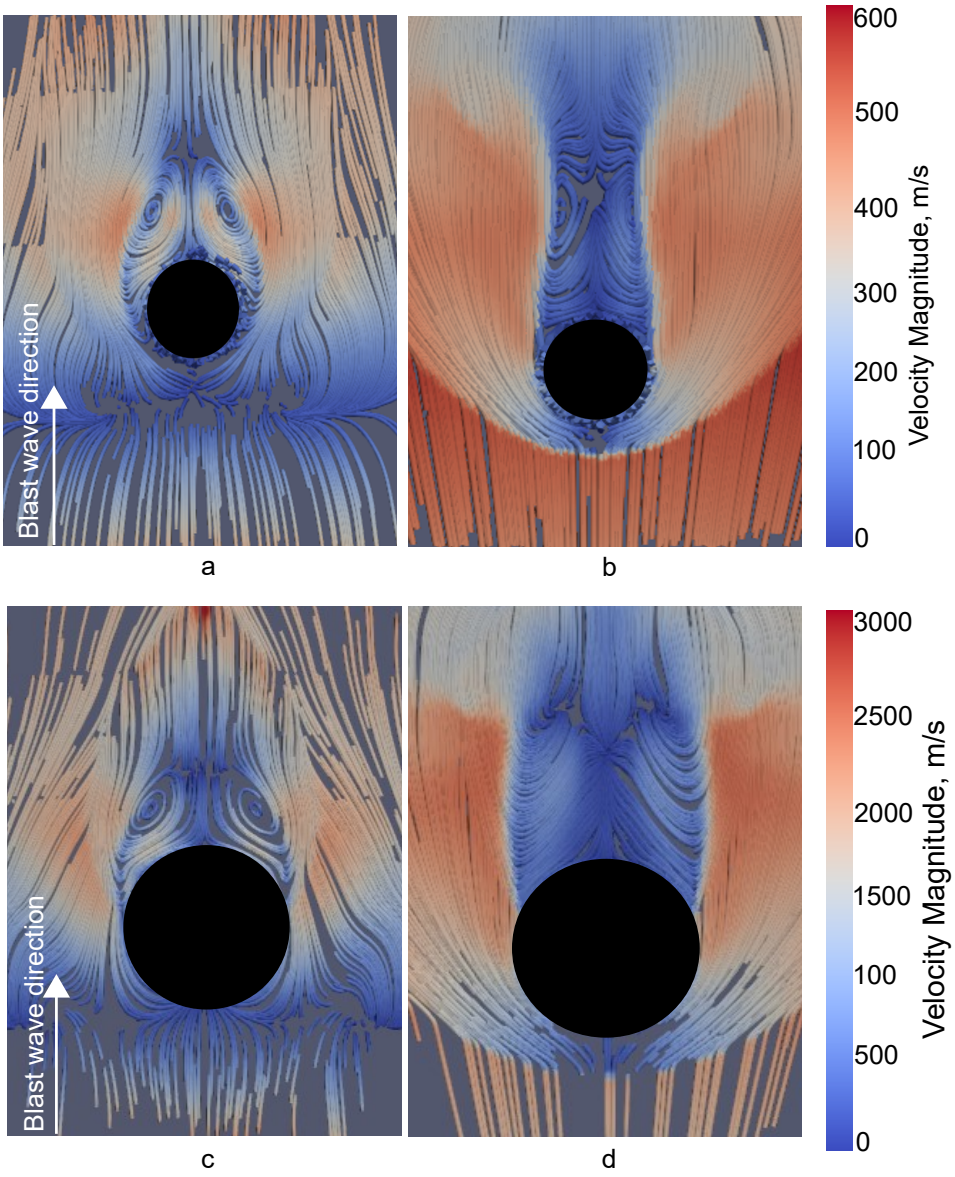

Figure 5.5: Contours of the streamlines showing the velocity magnitude for (a): Z_{do}= 1.04 m/kg$^{1/3}$, M= 3.5, D= 12 cm, (b): Z_{do}= 1.04 m/kg$^{1/3}$, M= 3.5, D= 24 cm, (c): Z_{do}= 0.44 m/kg$^{1/3}$, M= 7.3, D= 12 cm, (d): Z_{do} = 0.44 m/kg$^{1/3}$, M= 7.3, D= 24 cm.

including the cylinder diameter, the target distances, and the target length have first been collected and plotted as a function of obstacle scaled distance in Fig. 5.6.

From these plots, it appears that the effective mitigation mainly depends on obstacle scaled distance and cylinder size. Significant EEI reduction ranging from 50% to 20% was obtained for near-field denotations with larger obstacle sizes. This reduction though, is highly reliant on the target distance behind the obstacle. For example, consider target

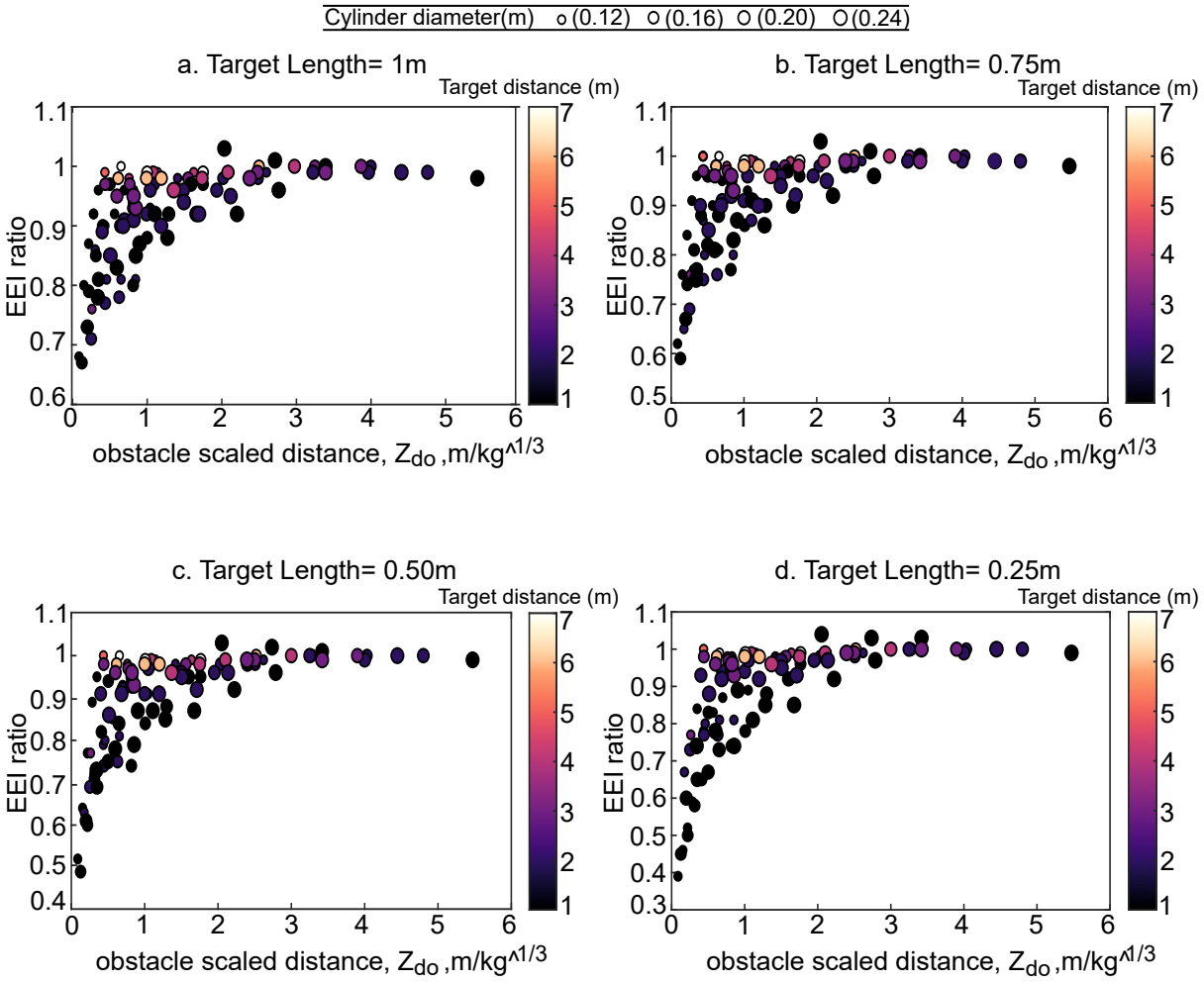

Figure 5.6: A scatter plot of EEI ratio as a function of obstacle scaled distance Z_{do} for cylinder diameters of 12, 16, 20 and 24 cm. These EEI ratios have been computed over target lengths of (a) 1 m, (b) 0.75 m, (c) 0.5 m and (d) 0.25 m.

distances d_t less than a metre: for cylinder diameters of 12 cm, 16 cm, 20 cm, and 24 cm, a no-mitigation limit (EEI = 1) is reached at obstacle scaled distances Z_{do}=1 m/kg$^{1/3}$, 1.5 m/kg$^{1/3}$, 1.6 m/kg$^{1/3}$, and 1.7 m/kg$^{1/3}$ respectively. This means that for closer stand-off distances ($<$ 1 m/kg$^{1/3}$), a cylinder with larger diameter is required to achieve good attenuation with more than 35% by disrupting the flow-field downstream. So in addition to the others, the distance to target measure d_t is a significant parameter as it regulates the wave detachment process (Christiansen & Bogosian 2012, Dey et al. 2020, Hahn et al. 2021).

To enable a closer look at the relationship amongst the variables d_t, Z_{do}, TL, and EEI, a representative scatter plot was then employed.

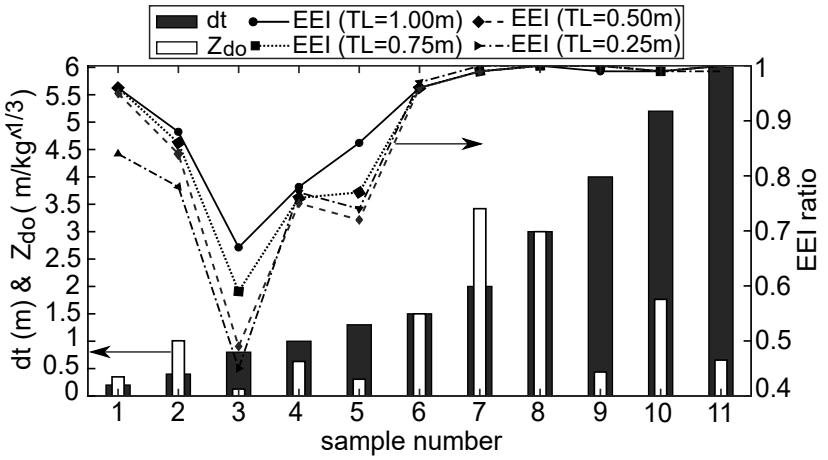

Figure 5.7: A plot showing the effect of TL, d_t and Z_{do} on the EEI ratios. To reduce the clutter, only data from 11 simulations were chosen to demonstrate the general trend.

EEI data for 11 out of the 106 CFD runs were carefully selected to illustrate the interplay amongst these factors as shown in Fig. 5.7. From this plot, the following may be gathered:

- An increase in the target distance (height of dark shaded bar) can lead to reduced mitigation effectiveness (> 0.9), irrespective of the target length used to calculate EEI ratios

- An inverse relationship exists between the target distance and mitigation, but this is linked to the obstacle scaled distance for all target lengths regardless of the cylinder radius.

- For closer targets ($d_t < 0.4$ m), the mitigation is localized over a small area just behind the pole (TL ~ 0.25 m) and it becomes less-significant on considering a wider area.

- Amplification can occur due to wave trapping, especially for the large cylinders placed close to the target. For instance, a 24 cm diameter cylinder for Z_{do}= 2.05 m/kg$^{1/3}$ and $d_t = 0.3$ m reported EEI ratios of 1.03 and 1.04 for target lengths

of 1 m and 0.25 m respectively due to wave trapping.

- For near-field events (height of lighter bars), mitigation is high (20% to 50%) for 0.5 m $\leqslant d_t <$ 2 m, which may be interpreted as the required length for the wave cancellation to occur.

To highlight a few observations not explicitly clear in Fig. 5.7, an exponential curve fit of certain data points has been presented in Fig.5.8. The d_t dependence was not explicitly considered while generating these fits. These fits were formulated using the most effective mitigation cases, regardless of the influence of target distance. The plots suggest that increased mitigation occurs when the obstacle is closer to the explosive i.e., closer obstacle scaled distance. This mitigation also increases with cylinder size, and with shrinking target area.

For narrow target lengths such as $TL = 0.25$ m, the effect of cylinder size on mitigation is inconsistent. For example, in Fig.5.8d, with obstacle scaled distances varying from 0.3–1.1 m/kg$^{1/3}$, the cylinders with diameter of 16 and 20 cm lead to higher attenuation than a pole with 24 cm diameter. This could be due to the complex combination of shadowing (attenuation) and interference (amplification) effects arising from the cylinder-wave interaction. The effect of such a disruption on the downstream reflective target is different across the width of the target. Some regions can be shadow zones, others can be interference zones, or even a mixture of both. A few areas can remain undisturbed as well, especially when the target is far enough for the wave to reform. Figs.5.9a-d illustrate this using peak specific impulse ratio (I_{pole}/I_{free}) plots on the reflective target wall ($TL = 1$ m) for 4 simulations.

The plots show that whilst mitigation is relatively low ($< 5\%$) in the shadowing region, it is slightly higher in the interference region. It reaches reductions of 7% for 12 cm diameter case, 9% for 16 cm, 12% for 20 cm and 14% for 24 cm. The interference region in Fig. 5.9 also widens as the obstacle size increases because the trajectory of the shock-shock paths

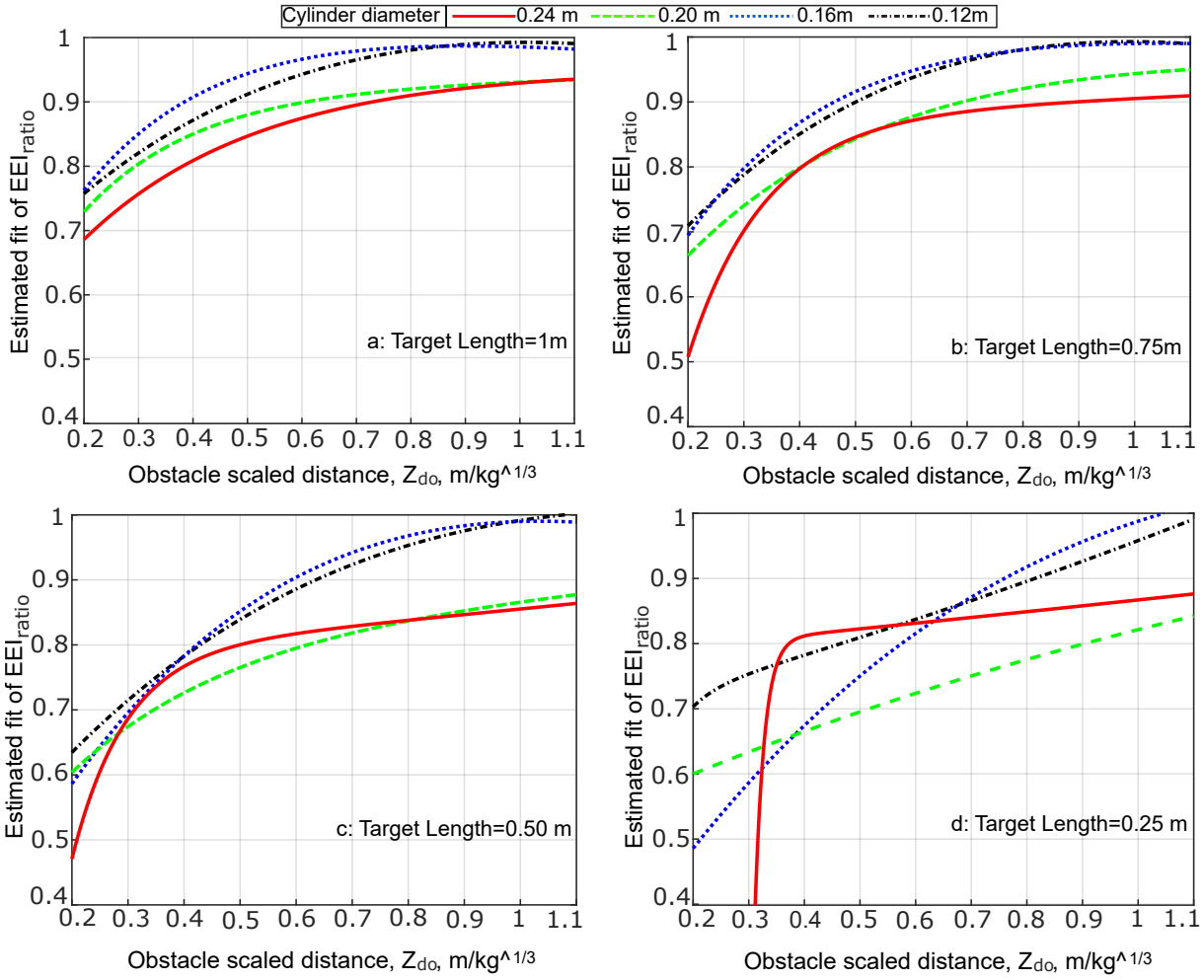

Figure 5.8: The trends of most effective EEI ratios for different cylinders, and for target lengths *TL*: (a) 1 m, (b) 0.75 m, (c) 0.50 m, and (d) 0.25 m.

described previously depends on the cylinder dimension (Bryson & Gross 1961, Heilig 1969). Now, from the target plane, gauge points were picked from the shadow region (G1) and the interference region (G2) as shown in Figs.5.9a-d. At these locations, the impulse and overpressure traces for different diameters are presented in Figs.5.10a-d. These plots show that in the shadowing region (Figs.5.10a,c) the arrival times are only slightly delayed, resulting in a non-significant reduction in the overpressure and impulse magnitudes. However, in the interference region (Figs.5.10b,d), a significant reduction in the peak overpressure and a change in the pressure decay pattern is obvious, which in turn leads to a reduction in the specific impulse.

Therefore, for improved attenuation and protection from blast threats using single ob-

stacle, large sized obstacles are recommended for interrupting the incoming blast wave. All these findings make it quite clear that the wave disruption depends strongly on the incoming blast wave intensity, the obstacle size, the target distance, and the width of the target. Inputs from these general mitigation trends were then used to develop a method to predict EEI mitigation on a target wall.

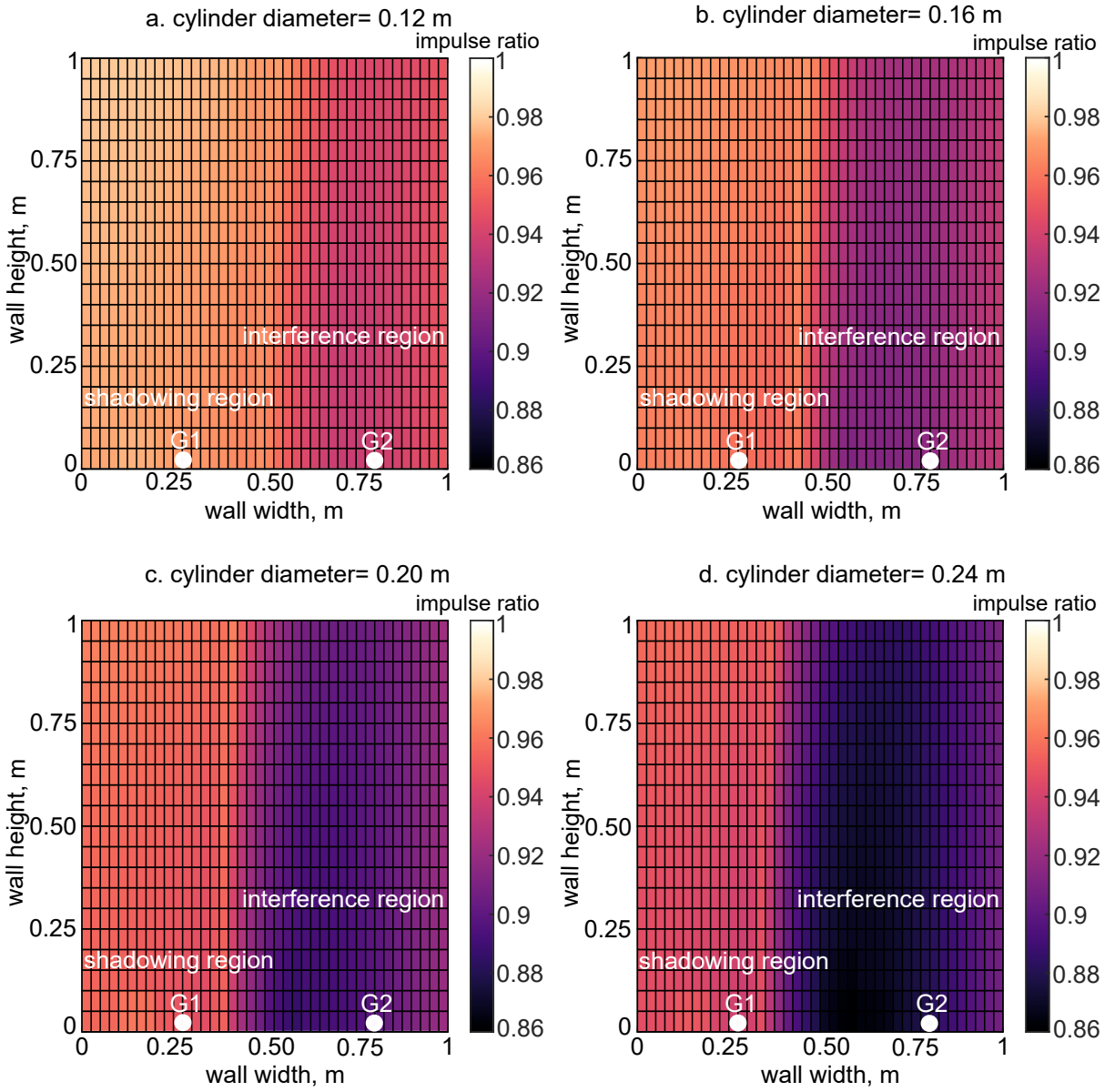

Figure 5.9: Pseudocolour plots of impulse ratio for Z_{do}=0.825 m/kg$^{1/3}$ and d_t= 1.5 m on reflective target for different pole diameters: (a) 12 cm, (b) 16 cm, (c) 20 cm, and (d) 24 cm.

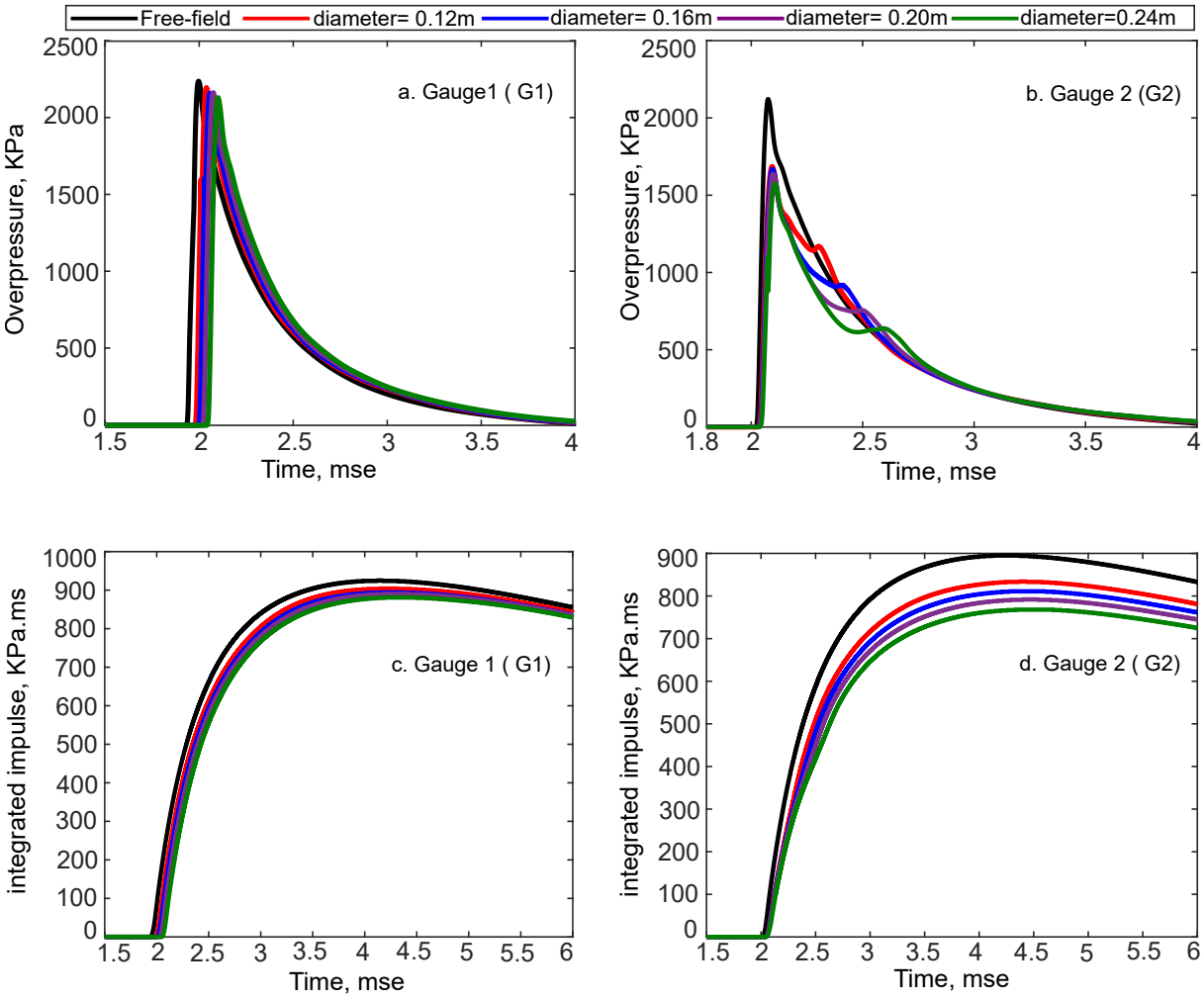

Figure 5.10: The overpressure and specific impulse traces at gauge 1 (shadowing region) and gauge 2 (interference region) for cylinders of different diameters.

5.4 Prediction using Artificial Neural Networks (ANNs)

5.4.1 The concept of artificial neural networks (ANNs)

Development of a fast-running tool to predict blast load mitigation (reduction in EEI) on a target wall behind the single obstacle of the cylinder is one of the primary aims of this Chapter. Having previously identified the parameters which influence the evolution of loading on a target wall, the next step is to use these findings to inform the design of an efficient and accurate engineering tool.

Artificial neural networks (ANNs) are a biologically-motivated computer code, which

operate in a manner similar to the way the human brain processes knowledge. ANNs gain their knowledge by identifying the patterns and relationships in input data and learn through understanding, not from a sequence programming. An ANN is constructed from multiple individual units, artificial neurons, with interconnected nodes connected with coefficients (weights and biases), and are arranged in layers. The behaviour of a neural network is governed by the transfer functions of its neurons, by the learning rule, and by the network architecture. The weights are adjustable through optimisation algorithms such as gradient descent and thus, a neural network is an adaptation system. The weighted summation of inputs into a given node can, if the signal is deemed strong enough, activate that node, which then propagates that signal onwards through the network. Throughout training, the weights and biases of the interconnected nodes are optimised to minimise the prediction error until the network reaches the required level of precision. After the network is successfully trained and is deemed satisfactory through subsequent testing, new 'unseen' data can be input and the network can forecast its output.

5.4.2 Validation of the scaled factors

The parameters d_0, D, d_t, TL, and W_{TNT} were identified as significant contributors to the evolution of the load on the target wall, and were grouped together in terms of scaled parameters to develop a tractable model. Prior to developing a prediction tool using these scaled parameters, it is vital to validate the ability of these scaled parameters to produce identical EEI ratios for various combinations of the physical values. Two simulations were then performed, for specific input values, chosen by design, to verify scalability (Table 5.4).

For these simulations, to accommodate the different stand-off distances, the extents of the numerical domain were different; 2×2×2 m and 3×4×3 m. This should not affect the outcome of the simulations, as the extents were chosen to minimize artificial wave interference from the boundaries. The respective EEI ratios were found to be 0.968 and 0.961, indicating the adequacy of the employed scaling parameters.

Table 5.4: The hand-picked values of physical parameters that were used for Apollo simulations to verify the validity of the scaled parameters.

Physical parameters						
No.	W_{TNT} (kg)	d_o (m)	Diameter D (m)	d_t (m)	TL (m)	TA (m^2)
1	1	0.12	1	1	1	1
2	8	0.24	2	2	2	4
Scaled parameters						
No.	Z_{do}= $d_o/W^{1/3}$		d_t/D	TL/d_t		TA/$W^{2/3}$
1	1		8.3	1		1
2	1		8.3	1		1

The relevance of each of these identified scaling parameters has been briefly described below:

- *Obstacle scaled distance,* Z_{do}: This plays an important role in the evolution of the diffraction pattern and it indicates the incident blast intensity,
- *Relative target distance to cylinder's diameter,* d_t/D: This characterizes the wave detachment and relieving effect downstream of the obstacle,
- *Solid angle of impingement,* TL/d_t: This value has direct association to EEI calculation for different target lengths, and
- *Scaled target area,* $TA/W^{2/3}$: This compares the EEI of free-field scenarios to the obstructed scenarios.

For different combinations of these parameters, 530 data points were obtained using Apollo to train the ANN model. These EEI data were scaled using Eq. 5.3 and the ratios higher than 1 that signify intensification were excluded by replacing them with unity. This was done to isolate cases which do not have any mitigation potential.

5.4.3 Feedforward Network Architecture

The development of a feedforward neural network is described in this section. This network has one hidden layer of *tan-sigmoid* neurons, followed by an output layer of linear

neurons. The use of several layers of neurons with a nonlinear activation function permits the network to learn both linear and non-linear relations between predictors and target vectors. A schematic drawing of the functional approximation of ANNs is provided in Fig. 5.11. The input layer is connected to a single hidden layer, typically known as a shallow neural network.

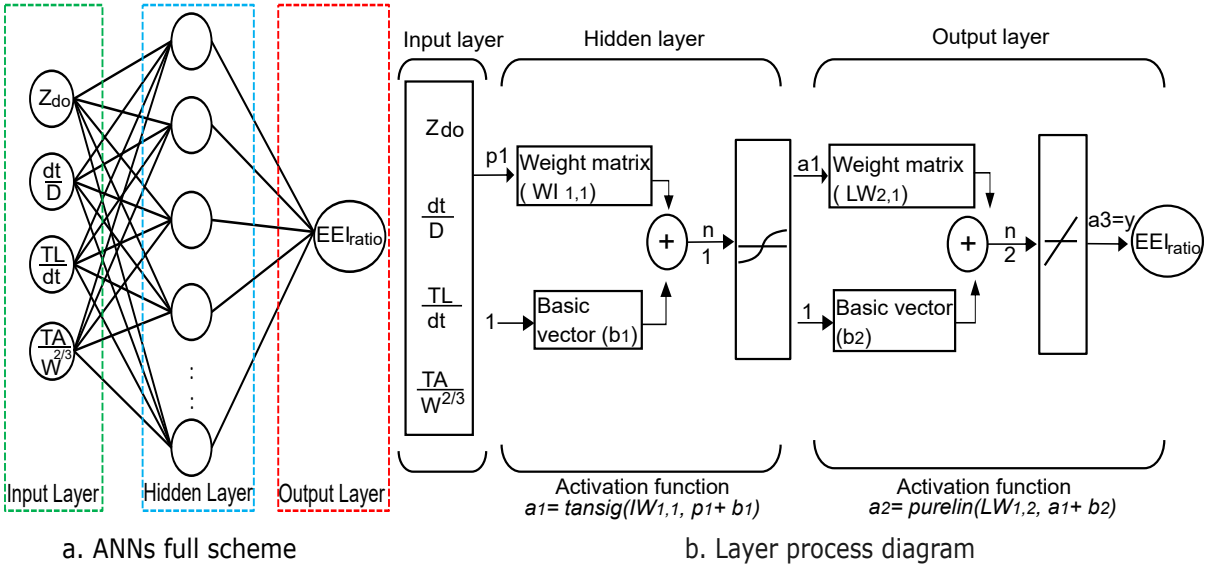

Figure 5.11: A chart showing the ANN architecture (a): the layout, (b): the layer processes.

Before training, the input parameters were pre-processed to constrain the values within [-1 1] (often termed 'min-max scaling') using MATLAB's inbuilt function `premnmx`. This function was also used to scale the target EEI values, which were then stored in matrix $p1$. Weights and biases were automatically initialized and stored in matrix W and vector $b1$. Upon initiating the network training, the weights multiplied by the normalized inputs are added to the bias values as depicted in Fig. 5.11 and are transferred by a tan-sigmoid function (equivalent to $tanh$) to a vector $a1$. A similar process is repeated on $a1$ and this is then transferred by a linear function (`purelin`) to the scaled output vector $a3$. Converting this back to absolute values gives the (attenuation) output vector y. Thereafter, this function approximation (nonlinear regression) is repeated by modifying the weights and biases of the network to minimize the network performance (mean square error, MSE). This minimization is carried out according to the gradient of the evolution of the out-

put values in a process termed back-propagation, which entails performing computations backward across the network. The easiest execution of back-propagation learning updates the network weights and biases in the direction where the performance function falls most rapidly, i.e. the negative of the gradient. An example of one such iteration may be written as:

$$x_{k+1} = x_k + \alpha_k g_k, \tag{5.4}$$

where x_k is a vector of current weights and biases, α_k is the learning rate, and g_k is the current gradient.

However, this simple form of back-propagation training algorithm, such as gradient descent, can be sluggish for functional problems and requires more computational effort and time. Therefore, the fastest training algorithm (Beale et al. 2010), Levenberg-Marquardt (LM), has been adopted here as it can approach second-order speed without involving extensive computational effort.

Besides employing the LM algorithm for training the network, an automated regularization method using a Bayesian framework is implemented in a combination algorithm called `'trainbr'`, an inbuilt MATLAB code which can effectively eliminate outliers and sift through noisy data without overfitting. This also eliminates the lengthy cross-validation step that would require the use of a larger training dataset. For further details the Bayesian regularization method, the interested reader may refer to the work of Burden & Winkler (2008). Details on using Bayesian regularization along with the Levenberg-Marquardt training procedure may be found in Foresee & Hagan (1997).

The activation function has a wide impact on the performance of the network as it describes the transformation of the weighted sum of the inputs to the output. While it is common for all the hidden layers to have the same activation function, in this case, due to the non-linearity of the input patterns, a hyperbolic tangent sigmoid function has been chosen ($\sim$ *tanh*) to allow the model to learn the complexity of functions. However,

the linear activation function (ReLU) has been assigned for the output layer to retain the weighted sum of the input. The values of parameters used in the LM Bayesian regularized back-propagation training may be found in Table 5.5.

Table 5.5: A summary of the parameters that were used for the LM Bayesian regularization backpropagation training.

Maximum number of iterations	1000
Mean square error goal	0
Marquardt adjustment parameter	0.005
Decrease factor for adaptation parameter of LM	0.1
Increase factor for adaptation parameter of LM	10
Maximum adaptation parameter of LM	1e10
Minimum Mean square error gradient	1e-7

5.4.4 Database Development

First, the number of hidden layers and the number of neurons inside each hidden layer needs to be determined, as a poor choice can affect the accuracy of training and the subsequent prediction. The entire dataset for development of the ANN comprises $N = 530$ data points, with the statistical variation of these parameters listed in Table 5.6.

Since the data points available for training and testing are relatively low (Bewick et al. (2011) used 17,882 data points in their ANN model), an extensive development of a single-layer shallow network was undertaken. The number of neurons was varied from 1 to 150, and 85% of the complete dataset was used for training with the remaining 15% retained for testing. Performance evaluation was primarily assessed using Young's

Table 5.6: A summary of statistical ANNs input variables

input variable	Mean	Mode	Max	Min
Obstacle scaled distance, Z_{do}	1.37	0.825	5.47	0.087
Relative target distance, d_t/D	10.3	10.0	50.0	1.25
Solid angle of impingement, TL/d_t	0.55	0.50	5.0	0.20
Scaled target area, TA/$W^{2/3}$	0.56	0.019	2.92	0.019

correlation coefficient (${R_t}^2$, Eq. 5.5a) and mean square error (MSE, Eq. 5.5b).

$$ {R_t}^2(o,m) = 1 - \frac{\sum_{n=1}^{N}(m_n - o_n)^2}{\sum_{n=1}^{N} {o_n}^2} \tag{5.5a} $$

$$ \text{MSE} = \frac{1}{N}\sum_{n=1}^{N}(m_n - o_n)^2 \tag{5.5b} $$

where N is the total number of data points, m_n is the predicted equivalent energy impulse ratio, and o_n is the target equivalent energy impulse ratio.

Fig. 5.12 shows the mean square error and correlation coefficient as a function of the number of neurons. The training dataset converges quickly within 8 neurons. However, the MSE and R^2 exhibits small fluctuations even up to 150 neurons, likely due to the random initiation of network properties (e.g. weights and biases). The average of these fluctuations for MSE and R^2 for neurons ranging from 8 to 150 was 0.00049 and 0.9824 respectively. The best performance was obtained for 90 neurons, for which the MSE was 0.00029 (training) and 0.0004 (testing) and the R^2 was 0.9899 (training) and 0.9853 (testing).

The final network design therefore contained 90 neurons in a single hidden layer along with the previously defined network architecture. The MATLAB script function of this ANN code is provided in *Appendix A*. For the maximum allowable 1000 iterations, the training returned an MSE of 0.000171 as shown in Fig. 5.13a. The calculated relative error of EEI outputs for the best MSE is plotted as a histogram in Fig. 5.13b. It is clear that the overall sample error close to zero, indicating the suitability of using the trained model for predicting new cases.

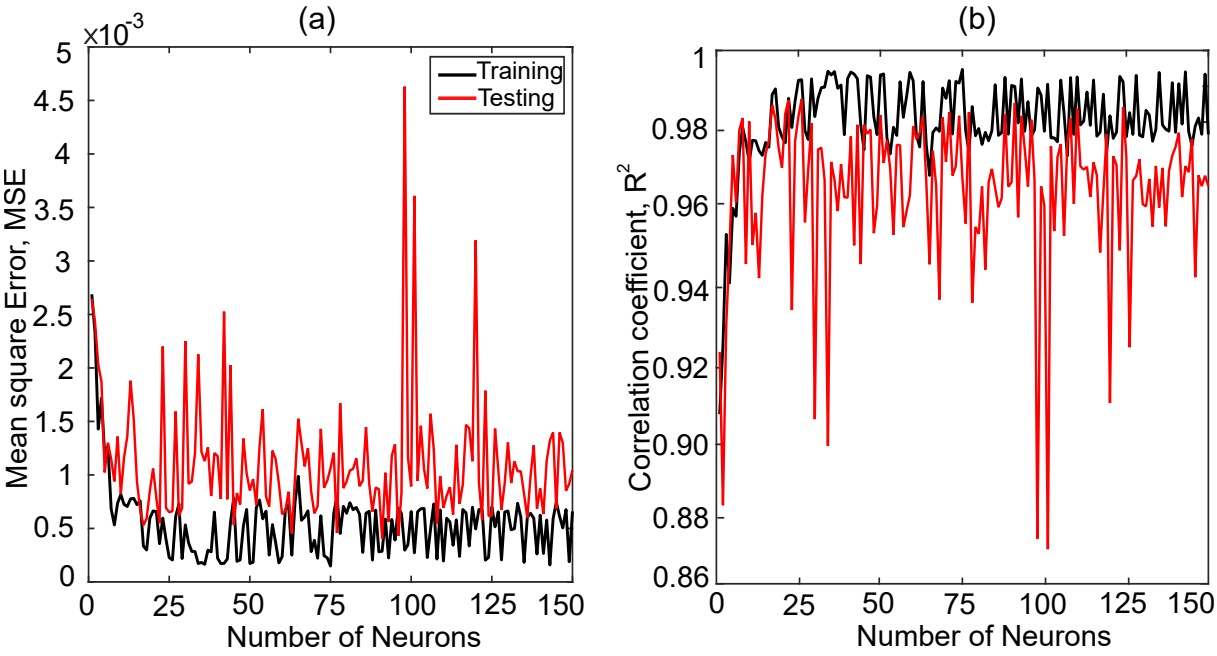

Figure 5.12: Variation of performance metrics of the ANN model as a function of the number of neurons: (a) mean square error, (b) correlation coefficient $R_t{}^2$

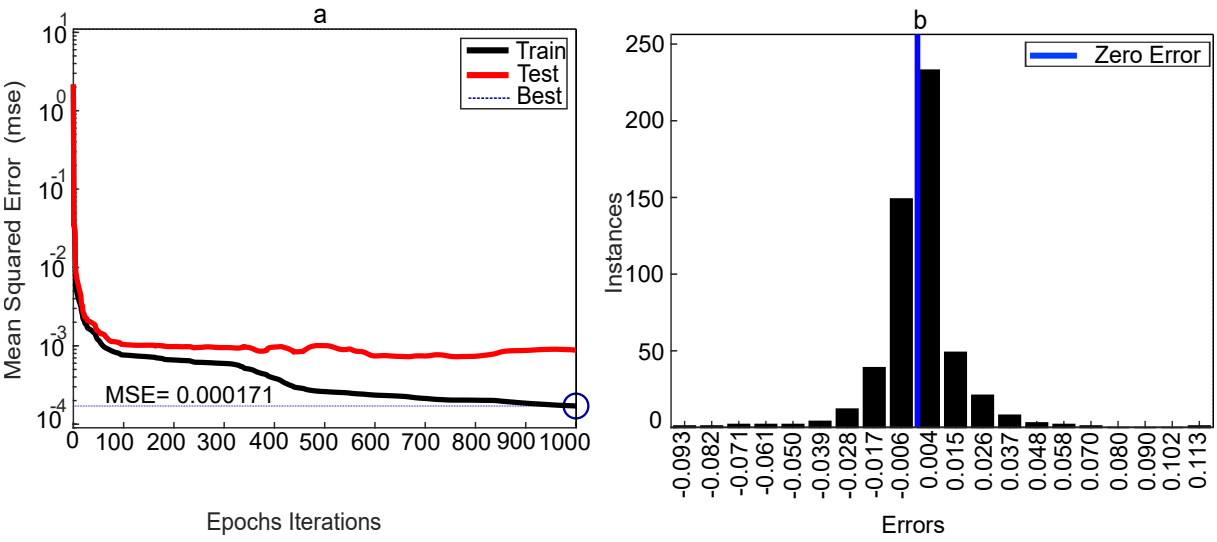

Figure 5.13: A plot of monitors while training the ANN model. (a) Evolution of mean square error with iteration, and (b) a histogram chart of the relative output error.

Fig. 5.14 shows the correlation plots for training, testing, and the combined datasets, with the dashed line representing a perfect prediction. The correlation plot for the training dataset, Fig. 5.14a, shows an excellent $R_t{}^2$ of 0.9936 with almost all samples falling onto the dashed line except for three points which had an EEI ratio > 0.8. Fig. 5.14b shows the testing dataset which also has a satisfactory correlation coefficient of 0.9765, thereby demonstrating that it is a robust and efficient network model. The overall correlation coefficient for the entire dataset was over 0.99 (Fig. 5.14c).

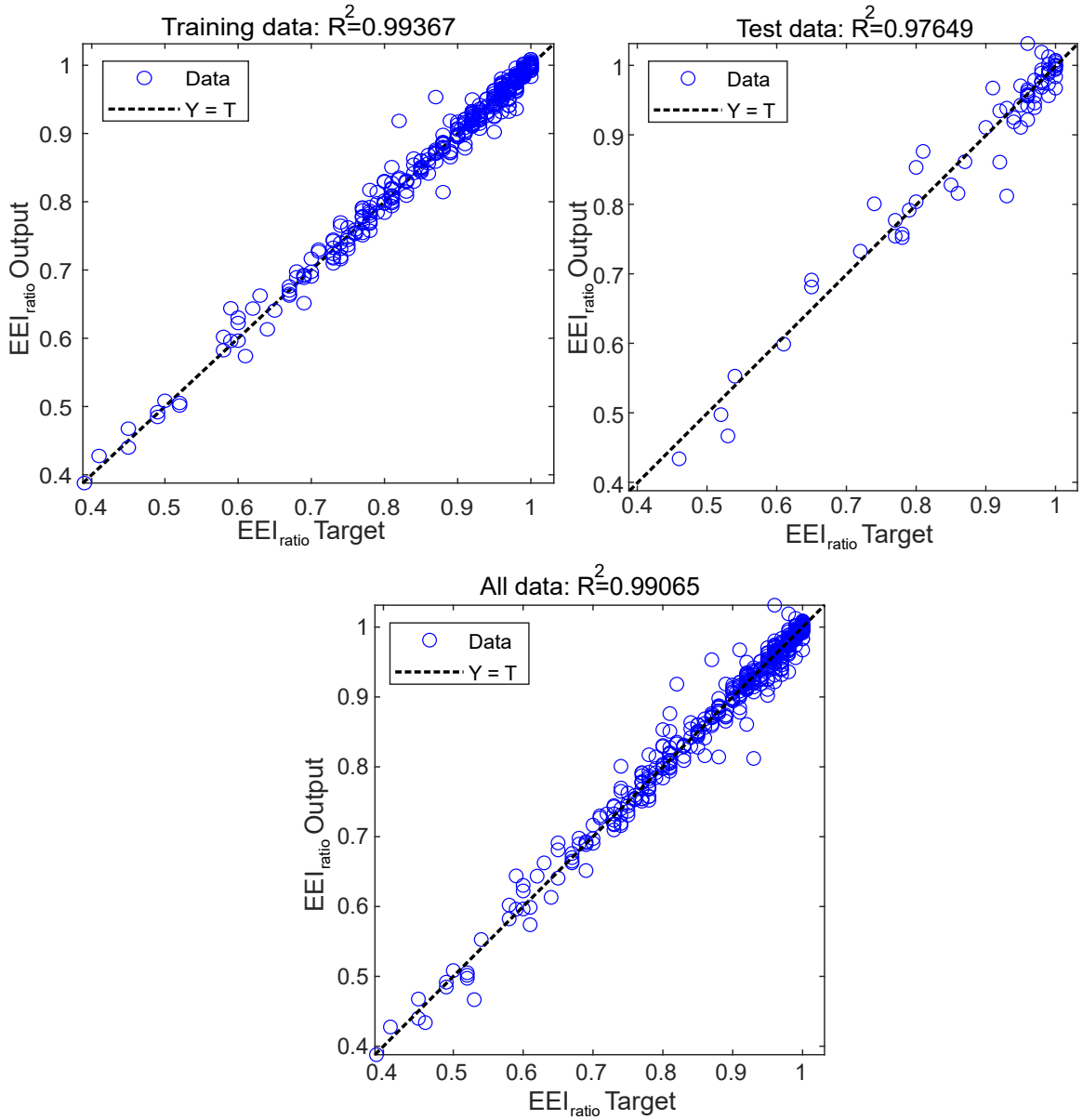

Figure 5.14: Correlation plots for the ANN training dataset (top left), the test dataset (top right), and all datasets (bottom).

The distribution of the relative error of the predicted EEI ratios for each input parameter has been presented in Fig. 5.15. The error falls mostly within the 5% limit and the trend for all input parameters is mostly similar (i.e. decreasing relative error with increasing input parameter), showing the successful generalization of this network model.

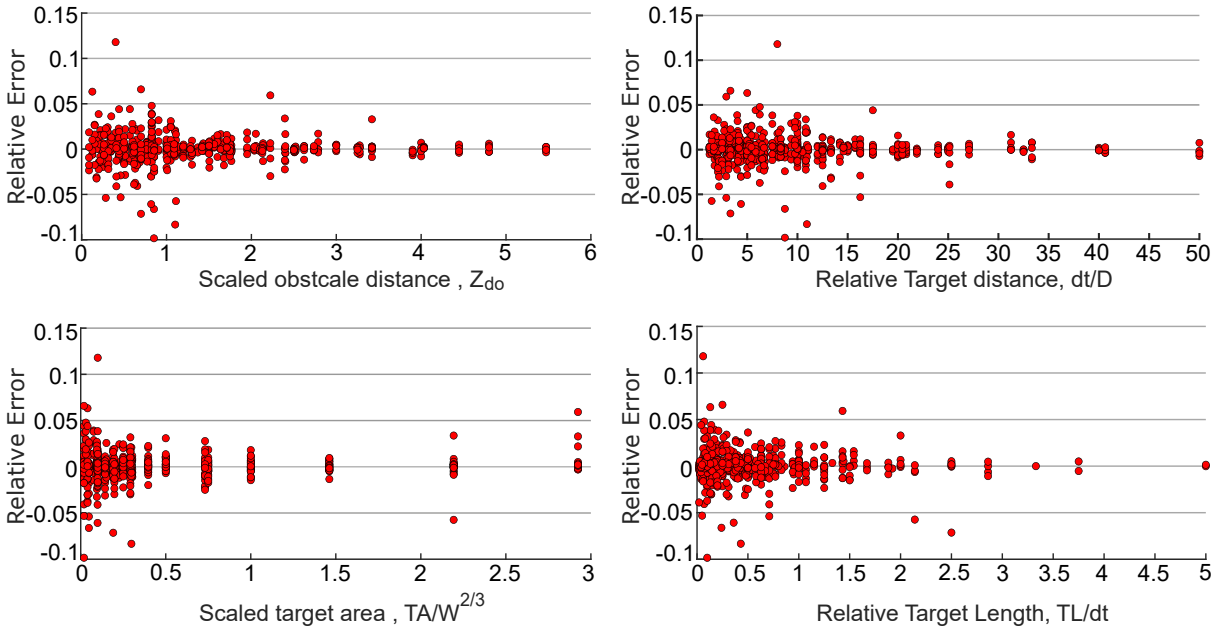

Figure 5.15: Plots of relative error for ANN outputs against each of the scaled input parameters.

5.4.5 Testing the ANN Predictive Model Against Unseen Data

With the ANN model performing well using training data which was based on 530 samples, originally collected from 106 simulations, it is vital that the engineering model is additionally tested to check its ability to predict EEI ratio from previously unseen data. This involves carrying out additional simulations utilising new physical input parameters and scaled values. A number of physical inputs were chosen to be very different to the *unscaled* inputs of the training data (with the *scaled* values still being within the limits of the original training dataset). For example, the charge size W_{TNT} was doubled to 24 kg, the cylinder diameter was extended to 30 cm, and the target length ranged from 0.1 m to 2 m. A summary of these new input values and a comparison of their outputs has been given in Table 5.7. The comparison has been given in terms of percentage differences

Table 5.7: A summary of the new input values to generate unseen data for the ANN model. The EEI values from the Apollo simulations and the ANN model have been compared in terms of percentage differences

Physical variables							Scaled variables				Results in ratio		
W	**D**	**R**	$\mathbf{d_0}$	$\mathbf{d_t}$	**TA**	TL	$\mathbf{Z_{do}}$	$\mathbf{d_t/D}$	$\mathbf{TA/W^{2/3}}$	$\mathbf{TL/d_t}$	**EEI, Apollo**	**EEI, ANN**	**Difference in %**
24	0.3	4	2	2	2	2	0.693	6.67	0.2404	1	0.86	0.87	1.3%
24	0.3	4	2	2	1.75	1.75	0.693	6.67	0.2103	0.88	0.85	0.85	0.3%
24	0.3	4	2	2	1.5	1.5	0.693	6.67	0.1803	0.75	0.84	0.83	0.7%
24	0.3	4	2	2	1.25	1.25	0.693	6.67	0.1502	0.63	0.83	0.82	0.9%
24	0.3	4	2	2	1.1	1.1	0.693	6.67	0.1322	0.55	0.83	0.82	1.3%
24	0.3	4	2	2	1	1	0.693	6.67	0.1202	0.5	0.83	0.82	1.2%
24	0.3	4	2	2	0.75	0.75	0.693	6.67	0.0901	0.38	0.83	0.83	0.1%
24	0.3	4	2	2	0.5	0.5	0.693	6.67	0.0601	0.25	0.85	0.85	0.3%
24	0.3	4	2	2	0.25	0.25	0.693	6.67	0.03	0.13	0.86	0.89	2.9%
24	0.3	4	2	2	0.1	0.1	0.693	6.67	0.012	0.05	0.86	0.91	6.0%
8	0.22	1.4	0.6	0.8	1	1	0.3	3.64	0.25	1.25	0.78	0.78	0.0%
8	0.22	1.4	0.6	0.8	0.75	0.75	0.3	3.64	0.1875	0.94	0.69	0.70	1.4%
8	0.22	1.4	0.6	0.8	0.5	0.5	0.3	3.64	0.125	0.63	0.58	0.61	4.6%
8	0.22	1.4	0.6	0.8	0.25	0.25	0.3	3.64	0.0625	0.31	0.54	0.57	5.6%
8	0.22	1.4	0.6	0.8	0.1	0.1	0.3	3.64	0.025	0.13	0.61	0.61	0.5%
0.5	0.08	2	1	1	1	1	1.26	12.5	1.5874	1	0.97	0.97	0.5%
0.5	0.08	2	1	1	0.75	0.75	1.26	12.5	1.1906	0.75	0.97	0.99	1.6%
0.5	0.08	2	1	1	0.5	0.5	1.26	12.5	0.7937	0.5	0.97	0.98	1.5%
0.5	0.08	2	1	1	0.25	0.25	1.26	12.5	0.3969	0.25	0.98	0.98	0.4%
0.5	0.08	2	1	1	0.1	0.1	126	125	0.1587	0.1	0.98	0.97	0.5%

between the Apollo CFD values and the trained ANN output. A correlation plot of the output has also been shown in Fig. 5.16.

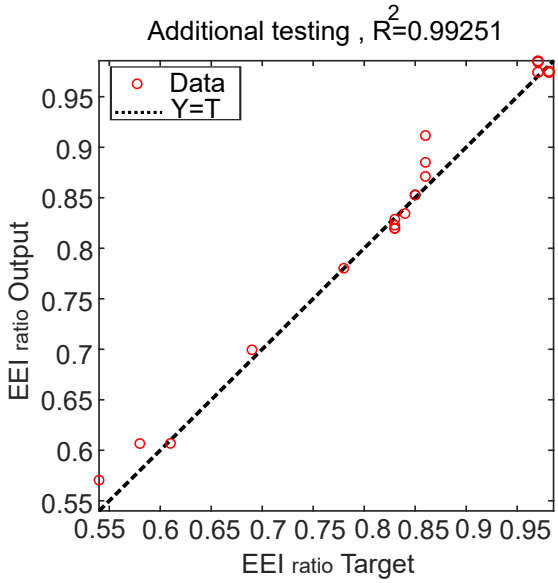

Figure 5.16: A plot showing the correlation coefficients for the output of the ANN model against CFD results. This is for data previously not seen by ANN.

The typical difference between Apollo and ANN output is less than 2% (only four out of the 20 results exceed this value), with no results exhibiting a difference of more than

6%. The correlation coefficient, R^2, of the ANN predictions against this unseen dataset in Fig. 5.16 is 0.9925, indicating the robustness of the ANN model in capturing the mitigation potential of various blast-cylinder interaction scenarios within 10% of the actual EEI ratio due to CFD prediction error.

5.5 Summary and Conclusion

A numerical investigation of blast wave interaction with single cylindrical obstacle was performed in this Chapter using a high-fidelity, physics-based CFD solver; Apollo Blast-simulator. The overall aim of this Chapter was to understand and characterize the altered flow field downstream of a single obstacle ,with cylindrical geometry in this study, loaded by a blast wave, due to wave interference. Results were interrogated over two planes, with consideration of the following parameters:

- *Ground plane downstream of single obstacle:* The blast wave intensity Z_{do} and the obstacle size D
- *Target plane downstream of single obstacle:* The blast wave intensity Z_{do}, the obstacle size D, the obstacle location ratio d_0/R, and the target size TL.

Results from these characterisation studies were then used to develop a fast-running model – an artificial neural network (ANN) – to predict equivalent energy impulse (EEI) values on the wall. The input parameters for the ANN had been identified and scaled based on the findings from the characterisation studies.

Apollo was used to generate pressure and impulse values behind a cylinder for 6 ground plane simulations and 131 simulations for the reflective wall (106 obstacle cases and 25 reference cases). The simulations showed that the evolution of the pressure and impulse values due to wave interference are mainly dependent on obstacle size and blast wave intensity, according to Hopkinson scaled distance. Higher intensity blast waves (faster particle velocities) were found to introduce more disruption to the flow-field by generat-

ing a stronger vortex. This led to increased attenuation of the specific impulse values downstream.

The ratio of equivalent energy impulse (EEI) values on a reflective wall target was calculated and characterised in terms of the blast wave strength, the obstacle size of single cylinder, distance to the target, and target length. It was found that a strong relationship exists between EEI mitigation, the blast wave strength (defined by obstacle scaled distance), and the cylinder size. Another factor influencing EEI mitigation is the reattachment/coalescing of waves behind the obstacle which was shown to be associated with target distance. A shorter target distance (< 0.4 m) could cause localised EEI mitigation over a small target area but an intensification was observed when considering a wider target distance as wave trapping then appears to dominate the response. In general, enhanced EEI attenuation was observed for target distances ranging from 0.5 m to 2 m for stronger blasts, and a larger sized obstacle could induce localised attenuation on the target wall.

The general pattern of blast loading distribution on a reflective structural target wall could be such that the region can entirely lie in the shadowing region, or in the wave interference zone, or have a combination of both shadowing and wave interference regions. On such a wall, the peak impulse reduction ratio was found to be mild at the shadow zones ($< 5\%$) and somewhat prominent ($<14\%$) at the wave interference zones, subject to the size of the cylindrical barrier.

Finally, an artificial neural network model (ANN) using Bayesian regularisation with a Levenberg-Marquardt (LM) training algorithm was developed to predict EEI mitigation. The following scaled parameters were used as input variables: Hopkinson scaled distance to the obstacle Z_{do}, the ratio of distance to the target and diameter of the cylinder d_t/D, the solid angle of impingement TL/d_t, and scaled target area TA/$W^{2/3}$. A total of 530 (106×5) data points were available for training the ANN. 85% of these values were used for training the model with the remainder used for testing. After optimizing the network

model, 90 neurons were used in a single hidden layer. The results showed a very low variation with a mean square error of 0.000171 and a correlation coefficient R^2 of 0.994 and 0.976 for the training and testing datasets respectively.

The trained ANN model was then used to predict the results of previously unseen analyses, outside of the previous 530 CFD data points. The model exhibited excellent accuracy, with 80% of the predicted data points having less than 2% difference from the CFD results, with the remaining predictions all within 6% of the CFD data. Thus, it may be concluded that appropriate ANN models can be used to obtain the total load on a target wall downstream of a cylinder despite the complex wave interactions. This fast prediction of EEI ratio has within 10% variation from actual blast loading due to CFD modelling limitation. Overall, the blast mitigation analyses for similar complex models can thus be reliably carried out using the proposed ANN model for fast assessment.

Chapter 6

Numerical analysis of blast mitigation of multi-obstacles

6.1 Introduction

This Chapter focuses on numerically characterising the blast mitigation behaviour due to the interaction with multi-scales obstacles such as the arrangements of Sierpinski carpet pre-fractal which their mitigating capabilities were tested in the experimental work in Chapter 3 and showed some promising results. In that experiment , the first three iterations of a Sierpinski carpet pre-fractal were tested, with each obstacle in the set (Figure 6.1) an iteration of the previous one. It can be seen that, by design, these obstacles automatically incorporate multiple length scales. However, the true extent of the mitigation behaviour of multi-scale obstacles is yet to be fully characterised, and therefore their use for protective purpose is currently limited.

Hence, numerical simulations are performed in this Chapter to recreate the setups of the pre-fractal experiment of Chapter 3 for further investigation. For convenience, the important details of experimental setup including dimension of pre-fractal elements with blast loading generations and the discussed results are summarised here.

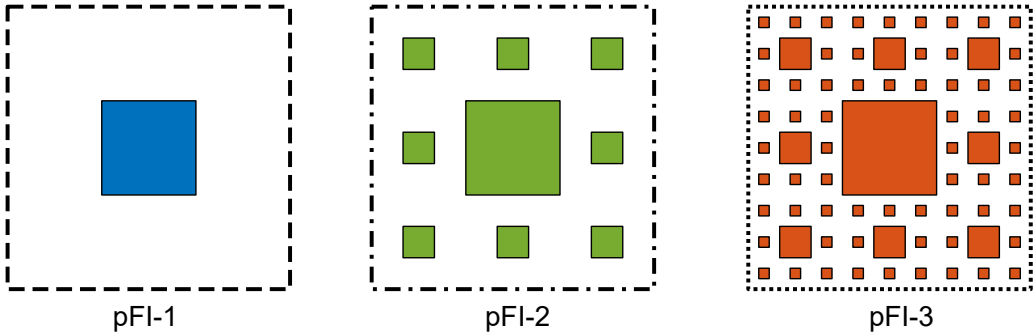

Figure 6.1: Plan view illustration displaying the first three iterations of a Sierpinski carpet. These designs were also the obstacles chosen for this work–iteration 1 (pFI-1), iteration2 (pF-2) and iteration 3 (pFI-3).

The first fractal iteration (pFI-1, Figure 6.2a) contains only a 180 mm square hollow section. The second fractal iteration (pFI-2) has eight additional 60 mm square poles surrounding the 180 mm section, with a 60 mm gap between the 180 mm and 60 mm obstacles (see Figure 6.2b). The third fractal iteration (pFI-3, Figure 6.2c) comprises eight 20 mm square rods surrounding each 60 mm square pipe from the second iteration, with a 20 mm air gap. The fractal dimension for this obstacle is given by $D = \log(N)/\log(S) = 1.89$, where N is the number of copies of the original in each iteration ($N = 8$), and S is the scale factor between an original and its copy ($S = 3$). The height of each of these obstacles is 1 m.

The pre-fractal obstacles were exposed to a 250 g PE4 surface blast loading at 3 different stand-off distances (SoD) of 125 cm, 150 cm, and 200 cm, each measured from the centre of the explosive to the front face of the central obstacle. A triplicate of free-field experiments (pFI-0, a no-obstacle case) was also carried out for all of these SoDs. For these experiments, Hopkinson Cranz (TNT equivalent) scaled distances were $Z_{SOD125} = 1.87$ m/kg$^{1/3}$, $Z_{SOD150} = 2.24$ m/kg$^{1/3}$, and $Z_{SOD200} = 2.99$ m/kg$^{1/3}$, assuming a PE4 TNT equivalence of 1.20 (Rigby & Sielicki 2014).

The blast wave interaction process was quantitatively and qualitatively investigated using pressure measurements and a high speed camera. A total of 12 pressure sensors were

placed at locations both along the upstream, and the downstream regions (see Figure 6.2d) of the obstacle. The resulting incident and reflected overpressure histories were used to carefully extract the peak pressure, peak specific impulse and arrival time. To visualise the evolution of shock patterns, a high speed camera was used to capture time-resolved images against a zebra-board background.

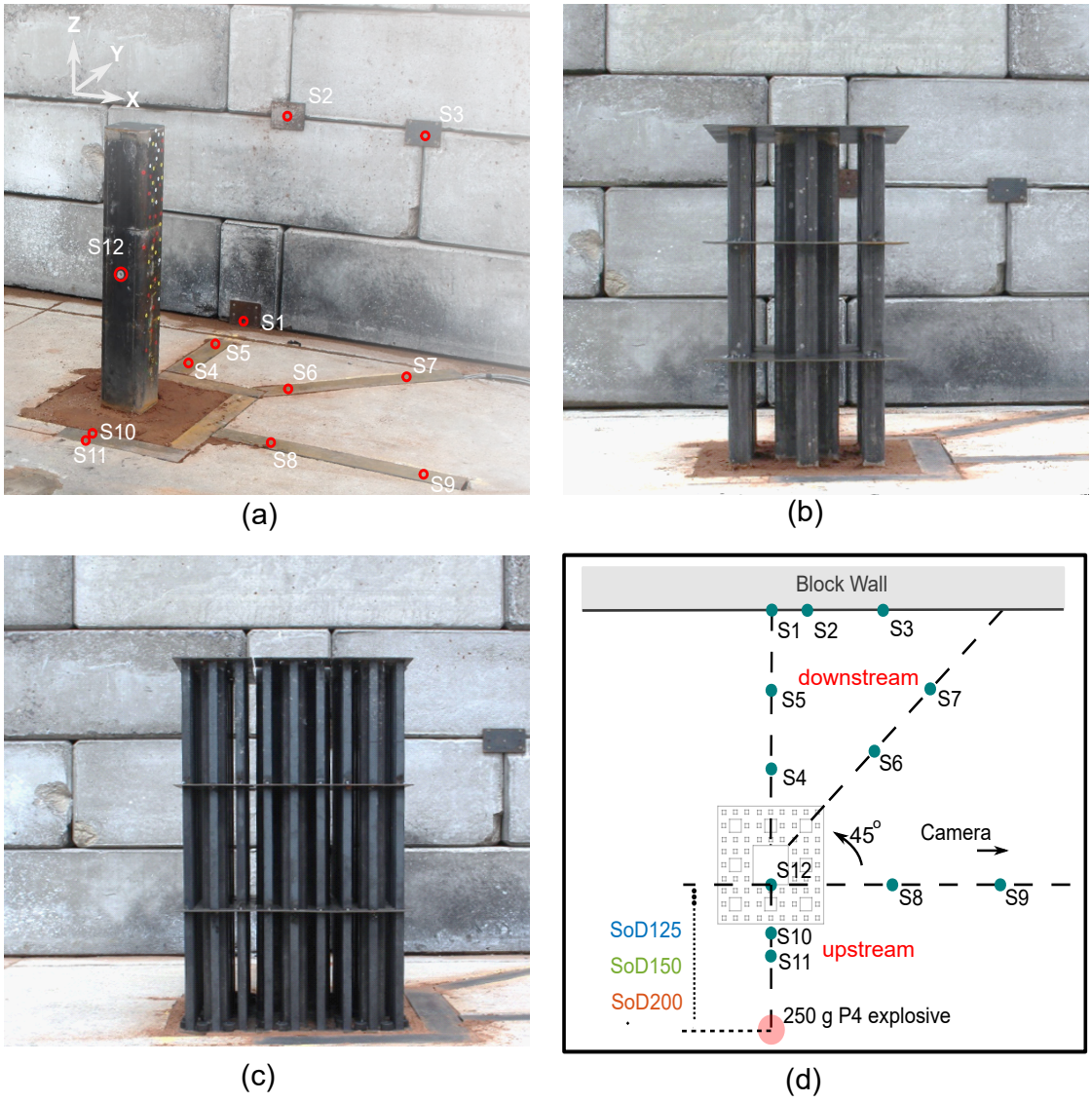

Figure 6.2: A photograph of each of the pre-fractal shapes **(a)** pFI-1, **(b)** pFI-2, and **(c)** pFI-3, as installed at site. **(d)** A schematic layout showing the locations of the explosive, the obstacle, the target wall, the camera and the pressure sensors. Figures were recreated and taken from Chapter 3

The important observations from the experiment, taken from Chapter 3, were as follows:

- The reflected pressure measurements on the block wall showed that: (i) pressure mitigation became significant with increasing complexity of the obstacles and this attenuation was quantitatively similar within the range of blast intensities (SoDs) that were tested. However, the attenuation pattern of specific impulse did not correlate well with the complexity of a given pre-fractal configuration and it was also found to be sensitive to the SoD. (ii) The delay in the arrival time was found to be a function of the pre-fractal iteration number.

- The incident pressure gauges downstream and within the vicinity of the obstacle showed that: (i) pressure and impulse mitigations were only pronounced for shapes that more closely resembled a true fractal, i.e., pFI-3. Conversely, for the simpler obstacles (pFI-1 & pFI-2) a pressure *enhancement* was observed . This was proposed to be due to the pressure waves coalescing and re-forming after being deflected around the obstacle, but this has not been confirmed through direct observation. This enhancement was only for a limited distance downstream and did not persist. (ii) For such pre-fractal configurations, regions beyond 6 primary length scales (6 $\times$ 180 mm) along the 45° line downstream (at sensor 7 in Figure 6.2d) were found to be undisturbed by the obstacle, indicating that the effectiveness of mitigation is spatially limited.

- It was also reported that when an obstacle becomes more fractal-like (such as pFI-3), a consistent mitigation pattern of peak pressure and specific impulse was observed. This was attributed to 'wave trapping' within this obstacle and an enhanced break-up of the incident blast wavefront which effectively prevented it from coalescing behind the obstacle. This was also verified using the high-speed video footage, but again has not been confirmed through direct observation.

While it is clear that an enhanced blast mitigation occurs when the configuration shape approaches a fractal-like shape such as iteration 3 due the initiation of waves tapping and the complex wave interference occurred from waves' transmission through openings , the following questions naturally arise regarding the performance of fractal-like obstacles:

1. What are the precise mechanisms governing this mitigation?
2. What amount of additional mitigation would be present if the complexity of pre-fractal is increased further (i.e., the 4th iteration)?
3. What is the relationship between the spatial bounds of the mitigation and the fractal iteration and size?

This Chapter thus aims to perform a comprehensive numerical study addressing the above questions through developing a CFD numerical models using Apollo Blastsimulator in order to attempt to fully characterise the mechanics of interaction. The primary content of this chapter was derived from the published paper titled: ***Numerical modelling of blast mitigation of pre-fractal obstacles***, as elucidated in Chapter 1 (refer to section 1.4).

6.2 Numerical Modelling Methodology

6.2.1 Apollo Blastsimlautor Overview

Apollo CFD solver herein was used to numerically replicates the geometry of the experimental work in Chapter 3, in which 0.25 kg hemispheres of PE4 were detonated on a flat ground surface at different stand-off distances from the central obstacle. The blast wave-obstacle interaction process of pFI-3 with SoD=1.25m was previously validated in Apollo in Chapter 4 (see 4.3.2.2). In such a problem, it was recommended to use obstacle-cell ratio (number of cells discretizing the smallest geometry in the obstacle) ≥ 2, or for a better results ≥ 4 if the computational capabilities of the machine can allow. Therefore,

2.5 mm mesh size is picked in computational domain in this methodology.

Explosives in this work were modelled as C4, which is nominally identical to PE4 (Bogosian et al. 2016). The Chapman-Jouget model was used in Apollo to model detonation and the Jones-Wilkins-Lee (JWL) equation of state was used to model the products of reaction

6.2.2 Simulation details: with wall

This section provides details of numerical setups for simulating the geometry of the experimental work which had a reflective wall at the end of the domain. Figure 6.3 shows the general numerical model layout adopted for each of the 9 simulations (3 SoDs and 3 pre-fractal arrangements). This Octant domains used for the 3D simulations had different dimensions based on the stand-off distance between the explosive and the obstacle, namely 2.5 x 2.5 x 2.5 m , 2.75 x 2.75 x 2.75 m, and 3 x 3 x 3 m for the 1.25 m, 1.50 m and 2.0 m SoDs respectively. Rigid boundaries were located along the x=0, y=0, and z=0 planes, with a reflecting wall at either y = 2.5, 2.75, and 3 m for each different SoD. Outflow planes were specified for the remaining two sides. 0.5 kg of C4 explosive was placed on the reflective ground level to produce a blast intensity identical to 0.25 kg of C4 due to the symmetry.
The numerical simulations in Fig. 6.3a-c first aimed to qualitatively study the mechanism of the experimentally observed mitigation through comparing the visualised numerical solution of the flow field (using Paraview) for each pre-fractal iteration.

In addition to these, a configuration that is the fourth iteration of the Sierpinski carpet based fractal (the virtual pFI-4, illustrated in Fig 6.4) was created. This obstacle has 5 mm square rods surrounding each 20 mm square pipe from the pFI-3 configuration, with a 7.5 mm air gap. Ideally, it should have been a square rod of side = $1/3^{rd}$ of 20 mm (since S=3 for this fractal) with an identical 6.33 mm gap, but due to certain constraints in mesh generation, 7.5 mm has been used herein. The pFI-4 configuration was added to

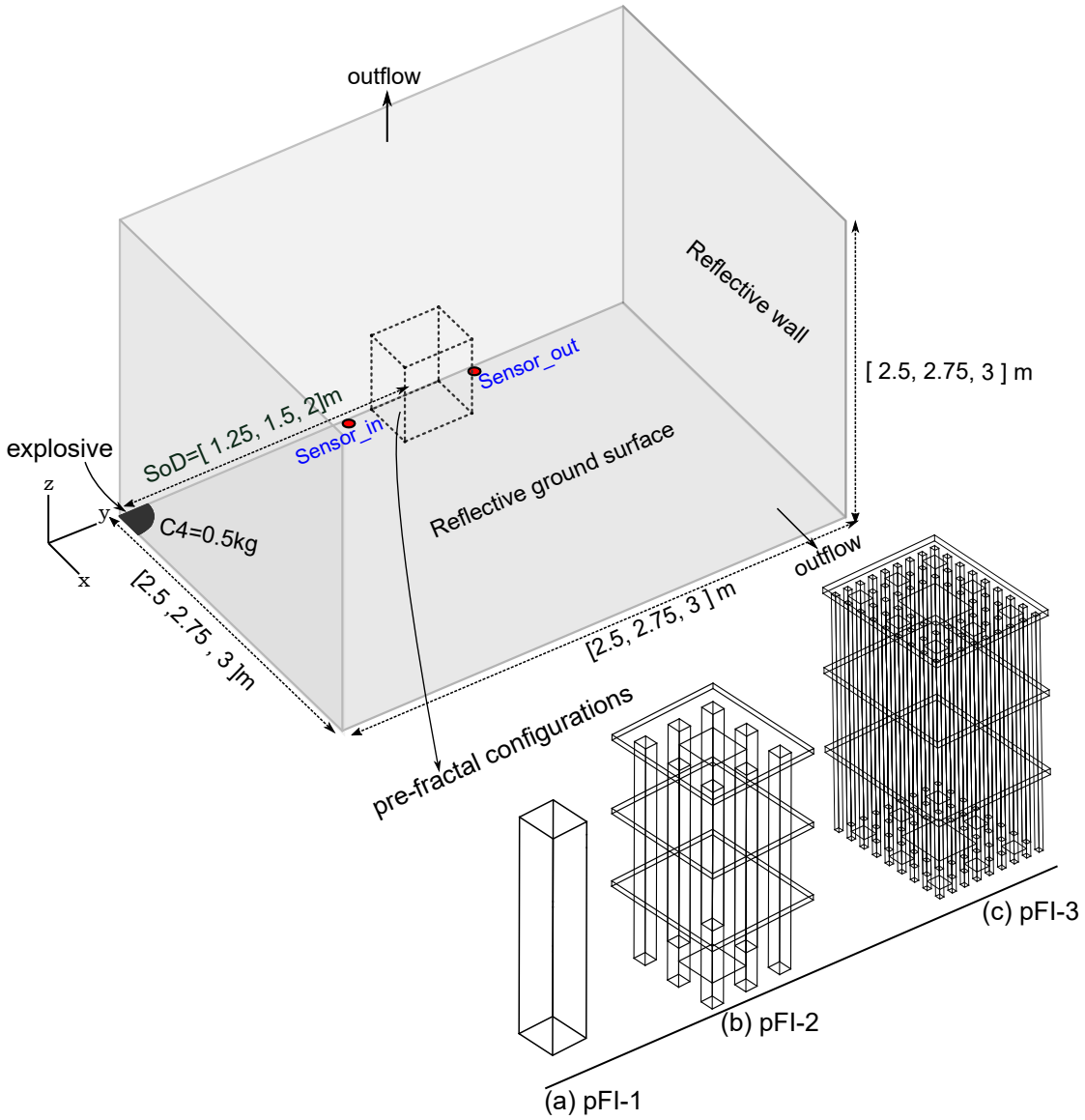

Figure 6.3: The 3D symmetric numerical domain octant for 9 different numerical configurations involving a combination of SoDs (viz., 1.25, 1.50, 2.00 m) and pre-fractal configurations – **(a)** pFI-1, **(b)** pFI-2, **(c)** pFI-3.

numerical domain of Fig. 6.3 which therefore increased the total number of the simulations to 12.

These simulations were then used to numerically compute the mitigation enhancement on increasing pre-fractal complexity (i.e., iteration number). The enhancement was rationalised in terms of wave impedance, represented in general by the difference in the measured value ahead of, and behind the obstacle at fixed locations (sensor_{in} & sensor_{out} in Fig. 6.3). For more clarity, an impedance of zero would result in zero reflection and

full transmission of the wave, an infinite impedance would result in full reflection and zero transmission, therefore an increase in reflection and decrease in transmission signifies an increase in apparent impedance. These locations sensor_{in} & sensor_{out}, which were retained for all the obstacles, are shown for pFI-4 in Fig 6.4. Table 4.5 summarises this list of simulations with a rigid wall 1.25 m behind the central obstacle, with the aim of answering the first two research questions in this study (see *Introduction*).

Table 6.1: Details of all simulations including a wall for a domain size as in Figure 6.3

No.	Pre-fractal configuration	Stand-off distance (SoD)	Explosive charge	Domain dimensions [X, Y, Z] in m	Element size	Simulation Time
1	**pFI-1**	1.25m	0.25 kg C4	2.50 ×2.50 ×2.50	2.5 mm	70 hours
2	**pFI-2**					
3	**pFI-3**					
4	**pFI-4**					
5	**pFI-1**	1.50m		2.75 ×2.75 ×2.75		72 hours
6	**pFI-2**					
7	**pFI-3**					
8	**pFI-4**					
9	**pFI-1**	2.00m		3.0×3.0 ×3.0		75 hours
10	**pFI-2**					
11	**pFI-3**					
12	**pFI-4**					

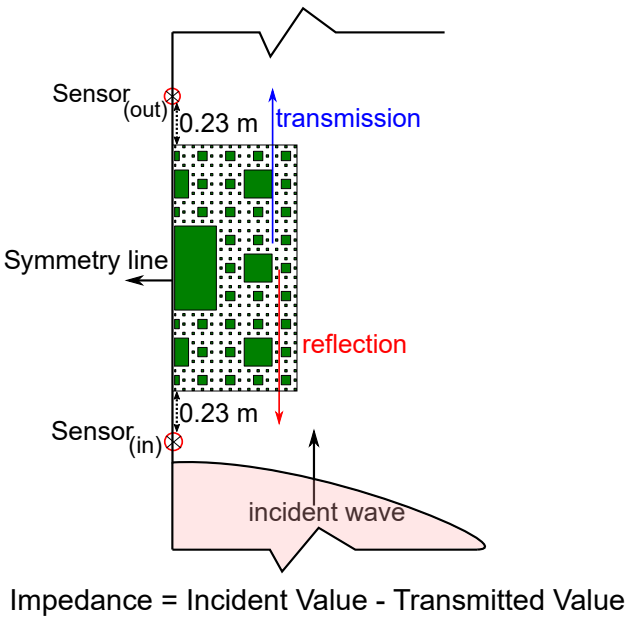

Figure 6.4: Input parameters for the impedance measurement of an incident blast wave for all simulations in Fig. 6.3. Here is only illustrated for the pFI-4 configuration.

6.2.3 Simulation details: without wall

The relationship between pre-fractal iteration number and the pre-fractal's zone of influence (spatial bounds of mitigation) was subsequently investigated by developing a new set of numerical models (Fig 6.5). This aims to address the final research question posed in this study (see *Introduction*). In these new simulations, the rigid wall in Figure 6.3 was removed in order to eliminate complications to the downstream flow field that arise due to reflection. A 3D quarter symmetric CFD domain, with dimensions of 2.8 m× 4.4 m × 2.8 m was chosen to simulate each of the 4 pre-fractal obstacles facing a blast load from the detonation of a hemispherical 0.25 kg C4 (modelled as 0.5 kg sphere in Apollo). The stand-off distance between the explosive centre and the front face of the central obstacle within the pre-fractal was 1.25 m and the other distances were not simulated. This is because SoD125 gives a single Hopkinson Cranz scaled distance of 1.87 m/kg$^{1/3}$, which is sufficiently representative of changes in the mitigation behaviour for all these scaled distances according to the findings of Chapter 5. Therefore, 5 simulations were carried out, one for each pre-fractal arrangement, and one for the reference (free-field) scenario, to calculate the mitigation.

The domain of observation was extended to 10D on either side of the obstacle, where D is the widest length scale in any obstacle (180 mm). A uniform array of sensors (numbering a total of 1296) was placed on the ground, downstream of the obstacle to quantify the mitigation in terms of ratios of overpressure and specific impulse (Eqn. 6.1). The height of the obstacles in the 3D model was 1 m.

$$P_{ratio} = P_{max,obstructed}/P_{free} \tag{6.1a}$$

$$I_{ratio} = I_{max,obstructed}/I_{free} \tag{6.1b}$$

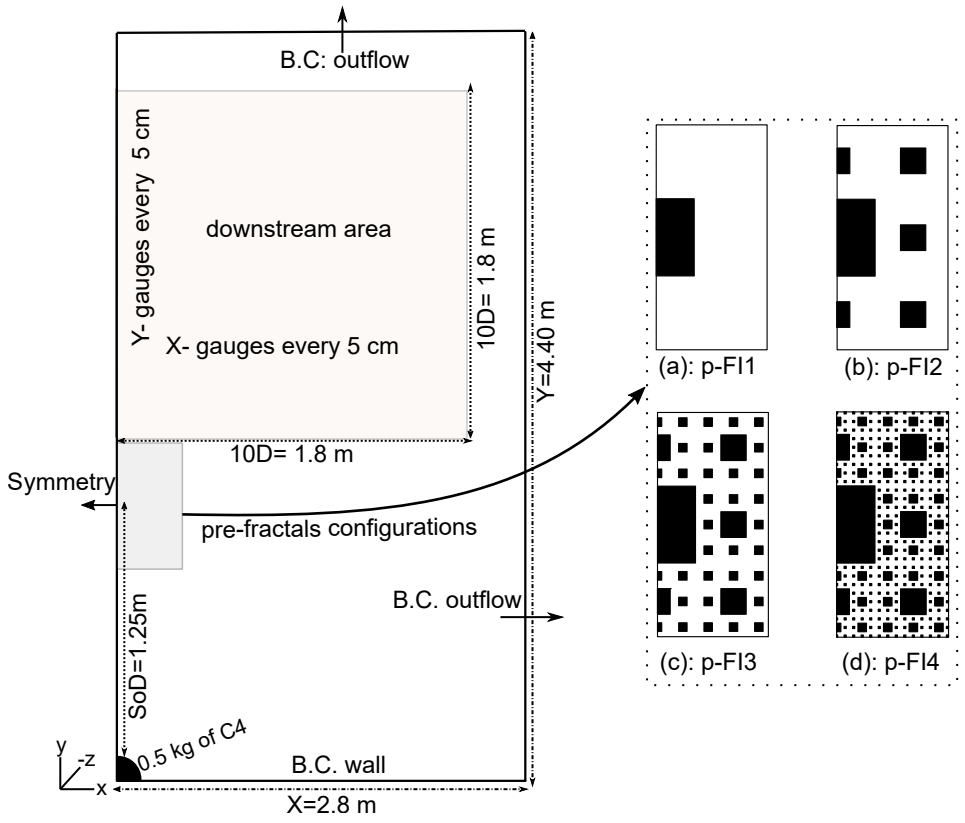

Figure 6.5: A schematic diagram of the plan view of the 3D numerical model, with the inset showing the obstacles: (a) pFI-1 (b) pFI-2 (c) pFI-3 and the virtual obstacle (d) pFI-4.

6.3 Results and Discussion

6.3.1 Understanding the mechanics of mitigation

The mechanics of fractal-like blast loading mitigation are explored using fringe plots for the first three obstacle iterations. Figure 6.6 shows a comparison of the wave propagation behaviour at different times for the SoD200 simulations (numbers 9, 10, and 11 in Table 6.1). The initial observation is that the strength of the reflected wave for the most fractal-like shape (pFI-3, see right of Figure 6.6b) is much larger than the reflected wave from the previous iterations. Moreover, the blast wave trapping is considerably more in-

tense in pFI-3 at 2.8 ms (Figure 6.6b) due to its high area-volume ratio and large number of reflecting surfaces (air gap is only 20 mm). This trapping is not very evident for the pFI-2 arrangement since the 60 mm air gap results in reduced blockage. The pFI-1, on the other hand, experiences only a normal reflection at the front face and a diffraction off its corners, resulting in only a minimal mitigation. As a result, the proportion of the pressure wave transmitted through these obstacles is clearly weaker at t=4 ms for pFI-3 arrangement (right end of Figure 6.6c). To reiterate, this is due to the strong break-up of the wave front for pFI-3 as compared to pFI-2 and pFI-1 (Figure 6.6c).

The changes to the directionality of the incident wave, and the formation of vortices were then visualised using streamline plots for all the obstacles, (at 4 ms after detonation). Streamline plots in terms of the velocity ($\vec{v}$) component parallel to the direction of flow (y-axis), and the total velocity magnitude are shown in Figures 6.7a-c and Figures 6.7d-f respectively. From these plots, it is clear that there are considerably more induced vortices for the pFI-3 iteration than the others, and these are caused by the obstacle redirecting the blast wave and thereby reducing its y-component of velocity (Figure 6.7c).

To illustrate this in further detail, the vorticity ($\nabla \times \vec{v}$), and the kinetic energy, at 4 ms after detonation are plotted in Figures 6.8a-c and Figures 6.8d-f respectively, for each obstacle. It is quite clear from these plots that the interaction of the blast wave with pFI-3 arrangement has significantly influenced the flow field and created more vortices compared to the others, as seen in Fig. 6.8c. The interaction of diffracted waves with these vortices can significantly influence the flow characteristics (Igra et al. 2013). These vortices serve to transfer energy from the blast wave into lower forms of energy (Needham 2018), eventually dissipating it as heat, by the lossy viscous action.

The enhanced activity due to the additional vortices in the pFI-3 arrangement directly result in a reduced intensity of kinetic energy in the downstream region, as seen in Fig. 6.8f when compared to other arrangements (Figures 6.8d&e). Caused by a diversion and dissipation of the kinetic energy, the result is additional downstream mitigation for the

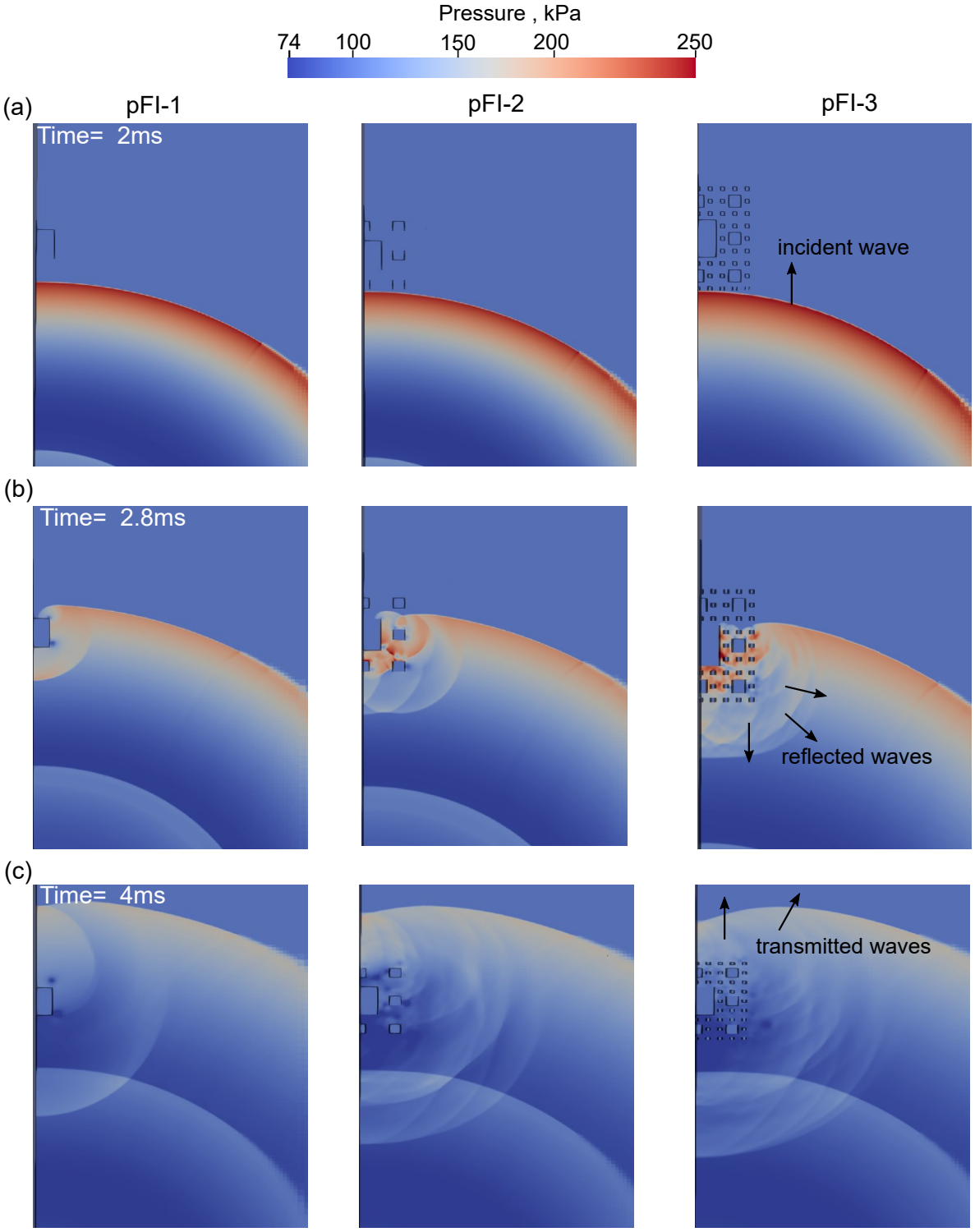

Figure 6.6: Ground pressure contours at three different time instants arranged row wise: (a) 2ms, (b) 2.8ms, and (c) 4ms for SoD=2.00m case. The corresponding obstacles have been arranged column wise: (Left) pFI-1, (Middle) pFI-2, and (Right) pFI-3.

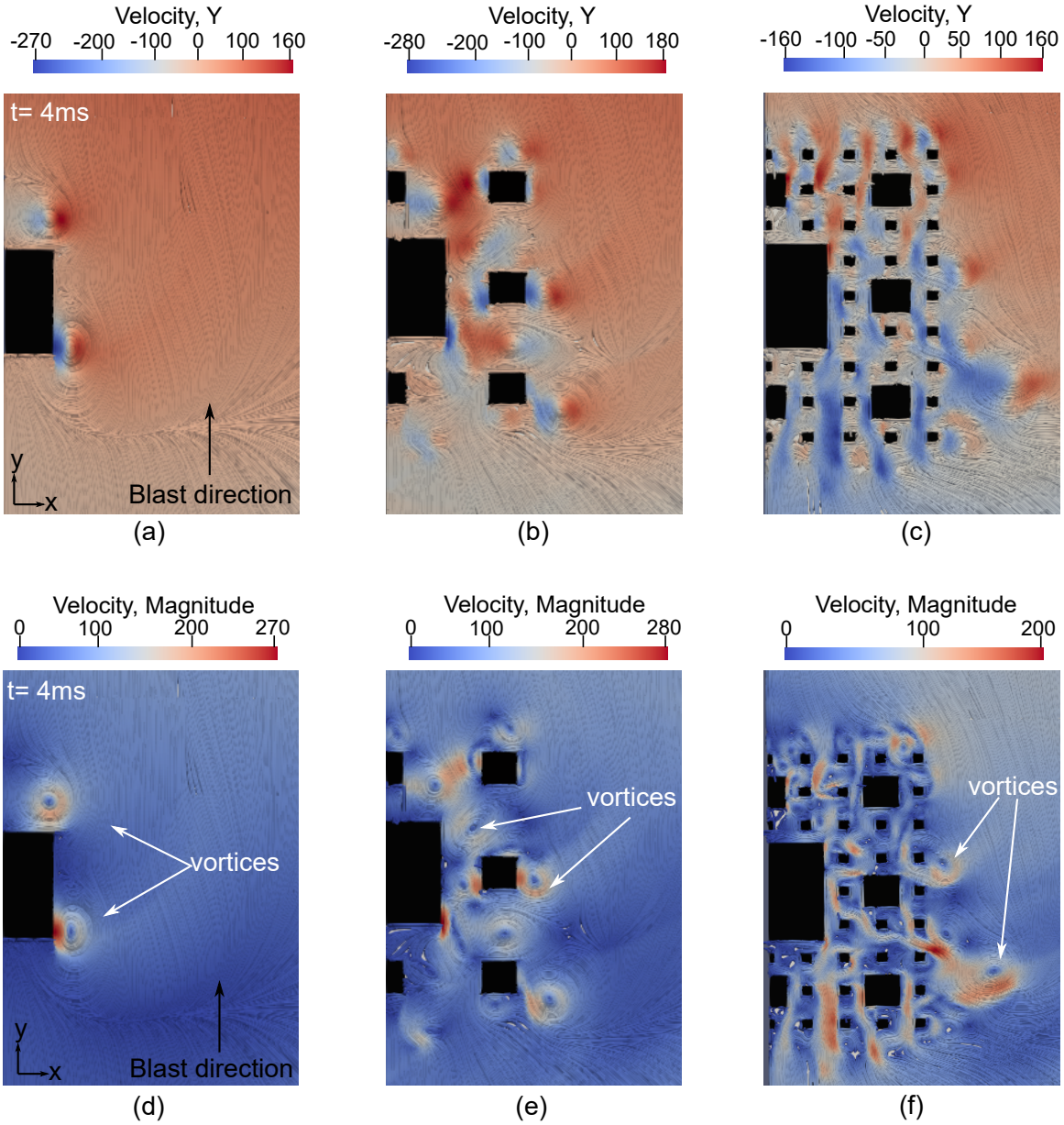

Figure 6.7: A visualisation of the streamlines at 4 ms coloured in terms of y-velocity magnitude for (a) pFI-1, (b) pFI-2, and (c) pFI-3. The velocity magnitude contours are also given for (d) pFI-1, (e) pFI-2, and (f) pFI-3.

pFI-3 arrangement. It has therefore been shown that obstacles with increasingly fractal-like shapes substantially alter the direction of the blast wave from its original path and induce strong vortices, which reduce the kinetic energy and the components of momentum directed downstream (i.e., in the original direction of propagation).

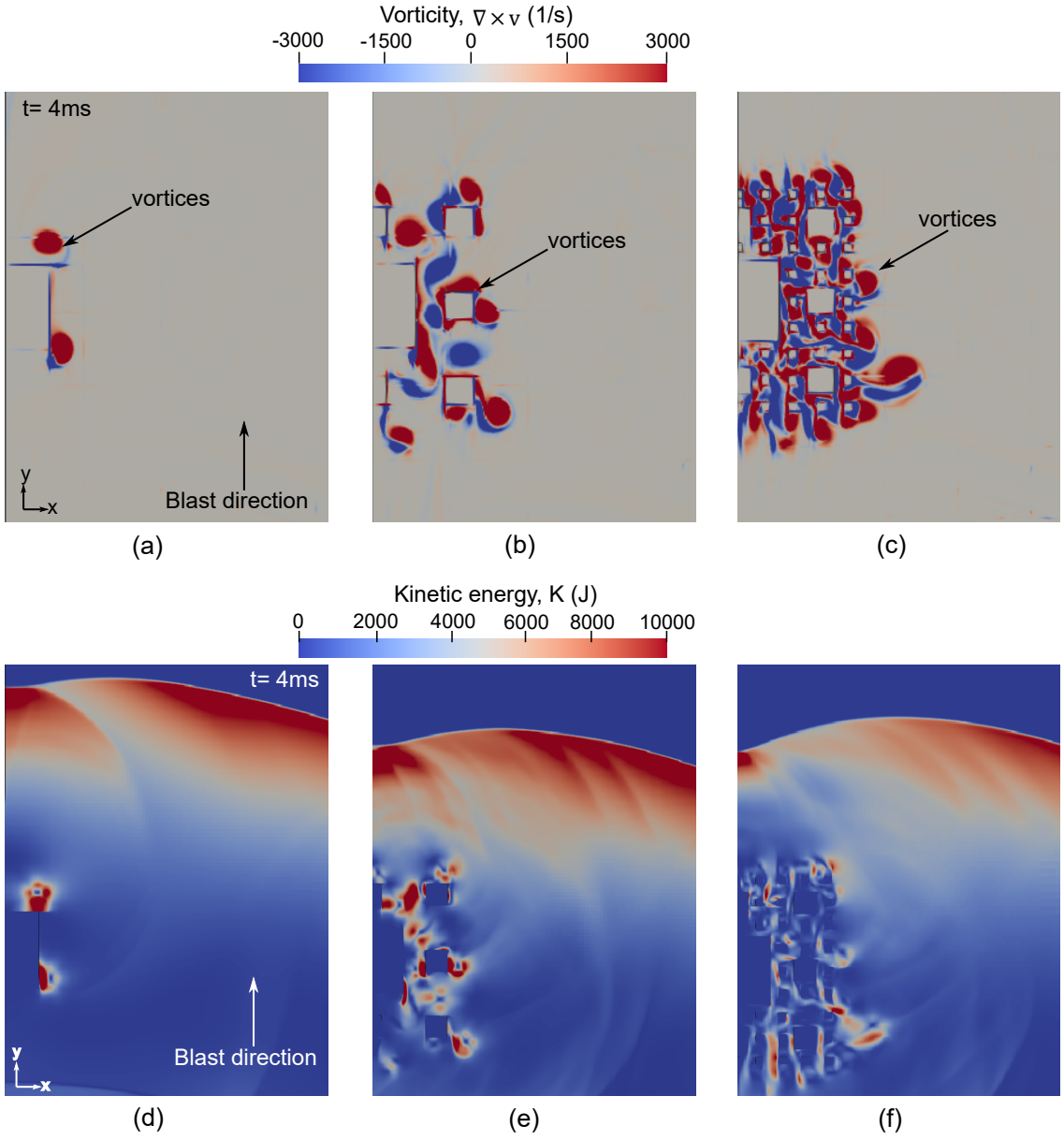

Figure 6.8: An instantaneous snapshot of the vortices at 4 ms, coloured by magnitude of vorticity for (a) pFI-1, (b) pFI-2, and (c) pFI-3. The contour plots of spatially calculated kinetic energy of the flow field at 4 ms are also given for (d) pFI-1, (e) pFI-2, and (f) pFI-3.

6.3.2 Obstacle impedance

The impedance of each pre-fractal iteration, as defined previously (Figure 6.4), has been used to quantify and evaluate the role of the pre-fractal complexity in attenuating the strength of the incident blast wave. The reflection and the transmission of the blast wave for all the three blast intensities (SoD125, SoD150, and SoD200) impacting each of the 4

pre-fractal obstacles have been calculated and plotted in Figures 6.9a-c. At the outset, it is worth mentioning that the mitigation occurs due to changes in the wave reflection and transmission, and due to the formation of vortices. The overall impedance behaviour in Figure 6.9 is as expected, with increasing complexity of the pre-fractal impeding the blast wave further through enhanced reflection of the incoming wave and a subdued transmission of the incident wave. The inflexion point for both reflection and transmission curves are observed after pre-fractal iteration 2, when the configuration of the obstacles become more fractal-like. This helps verify yet again that the pFI-3 and pFI-4 configurations would produce higher blast mitigation than pFI-1 and pFI-2.

Ideally, iteration 4 should be the best mitigator since it mostly reflects the pressure wave (and consequently the specific impulse) with the lowest transmitted pressure. However in Figure 6.9, the specific impulse transmission patterns for pFI-3 and pFI-4 appear to have reached an asymptote as this impedance is at a specific location (sensor$_{out}$ in Figure 6.4) and so it does not account for the overall behaviour. In the following subsection this aspect of pFI-4 will be highlighted in terms of the blast mitigation in the entire downstream region of the pre-fractal arrangements.

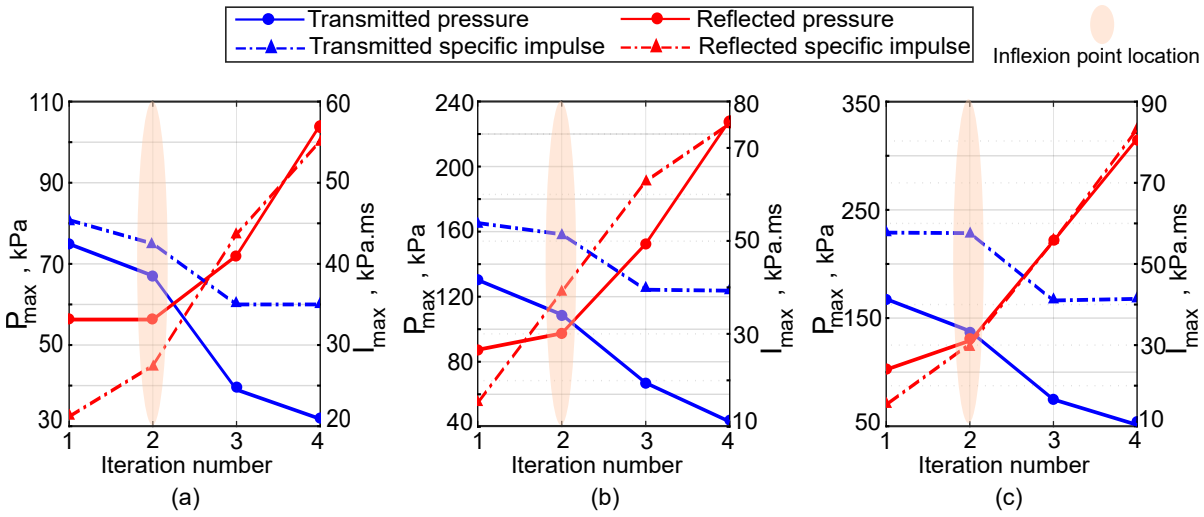

Figure 6.9: The pre-fractal iteration impedances for three blast wave intensities: (a) SoD=2.00 m, (b) SoD=1.50 m, and (c) SoD=1.25 m.

6.3.3 The spatial bounds of blast mitigation

The mitigation patterns in the downstream are shown as contour plots of pressure and specific impulse (Figures 6.10 & 6.12 respectively) for all four pre-fractal arrangements (pFI-1, pFI-2, pFI-3, and pFI-4). These plots also serve to indicate the spatial bounds of the mitigation arising due to the presence of a given obstacle. The spatial coordinates for these plots were normalised using D = 180 mm, the largest length scale in the cross-section of the pre-fractal obstacles.

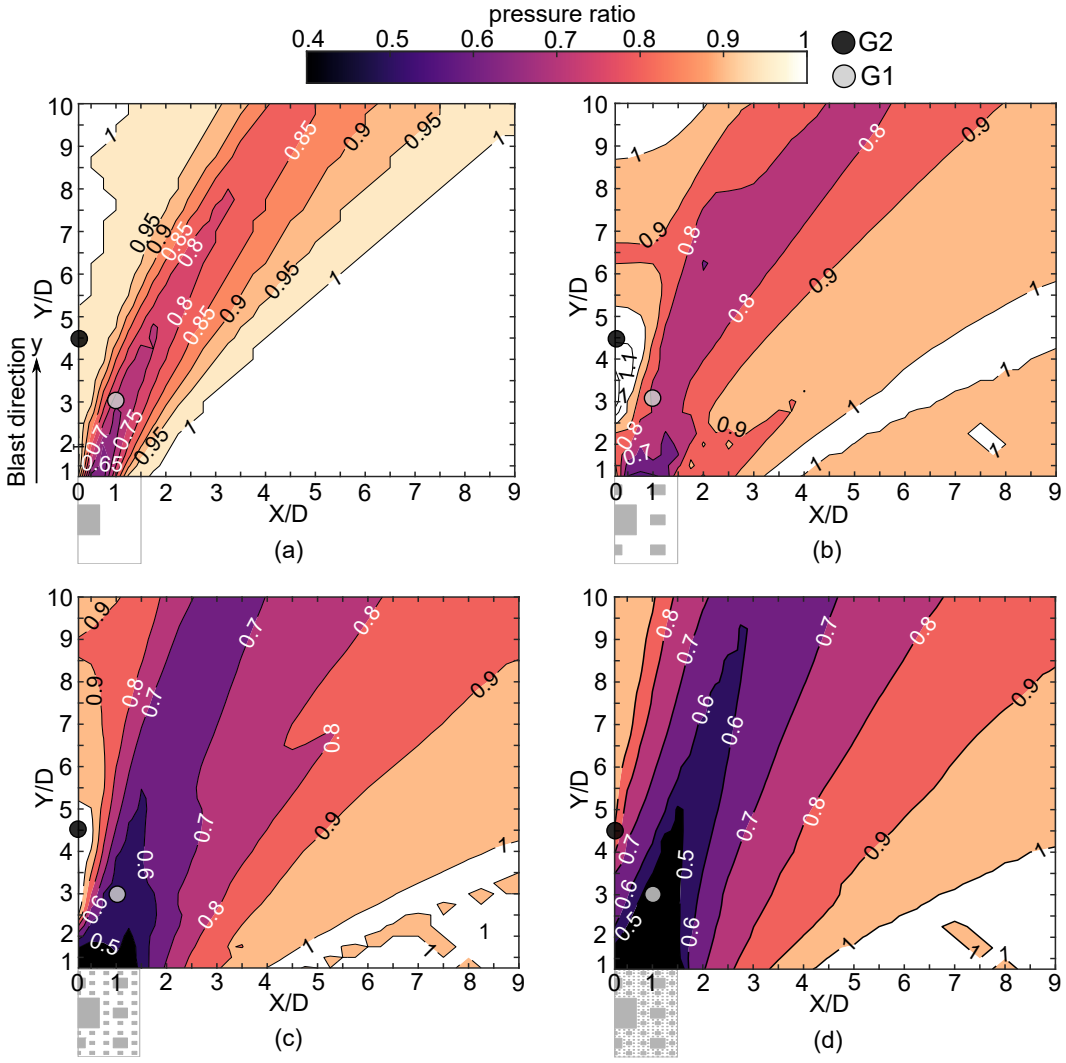

Figure 6.10: Contour plots of the peak overpressure ratios in the downstream region of the pre-fractal arrangements: (a) pFI-1, (b) pFI-2, (c) pFI-3, and (d) pFI-4.

From Figure 6.10, it is quite obvious that the pressure reduction behind the obstacle depends on the wave interference at a given location. The mitigation occurs over an increasingly wider zone as the complexity of the pre-fractal shape increases. Their corresponding mitigation values also improve, with up to 60% pressure reduction for pFI-4 (Figure 6.10d). It is worth noting that the more complex obstacle shapes viz., pFI-3 and pFI-4, do not have a strong shock-shock interaction (constructive wave interference) in the downstream (Figure 6.10c and 6.10d). Such an interaction would have resulted in pressure amplification, as Chapter 5 previously showed with supportive literature for 'blocky' obstacles (Hahn et al. 2021, Yang et al. 1987), also observed here for pFI-1 (Figure 6.10a), and pFI-2 (Fig 6.10b).

In addition, the spatial pressure ratios across the length of Y/D at X/D=0 for pFI-1, pFI-2, pFI-3, and pFI-4 are given in Figure 6.11, which quantitatively confirms the pressure mitigation effectiveness of pFI-3, and pFI4 and its effect over a greater downstream distance, as well as constructive wave interference of pFI-1 and, in particular, pFI-2.

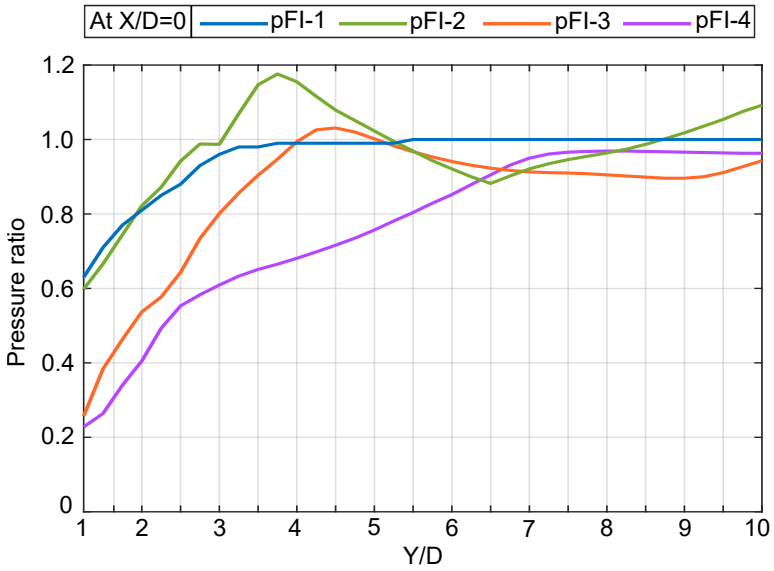

Figure 6.11: The spatial pressure ratios of pFI-1, pFI-2, pFI-3, pFI-4 extracted from Figure 6.10 for the length of Y/D at X/D=0.

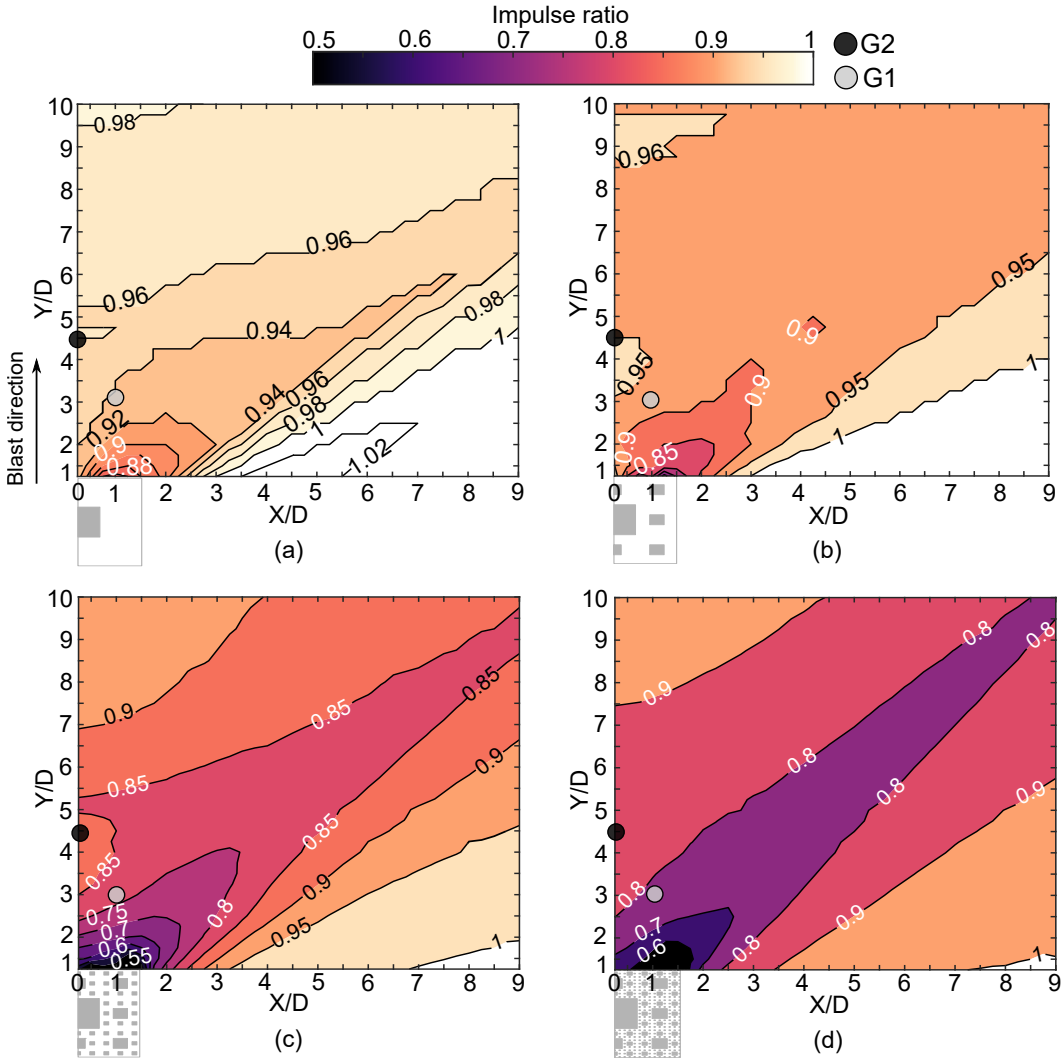

Figure 6.12: Contour plots of the peak specific impulse ratios in the downstream region of the pre-fractal arrangements: (a) pFI-1, (b) pFI-2, (c) pFI-3, and (d) pFI-4.

Instead, for these more fractal-like obstacles, a more diffuse and distributed pattern of pressure is obvious. The pressure has been distributed out over a broader region instead of a narrow zone, resulting in improved attenuation as seen in Figure 6.10d. The specific impulse mitigation plots in Figure 6.12 also show a similar pattern. Even in terms of specific impulse, an increasing complexity of the pre-fractal shape results in an enhanced and widened zone of mitigation. The corresponding specific impulse reduction (Figure 6.12d) reaches up to 40% locally behind the obstacle and remains at around 20% over most of the region that was monitored (10D). This may be attributed to an increase in the frontal

area of reflective surfaces, an enhanced wave trapping, and the altered wave interference patterns downstream due to modifications introduced in the directionality of the blast wave.

To probe the temporal evolution of these parameters in the downstream region, two gauges, G1 and G2 (labelled in Figures 6.10 & 6.12 and located at X/D=1, Y/D=3 and X/D=0, Y/D= 4.5 respectively) were chosen for further investigation. These time history plots, both in terms of the overpressure and the specific impulse, are shown in Figure 6.13 for all the pre-fractal configurations. With each iteration, there is a delay in the arrival of the shock front at both G1 and G2, and this delay is more pronounced with increasing pre-fractal complexity, supporting the experimental findings of Chapter 3.

At G1, the reductions in peak overpressure and peak specific impulse correlate with the complexity of the pre-fractal (Figure 6.13a & 6.13b). From this, it is likely that G1 falls in the destructive interference zone mentioned in Chapter 5. However, at G2, while there is a mild increase for the other obstacles, pFI-4 shows a strong attenuation (Figure 6.13c). The peak specific impulse values on the other hand, decreased with increasing complexity of the pre-fractal (Figure 6.13d). These results support the idea that obstacles with a more fractal-like shape can prevent the load amplification caused by constructive wave interference.

The effectiveness of obstructing a blast wave, measured in terms of intensity mitigation, may therefore be given as: pFI-4 > pFI-3 > pFI-2 > pFI-1, based on the average pressure mitigation of the flow-field in Fig 6.10a-d which was 5%, 10%, 14%, and 20% for pFI-1, pFI-2, pFI-3, and pFI-4 respectively.

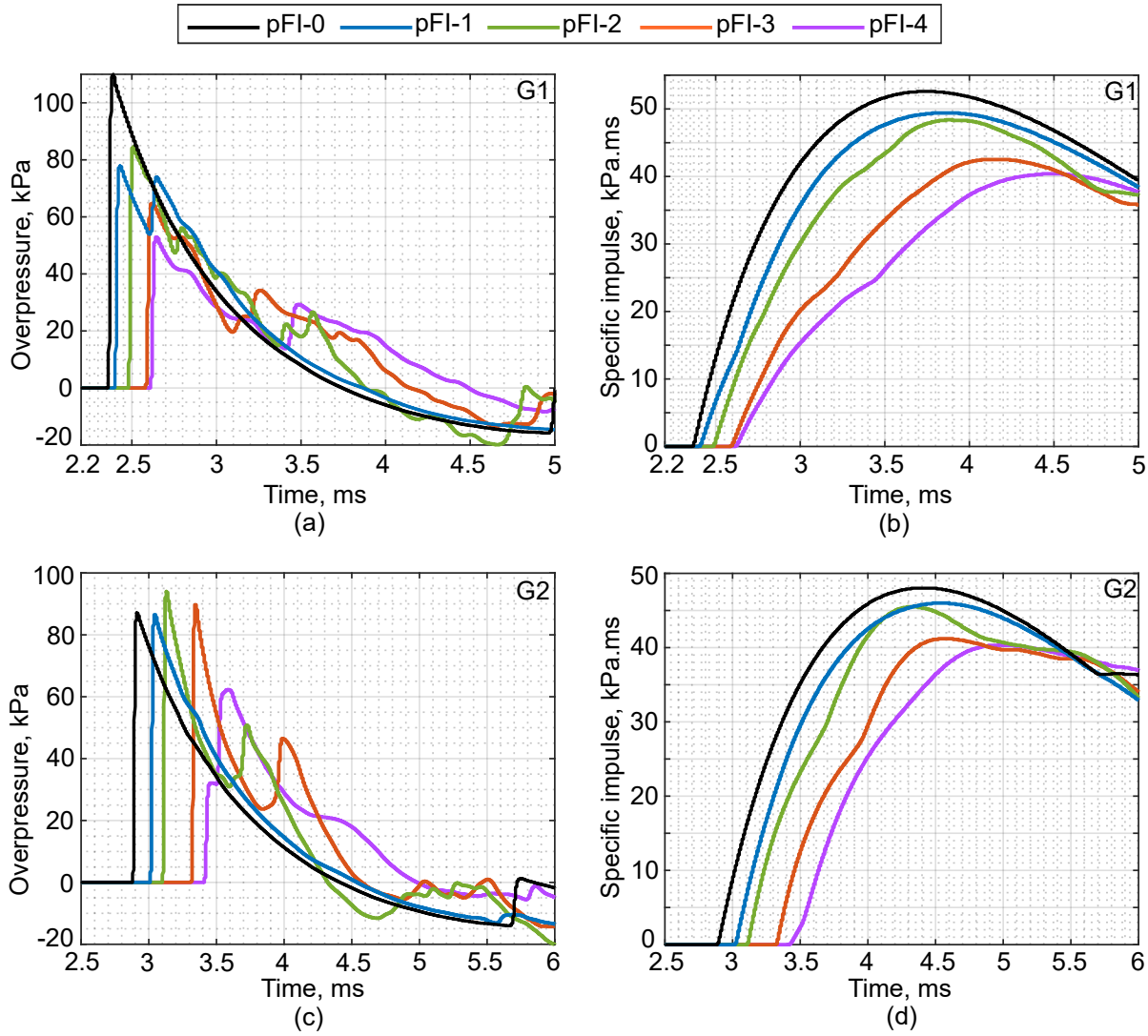

Figure 6.13: The overpressure and specific impulse histories at **(a,b)** G1 and **(c,d)** G2 for all pre-fractal obstacles: pFI-1, pFI-2, pFI-3, pFI-4 and the reference pFI-0.

6.4 Summary and Conclusion

A numerical investigation of blast wave mitigation using pre-fractal shaped obstacles based on the Sierpinski carpet were performed for the experimental configuration of Chapter 3 using a physics-based CFD solver, Apollo Blastsimulator. The blast waves in this numerical study were generated using a 0.25 kg hemispherical C4 explosive at three scaled distances $Z = 1.87, 2.24$, and 2.99 m/kg$^{1/3}$. Four pre-fractal obstacle configurations – pFI-1, pFI-2, pFI-3, pFI-4, were modelled recreating complex blast wave-obstacle inter-

actions.

The primary aim of this numerical work was to understand the mechanics of the enhanced blast mitigation reported experimentally for pre-fractal-like shapes such as pFI-3. Subsequently, the effectiveness of increasing the complexity of the pre-fractals by another iteration (pFI-4) was studied. Finally, the relationship between the pre-fractal configuration and the spatial bounds of the ensuing blast mitigation were explored.

The enhanced blast mitigation in the downstream region of obstacles that more closely resemble a true fractal (such as pFI-3) was due to the strength of the wave reflection and the intensification of trapping within the confines of the fractal, which resulted in a reduction in the proportion of incident pressure transmitted downstream. This was related to the concept of impedance, and therefore increasing pre-fractal iterations exhibited higher impedance. Moreover, fractal-like shapes were found to significantly alter the direction of the incident wave and generate additional vorticity that led to a further reduction of kinetic energy and momentum in the direction of the blast wave.

The role of increasing the pre-fractal complexity by another iteration (pFI-4) was assessed and it was confirmed that this higher order pre-fractal could further enhance reflection and diminish the transmission of the incident wave. As the obstacles took a more fractal-like shape, an inflexion point was observed in the impedance values, thereby supporting the idea that fractal-like shapes can be a more effective protective structure.

The mitigation of pressure and specific impulse in the downstream region occurred along zones associated with the location of destructive wave interference patterns in the downstream region. Such zones were found to widen spatially as the complexity of pre-fractal increased, leading to improved mitigation. Strong shock-shock interactions that result in load amplification, commonly encountered in downstream regions of a solitary block-like obstacle, were not observed for the ‘pre-fractal’ block shapes such as pFI-3 and pFI-4.

Specifically, the peak reduction in pressure and specific impulse in the downstream region of the pFI-4 pre-fractal arrangement was found to be 60% and 40% respectively. It was thus concluded that complex pre-fractal obstacles (pFI-4 > pFI-3 > pFI-2 > pFI-1) can more effectively mitigate an explosion in the mid-field. The findings in this work are significant in that they confirm the complex behaviour driving mitigation through blast interaction with complex obstacles, and facilitate further research and design in this area.

Chapter 7

Summary and Conclusion

7.1 Summary

This thesis has aimed to develop a comprehensive understanding of the blast mitigation behaviour of fractal obstacles of increasing complexity through combining experimental and numerical investigations.

When a high explosive is detonated, the explosive charge experiences a quick change in state and is transformed into a high-pressure, high-temperature gas, resulting in a rapid release of energy. The surrounding air becomes compressed and is displaced when the gas expands, resulting in a high-pressure shock discontinuity (shock wave). As the shock wave travels away from the explosive at supersonic speed, it may cause catastrophic damage to any building it directly interacts with. To protect buildings and their residents from such risky interaction, blast protection engineers have recently been challenged with inventing efficient, sustainable protective barriers that suitably could fit in urban environments to redirect and mitigate the incoming blast wave. The recent employment of trees and hedges as blast protective obstacles showed promising mitigation results due to the existence of multi-scale and self-similarity features.

Hence, this thesis worked on extensively understanding the mitigation of blast wave interaction with rigid structures having multi-scale and self-similarity features such as fractal. A fractal is an object that has a self-repeating pattern embedded within itself, i.e., it is multi-scale and self-similar by definition. So, it is a method of creating an obstacle of increasing complexity. Blast wave mitigation occurs as a combination of blast wave reflection, diffraction around edges, and transmission through a permeable surface or the openings in the protective structure. In addition to this, the interference between the transmitted and diffracted waves in certain regions behind the protective structure can enhance the level of mitigation.

To this end, this thesis experimentally and numerically studied the blast mitigation behaviour resulting from the interaction of blast waves with fractal obstacles of increasing complexity with the overall goal of better understanding these new, sustainable, nature-inspired blast protection systems and predicting the mitigation.

Chapter 2 presented the theoretical considerations of blast loading, and reviewed the current knowledge of blast-structure interactions. It demonstrated the direct interaction of blast wave with structural target itself highlighting the blast loading amelioration due to clearing phenomena. Then, it explained the indirect interaction of blast wave with structural target in the presence of the wall barrier, single obstacle, multiple obstacles, and hybrid obstacle with particular focus on blast mitigation due to the evolution of blast wave at downstream, and the determination of the blast loading acting on structural target among various predictive tools. It illustrated the process of blast wave interaction phenomena which significantly affect the level of blast wave mitigation from the interaction with obstacles including diffraction, reflection (diverting away from the target structure), expansion/volume increase, vortex creation/- growth, porosity, and surface roughness. It thus fully has met objective 1:

'To review current literature on blast mitigation arising from interaction with obstacles where the behaviour and prediction of mitigation are discussed, together with the key mech-

anisms and factors governing the attenuation.'

Chapter 3 demonstrated the design requirements of choosing Sierpinski carpet configurations to create practical obstacles with increasing complexity through performing a finite number of iterations. It is therefore, a so-called pre-fractal obstacle with increasing complexity. Then, the attenuation of blast wave after interacting with different pre-fractal complexity orders were experimentally quantified for evaluating the role of increasing complexity of pre-fractals amongst comparing the performance with the reference case. It further explored the mechanics of a such complex blast wave interaction for a better understanding of blast wave mitigation behaviour and developed a relation of predicting blast loading parameters to enable a fast assessment of using pre-fractal configurations in blast protection strategies. Chapter 3 successfully has met objective 2 :
'To experimentally quantify the blast wave attenuation after interaction with a functional arrangement of different fractal obstacles of increasing complexity and understand the performance of each obstacle, and develop relations for blast loading mitigation behind fractals.'

In Chapter 4, the numerical modelling of simulating the blast wave propagation in free-field and in the presence of pre-fractal obstacles of increasing complexity where the blast mitigation occurs was implemented using CFD software called Apollo. The fidelity of Apollo in predicting blast loading of free-field scenario and also the abilities of recreating complex blast wave-obstacle interactions in pre-fractals scenarios were demonstrated using a detailed, multi-part mesh sensitivity analysis that involved both quantitative and qualitative comparisons with the experimental data taken from Chapter 3 and special data from the literature. Based on these mesh studies, the required computational cell element lengths for accurately simulating blast wave interactions with pre-fractal obstacles of increasing complexity having geometrical shapes either square, rectangular, or circular were identified in which these findings were used for simulations setups of Chapter 5 and Chapter 6. Chapter 4 hence has accomplished objective 3:

'To implement a high-fidelity CFD numerical model that can accurately simulate the propagation of blast waves both in free-field and complex- domains involving interaction with fractal obstacles having various levels of complexity, with a view to accurately predicting the blast loading behind them.'

In Chapter 5, the numerical analysis of blast loading attenuation due to blast wave interaction with a single standalone obstacle was performed using Apollo to understand and characterise the altered flow field downstream of a single obstacle, cylindrical obstacle in this study, loaded by a blast wave, due to wave interference. A parametric study was developed to explore the influences of the size of the obstacle, blast wave intensity, location of the obstruction, and the size of the target- chosen based on observations of experimental work in Chapter 3- on blast loading reduction behind the obstacle. Finally, an artificial neural network (ANN) scheme was trained using scaled input data reused from a parametric study to predict the mitigation ratio of blast loading of a single obstacle. Chapter 5 fully achieved object 4:
'To perform a parametric numerical study of the interaction of blast waves of different strengths with a single obstacle to understand and characterise the altered flow field in its downstream region due to wave interference with a view to developing a fast-running tool to predict blast mitigation behind the obstacle.'

In Chapter 6, numerical analysis to investigate the mechanisms governing blast wave mitigation due to interaction with pre-fractal obstacles of increasing complexity, based on the Sierpinski carpet, were performed using Apollo in accordance with experimental configurations in Chapter 3. They also addressed the questions of 'What amount of additional mitigation would be present if the complexity of pre-fractal is increased further?' 'What is the relationship between the spatial bounds of the mitigation and the fractal complexity and size?' It, therefore, met objective 5:
'To perform numerical analysis of blast wave interaction with fractal obstacles of increasing complexity to explain the precise mechanisms governing blast mitigation, and to study

the role of increasing complexity on attenuation patterns, and to characterise the spatial bounds of mitigation due to fractals in the downstream.'

7.2 Conclusions

The following are summaries of the key conclusions of this thesis, arranged in the order in which they appear in this thesis:

- The current literature review showed structures with multi-scale and self-similarity features such as hedges and plants (naturally occurring fractal-like structures) demonstrated excellent blast mitigation behaviour (Gebbeken et al. 2017, Warnstedt & Gebbeken 2020). The results of experimental work in this thesis have shown that obstacles resembling true fractals can produce similar levels of blast mitigation since it showed reductions in peak overpressure up to 26% and peak specific impulse up to 19%.

- The mechanism of blast mitigation of pre-fractal obstacles of increasing complexity is fundamentally different from singular or arrays of regular obstacles because of the multiple wave reflections off the smaller obstacles in a process known as 'trapping', and it, therefore, makes a strong case for the use of pre-fractal obstacles in urban blast protection settings.

- Blast parameters such as arrival time, peak overpressure, and peak specific impulse at any given location behind pre-fractal obstacles with increasing complexity (first three iterations) are linearly dependent on the newly defined obstruction factor, OF, suggesting that this behaviour is inherently determinable.

- Apollo CFD solver can be used to accurately predict the blast loading such as overpressure and impulse in the free-field event (no obstruction) with the requirement of mesh resolution to be, $h < SoD/160$ for overpressure, and $h < SoD/30$ for specific impulse, where SoD is the stand-off distance to the nearest gauge.

- Apollo CFD solver can reliably predict the blast loading affected by all waves interference occurring downstream of pre-fractal obstacles of increasing complexity having square and rectangular shapes, using obstacle cell ratio ≥ 2. This ratio is defined as the width of the smallest obstacle over the mesh element size. Apollo can also faithfully simulate the blast wave trapping behaviour and multiple wave reflections which are generated due to the interactions with shapes with more fractal-like when the obstacle cell ratio is increased more than 4.

- When cylindrical poles are used to create any pre-fractal obstacle arrangement, Apollo can efficiently simulate the blast wave diffraction around the cylindrical surface and predict the blast loading under the influence of the blast waves interference at the downstream region using obstacle cell ratio ≥ 10.

- To obtain a high level of blast mitigation behind a single obstacle, key parameters including the blast wave strength, obstacle size, distance between target and obstacle, and target length governing the mitigation of equivalent energy impulse, EEI (total blast load), are carefully to be considered.

- The general pattern of blast loading mitigation on a reflective target wall behind the single obstacle can be such that the region can entirely lie in the shadowing region, or in the wave interference zone, or have a combination of both shadowing and wave interference regions where the mitigation level of each region varies depending on obstacle size and distance between obstacles and target.

- An artificial neural network model (ANN) can be used to obtain the total load on the target wall downstream of a single, cylindrical obstacle despite the complex wave interactions.

- The further numerical investigation of the performance of different pre-fractal complexity arrangements showed reductions in peak pressure up to 60% and specific impulse of up to 40% recorded for the highest iteration pre-fractal, i.e., obstacles

that most closely represent a true fractal. The mechanism of enhancing blast mitigation in the downstream region of obstacles that more closely resemble a true fractal is demonstrated due to the strength of the wave reflection and the intensification of trapping within the confines of the fractal, which results in a reduction in the proportion of incident pressure transmitted downstream.

- Increasing the complexity of pre-fractal configuration produces better impedance and substantially alters the direction of the incident wave and generates additional vorticity that leads to a further reduction of kinetic energy and momentum in the direction of the blast wave propagation.

- High complexity order in pre-fractals can widens zones associated with the location of destructive wave interference patterns in downstream region and eliminates the shock-shock phenomena that results in load amplification, commonly encountered in downstream regions of a solitary block-like obstacle.

- The effectiveness of obstructing a blast wave, measured in terms of blast intensity mitigation, are classified according to the pre-fractal's complexity from lowest level to the highest level.

7.3 Evaluation and Future Work

In this thesis, Chapters 3 and 6 showed the ability of increasing the complexity level of Sierpinski carpet fractals (termed there as pre-fractals) to improve blast wave attenuation compared to ones with a lower complexity level. However, the construction of those pre-fractals was based on fixed parameters including fractal dimension, geometrical shape, and orientation. Therefore, future research interest in designing Sierpinski carpet fractals as effective protective structures would also consider the role of these parameters in the evolution of blats wave at downstream region and the impedance.

Moreover, whilst experimental and numerical investigations in Chapters 3 and 6 used

a single arrangement of the pre-fractal obstacle, a collection of thesis complex obstacles arranged into a fence-type protective structure will likely result in more significant breakup of the blast wave and greater mitigation over a larger area. Further, the configuration tested was that of a pseudo-2D Sierpinski carpet fractal extruded along its height. It is probable that a pre-fractal that is self-similar in all three dimensions such as Menger sponge (cube) would result in even greater attenuation than observed herein and its mitigation behaviour should be studied in future.

As this thesis effectively provided a comprehensive understanding of mechanisms governing mitigation behaviour behind complex obstacles constructed as pre-fractals with various iterations, further work of this thesis can be towards developing a semi-empirical predictive method for rapidly estimating the perturbed blast loading behind any such complex arrangement. Although the obstruction factor formula in Chapter 3 shows strong linearity with blast wave parameters, it only provides initial measurements of the effectiveness of blast attenuation behind certain pre-fractal arrangements since it only depends on the frontal area of pre-fractal elements and the distance between explosives and obstacles without considering other important factors such as blockage ratio, and the distance in the downstream. Herein, the development procedure of the rapid predictive approach in the future would be suggested.

In similar steps to the work of the development ANN model for predicting total blast loads in downstream region of a single obstacle (sample configuration) which was executed in Chapter 5, this future work could be completed in two parts: first, developing a parametric study to characterise the alterations of blast wave parameters behind complex pre-fractal configurations; second, using outcomes of the parametric study to derive more sophisticated relations of blast wave parameters attenuation in addition to the obstruction factor relation in order to develop a comprehensive predictive approach.

The parametric study would be conducted by implementing various numerical simulations using a high-fidelity CFD solver such as Apollo Blastsimulator which would include the

most influential key factors observed from Chapter 3, 5, and 6 such as blockage ratio, blast wave strength, pre-fractal obstacle size (outer and inner), obstruction location ratio and target distance. The behaviour of blast wave attenuation would be then characterised and the significant contributors to the evolution of the load would be identified and scaled for a generalisation scheme.

The development of sophisticated predictive methods could be based on grey-box modelling such as ANNs, gene expression programming, or any other machine learning approach; making use of physical observation and insight to derive meaningful and robust data-driven methods (see Chapter 5). This tool/function could be therefore used to design an optimal arrangement of obstructions to achieve a maximum reduction in blast loading in order to lower cost or volume of material.

The conclusions of this thesis should be used as persuasive evidence in supporting fractal obstacles of increasing complexity being utilised in the design of protective structures for improved blast mitigation, and the research methodologies presented here could be applied to other future research topics.

7.4 Limitation

The outcomes and the methods of this thesis have some limitations. Firstly, the CFD prediction of blast wave loading in Chapter 4 for both free-field and complex scenarios is subjected to a numerical error within 10% of the actual value. Therefore, the ANN code in Chapter 5 consecutively has a 10% deviation from the real values. Secondly, the adopted numerical scheme of simulating the blast mitigation due to interactions with pre-fractal obstacles in Chapter 6 has not considered the topology of the ground surface which has induced significant variation in the incident blast wave measurements. Hence, the future completion of this thesis's work should take into account these two limitations and work on enhancing the numerical prediction error.

Appendix A

Matlab Script function of ANN

This chapter presents a Matlab script function of artificial neural network developed in Chapter 5 to predict the ratio of equivalent energy impulse (EEI).

```
function [y1] = myNeuralNetworkFunction(x1)
%MYNEURALNETWORKFUNCTION neural network simulation function.
%
% Auto-generated by MATLAB, 08-Dec-2021 16:14:36.
%
% [y1] = myNeuralNetworkFunction(x1) takes these arguments:
%   x = Qx4 matrix, input #1 ex:==>  x1=[ Z_do,dt/D,TA/W^(2/3),TL/dt];
% and returns:
%   y = Qx1 matrix, output #1 == > y is the EEI mitigation ratio.
% where Q is the number of samples.

%#ok<*RPMT0>

% ===== NEURAL NETWORK CONSTANTS =====

% Input 1
x1_step1.xoffset = [0.087;1.25;0.019;0.02];
```

```
x1_step1.gain = [0.371402042711235;0.041025641025641;0.688468158347676;
0.401606425702811];
x1_step1.ymin = -1;

% Layer 1
b1 = [0.04727711996145469997;-0.048535614575326513354;
-0.047814664649781242478;0.049005617688630653817;
-0.044104890593911032226;-0.043363084626818551581;
0.047625211958855211136;-1.0935408215093722628;
0.046588390832450046752;-0.048346731272902315757
;0.52545761834422710645;0.049608145099861715444;
-0.047728154560645483229;0.047444300849130260911;
0.047489987599735244972;0.051060062400189183685;
-0.019681197683052067265;-0.047338969611454520536;
-0.047410617245111745521;0.046107887574891079363;
0.27862310362044689915;-4.2855770739514520429;
0.047203997397045928397;0.048140919627853870355
;-0.047001951897401146596;0.047288875745188481414;
-0.047092662485394475025;-1.6130502728447204674;
0.66348233227033226456;0.047342915100695798225;
0.63543760224801182357;-0.048834037455762473179;
-0.049678264655882313494;-0.047429633225960277088;
-0.047275075328670618235;0.047783011647723139248;
-0.047921365907739106593;0.048628790220774043007;
0.037843659340467093732;-0.047733356823698655513;
-0.041954722928701920777;0.047498145353137254111;
0.047255115969013251898;-0.047283716339271079922;
-0.047723787162629434377;0.048973494966750560908;
0.048240143789176910538;-0.047445422908030332465;
-0.71138139049400395122;-0.047617708832831090461;
-0.047556129044268057038;-0.050895035198338392513;
0.047822646626937227732;-0.050049785454062002688;
0.047439492693672723232;-0.045369005933349644544;
0.047984026395637244256;0.047963324358902166555;
```

```
0.048540661897905186539;0.04853602605881390808;
-0.047140252225219315962;0.047518411906274343748;
0.047674698450593862298;-0.04544402042495041677;
-0.048016617709139633452;-0.048458558320049846535;
-0.34504783443804248888;0.28415747286638926017;
0.050285736290765527257;-0.047140044418987822605;
0.048318086876786008055;-0.047284541010840293318;
-1.587350743723449753;-4.1178841096056011395;
0.0479099478239208634 3;-0.049461693323247055143;
0.028347510205302735992;-1.0650015299152659765;
-0.047563452618000968963;0.67624635203282923435;
-3.0277090279853995369;0.048367111605963422627;
-0.048753918688857138253;-0.04961574236810565447;
-0.048695432022450135801;-0.16807870349633813323;
1.372062854929150699 2;-0.49042467885272189587;
0.046900674287152263608;0.043793024304675708114];
IW1_1 = [-0.011415058428845598418 0.031325462321029451385 ...
    0.01190025918228931022 ...
    -0.096274538503317574 9;0.011657994281087772498 ...
    -0.031904610987446894999 -0.012642519101036853862 ...
    0.098661300001961507733;0.011518717317899711261 ...
    -0.031574691585017876372 -0.012214038921077278663 ...
    0.097295609425164630846;-0.011748988811883329803 ...
    0.032117024897905271 93 0.012926561384710792343 ...
    -0.099549286442506670913;0.010804254271937943632 ...
    -0.029797776140654275679 -0.010147755123142865319 ...
    0.090200659612634223605;0.010661080370212157667 ...
    -0.029426368873817256022 -0.009762411046098352918 1 ...
    0.088768646847909471465;-0.011482167943723661438 ...
    0.031487169546788172647 0.012102893954503849208 ...
    -0.096936013752690688983;-2.4743704184516976952 ...
    -0.29884243130996834825 -3.7709644045064423246 ...
    4.263440025984063908;-0.011282404588300565598 ...
    0.031002073513015170059 0.011505346752503689198 ...
```

```
-0.094962803594256947615;0.011621471420661057608 ...
-0.031818655566837515669 -0.012529415576275980404 ...
0.098303927166919866099;0.82004757851044762784 ...
0.79362441259467997323 -1.2051985634963262584 ...
-0.69458091676076783028;-0.011865918850453070418 ...
0.032386268629626839555 0.013296118656981903774 ...
-0.10068494452574340559;0.011502025697116974312 ...
-0.031534768834555505779 -0.012163211882701970706 ...
0.097131443541276576981;-0.011447283050439701832 ...
0.031403271705469776309 0.01199732456516325492 ...
-0.096592351284518790377;-0.011456091822567524355 ...
0.031424488959614145511 0.012023934408174735342 ...
-0.096679170971658637268;-0.012149303539232041149 ...
0.033021043735559446608 0.014211616549740726731 ...
-0.10340897748242028342;0.005478495729916043298 4 ...
-0.014871491119559756763 -0.001969931993621900322 1 ...
0.041160027821093667089;0.011426978979195699312 ...
-0.031354279780790209053 -0.011936114796522073397 ...
0.096392144156933340371;0.011440788799263182027 ...
-0.031387616033836461538 -0.011977727760739549992 ...
0.096528329286493672057;-0.011189910103938440281 ...
0.030773738142558147712 0.011234538427851525552 ...
-0.094045251106618446557;1.328648796155776024 ...
-0.35769209051222949913 1.4177827550772026388 ...
-1.0151115302639974747;-3.0471321863490268278 ...
-0.55214148798720574796 -1.589149354587517049 ...
0.23096740911549260011;-0.011400967454835644541 ...
0.031291344527685206744 0.011857951127033913158 ...
-0.096135451918691369744;-0.011581704603870703399 ...
0.031724607001603913337 0.012406857924299491414 ...
-0.097914170383075524451;0.011362038768280282794 ...
-0.031196805989964458694 -0.011741510345450355962 ...
0.095750894476937895017;-0.011417324102654998613 ...
0.031330942638228179153 0.011907069760530542349 ...
```

```
-0.09629689661427866 2;0.011379516178383747987 ...
-0.031239299277232391444 -0.011793707473044954398 ...
0.095923603445096719544;-1.2842289864192222293 ...
-0.58209637555083648675 1.3112464096205291852 ...
-2.6034267974139218005;1.1795330805013910513 1.08457689948634739 ...
-0.77664851639398202465 ...
-0.55428891909089550438;-0.011427739621026267863 ...
0.031356116708147814542 0.011938404295849969206 ...
-0.09639964445992890707;-0.67127948388363134491 ...
0.073215841438393353124 1.9191385020458926469 ...
-0.26930200797249403966;0.011715750520935201695 ...
-0.032039723439084559498 -0.012822438278858256169 ...
0.099225327379357311508;0.011879549659807460069 ...
-0.032417378716607263278 -0.013339520709812117613 ...
0.10081690228656918495;0.011444455577870382701 ...
-0.031396455993697731934 -0.011988790548849570863 ...
0.096564480491903609272;0.011414664473312109705 ...
-0.031324508538536889601 -0.011899073939685964052 ...
0.096270643612716519377;-0.011512609676510873399 ...
0.031560092598948971676 0.012195427337402277995 ...
-0.097235550062350031841;0.011539311007862177935 ...
-0.031623833230708116304 -0.012276903769109431125 ...
0.097498008249240999956;-0.011676019867733082591 ...
0.031946888831219489461 0.01269853518541370907 ...
-0.098837492353030936831;-0.009578010007777689599 5 ...
0.026493650643201499539 0.007183835327473590305 6 ...
-0.077981997728306898243;0.011503028822890500743 ...
-0.031537172168796721861 -0.012166265043645908828 ...
0.097141322094402307585;0.010388205458605928588 ...
-0.028706417824675100475 -0.009056253124087750711 ...
0.086038040602780710 42;-0.011457664566732410349 ...
0.031428275148607222322 0.01202868844797506595 ...
-0.096694667059034802858;-0.011410818156105246 44 ...
0.031315200844663000634 0.011887518363874374772 ...
```

```
-0.096232687978698619458;0.011416329853288947546 ...
-0.031328537592561191139 -0.011904080714709506031 ...
0.096287084952762488891;0.011501183322820534086 ...
-0.031532751051742427539 -0.012160648649233087026 ...
0.097123149531679317525;-0.011742764303861093558 ...
0.032102574678521615670 0.012907032374039608888 ...
-0.099488666281898674448;-0.011600873553373599809 ...
0.031769998804836843687 0.012465854626832046509 ...
-0.098102114285011116079;0.011447499593007573471 ...
-0.031403793232524630785 -0.011997978636779493139 ...
0.096594487663535330557;0.81960266343243171061 ...
-0.060843839672870665691 0.80978418288670050984 ...
0.27364840824070918446;0.011480721290103360760 ...
-0.031483695926300951651 -0.012098504967554961007 ...
0.096921765242572496812;0.011468844344729436577 ...
-0.031455169437523015918 -0.012062514845204307459 ...
0.096804812549345073402;0.012116961268052724859 ...
-0.032949885236431726565 -0.014105783865611449049 ...
0.10310024397360795234;-0.011520258036641209398 ...
0.031578371232225808940 0.012218735242852798301 ...
-0.097310752407519282570;0.011951855661522044552 ...
-0.032581443264072411370 -0.013570862049744534389 ...
0.10151541972317569551;-0.011446354883197821031 ...
0.031401037771255080333 0.011994523956655010408 ...
-0.096583208543044599126;0.011047728198325956067 ...
-0.030418262214246018227 -0.010825779181298700662 ...
0.092630853711319446897;-0.011551407381086176152 ...
0.031652640705174324431 0.012313909387047915905 ...
-0.097616817919408085946;-0.011547410289906516467 ...
0.031643127371633182621 0.012301675204535917479 ...
-0.097577566592294301406;-0.011658971348340011961 ...
0.031906902760226937832 0.012645550266729262134 ...
-0.098670844474555347015;-0.011658073216874854580 ...
0.031904798670116099601 0.012642766744490736147 ...
```

```
-0.098662085605437377378;0.011388684444479260302 ...
-0.031261560859821457825 -0.011821142577139991808 ...
0.096014172776274525622;-0.011461572057041940348 ...
0.031437678330458122822 0.012040503736551763 3 ...
-0.096733160101989887347;-0.011491712391664786821 ...
0.031510064146291413834 0.012131865659497736293 ...
-0.097029966281642038295;0.01106216514395943519 ...
-0.030454594108876020808 -0.010866861010526931985 ...
0.092774661084808779377;0.011557698710176499135 ...
-0.0316676104724922594 1 -0.0123331831976569474 ...
0.097678609183022915841;0.011643091704410709827 ...
-0.031869585848383272242 -0.012596305493160344507 ...
0.098515543205186628661;-0.24272631637963693052 ...
1.6895375536841088504 0.12149111507198354087 ...
-2.327441181501108236 1;-0.221011799748032811 14 ...
-0.86590926495515085914 -1.8258681812311254866 ...
3.6104178322424407277;-0.011997857581342625741 ...
0.032684964946929080665 0.013718982336282775289 ...
-0.10195841839212088642;0.011388639691615983981 ...
-0.031261464112642731172 -0.011821013502039193 21 ...
0.096013758794904410787;-0.011615934645597392888 ...
0.031805590936372356292 0.012512316130931459141 ...
-0.098249708944884703299;0.011416487311024734949 ...
-0.031328920707015268932 -0.011904551975187459625 ...
0.096288626179467942667;-0.18929967283549983814 ...
-0.16386788719061926023 0.20346974232546921613 ...
-2.0149855286224891415;-3.1789654399385987027 ...
-0.38051141517780140422 -0.37365775280310464801 ...
0.12740046087190254331;-0.011537107341775756572 ...
0.031618579616180392255 0.012270167816502695543 ...
-0.097476353868012233228;0.011837465494386665427 ...
-0.032321142689392928782 -0.013205735678182372803 ...
0.10040920791893416519;-0.007562915365547625938 5 ...
0.02076703293256429439 0.003885391970246275441 4 ...
```

```
      -0.058943923034840223218;0.53256737574288226522 ...
      -0.29446358275492978684 1.3310246194352415294 ...
      -2.1219616374841590023;0.011470257696788702453 ...
      -0.031458563847257106638 -0.012066793668955520455 ...
      0.096818727277292793154;0.71030459947587343272 ...
      0.20003410439916011199 0.33168672140728289177 ...
      1.3060054424667593143;-1.4706983437288416727 ...
      -0.96603199080766133378 -2.0607020937966380458 ...
      0.70694295011389507444;-0.011625412770335161877 ...
      0.03182794593842010189 0.012541593311395093924 ...
      -0.098342506928120798637;0.011700238490819877754 ...
      -0.032003533241602773185 -0.012773991818530136197 ...
      0.099073992663198662267;0.011867394842574889927 ...
      -0.032389642955625665144 -0.013300819808880405548 ...
      0.10069926228591512263;0.011688916554670808132 ...
      -0.03197707451117372951 -0.012738686870417018776 ...
      0.098963451961715867555;-1.4726206587284451643 ...
      -0.2542270476968409576 -2.9374759651374930947 ...
      4.1587192383125213269;1.4939061312719770225 2.2237174636149115159 ...
      -0.62259123621232992374 ...
      -0.52629466987838247061;-0.92032913266917071304 ...
      -0.14970355935089013633 1.4151204859966257654 ...
      -1.437568528971153281;-0.011342528310293401375 ...
      0.031149267665829857843 0.011683393724726515162 ...
      -0.095557969885781399166;-0.010744097458944754792 ...
      0.029642278505998910509 0.009984621174228087633 9 ...
      -0.089599145777203278995];

% Layer 2
b2 = -0.41919922303886331116;
LW2_1 = [-0.11490466131717667897 0.11783309747342822493 ...
      0.11615684400932341225 -0.11892390781502713837 ...
      0.10747510418351320649 0.10572819182822408568 ...
      -0.11571575124686872549 1.9151293060836678261 ...
```

```
-0.11329738542836083337 0.11739429365906058067 ...
-0.83221303007162350518 -0.12031998572860085062 ...
0.11595545804940787793 -0.11529431073401388841 ...
-0.11540076763082723899 -0.12367336535026811351 ...
0.048545417102978515034 0.11504883887420813693 ...
0.11521581265493399671 -0.11217403827902791558 ...
-1.6088840074440919903 2.1900122613395116566 ...
-0.11473416672761849178 -0.11691586134114159701 ...
0.11426286470677032847 -0.1149320693953471556 ...
0.1144745105443355504 1.2450124733132923449 2.0279157849333366848 ...
-0.11505803446277945712 0.692552753414792166 ...
0.11852587305326151013 0.12048227969142996652 ...
0.11526013560412186332 0.11489988854200877677 ...
-0.11608316512743788174 0.11640516331843318854 ...
-0.11804947572183441262 -0.092625757085970414351 ...
0.11596757426321208095 0.10240204769716067246 ...
-0.11541977072927124548 -0.11485335883141098434 ...
0.11492004130603361567 0.11594528557185054818 ...
-0.11884941577543700619 -0.11714655026615536371 ...
0.11529692908117493422 0.58406844459167595041 ...
0.11569827610537969376 0.11555484465498348789 ...
0.12329297505154805659 -0.116175421673989962 ...
0.12134162734719459997 -0.1152831019203054419 ...
0.11044380420463639769 -0.11655094725202512496 ...
-0.11650278366541187702 -0.11784481856531771327 ...
-0.11783406008284418032 0.11458551290378117538 ...
-0.115466976856515413 1 -0.11583098727331322952 ...
0.11061964047019062773 0.11662677010309911718 ...
0.11765411476600300122 1.2183553706627201496 ...
2.2431912022876234758 -0.12188685631759582639 ...
0.11458501128246961764 -0.11732773010309417716 ...
0.11492193878856843403 -1.9933057320373255283 ...
-3.0574290078541772608 -0.11637859425804333857 ...
0.11998090812872366784 -0.069723745401989847825 ...
```

```
      2.2012945409549029563 0.11557190782493613479 ...
      -1.0377598173820212768 -1.8151390453757874077 ...
      -0.11744165698830275057 0.11833996025229145954 ...
      0.12033758883512388205 0.11820418512133408495 ...
      -3.4607900625716498944 -1.1443761275061434812 ...
      -2.2586408465018359415 -0.11402648179859738164 ...
      -0.10674110113562519653];

% Output 1
y1_step1.ymin = -1;
y1_step1.gain = 3.27868852459016;
y1_step1.xoffset = 0.39;

% ===== SIMULATION ========

% Dimensions
Q = size(x1,1); % samples

% Input 1
x1 = x1';
xp1 = mapminmax_apply(x1,x1_step1);

% Layer 1
a1 = tansig_apply(repmat(b1,1,Q) + IW1_1*xp1);

% Layer 2
a2 = repmat(b2,1,Q) + LW2_1*a1;

% Output 1
y1 = mapminmax_reverse(a2,y1_step1);
y1 = y1';
end

% ===== MODULE FUNCTIONS ========
```

```
100
101 % Map Minimum and Maximum Input Processing Function
102 function y = mapminmax_apply(x,settings)
103 y = bsxfun(@minus,x,settings.xoffset);
104 y = bsxfun(@times,y,settings.gain);
105 y = bsxfun(@plus,y,settings.ymin);
106 end
107
108 % Sigmoid Symmetric Transfer Function
109 function a = tansig_apply(n,¬)
110 a = 2 ./ (1 + exp(-2*n)) - 1;
111 end
112
113 % Map Minimum and Maximum Output Reverse-Processing Function
114 function x = mapminmax_reverse(y,settings)
115 x = bsxfun(@minus,y,settings.ymin);
116 x = bsxfun(@rdivide,x,settings.gain);
117 x = bsxfun(@plus,x,settings.xoffset);
118 end
```

Bibliography

Abate, G. & Shyy, W. (2002), 'Dynamic structure of confined shocks undergoing sudden expansion', *Progress in Aerospace Sciences* **38**(1), 23–42.

Abe, A., Takayama, K. & Itoh, K. (2001), 'Experimental and numerical study of shock wave propagation over cylinders and spheres', *WIT Transactions on Modelling and Simulation* **30**.

Alshammari, O. G., Isaac, O. S., Clarke, S. D. & Rigby, S. E. (2022), 'Mitigation of blast loading through blast–obstacle interaction', *International Journal of Protective Structures* p. 20414196221115869.

Alshammari, O. G., Isaac, O. S., Clarke, S. D. & Rigby, S. E. (2023), 'Numerical modelling of blast mitigation of pre-fractal obstacles', *Submitted for publication in International Journal of Protective Structures* .

Anthistle, T., Fletcher, D. & Tyas, A. (2016), 'Characterisation of blast loading in complex, confined geometries using quarter symmetry experimental methods', *Shock Waves* **26**, 749–757.

Aune, V., Valsamos, G., Casadei, F., Langseth, M. & Børvik, T. (2017), 'On the dynamic response of blast-loaded steel plates with and without pre-formed holes', *International Journal of Impact Engineering* **108**, 27–46.

Baker, W. E. (1973), *Explosions in Air*, University of Texas Press, Austin.

Ballantyne, G. J., Whittaker, A. S., Dargush, G. F. & Aref, A. J. (2010), 'Air-blast effects on structural shapes of finite width', *Journal of Structural Engineering* **136**(2), 152–159.

Barakat, M. A. & Hetherington, J. G. (1998), New architectural forms to reduce the effects of blast waves and fragments on structures, *in* 'Structures Under Shock and Impact V', WIT Transactions on The Built Environment, pp. 53–62.

Barakat, M. A. & Hetherington, J. G. (1999), Architectural approach to reducing blast effects on structures, *in* 'Proceedings of the Institution of Civil Engineers - Structures and Buildings'.

Bazhenova, T. V., Gvozdeva, L. G. & Nettleton, M. A. (1984), 'Unsteady interactions of shock waves', *Progress in Aerospace Sciences* **21**, 249–331.

Beale, M. H., Hagan, M. T. & Demuth, H. B. (2010), 'Neural network toolbox user's guide', *The MathWorks* pp. 77–81.

Ben-Dor, G. & Takayama, K. (1985), 'Analytical prediction of the transition from mach to regular reflection over cylindrical concave wedges', *Journal of Fluid Mechanics* **158**, 365–380.

Benselama, A. M., William-Louis, M. J. P. & Monnoyer, F. (2010), 'Prediction of blast wave effects on a developed site', *International Journal of Impact Engineering* **37**(4), 385–396.

Berger, S., Ben-Dor, G. & Sadot, O. (2015), 'Experimental and numerical investigation of shock wave attenuation by dynamic barriers', *Journal of Fluids Engineering* **138**(3).

Berger, S., Sadot, O. & Ben-Dor, G. (2010), 'Experimental investigation on the shock-wave load attenuation by geometrical means', *Shock waves* **20**(1), 29–40.

Beshara, F. B. A. (1994*a*), 'Modelling of blast loading on aboveground structures–I. General phenomenology and external blast', *Computers & Structures* **51**(5), 585–596.

Beshara, F. B. A. (1994*b*), 'Modelling of blast loading on aboveground structures–II. Internal blast and ground shock', *Computers & Structures* **51**(5), 597–606.

Bewick, B., Flood, I. & Chen, Z. (2011), 'A neural-network model-based engineering tool for blast wall protection of structures', *International Journal of Protective Structures* **2**(2), 159–176.

Beyer, M. E. (1986), 'Blast loads behind vertical walls', Prepared for Twenty-Second DoD Explosives Safety Seminar Anaheim, California.

Bhatti, A. Q., Badshah, E., Naseer, A., Ashraf, M., Shah, F. & Akhtar, K. (2017), 'Review of blast loading models, masonry response, and mitigation', *Shock and Vibration* **2017**, 6708341.

Biggs, J. M. (1964), *Introduction to structural dynamics*, McGraw-Hill, New York.

Blazek, J. (2015, chap.2), *Computational fluid dynamics : principles and appli- cations*, Butterworth-Heinemann.

Bogosian, D., Ferritto, J. & Shi, Y. (2002), Measuring uncertainty and conservatism in simplified blast models, *in* '30th Explosives Safety Seminar', Atlanta, GA, USA, pp. 1–26.

Bogosian, D., Yokota, M. & Rigby, S. (2016), 'TNT equivalence of C-4 and PE4: A review of traditional sources and recent data', *Proceedings of the 24th military aspects of blast and shock* .

Børvik, T., Hanssen, A. G., Langseth, M. & Olovsson, L. (2009), 'Response of structures to planar blast loads - a finite element engineering approach', *Computers & Structures* **87**(9), 507–520.

Britan, A., Igra, O., Ben-Dor, G. & Shapiro, H. (2006), 'Shock wave attenuation by grids and orifice plates', *Shock Waves* **16**(1), 1–15.

Bryson, A. E. & Gross, R. W. F. (1961), 'Diffraction of strong shocks by cones, cylinders, and spheres', *Journal of Fluid Mechanics* **10**(1), 1–16.

Burden, F. & Winkler, D. (2008), 'Bayesian regularization of neural networks', *Artificial neural networks* pp. 23–42.

Chapman, T. C., Rose, T. A. & Smith, P. D. (1995*a*), 'Blast wave simulation using AUTODYN2D: A parametric study', *International Journal of Impact Engineering* **16**(5), 777–787.

Chapman, T. C., Rose, T. A. & Smith, P. D. (1995*b*), 'Reflected blast wave resultants behind cantilever walls: A new prediction technique', *International Journal of Impact Engineering* **16**(3), 397–403.

Chaudhuri, A., Hadjadj, A., Sadot, O. & Ben-Dor, G. (2013), 'Numerical study of shock-wave mitigation through matrices of solid obstacles', *Shock Waves* **23**(1), 91–101.

Christiansen, A. P. & Bogosian, D. D. (2012), Limitations and consequences of fragment protection for near-field airblast measurements, *in* '83rd Shock & Vibration Symposium'.

Codina, R. H., Ambrosini, D. & de Borbón, F. (2013), 'Numerical study of confined explosions in urban environments', *International Journal of Protective Structures* **4**(4), 591–617.

Coughlin, A., Musselman, E., Schokker, A. & Linzell, D. (2010), 'Behavior of portable fiber reinforced concrete vehicle barriers subject to blasts from contact charges', *International Journal of Impact Engineering* **37**(5), 521–529.

Cra (2009), *ProSAir Propagation of Shocks in Air (A Computational Fluids Dynamics Code Developed by the Department of Engineering Systems and Management).*

Craig, J. E. (1977), Weak shocks in open-ended ducts with complex geometry, PhD thesis,

California Institute of Technology.

Crepeau, J., Needham, C. & Hikida, S. (2001), *SHAMRC Second-Order Hydrodynamic Automatic Mesh Refinement Code*, Applied Research Associates, Albuqurque, NM.

Dennis, A. A., Pannell, J. J., Smyl, D. J. & Rigby, S. E. (2020), 'Prediction of blast loading in an internal environment using artificial neural networks', *International Journal of Protective Structures* **12**(3), 287–314.

Dennis, A. A., Pannell, J. J., Smyl, D. J. & Rigby, S. E. (2021), 'Prediction of blast loading in an internal environment using artificial neural networks', *International Journal of Protective Structures* **12**(3), 287–314.

Dey, S., Murugan, T. & Chatterjee, D. (2020), 'Blast wave interaction with generic objects and the measurement of blast wave reattachment distances', *Journal of The Institution of Engineers (India): Series C* **101**(5), 747–760.

Dosanjh, D. S. (1956), Interaction of Grids with Traveling Shock Waves, techreport 3680, Johns Hopkins University: Washington, DC, USA.

Epstein, D. B. & Kudryavtsev, A. N. (2012), Shock and blast wave propagation through a porous barrier, *in* K. Kontis, ed., '28th International Symposium on Shock Waves', Springer Berlin Heidelberg, Berlin, Heidelberg, pp. 537–542.

Éveillard, S., Lardjane, N., Vinçont, J.-Y. & Sochet, I. (2013), 'Towards a fast-running method for blast-wave mitigation by a prismatic blast wall', *Comptes Rendus Mécanique* **341**(8), 625–635.

Fairlie, G. (1998), 'The numerical simulation of high explosives using AUTODYN-2D & 3D', *In Institute of Explosive Engineers 4th Biannual Symposium* pp. 743–751.

Farrimond, D. G., Rigby, S. E., Clarke, S. D. & Tyas, A. (2022), 'Time of arrival as a diagnostic for far-field high explosive blast waves', *International Journal of Protective*

Structures **13**(2), 379–402.

FEMA (2007), Site and urban design for security–guidance against potential terrorist attacks, Technical report, FEMA, Washington, DC, USA.

Foresee, F. D. & Hagan, M. T. (1997), Gauss-newton approximation to bayesian learning, *in* 'Proceedings of international conference on neural networks (ICNN'97)', Vol. 3, IEEE, pp. 1930–1935.

Fouchier, C., Laboureur, D., Youinou, L., Lapebie, E. & Buchlin, J. M. (2017), 'Experimental investigation of blast wave propagation in an urban environment', *Journal of Loss Prevention in the Process Industries* **49**, 248–265.

Fraunhofer EMI (2018), 'Apollo blastsimulator manual, version: 2018.2', *Fraunhofer Institute for High-Speed Dynamics, Ernst-Mach-Institut, Freiburg, Germany* .

Gajewski, T., Peksa, P., Studziński, R., Malendowski, M., Sumelka, W. & Sielicki, W. P. (2022), 'Application verification of blast mitigation through the use of thuja hedges', *International Journal of Protective Structures* **13**(2), 363–378.

Gan, E. C. J., Remennikov, A. & Ritzel, D. (2021), 'Investigation of trees as natural protective barriers using simulated blast environment', *International Journal of Impact Engineering* **158**, 104004.

Gan, K., Brewer, T., Pope, D. & Rigby, S. (2022), 'Probabilistic analysis of blast–obstacle interaction in a crowded internal environment', *Probabilistic Engineering Mechanics* **68**, 103227.

Gauch, H. L., Bisio, V., Rossin, S., Montomoli, F. & Tagarielli, V. L. (2019), 'Predictions of the transient loading on box-like objects by arbitrary pressure waves in air', *Proceedings of the Royal Society A: Mathematical, Physical and Engineering Sciences* **475**(2229), 20190360.

Gebbeken, N. & Döge, T. (2010), 'Explosion protection—Architectural design, urban planning and landscape planning', *International Journal of Protective Structures* **1**(1), 1–21.

Gebbeken, N., Rüdiger, L. & Warnstedt, P. (2018), 'Urbane sicherheit bei explosionen - schutz durch ringgeflecht mit wasser', *Bautechnik* **95**(7), 463–476.

Gebbeken, N., Warnstedt, P. & Rüdiger, L. (2017), 'Blast protection in urban areas using protective plants', *International Journal of Protective Structures* **9**(2), 226–247.

Gencel, O., Asprone, D., Prota, A., Manfredi, G. & Nanni, A. (2015), 'Behavior of full-scale porous gfrp barrier under blast loads', *International Journal of Polymer Science* p. 349310.

Glasstone, S. & Dolan, P. J. (1977), *The Effects of Nuclear Weapons*, U.S. Department of Defense.

Golovastov, S., Mikushkin, A., Mikushkina, A. & Zhilin, Y. (2022), 'Interaction of weak shock waves with perforated metal plates', *Experiments in Fluids* **63**(6), 1–15.

Hahn, A., Mensinger, M. & Rutner, M. (2021), 'Peak overpressure and impulse due to diffraction over a cylinder and/or multi-reflection of a shock wave in structural design-Part I', *International Journal of Protective Structures* **12**(1), 22–48.

Hajek, R. & Foglar, M. (2015), 'Numerical and experimental analysis of the effect of rigid barriers on blast wave propagation', *Journal of Structural Engineering* **141**, 04015061.

Hajek, R., Foglar, M. & Fladr, J. (2016), 'Influence of barrier material and barrier shape on blast wave mitigation', *Construction and Building Materials* **120**, 54–64.

Hallquist, J. O. (2006), *LS-DYNA Theory Manual*, Livermore Software Technology Corporation, CA, USA.

Hao, H., Hao, Y., Li, J. & Chen, W. (2016), 'Review of the current practices in blast-

resistant analysis and design of concrete structures', *Advances in Structural Engineering* .

Hao, Y., Hao, H., Shi, Y., Wang, Z. & Zong, R. (2017), 'Field testing of fence type blast wall for blast load mitigation', *International Journal of Structural Stability and Dynamics* **17**, 1–22.

Heilig, W. (1969), 'Diffraction of a shock wave by a cylinder', *The Physics of Fluids* **12**(5), I–154.

Heylmun, J., Vonk, P. & Brewer, T. (2019), *blastFoam Theory and User Guide*.

Higham, J. E. & Brevis, W. (2018), 'Modification of the modal characteristics of a square cylinder wake obstructed by a multi-scale array of obstacles', *Experimental Thermal and Fluid Science* **90**, 212–219.

Higham, J. E. & Vaidheeswaran, A. (2022), 'Modification of modal characteristics in the wakes of blockages of square cylinders with multi-scale porosity', *Physics of Fluids* **34**(2), 025114.

Higham, J. E., Vaidheeswaran, A., Brevis, W., Nicolleau, F. C. G. A. & Marlow, J. (2021), 'Modification of modal characteristics in wakes of square cylinders with multi-scale porosity', *Physics of Fluids* **33**(4), 045117.

Holgado, D., Montalva, A., Florek, J., El-Domiaty, K. & Calidonna, B. (2022), Deep neural network (DNN) model to predict close-in blast load, *in* 'Structures Congress 2022, Atlanta, Georgia, 20-–23 April', pp. 10–25.

Honghui, S. & Yamamura, K. (2004), 'The interaction between shock waves and solid spheres arrays in a shock tube', *Acta Mechanica Sinica* **20**(3), 219–227.

Hudson, C. (1955), Sound pulse approximations to blast loading (with comments on transient drag), techreport SC-TM-191-55-5., Sandia Corporation.

Hyde, D. (1991), *Conventional Weapons Program (ConWep)*, US Army Waterways Experimental Station, Vicksburg, MS, USA.

Igra, O., Falcovitz, J., Houas, L. & Jourdan, G. (2013), 'Review of methods to attenuate shock/blast waves', *Progress in Aerospace Sciences* **58**, 1–35.

Igra., O., Wu, X., Falcovitz, J., Meguro, T., Takayama, K. & Heilig, W. (2001), 'Experimental and theoretical study of shock wave propagation through double-bend ducts', *Journal of Fluid Mechanics* **437**(210892261), 255–282.

Irving, C. (1995), *In Their Name: Dedicated to the Brave and the Innocent, Oklahoma City, April 1995*, Random House Incorporated.

Isaac, O. S., Alshammari, O. G., Clarke, S. D. & Rigby, S. E. (2022), 'Experimental investigation of blast mitigation of pre-fractal obstacles', *International Journal of Protective Structures* .

Isaac, O. S., Alshammari, O. G., Pickering, E. G., Clarke, S. D. & Rigby, S. E. (2022), 'Blast wave interaction with structures–An overview', *International Journal of Protective Structures* p. 20414196221118595.

Ivanov, A., Fassardi, N., Scafidi, C., Shemen, T. & Eliasson, V. (2019), 'Shock wave attenuation using rigid obstacles with large- and small-scale geometrical features', *Multiscale and Multidisciplinary Modeling, Experiments and Design* **2**, 269–279.

Jin, M., Hao, Y. & Hao, H. (2019), 'Numerical study of fence type blast walls for blast load mitigation', *International Journal of Impact Engineering* **131**, 238–255.

Johansson, M., Larsen, O. P., Laine, L. & REINERTSEN Sverige, A. B. (2007), Explosion at an intersection in an urban environment-experiments and analyses.

Kingery, C. N. & Bulmash, G. (1984), Airblast parameters from TNT spherical air burst and hemispherical surface burst, TR 02555, Ballistics Research Laboratory, Aberdeen

Proving Ground, Maryland, USA.

Kinney, G. F. (1985), *Explosive shocks in air.*, 2nd ed. / gilbert f. kinney and kenneth j. graham. edn, Springer, Berlin.

Klomfass, A. (2018), Accuracy of cfd predictions for explosive far fields, *in* '25th International Conference on Military Aspects of Blast and Shock (MABS252), The Hague, Netherlands'.

Kumar R, A. & Pathak, V. (2020), 'Shock wave mitigation using zig-zag structures and cylindrical obstructions', *Defence Technology* .

Langlet, A., Souli, M., Aquelet, N., Pennetier, O. & Girault, G. (2015), 'Air blast reflecting on a rigid cylinder: simulation and reduced scale experiments', *Shock Waves* **25**(1), 47–61.

Larcher, M. & Casadei, F. (2010), 'Explosions in complex geometries — a comparison of several approaches', *International Journal of Protective Structures* **1**(2), 169–195.

Lee, E., Hornig, H. & Kury, J. (1968), Adiabatic expansion of high explosive detonation products, Technical Report UCRL-50422, Univ. of California Radiation Lab. at Livermore, Livermore, CA (United States).

Lien, F.-S. & Leschziner, M. (1994), 'Upstream monotonic interpolation for scalar transport with application to complex turbulent flows', *International Journal for Numerical Methods in Fluids* **19**(6), 527–548.

Liepmann, H. & Roshko, A. (2013), *Elements of Gas Dynamics*, Dover Books on Aeronautical Engineering, Dover Publications.
URL: *https://books.google.co.in/books?id=IWrCAgAAQBAJ*

Makki, E. A. (2017), Experimental Studies on Mitigating the Risk of Air Blast Loading, Open access dissertations. paper 601, University of Rhode Island.

Mays, G. C., Hetherington, J. G. & Rose, T. A. (1999), 'Response to blast loading of concrete wall panels with openings', *Journal of structural Engineering* **125**(12), 1448–1450.

McGlaun, J., Thompson, S. & Elrick, M. (1990), 'CTH: A three-dimensional shock wave physics code', *International Journal of Impact Engineering* **10**(1-4), 351–360.

Miller, P. (2004), Towards the modelling of blast loads on structures, Master's thesis, University of Toronto.

Miura, H., Matsuo, A. & Tabuchi, G. (2013), 'Numerical investigation for pressure mitigation effects of dike on blast wave', *Journal of Loss Prevention in the Process Industries* **26**(2), 329–337.

Monti, R. (1970), 'Normal shock wave reflection on deformable solid walls', *Meccanica* **5**(4), 285–296.

Mougeotte, C., Carlucci, P., Recchia, S. & Ji, H. (2010), Novel approach to conducting blast load analyses using Abaqus/Explicit-CEL, Technical report, Army Armament Research Development And Engineering Center, Picatinny, Arsenal NJ.

Mulligan, P. (2018), 'Shock wave interaction with a cylindrical structure', *AIP Conference Proceedings* **1979**(1), 160019.

Needham, C. (2018), *Blast Waves*, Cham: Springer International Publishing.

Needham, C. E. (2010), *Blast Waves*, Springer, Berlin, Heidelberg.

Nguyen-Van, V., Wu, C., Vogel, F., Zhang, G., Nguyen-Xuan, H. & Tran, P. (2021), 'Mechanical performance of fractal-like cementitious lightweight cellular structures: Numerical investigations', *Composite Structures* **269**, 114050.

Nichols, J. & Doyle, G. (2014), Current engineering models and capabilities in the vulnerability assessment and protection option (VAPO) software, *in* 'Structures Congress'.

Niollet, J., Yuen, S. C. K. & Nurick, G. (2015), 'A study to assess the use of cylindrical bars as blast barriers', *International Journal of Protective Structures* **6**(2), 263–286.

Norris, C. H., Hansen, R. J., Myle J Holley, J., Biggs, J. M., Nymet, S. & Minami, J. K. (1959), *Structural Design for Dynamic Loads*, McGraw-Hill Book Company, Inc.

Ofengeim, D. K. & Drikakis, D. (1997), 'Simulation of blast wave propagation over a cylinder', *Shock Waves* **7**(5), 305–317.

Pannell, J. J., Panoutsos, G., Cooke, S. B., Pope, D. J. & Rigby, S. E. (2021), 'Predicting specific impulse distributions for spherical explosives in the extreme near-field using a gaussian function', *International Journal of Protective Structures* **12**(4), 437–459.

Pannell, J. J., Rigby, S. & Panoutsos, G. (2022a), 'Physics-informed regularisation procedure in neural networks: an application in blast protection engineering', *International Journal of Protective Structures (accepted)* .

Pannell, J. J., Rigby, S. & Panoutsos, G. (2022b), 'Application of transfer learning for the prediction of blast impulse', *International Journal of Protective Structures (accepted)* .

Parkinson, G. & Jandali, T. (1970), 'A wake source model for bluff body potential flow', *Journal of Fluid Mechanics* **40**(3), 577–594.

Payne, T., Williams, A., Worfolk, T. & Rigby, S. (2016), 'Numerical investigation into the influence of cubicle positioning in large-scale explosive arena trials', *International Journal of Protective Structures* **7**(4), 547–560.

Prasanna Kumar, S. S., Patnaik, B. S. V. & Ramamurthi, K. (2018), 'Prediction of air blast mitigation in an array of rigid obstacles using smoothed particle hydrodynamics', *Physics of Fluids* **30**(4), 046105.

Qasrawi, Y. & Heffernan, P. J. (2016), 'Improved procedure for calculating the cleared pressure acting on a finite target due to a mid-field blast', *International Journal of*

Protective Structures **7**(3), 305–324.

Qasrawi, Y., Heffernan, P. J. & Fam, A. (2015), 'Numerical determination of equivalent reflected blast parameters acting on circular cross sections', *International Journal of Protective Structures* **6**(1), 1–22.

Qi, S., Zhi, X., Fan, F. & Flay, R. G. J. (2020), 'Propagation behaviour of a hemispherical blast wave on a dome roof', *Engineering Structures* **212**, 110524.

Rajkumar, D., Senthil, R., Bala Murali Kumar, B., AkshayaGomathi, K. & Mahesh Velan, S. (2020), 'Numerical study on parametric analysis of reinforced concrete column under blast loading', *Journal of Performance of Constructed Facilities* **34**(1), 04019102.

Ram, O. & Sadot, O. (2013), 'A simple constitutive model for predicting the pressure histories developed behind rigid porous media impinged by shock waves', *Journal of Fluid Mechanics* **718**, 507–523.

Remennikov, A. (2003), 'A review of methods for predicting bomb blast effects on buildings', *Journal of Battlefield Technology* **6**(3).

Remennikov, A. M. & Rose, T. A. (2005), 'Modelling blast loads on buildings in complex city geometries', *Computers & Structures* **83**(27), 2197–2205.

Remennikov, A. M. & Rose, T. A. (2007), 'Predicting the effectiveness of blast wall barriers using neural networks', *International Journal of Impact Engineering* **34**(12), 1907–1923.

Rickman, D. D. & Murrell, D. W. (2006), 'Development of an improved methodology for predicting airblast pressure relief on a directly loaded wall', *J. Pressure Vessel Technol* **129**(1), 195–204.

Rigby, S., Akintaro, O., Fuller, B., Tyas, A., Curry, R., Langdon, G. & Pope, D. (2019), 'Predicting the response of plates subjected to near-field explosions using an energy

equivalent impulse', *International Journal of Impact Engineering* **128**, 24–36.

Rigby, S. E. (2021), Blast wave time of arrival : A reliable metric to determine pressure and yield of high explosive detonations, Technical Report 079, Fire and Blast Information Group Technical Newsletter.

Rigby, S. E., Chaudhary, N., Bogosian, D., Payne, T. & Tyas, A. (2017a), Large-scale validation of Hudson clearing predictions, *in* 'Proceedings of The 17th International Symposium for the Interaction of Munitions with Structures (ISIEMS17), Bad Neuenahr, Germany'.

Rigby, S. E., Fay, S. D., Tyas, A., Warren, J. & Clarke, S. D. (2015), 'Angle of incidence effects on far-field positive and negative phase blast parameters', *International Journal of Protective Structures* **6**(1), 23–42.

Rigby, S. E., Lodge, T. J., Alotaibi, S., Barr, A. D., Clarke, S. D., Langdon, G. S. & Tyas, A. (2020), 'Preliminary yield estimation of the 2020 beirut explosion using video footage from social media', *Shock Waves* **30**(6), 671–675.

Rigby, S. E. & Sielicki, P. (2014), 'An investigation of TNT equivalence of hemispherical PE4 charges', *Engineering Transactions* **62**(4), 423–435.

Rigby, S. E., Tyas, A. & Bennett, T. (2012), 'Single-degree-of-freedom response of finite targets subjected to blast loading – the influence of clearing', *Engineering Structures* **45**, 396–404.

Rigby, S. E., Tyas, A. & Bennett, T. (2014a), 'Elastic-plastic response of plates subjected to cleared blast loads', *International Journal of Impact Engineering* **66**, 37–47.

Rigby, S. E., Tyas, A., Bennett, T., Fay, S. D., Clarke, S. D. & Warren, J. A. (2014b), 'A numerical investigation of blast loading and clearing on small targets', *International Journal of Protective Structures* **5**(3), 253–274.

Rigby, S. E., Tyas, A., Bennett, T., Warren, J. A. & Fay, S. (2013), 'Clearing effects on plates subjected to blast loads', *Proceedings of the Institution of Civil Engineers - Engineering and Computational Mechanics* **166**(3), 140–148.

Rigby, S. E., Tyas, A., Clarke, S. D. & Razaqpur, G. (2017b), 'Approach to developing design charts for quantifying the influence of blast wave clearing on target deformation', *Journal of Structural Engineering* **143**(1), 04016150.

Rigby, S. E., Tyas, A., Fay, S. D., Clarke, S. D. & Warren, J. A. (2014c), Validation of semi-empirical blast pressure predictions for far field explosions – Is there inherent variability in blast wave parameters?, *in* '6th International Conference on Protection of Structures Against Hazards (PSH14)', Tianjin, China, 16–17 October.

Ritzel, D., Van Albert, S., Sajja, V. & Long, J. (2018), 'Acceleration from short-duration blast', *Shock Waves* **28**(1), 101–114.

Robert, B. J., Ranta, D. E. & Joachim, C. E. (2001), *BlastX Code*, Version 4.2, User's Manual, ERDC edn, US Army Engineer Research and Development Center, Vicksburg, MS. GSL TR-01-2.

Rose, T. A., Smith, P. D. & May, J. H. (2006), 'The interaction of oblique blast waves with buildings', *Shock Waves* **16**(1), 35–44.

Rose, T. A., Smith, P. D. & Mays, G. C. (1995), 'The effectiveness of walls designed for the protection of structures against airblast from high explosives.', *Proceedings of the Institution of Civil Engineers - Structures and Buildings* **110**(1), 78–85.

Rose, T. A., Smith, P. D. & Mays, G. C. (1997), 'Design charts relating to protection of structures against airblast from high explosives.', *Proceedings of the Institution of Civil Engineers - Structures and Buildings* **122**(2), 186–192.

Rose, T. A., Smith, P. D. & Mays, G. C. (1998), 'Protection of structures against airburst using barriers of limited robustness.', *Proceedings of the Institution of Civil Engineers*

- *Structures and Buildings* **128**(2), 167–176.

Rose, T. A., Smith, P. D. & McLennan, C. P. (2004), 'Blast loading and clearing on tall buildings', *Journal of Battlefield Technology* **7**(3), 1–8.

Sachs, D. C. & Cole, E. (1976), Air blast measurement technology, Contractor Report DNA 4115F, Defence Nuclear Agency.

Santos, F., Larcher, M., Valsamos, G. & Karlos, V. (2018), 'Access control points: Reducing a possible blast impact by meandering', *Advances in Civil Engineering* **2018**, 3506892.

Sasoh, A., Matsuoka, K., Nakashio, K., Timofeev, E., Takayama, K., Voinovich, P., Saito, T., Hirano, S., Ono, S. & Makino, Y. (1998), 'Attenuation of weak shock waves along pseudo-perforated walls', *Shock Waves* **8**(3), 149–159.

Schunck, T. & Eckenfels, D. (2021), 'Experimental study of explosion mitigation by deployed metal combined with water curtain', *Applied Sciences* **11**(14).

Seeraj, S. & Skews, B. W. (2009), 'Dual-element directional shock wave attenuators', *Experimental Thermal and Fluid Science* **33**, 503–516.

Sha, S., Chen, Z. & Jiang, X. (2014), 'Influences of obstacle geometries on shock wave attenuation', *Shock Waves* **24**, 573–582.

Shi, Y., Hao, H. & Li, Z.-X. (2007), 'Numerical simulation of blast wave interaction with structure columns', *Shock Waves* **17**(1), 113–133.

Shin, J. & Whittaker, A. S. (2019), 'Blast-wave clearing for detonations of high explosives', *Journal of Structural Engineering* **145**(7), 04019049.

Skews, B. W., Draxl, M. A., Felthun, L. & Seitz, M. W. (1998), 'Shock wave trapping', *Shock Waves* **8**(1), 23–28.

Smith, P. (2010), 'Blast walls for structural protection against high explosive threats: A review', *International Journal of Protective Structures* **1**(1), 67–84.

Smith, P. D. & Rose, T. A. (2006), 'Blast wave propagation in city streets—an overview', *Progress in Structural Engineering and Materials* **8**(1), 16–28.

Smith, P. D., Rose, T. A., Krahe, S. L. & Franks, M. A. (2003), 'Façade failure effects on blast propagation along city streets', *Proceedings of the Institution of Civil Engineers - Structures and Buildings* **156**(4), 359–365.

Smith, P., Rose, T. & Ng, S. (2004), 'The influence of areal density on the shielding and channelling of blast by buildings', *18th International Symposium on Military Aspects of Blast and Shock* .

Sreenivasan, K. R. (1991), 'Fractals and multifractals in fluid turbulence', *Annual Review of Fluid Mechanics* **23**(1), 539–604.

Steven, S. & Khaled, E.-R. (2017), 'Quantifying blast effects on constructed facilities behind blast walls', *Journal of Performance of Constructed Facilities* **31**(4), 04017027.

Sugiyama, Y., Wakabayashi, K., Matsumura, T. & Nakayama, Y. (2015), 'Effect of a small dike on blast wave propagation', *Science and Technology of Energetic Materials* **76**(4).

Sung, S.-H. & Chong, J.-W. (2020), 'A fast-running method for blast load prediction shielding by a protective barrier', *Defence Technology* **16**(2), 308–315.

Suzuki, K., Himeki, H., Watanuki, T. & Abe, T. (2000), 'Experimental studies on characteristics of shock wave propagation through cylinder array', *The Institute of Space and Astronautical Science* **676**.

Tomasz, G., Piotr, P., Robert, S., Michał, M., Wojciech, S. & Piotr, S. W. (2022), 'Application verification of blast mitigation through the use of thuja hedges', *International*

Journal of Protective Structures **13**(2), 363–378.

Trélat, S., Sochet, I., Autrusson, B., Loiseau, O. & Cheval, K. (2007), 'Strong explosion near a parallelepipedic structure', *Shock Waves* **16**(4), 349–357.

Trélat, S., Sturtzer, M.-O. & Eckenfels, D. (2020), 'Multi-scale experimental study of blast propagation around a hemi-cylindrical barrier', *WIT Transactions on The Built Environment* **198**, 53 – 64.

Turcotte, D. L. (1988), 'Fractals in fluid mechanics', *Annual Review of Fluid Mechanics* **20**(1), 5–16.

Tyas, A., Warren, J. A., Bennett, T. & Fay, S. (2011), 'Prediction of clearing effects in far-field blast loading of finite targets', *Shock Waves* **21**(2), 111–119.

Ullah, A., Ahmad, F., Jang, H.-W., Kim, S.-W. & Hong, J.-W. (2017), 'Review of analytical and empirical estimations for incident blast pressure', *KSCE Journal of Civil Engineering* **21**(6), 2211–2225.

US Army Corps of Engineers (1990), *TM5-1300, Structures to Resist the Effects of Accidental Explosions*, Washington, DC, USA.

US Department of Defence (2008), *UFC 3-340-02, Structures to resist the effects of accidental explosions*, Washington, DC, USA.

US General Services Administration (2004), *Oklahoma City Federal Building*, GSA, Washington DC, USA.

von Rosen, B., Guilbeault, R. & Contestabile, E. (2004), A preliminary investigation into the propagation of shock waves behind a simple rectangular structure, *in* 'MABS18, Bad Reichenhall, Germany'.

Wager, P. (2005), *Shock User's Manual Version 1.0*, Naval Facilities Engineering Service Center, Port Hueneme CA.

Wan, Q. & Eliasson, V. (2015), 'Numerical study of shock wave attenuation in two-dimensional ducts using solid obstacles: How to utilize shock focusing techniques to attenuate shock waves', *Aerospace* **2**, 203–221.

Warnstedt, P. & Gebbeken, N. (2020), 'Innovative protection of urban areas –experimental research on the blast mitigating potential of hedges', *Landscape and Urban Planning* **202**, 103876.

Werner, D. H. & Ganguly, S. (2003), 'An overview of fractal antenna engineering research', *IEEE Antennas and Propagation Magazine* **45**(1), 38–57.

Whitham, G. (1959), 'A new approach to problems of shock dynamics Part 2: Three-dimensional problems', *Journal of Fluid Mechanics* **5**(3), 369–386.

Whitham, G. B. (1957), 'A new approach to problems of shock dynamics Part 2. Three-dimensional problems', *Journal of Fluid Mechanics* **5**, 369–386.

Williams, G. D. & Williamson, E. B. (2012), 'Procedure for predicting blast loads acting on bridge columns', *Journal of Bridge Engineering* **17**(3), 490–499.

Xiao, W., Andrae, M. & Gebbeken, N. (2017), Numerical prediction of the shock wave mitigation effect using protective barriers made of steel posts with a square hollow section, *in* '17th International Symposium on the Interaction of the Effects of Munitions with Structures (ISIEMS)', Bad Neuenahr, Germany, 16–20 October.

Xiao, W., Andrae, M. & Gebbeken, N. (2018), 'Experimental and numerical investigations of shock wave attenuation effects using protective barriers made of steel posts', *Journal of Structural Engineering* **144**(11), 04018204.

Xiao, W., Andrae, M. & Gebbeken, N. (2019), 'Experimental and numerical investigations on the shock wave attenuation performance of blast walls with a canopy on top', *International Journal of Impact Engineering* **131**, 123–139.

Xiao, W., Andrae, M. & Gebbeken, N. (2020*a*), 'Numerical study of blast mitigation effect of innovative barriers using woven wire mesh', *Engineering Structures* **213**.

Xiao, W., Andrae, M. & Gebbeken, N. (2020*b*), 'Numerical study on impulse reduction performance of protective barriers made of steel posts', *Journal of Structural Engineering (United States)* **146**, 1–13.

Xiao, W., Andrae, M., Steyerer, M. & Gebbeken, N. (2021), 'Investigations of blast loads on a two-storeyed building with a gable roof: Full-scale experiments and numerical study', *Journal of Building Engineering* **43**, 103111.

Yang, J. Y., Liu, Y. & Lornax, H. (1987), 'Computation of shock wave reflection by circular cylinders', *AIAA Journal* **25**(5), 683–689.

Zhang, J., Li, Y., Zhao, T., Zhang, Q., Zuo, L. & Zhang, K. (2021), 'Machine-learning based design of digital materials for elastic wave control', *Extreme Mechanics Letters* **48**, 101372.

Zhi, X.-d., Qi, S.-b. & Fan, F. (2019), 'Temporal and spatial pressure distribution characteristics of hemispherical shell structure subjected to external explosion', *Thin-Walled Structures* **137**, 472–486.

Zhou, X. Q. & Hao, H. (2008), 'Prediction of airblast loads on structures behind a protective barrier', *International Journal of Impact Engineering* **35**(5), 363–375.

Zong, R., Hao, H. & Shi, Y. (2017), 'Development of a new fence type blast wall for blast protection: Numerical analysis', *International Journal of Structural Stability and Dynamics* **17**(6).